

QUANTUM PLASMONIC SENSING WITH APPLICATION TO HIV RESEARCH



Kelvin Tafadzwa Mpofu (213572387)

School of Health Sciences

University of KwaZulu-Natal

A thesis submitted in fulfillment of the requirements for the degree of

Doctor of Philosophy

December, 2020

Abstract

The main goal of this thesis is to show how the use of quantum states of light in bio-sensing with surface plasmon resonance (SPR) gives an enhancement over using classical states. SPR is a highly sensitive technique for monitoring changes in the optical properties of a substance in the immediate vicinity of a sensor surface, which makes it very useful in biosensing and surface science research. We focus primarily on a bio-sensing SPR setup known as the Kretschmann configuration in which surface plasmons are excited using a bulk prism and a gold coated microscope slide. The excitation is performed by means of an evanescent field arising from total internal reflection from the backside of the sensor surface.

We show theoretically that using quantum states of light such as the Fock state, two-mode squeezed vacuum and two-mode squeezed displaced state improves the precision in the estimation of kinetic parameters measured from the sensorgrams produced by the Kretschmann configuration. Quantum states of light allow us to measure the parameters more accurately in comparison to the use of classical states of light. We look at a theoretical application of quantum bio-sensing in an immobilized Bovine serum albumin (BSA) interaction with anti-BSA, a binding reaction between a phosphate-buffered saline (PBS) solution that contains Bovine carbonic anhydrase and its inhibitor benzene-sulfonamide, and a HIV case study. In our HIV case study we look at the binding reaction between a variant of HIV-1 protease and nelfinavir which is an inhibitor.

The thesis also looks at an experimental implementation of the Kretschmann configuration with light from a single-photon source and shows an enhancement in sensitivity. We use the spontaneous parametric down conversion process to generate our single photons which we use to study the binding kinetics of BSA on a gold slide. This experiment is done with the anticipation that it will be extended in future to a drug kinetics study with HIV protease as we look at drug development.

Preface

The work reported in this thesis was theoretical and experimental in nature, and was carried out in the School of Health Sciences, at the University of KwaZulu-Natal and the School of Physics, at Stellenbosch University under the supervision of Prof. Gert Kruger and Prof. Mark Tame.

As the candidate's supervisor I have approved this thesis for submission.

Prof. Gert Kruger

Date

Prof. Mark Tame

Date

Declaration

I, Kelvin Mpofu declare that

1. The research reported in this thesis, except where otherwise indicated, is my original research.
2. This thesis has not been submitted for any degree or examination at any other university.
3. This thesis does not contain other persons' data, pictures, graphs or other information, unless specifically acknowledged as being sourced from other persons.
 - (a) This thesis does not contain other persons' writing, unless specifically acknowledged as being sourced from other researchers. Where other written sources have been quoted, then:
 - (b) Their words have been re-written but the general information attributed to them has been referenced. Where their exact words have been used, their writing has been placed inside quotation marks, and referenced.
4. This thesis does not contain text, graphics or tables copied and pasted from the Internet, unless specifically acknowledged, and the source being detailed in the thesis and in the References sections.

Signed: _____

Manuscripts

At the time of writing, two manuscripts were prepared:

1. K. Mpofu, C. Lee, G. Maguire, G. Kruger and M. Tame, Measurement of binding kinetics using quantum plasmonic resonance sensing, in preparation (2020).

My contribution: I coded the simulations, performed data processing and analysis, and wrote the related sections of the paper.

2. K. Mpofu, C. Lee, G. Maguire, G. Kruger and M. Tame, Experimental measurement of binding kinetics using quantum plasmonic resonance sensing, in preparation (2020).

My contribution: I built the SPDC single-photon source and the SPR setup, performed data processing and analysis, and wrote the related sections of the paper.

Acknowledgements

First and foremost I would like to thank my supervisor Prof. Mark Tame for the experience I have gained over my tenure as a PhD student and the great support he has given me over the tenure of my PhD. This thesis would not have had been possible without him. I would also like to thank my friends and family for all the support over the course of my thesis. I could not have had been able to get as far as I have without their continuing support. I would also like to thank all the scientists and researchers who have contributed and those who continue to contribute to our body of scientific knowledge. Were it not for their relentless pursuit of knowledge then certainly none of this would be possible. Special thanks to Jennifer Saunders for making my stay in Stellenbosch a pleasant one, especially given the fact that it was in the midst of a pandemic. I would also like to thank my uncle and aunt Tapson and Rubie Rukuni for their support over the course of my studies.

Finally, I would like to thank my mother, Mary Rukuni. I would not have the courage to do what I do were it not for her support. She is at the heart of all that I have achieved, so much so that I fear there may not be words which I feel sufficient enough to describe my gratitude.

Contents

1	Introduction and overview	1
1.1	Overview of the thesis	3
2	Plasmonic sensing and quantum metrology	5
2.0.1	Scaling and the effect of noise	5
2.0.2	Quantum metrology and its application to biology	7
2.1	Surface plasmon resonance	8
2.1.1	Evanescent waves	11
2.1.2	Evanescent waves and surface plasmons	13
2.1.3	Coupling strategies and sensing techniques	16
2.1.4	SPR experimental setup	17
2.1.5	SPR in biology	18
2.1.6	SPR in drug kinetics	19
2.1.7	Interaction kinetics	20
2.2	Introduction to estimation theory	23
2.2.1	Classical parameter estimation	23
2.2.2	Deriving the Cramér Rao bound	23
2.2.3	Quantum parameter estimation	25
2.2.4	Quantum Fisher information	26
2.2.5	Quantum Fisher information example calculation	26
2.3	Quantum description of light	27
2.3.1	Quantum states of light	28
2.4	Spontaneous parametric down conversion	32
2.4.1	Experimental setup for SPDC	33
2.4.2	Polarisation in non-linear optical materials	34
2.4.3	Second-order non-linear processes	34
2.4.4	SPDC fundamentals	36
2.4.5	Choosing an appropriate crystal for SPDC	37
2.4.6	Phase matching	38
2.5	Quantum plasmonic sensing	38
2.5.1	Classical intensity based sensing	39
2.5.2	Quantum intensity-based plasmonic sensing	41
2.5.3	Quantum case with two-mode Fock state	42
2.5.4	Classical case with two-mode coherent state	42
3	Measurement of binding kinetics using quantum plasmonic sensing	45
3.1	Large sensorgram deviation	48
3.1.1	Optimized two-mode case	54
3.1.2	Single-mode	56
3.1.3	Enhancement with changing R value	58
3.1.4	M-enhancement	61
3.1.5	Conclusion	62

3.2	Small sensorgram deviation	62
4	Application of quantum plasmonic sensing to HIV case study	67
4.0.1	Standard two-mode case	68
4.0.2	Optimized two-mode case	70
4.0.3	Single-mode case	72
4.0.4	Conclusion	74
5	Experimental quantum plasmonic sensing	75
5.1	Plasmonic sensing with single photons from SPDC source	75
6	Conclusion	81
A	Calculations for phase measurements using NOON and coherent states	83
A.1	Phase measurements using NOON states	83
A.1.1	Optimizing the quantum case	86
A.2	Phase measurements using coherent states	87
A.2.1	Optimizing the classical case	89
B	Calculation of the precision for a two-mode squeezed displaced vacuum state	90
C	Two-dimensional and three-dimensional plots in quantum surface plasmon sensing	93
D	General formula for the noise reduction in a two-mode system	97
E	Noise ratio (Noise reduction factor)	99
F	Inferring a parameter from a quantum observable	101
G	From the Heisenburg picture to the Schrdinger picture	102
H	Calculating $\langle \hat{a}_{\text{out}}^\dagger \hat{a}_{\text{out}} \rangle$ used in the general formula for $\langle \Delta \hat{M} \rangle$	103
I	Beamsplitter and phaseshifter	104
I.1	Action of the beam splitter	104
I.1.1	The action of a beam splitter on coherent states	104
I.1.2	Phase shifter on coherent states	105
J	Abbreviations	106

List of Figures

2.1	Model for general two-mode sensing setup. The brown box represents an intermediate process which depends on the type of sensing being done, e.g., it could be a phase shifter if we are doing phase sensing or transmissive device if we are doing intensity sensing.	6
2.2	Mach-Zehnder setup showing how we can physically implement a two-mode sensing setup. By taking an intensity-difference measurement between detectors a and b we can perform phase sensing. The dotted box around the lasers shows where the region which can be considered as the input preparation region. The dotted box around the phase shifter shows where the region which can be considered as the intermediate process region. The dotted box around the detectors shows where the region which can be considered as the measurement region.	7
2.3	Length scales in biology. The diffraction limit of visible light restricts far-field imaging resolution to around 200 nm, which is the approximate scale of organelles. Single proteins or other biomolecules are not typically observable with a light microscope and super-resolution techniques are required to study their function and structure. Taken from Ref. [12].	8
2.4	Exciting surface plasmons. The surface plasmon is on the surface of the metals plate.	9
2.5	SPR dip with resonance angle. R is the reflected intensity at fixed refractive index of the dielectric materials $n_1 = 1.5$ and $n_2 = 1.39$	9
2.6	SPR dip with refractive index of the dielectric material. R is the reflected intensity at fixed incident angle $\theta = 73^\circ$ and $n_1 = 1.5$	9
2.7	SPR dip with refractive index of both the dielectric material and incident angle. The refractive index $n_1 = 1.5$	10
2.8	Ray diagram showing that a portion of the wave will be transmitted at an angle, θ_t , and a portion will be reflected back at an angle, θ_r	12
2.9	Frustrated total internal reflection.	13
2.10	A two-layer geometry for a surface plasmon field. The region $z < 0$ is metallic with complex dielectric function $\epsilon(\omega)$. The dielectric region ($z > 0$) is air with $\epsilon = 1$. The interface between the regions is $z = 0$	14
2.11	Figure showing propagation relations in different media. The h in the subscript of the wave number k stands for high index medium. This Figure was taken from Ref. [79].	16
2.12	Figure showing propagation relations in a Kretschmann prism setup and why surface plasmons at the metal-glass interface cannot be excited. Surface plasmons are excited at the metal-air interface by making use of a SiO_2 prism. We can see this from the meeting of the blue dispersion line from the prism with the red dispersion curve of the surface plasmon in the air/metal interface. Surface plasmons at the metal/glass interface can not be excited, i.e., the green curve. This figure was taken from Ref. [79].	17
2.13	The experimental setup used for SPR. 785nm laser light is sent through two half wave plates and a PBS before hitting the prism with the gold slide exciting the surface plasmons in the metal-air interface. The light reflected from the prism is collected into a CCD detector.	18

2.14	Shift in the angular position of the dip due to changing refractive index of the dielectric on top of the gold surface. At a refractive index of 1.39 we have the orange resonance curve but as the refractive index changes to 1.4 the dip shifts to the right and aligns with the red curve.	19
2.15	The three phases of interaction kinetics. The response unit is a generalization which can refer to a change in the resonance angle, the intensity or refractive index depending on what you are measuring.	20
2.16	The figure shows the use of equilibrium dialysis technique to measure the affinity of a ligandreceptor interaction with a semi-permeable membrane shown by the dashed line in the middle of a water chamber. An important assumption is that the association and dissociation rates are of the same order of magnitude. Figure is taken from Ref. [64].	21
2.17	The three phases of interaction kinetics. The response unit is a generalization which can refer to a change in the resonance angle, the intensity or refractive index depending on what you are measuring. Figures were taken from [48].	22
2.18	Setup of the single-photon source. A and B are the two modes.	33
2.19	Second-order non-linear processes. When an electromagnetic field interacts with a non-linear medium having a non-linear susceptibility χ^2 , the resulting electromagnetic field contains second harmonics ($2\omega_1, 2\omega_2$), sum-frequency ($\omega_1 + \omega_2$) and difference-frequency ($\omega_1 - \omega_2$) components [66].	35
2.20	Spontaneous parametric down-conversion. A pump photon with frequency ω_p propagating towards a non-linear crystal is spontaneously down-converted into two photons with frequencies ω_s and ω_i [66].	36
2.21	Energy and momentum diagrams of a single SPDC process. The process conserves energy and momentum, which implies that the frequencies of the photons satisfy $\omega_s + \omega_i = \omega_p$ and their wave vectors $\mathbf{k}_s + \mathbf{k}_i = \mathbf{k}_p$ [66].	36
2.22	SPDC Type-I: Degenerate, idler and signal cone are identical and overlap.	38
2.23	Theoretical model for two-mode plasmonic intensity sensing.	39
2.24	Comparing $\langle \Delta \hat{M}_{\text{coherent}} \rangle$ with $\langle \Delta \hat{M}_{\text{fock}} \rangle$. (a) The case where the refractive index of the analyte being sensed is fixed and we change the resonance angle. The refractive index of the analyte is 1.39. (b) The case where the resonance angle of the analyte being sensed is fixed and we change the refractive index. The resonance angle is 73° . The red line is the Fock state and the black line is the coherent state. These plots assume that there is no system loss in the setup, i.e., $\eta_a = \eta_b = 1$. The photon number $N= \alpha ^2=10$	43
2.25	Enhancement ratio R. (a) The case where the refractive index of the analyte being sensed is fixed and we change the resonance angle. The refractive index is 1.39 (b) The case where the resonance angle of the analyte being sensed is fixed and we change the refractive index. The resonance angle is 73° . These plots assume that there is no system loss in the setup, i.e., $\eta_a = \eta_b = 1$. The photon number $N= \alpha ^2=10$	44
3.1	Reflectance as a function of time sensorgram for a binding reaction whose refractive index goes from 1.3352 to 1.3458. This is an ideal case where we have just extracted the kinetic parameters and used them to generate our model. In this model we used, $k_s = 10.5193 \times 10^{-3} \text{s}^{-1}$, $k_d = 7.85 \times 10^{-3} \text{s}^{-1}$, $\tau = 1100 \text{s}$, $A_\infty = 2.63928^\circ$, $A_\tau = 2.6393^\circ$, $\theta(0) = 71.0966^\circ$	46
3.2	The blue line represents the non-linear response of an example R model, the orange line is the linear response. The corresponding sensorgrams (cf. Fig 3.1) are slightly distorted with respect to each other.	47
3.3	Plot of sensorgram with noise added to it. After we add noise to our ideal case it generally looks like this. The upper and lower dashed lines represent $\pm \frac{\langle \Delta \hat{M} \rangle}{\sqrt{\nu}}$. The middle dashed line is $\langle \Delta \hat{M} \rangle$ for $\nu \rightarrow \infty$. In the plot here we used photon number $N=5$, $\eta_a = 0.8$ and $\eta_b = 0.8$	48

3.4	Standard deviation vs p values for k_s and k_d . The plots are for a coherent state, $m=10$ and $\nu = 100$	48
3.5	The angle model from Ref. [20].	49
3.6	The R model for the angle model in Ref. [20].	49
3.7	Two-mode standard results, ν dependence, with $p=1500$, photon number=10 and $m=10$ (no loss, i.e. $\eta_a = \eta_b = 1$).	50
3.8	Two-mode standard results, ν dependence, with $p=1500$, photon number=10 and $m=50$ (no loss, i.e. $\eta_a = \eta_b = 1$).	51
3.9	Two-mode standard results, photon number dependence, $m=10$, $p=1500$, $\nu = 100$ (no loss, i.e. $\eta_a = \eta_b = 1$).	51
3.10	Two-mode standard results, ν dependence, with $p=1500$, photon number=10 and $m=10$ (loss, i.e. $\eta_a = \eta_b = 0.8$).	52
3.11	Two-mode standard results, ν dependence, with $p=1500$, photon number=10 and $m=50$ (loss, i.e. $\eta_a = \eta_b = 0.8$).	52
3.12	Two-mode standard results, photon number dependence, $m=10$, $p=1500$, $\nu = 100$ (loss, i.e. $\eta_a = \eta_b = 0.8$).	53
3.13	Two-mode standard results optimized, ν dependence, with $p=1500$, photon number=10 and $m=10$ (Optimized loss, i.e. $\eta_a = 1$ and $\eta_b = R\eta_a$).	54
3.14	Two-mode standard results optimized, photon number dependence, with $p=1500$, $\nu = 100$ and $m=10$ (Optimized loss, i.e. $\eta_a = 1$ and $\eta_b = R\eta_a$).	55
3.15	Two-mode standard results optimized, ν dependence, with $p=1500$, photon number=10 and $m=10$ (Optimized loss, i.e. $\eta_a = 0.8$ and $\eta_b = R\eta_a$).	55
3.16	Optimized two-mode results, photon number dependence, with $p=1500$, $\nu = 100$ and $m=10$ (Optimized loss, i.e. $\eta_a = 0.8$ and $\eta_b = R\eta_a$).	56
3.17	Single-mode results, ν dependence, with $p=1500$, photon number=10 and $m=10$ (No loss, i.e. $\eta_a = 1$ and $\eta_b = 0$).	56
3.18	Single-mode results, photon number dependence, with $p=1500$, $\nu = 100$ and $m=10$ (No loss, i.e. $\eta_a = 1$ and $\eta_b = 0$).	57
3.19	Single-mode results, ν dependence, with $p=1500$, photon number=10 and $m=10$ (loss, i.e. $\eta_a = 0.8$ and $\eta_b = 0$).	57
3.20	Single-mode results, photon number dependence, with $p=1500$, $\nu = 100$ and $m=10$ (loss, i.e. $\eta_a = 0.8$ and $\eta_b = 0$).	58
3.21	Enhancement with changing R value, $m=10$, $p=1500$, $\nu = 100$ and photon number=10.	59
3.22	Enhancement with changing R value, $m=10$, $p=1500$, $\nu = 100$ and photon number=10.	59
3.23	Enhancement with changing R value, $m=10$, $p=1500$, $\nu = 100$. This is for the standard two-mode.	59
3.24	Enhancement with changing R value, $m=10$, $p=1500$, $\nu = 100$. This is for the optimized two-mode.	60
3.25	m-Enhancements for the k_d parameter, $\eta_a = \eta_b = 1$, $p=1500$ and photon number=10.	61
3.26	m-Enhancements for the k_s parameter, $\eta_a = \eta_b = 1$, $p=1500$ and photon number=10.	62
3.27	m-Enhancements for the k_a parameter, $\eta_a = \eta_b = 1$, $p=1500$ and photon number=10.	62
3.28	The R model for the angle model in Ref. [21].	63
3.29	Two-mode standard results, photon number dependence, $m=10$, $p=1500$, $\nu = 100000$ (no loss, i.e. $\eta_a = \eta_b = 1$).	64
3.30	Two-mode standard results, photon number dependence, $m=10$, $p=1500$, $\nu = 100000$ (loss, i.e. $\eta_a = \eta_b = 0.8$).	64
3.31	Two-mode standard results, photon number dependence, $m=10$, $p=1500$, $\nu = 100000$ (Optimized loss, i.e. $\eta_a = 1$ and $\eta_b = \eta_a R$).	65
3.32	Two-mode standard results, photon number dependence, $m=10$, $p=1500$, $\nu = 100000$ (Optimized loss, i.e. $\eta_a = 0.8$ and $\eta_b = \eta_a R$).	65
3.33	Single-mode standard results, photon number dependence, $m=10$, $p=1500$, $\nu = 100000$ (loss, i.e. $\eta_a = 1$ and $\eta_b = 0$).	66
3.34	Single-mode standard results, photon number dependence, $m=10$, $p=1500$, $\nu = 100000$ (loss, i.e. $\eta_a = 0.8$ and $\eta_b = 0$).	66

4.1	The R model for the angle model in Ref. [95].	67
4.2	Structural model of the HIV-1 protease structure in a complex with an inhibitor taken from Ref. [16].	68
4.3	Two-mode standard results, ν dependence, $m=10$, $p=1500$, photon-number=5000 (no loss, i.e., $\eta_a = \eta_b = 1$).	68
4.4	Two-mode standard results, photon number dependence, $m=10$, $p=1500$, $\nu = 10^6$ (no loss, i.e., $\eta_a = \eta_b = 1$).	69
4.5	Balanced two-mode standard results, ν dependence, $m=10$, $p=1500$, photon-number=5000 (loss, i.e., $\eta_a = \eta_b = 0.8$).	69
4.6	Two-mode standard results, photon number dependence, $m=10$, $p=1500$, $\nu = 10^6$ (loss, i.e., $\eta_a = \eta_b = 0.8$).	70
4.7	Optimized two-mode standard results, ν dependence, $m=10$, $p=1500$, photon-number=5000 (loss, i.e., $\eta_a = 1$ and $\eta_b = R$).	70
4.8	Optimized two-mode standard results, photon number dependence, $m=10$, $p=1500$, $\nu = 10^6$ (no loss, i.e., η_a and $\eta_b = R$).	71
4.9	Optimized two-mode results, ν dependence, $m=10$, $p=1500$, photon-number=5000 (loss, i.e., $\eta_a = 0.8$ and $\eta_b = 0.8R$).	71
4.10	Optimized two-mode standard results, photon number dependence, $m=10$, $p=1500$, $\nu = 10^6$ (loss, i.e., $\eta_a =$ and $\eta_b = 0.8R$).	72
4.11	Single-mode standard results, ν dependence, $m=10$, $p=1500$, photon-number=5000 (no loss, i.e., $\eta_a = 1$ and $\eta_b = 0$).	72
4.12	Single-mode standard results, photon number dependence, $m=10$, $p=1500$, $\nu = 10^6$ (no loss, i.e., $\eta_a = 1$ and $\eta_b = 0$).	73
4.13	Single-mode results, ν dependence, $m=10$, $p=1500$, photon-number=5000 (loss, i.e., $\eta_a = 0.8$ and $\eta_b = 0$).	73
4.14	Single-mode results, photon number dependence, $m=10$, $p=1500$, $\nu = 10^6$ (loss, i.e., $\eta_a = 0.8$ and $\eta_b = 0$).	74
5.1	Experimental implementation of plasmonic sensing with single photons from a SPDC source.	75
5.2	Plots (a) and (b) show how the counts change with time in the signal mode as the refractive index changes and how they are constant in the idler mode.	76
5.3	Plots (a) and (b) show the relationship between T and ΔT , the orange line represents the region for quantum states and the blue line shows the region for classical states. The blue points in (a) are the data points we measured in our experiment. (b) Zoom in shows them more clearly for us to see the points.	77
5.4	Plots (a) and (b) show the sensorgram as T changes with time. (b) shows how the uncertainty in T changes for the predicted classical case (blue line) and for the quantum case we measured (orange line).	77
5.5	(a) Error-plot for quantum experimental data. (b) Error plot for classical simulated data. (c) shows these plots side by side, where a small reduction in the error can be seen for the quantum case over time. (d) shows how R changes at each point in time over the duration of the experiment, the grey shaded region represents the classical area and anything above represents the quantum area, the dotted blue line shows a general trend.	78
5.6	(a) Sensorgram fit using Gauss-Newton non-linear fit. (b) A histogram of the k_s value extracted from the fit using quantum data. (c) A histogram of the k_s value extracted from the fit using simulated classical data.	79
5.7	(a) Box-and-whisker plot for comparison of quantum experiment and classical simulation. The box plot shows us the shape of the distribution of the parameter k_s , its central value, and its variability. (b) A plot showing k_s values and Δk_s for the quantum and classical data.	79
5.8	Picture of the plasmonic sensing setup and the SPDC single photon source.	80

A.1	Theoretical model for two-mode phase sensing using NOON states.	83
A.2	Theoretical model for two-mode phase sensing using coherent states.	87
B.1	Theoretical model for 2 mode intensity sensing.	90
C.1	SPR dip with refractive index of both the dielectric material and incident angle. . .	93
C.2	SPR dip with changing refractive index of the dielectric material and incident angle fixed.	94
C.3	SPR dip with fixed refractive index of the dielectric material and incident angle changing.	94
C.4	Derivative of reflectivity, R, with respect to refractive index.	95
C.5	Three-dimensional plot for the derivative of the reflectivity, R.	95
C.6	Inflection point at which the sensitivity is maximized for different states.	95
C.7	Inflection point at which the estimate precision is minimized for different states. . .	96
E.1	Plot (a) shows the legend for the different states. Plots (b) and (c) show how the ratios for the different states vary with changing T values. Plot (b) shows the general behaviour whilst (c) shows the region where the quantum states beat the coherent state, i.e., the ratio values < 1	100
E.2	Plots (a) and (b) show how the ratios for the different states vary with changing T values. Plot (a) shows the general behavior whilst (b) shows the region where the quantum states beat the coherent state, i.e., the ratio values < 1	100
E.3	Plots (a) and (b) show how the ratios for the different states vary with changing T values. Plot (a) shows the general behavior whilst (b) shows the region where the quantum states beat the coherent state, i.e., the ratio values < 1	100
I.1	Model of beamsplitter action.	104

Chapter 1

Introduction and overview

Over the past few years there has been a rapid increase in the number of viral strains springing up around the world [1]. These viral strains are rapidly evolving, which leads to epidemics and pandemics. This has made the need for accurate diagnostics to be greater than ever. Along with accurate diagnostics, quick development of treatment has also become vital to halt the progressive march of associated diseases. Optical bio-sensors such as those based on surface plasmon resonance (SPR) have emerged in recent times as the most reliable diagnostic devices owing to their portability, reproducibility, sensitivity and specificity [1]. SPR allows us to analyse the kinetics of bio-molecular interactions in a label-free manner. It measures binding constants, association and dissociation rate constants and stoichiometry for bio-molecular binding interaction kinetics. The practical applications of SPR analyses include kinetic analysis, equilibrium analysis and concentration analysis, which are vital for the diagnosis of different stages of a disease such as the EpsteinBarr virus [2]. The diagnosis of different stages of a disease is done through the detection of antibodies interacting with different antigens (molecular structures on the surface of the virus) present on the virus, i.e., different antibodies are produced by the body to combat different stages of the virus development [2].

SPR technologies have also been used in food monitoring, this includes the detection of antibiotics in milk samples (using a portable six-channel SPR sensor) [3] and mycotoxin patulin (immunochemical SPR) [4]. SPR was also utilized to monitor the binding kinetics of a dengue antibody with corresponding dengue antigen in a real-time manner [5]. SPR technologies have been used in such a wide range of applications that the importance of SPR is not in question. We have seen applications ranging from the detection and quantification of Enterovirus 71 [6], membrane interaction studies for virus detection [13] and vaccine design [15]. SPR technology has surpassed the conventional virus detection methods in its utility, particularly in medical diagnostics and healthcare [15].

While Rufus Ritchie predicted the existence of surface plasmons in 1957 [17], the physical phenomenon of SPR was first observed in 1902 by R. M. Wood at Johns Hopkins University. He observed that if he shone polarised light onto a metal-backed diffraction grating, a pattern of unusual dark and light bands appeared in the reflected light [23]. A few years later, Lord Rayleigh in 1907 developed the first theoretical treatment of this observation of an esoteric optical phenomenon. In 1968 Otto showed that SPR can be excited by using attenuated total internal reflection [8], Kretschman and Raether obtained the same results from a different configuration of attenuated total internal reflection [9, 10]. In 1983 B. Liedberg demonstrated that SPR can be used for biosensing [74]. It has since become a very powerful label-free tool to study the interactions between target and bio-recognition molecules. In the early 1990s SPR became the underlying technology in affinity biosensors for bio-molecular interaction analysis (BIA), which studies the functional properties of biomolecules [26].

SPR involves the excitation (coherent oscillation) of conduction electrons in a metal at the interface between the metal and a dielectric medium [25]. This excitation is induced using an electromagnetic

wave, typically using laser light in the visible spectrum. This phenomenon gives rise to surface plasmons which are plane waves with a highly confined nano-scale optical field that can be harnessed and used for sensing purposes [25]. In practice, SPR can be used to develop highly sensitive bio-sensors [73]. Such bio-sensors are used in biology and medicine tests as they can be used to detect cancer cells, viruses and DNA material amongst many other organisms. SPR-based bio-sensors have already been commercialized since the 1990s, and represent a billion dollar industry worldwide, with companies such as BIACORE and Dynamic Biosensors. Bio-sensors from these companies work with lasers which produce coherent states of light, coherent light gives us the lower bound of sensitivity in classical metrology known as the standard quantum limit (SQL). Methods from theory in metrology gives us theoretical ways/models to quantify and study the sensitivity limitations of our SPR bio-sensors. In this thesis we will study the transition from the classical regime to the quantum, hence we require some understanding of quantum metrology in order to understand the limitations of our bio-sensor when quantum resources are used.

Quantum metrology is defined as the use of quantum theory to make high resolution and sensitive measurements of physical parameters [18]. Quantum metrology is an extension of classical metrology, meaning classical metrology is a subset of quantum metrology (a more fundamental theory). Quantum metrology extends classical metrology by exploiting quantum phenomena such as quantum entanglement and quantum squeezing. A central study of quantum metrology is how the precision, i.e., the variance of the parameter estimate, scales with the number of particles (in the case of optical bio-sensors this would be the number of photons passing through the system). Here interferometers can be used to implement general sensing models. The limit of precision or resolution in classical interferometers is well known and is called the shot-noise limit (another name for the standard quantum limit), quantum mechanical systems have been shown to be able to go beyond the shot-noise limit of precision, even setting a new limit known as the Heisenberg limit. Quantum metrology has many potential applications in practice such as the detection of gravitational waves with projects such as LIGO [24], Where high precision distance measurements must be made of two widely separated masses. Other possible applications include sensing in biological and biochemical experiments [30]. This will be the focus of this thesis, in particular we will look at quantum plasmonic based sensors, i.e., a sensor which requires the quantum excitation of surface plasmons to work. The topic of surface plasmons will be discussed further in the second chapter of the thesis.

An important parameter used to characterize a sensors performance is its limit of detection (LOD), which can be calculated by taking into account the noise in the transduction signal, Δ_s , i.e., the minimum resolvable signal: $\text{LOD} = \Delta_s/S$, where S is the sensitivity [35]. Hence one can improve the LOD by increasing the sensitivity or reducing the noise level. While there are obviously many other things that can be done to improve the sensitivity of SPR-based bio-sensors, the ultimate limitation is the intrinsic statistical nature of the classical light used, this leads to a shot-noise for Δ_s [42]. Studies have shown that by using quantum states of light one can reduce the noise, Δ_s , and thereby improve the LOD of plasmonic sensors and go beyond the shot-noise limit [35, 36, 38, 39].

The sensitivity of a sensor is defined as

$$S_y = \left| \frac{dy}{dx} \right|, \quad (1.1)$$

where x is a parameter to be estimated on the measurement of some quantity y . Precision in the estimate of x is defined as

$$\Delta x = \left| \frac{dy}{dx} \right|^{-1} \Delta y. \quad (1.2)$$

This project is aimed at harnessing the power of quantum states of light and to try and reduce the noise in the transduction signal Δy of modern bio-sensors beyond the classical limit known as the shot-noise limit imposed by classical metrology [28] and hence improve the precision in Δx . The aim is to design a quantum SPR-based bio-sensor model that can be used for sensing biological systems,

such as viruses and bacteria. This will be accompanied with a laboratory experiment in which we build a SPR setup and a single photon source setup to do sensing. The sensor works as follows, we have a sample material, also known as an analyte (it could be a virus, a protein or any molecule in general) which we allow to bind to another agent in solution, also known as a ligand. When the binding occurs, the refractive index of the bound solution (ligand-analyte complex) will be different from that of the ligand. The SPR sensor is great at tracking this change in refractive index and we can use it to monitor the binding and unbinding action of the analyte and ligand. In particular, we are interested in kinetic models in SPR, that is, we will plot sensorgrams (plots which show a change in some response unit as a function of time as the refractive index of the sample we are investigating changes). By using quantum states of light we will be able to lower the noise in the measurement of data in the system and hence have more accurate data measurements. We will discuss kinetics in the SPR chapter, but in general these studies are useful for understanding drug interactions with bacteria or viruses etc.

The quantum part of our research is in the later sections of the thesis, i.e., when we look at the measurement of binding kinetics using quantum plasmonic resonance sensing. We are interested in intensity-based measurements in our setup. The goal is to show that by using quantum states of light the measurement noise in our sensorgram data will be lower than with coherent light, in which case we can resolve the kinetic parameters better with quantum states.

1.1 Overview of the thesis

This thesis is aimed at studying the field of quantum sensing, in particular quantum plasmonic sensing and metrology. This thesis looks at a theoretical description of quantum sensing and goes on to describe an experiment designed to do quantum sensing using single photons. Chapter 2 takes an in-depth look at quantum sensing by starting with a description of how classical sensing is done.

Outline of the thesis

In chapter 2 we justify the use of quantum resources in biological sensing projects and motivate for the use of quantum sensing.

Section 2.1 gives an introduction and in depth discussion of classical SPR and how it is used in bio-sensing.

In section 2.2 we introduce estimation theory, which is vital when looking at metrology. We look at a derivation of the classical and quantum Fisher information equations.

Section 2.3 gives a brief description of the different states of light we look at in this thesis, i.e., both quantum states and the classical coherent state.

Section 2.4 goes into detail about single-photon sources. This is important when considering the experimental implementation of the quantum SPR setup with single photons.

Section 2.5 looks at intensity-based quantum plasmonic sensing.

Chapter 3 looks at new work: a theoretical analysis of SPR sensing using quantum states and parameter estimation from sensorgrams.

Chapter 4 looks at an application of quantum bio-sensing in an HIV study.

Chapter 5 looks at an experimental implementation of quantum sensing.

Chapter 6 gives the conclusion and a look at possible future work in this area of research.

How to read this thesis

The work in this thesis spans two separate fields of study, i.e., quantum metrology and plasmonics. It is a combination of a theoretical study and an experimental study. On the theoretical end, we focus primarily on formulating general sensing models and using techniques in metrology to study the sensitivity of these models, which is an important quantifiable property. The models we use are representative of real experimental setups and hence at times there can be a blurring of the distinction between a simulation of the model and a real experiment, however we try to distinguish between the two. From the experimental end we set up a plasmonic sensor which uses a configuration known as the Kretschmann configuration to excite surface plasmons and a single photon source with the intent of making a comparison of the precision achieved when using single photons versus classical coherent light.

So when reading the thesis please note that chapter 2 is about surface plasmons and their excitation. It is more important for the experimental side of things, but is also relevant for the theoretical work because our models are representative of the setup we describe in this chapter, especially when we start looking at the chapter on kinetics. It is also relevant for the theoretical work we do. Section 2.2 on the estimation theory is more important for the theoretical work because it gives a background of metrology. It helps us understand some fundamental ideas of metrology and how we find the bounds on precision of our models from metrology. Section 2.4 gives an in depth analysis of our single-photon source. It is important for the experimental component of our study. Section 2.3 looks at giving a brief description of the different states of light we used in the theoretical portion of the thesis and chapter 3 introduces and describes intensity based quantum plasmonic sensing, where we introduce our reflectivity based model for generating sensorgrams, this is new work. Chapter 4 looks at an application of our model to an HIV case study, also new work. In chapter 5 we look at experimental work done, where we used single photons from an SPDC source to do plasmonic sensing and the estimation of kinetic parameters which has not been done before. Chapter 6 is the conclusion chapter.

Chapter 2

Plasmonic sensing and quantum metrology

In this chapter we will motivate for the use of a quantum approach to sensing. We will look at the limitations of using classical states, i.e., the shot noise limit boundaries and how they are overcome by considering quantum states of light. We will also look at limitations in sensing in biology, limitations which can be overcome by using quantum mechanical systems and other limitations which can also be overcome by quantum mechanics.

The primary objective for researchers in quantum sensing and metrology is to surpass the standard quantum limit and ideally attain the Heisenberg-limited bounds to precision. Quantum correlated light can be used to suppress quantum shot noise in interferometric measurements brought about by coherent states, and thus enhance precision in measurements [41]. Quantum sensing and metrology are mature applications of quantum technologies as interferometers, atomic clocks, magnetometers, gyroscopes and accelerometers already operate at the standard quantum limit. In theory a researcher could enhance their measurements by increasing optical power in an optical setup. However the reason enhancement of precision in measurements remains a primary focus in metrology, is because there are situations where precision cannot be improved simply by increasing optical power, due, for example, to power constraints introduced by optical damage or quantum measurement back-action [51].

Metrology is defined as the science of measurement. This includes the study of both experimental and theoretical tools used to measure uncertainty in measurements. Metrology has applications in medical and health sciences. From a medical or health perspective the sensitivity, precision and specificity of our sensing devices needs to be very high. A device with a high sensitivity is good for screening, i.e., taking general people in a population to see if they have a certain disease [63]. Highly sensitive tests have fewer false negatives and highly specific tests have fewer false positives. A good diagnostic tool should have both high sensitivity and specificity [63].

2.0.1 Scaling and the effect of noise

A central question of quantum metrology is how the precision scales, i.e., how the variance of the parameter estimation, scales with the number of particles. In answering this question we begin by considering a general two-mode sensing model like the one shown in Figure 2.1. Most optical sensing setups only require a single mode, but they can easily be adapted into two-mode sensing setups. The reason we are interested in a two-mode setup is because a reference signal can be used to remove common noise between the signal and reference modes. This is the case for both the classical and quantum regimes. The model in Figure 2.1 can be adapted for both intensity sensing or phase sensing.

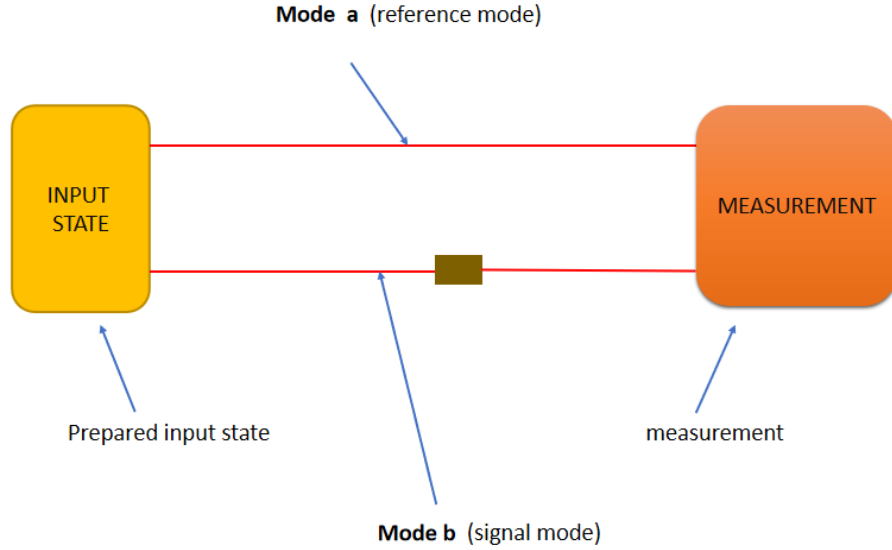


Figure 2.1: Model for general two-mode sensing setup. The brown box represents an intermediate process which depends on the type of sensing being done, e.g., it could be a phase shifter if we are doing phase sensing or transmissive device if we are doing intensity sensing.

In this section we will take a look at phase sensing, this is important because phase sensing helps us understand how we reach the noise limits which we have been mentioning so far, i.e., the shot noise limit otherwise known as the standard quantum limit and the Heisenberg limit. We can use the model in Figure 2.1 as a guide in implementing different sensing setups. For instance, this type of Mach-Zehnder setup (such as the one in Figure 2.2) can be used to implement a phase sensing experiment where mode a is one of the paths and mode b represents another path. By putting some material in path b which alters the phase, we can essentially, ‘sense’ its presence. We can detect light from both modes and take an intensity difference measurement to measure this phase shift ϕ .

Classical interferometers cannot overcome the shot-noise limit. The limit on the precision of the phase estimation of the phase ϕ , assuming there is no systematic noise in the system, is given by $\Delta\phi = \frac{1}{\sqrt{N}}$ [18] where N is the mean photon number of the state. Shot noise is a type of noise which can be modelled by a Poisson process. The coherent state described later in section 2.3 allows us to reach this limit of measurement or resolution. This is considered as the limit that a classical state can reach. In Appendix A, we have shown a calculation which shows that indeed the coherent state does reach this limit of resolution. The reasons behind this being the limit can be understood by having an understanding of the Fisher information discussed in section 2.2.

By using non-classical states such as the NOON state [19], we can reach the limit of precision achievable using quantum states, i.e., $\Delta\phi = \frac{1}{N}$. This is called the Heisenberg limit. We have shown a calculation in the Appendix A which shows that using NOON states we can indeed achieve the Heisenberg limit of precision assuming no systematic noise in the system.

It is clear that the using quantum mechanical systems we can better resolve phase shifts in experiments for fixed N . We will show the same for intensity sensing in this thesis. Effectively the ability to resolve sharper changes in these phase or intensity allows us to sense or detect the presence of the thing we want to sense or even changes in its properties. In the later chapters we will look at the shot noise in a two-mode intensity sensing setup, we will calculate the precision in an intensity-difference measurement, $\langle\Delta\hat{M}\rangle$ for the Fock and Coherent input states.

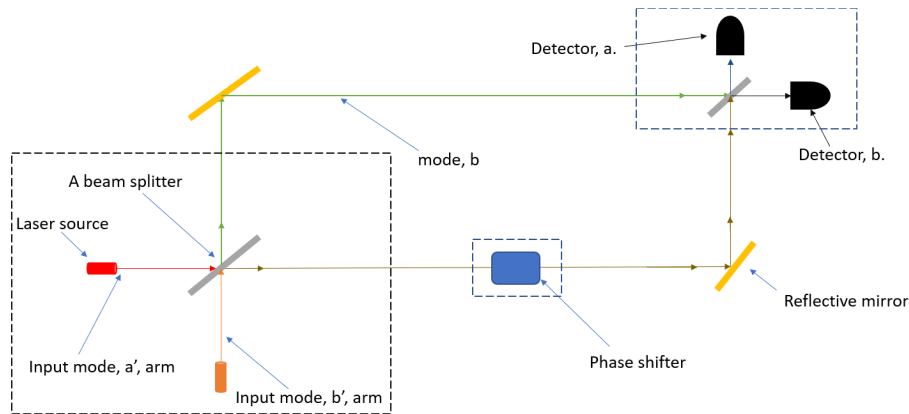


Figure 2.2: Mach-Zehnder setup showing how we can physically implement a two-mode sensing setup. By taking an intensity-difference measurement between detectors a and b we can perform phase sensing. The dotted box around the lasers shows where the region which can be considered as the input preparation region. The dotted box around the phase shifter shows where the region which can be considered as the intermediate process region. The dotted box around the detectors shows where the region which can be considered as the measurement region.

2.0.2 Quantum metrology and its application to biology

Quantum metrology offers a route to overcoming the precision benchmark for optical bio-sensors set in classical physics [28]. Quantum metrology is becoming particularly relevant in biology where the limitations on resolution factors imposed in classical physics limit the use of optical bio-sensors [28]. Quantum mechanics has already seen other important applications in biology, such as position emission tomography (PET) with entangled photons [29], magnetic resonance imaging (MRI) using nuclear magnetic resonance [14], and bio-magnetic imaging with superconducting quantum interference devices (SQUIDs) [11]. The ability to engineer coherence and correlations at the quantum level allows us to demonstrate quantum-enhanced plasmonic sensing [19, 30], resolution, reduction in technical noise, immunity to imaging artefacts and characterization of the biological response to light at the single-photon level.

Above the ability to engineer coherence is the development of new quantum measurements for improved multi-photon spectroscopy, magnetic imaging and sensing. All this has contributed to a wide-spread interest in cross-disciplinary research in both biology and quantum metrology. All measurement processes are governed by the laws of quantum mechanics which imposes constraints on the precision with which measurements can be made.

Biological system measurements come with many challenges which are linked to measurement precision as well as other physical challenges such as the effects of light on the biological system, environmental fluctuations and growth in complexity and dynamics of the system in question. Many measurements in biological systems are currently limited by the achievable precision, e.g., single-molecule sensing [28], as well as biological mass measurements.

The precision for some bio-systems has become saturated and their resolution is limited by external factors. For example, in distinguishing between healthy and cancerous cells, measurements are limited by cell-to-cell variations rather than instrument sensitivity [28]. Thermal fluctuations also affect sensitivity measurements because they introduce stochastic motion to small particles. The ideas in sensing can also be extended to image resolution in biology. The diffraction limit of visible light also restricts us from resolving images of the biological samples, as demonstrated in Figure 2.3. All this warrants the use of quantum mechanical systems. We will come back to quantum metrology in section 2.2.

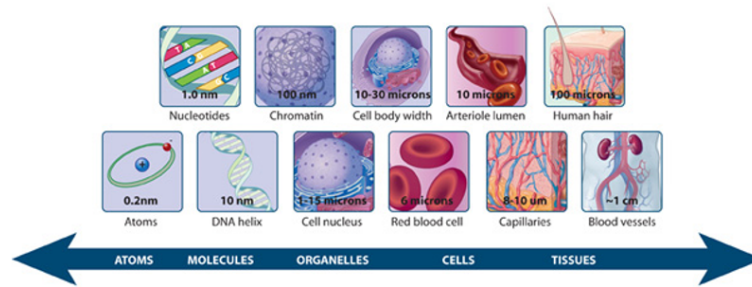


Figure 2.3: Length scales in biology. The diffraction limit of visible light restricts far-field imaging resolution to around 200 nm, which is the approximate scale of organelles. Single proteins or other biomolecules are not typically observable with a light microscope and super-resolution techniques are required to study their function and structure. Taken from Ref. [12].

2.1 Surface plasmon resonance

Surface plasmons are surface electromagnetic waves whose propagation is confined to a metal-dielectric interface, as shown in Figure 2.4. These surface plasmons can be excited by an electromagnetic wave. This phenomenon is called SPR. Looking at Figure 2.4 we can see that to excite SPR we need a source of electromagnetic radiation (laser source) which emits the wave, the electromagnetic wave hits the metal plate at different angles. In practice (lab experiments) we calibrate our setup to the point where we have total internal reflection. This is because we excite surface plasmons over the range of angles where we have total internal reflection in our system. This means that we need to find the critical angle of our system and scan over the range in which we have total internal reflection. It is important to note that our setup has a detector which measures the intensity of the reflected light, this can be a CCD camera or any other detector.

When SPR occurs, the intensity of the reflected electromagnetic wave in Figure 2.4 decreases sharply as a function of the incident angle, this is referred to as an SPR dip. In general it looks like the plot in Figure 2.5.

It should be noted that the SPR setup above is also sensitive to changes in the refractive index of the dielectric medium, n_2 , meaning if we fix the incident angle to an angle above the critical angle we can change the refractive index of the dielectric medium and also observe an SPR dip, as shown in Figure 2.6. This is a very useful property which we will use when we start looking at kinetics, where we are interested in mixing substances like protein or viruses with other solutions. Due to the mixing when the refractive index of the solutions change, our setup can measure changes in the reflectivity, R , to give us a profile of the kinetics of the mixing. Clearly the reflectivity is a function of both the incident angle and the refractive index, and to access it as a function of one of the parameters requires that we fix the other parameter. We may however be interested in seeing a profile in which both the angle and refractive index are changing which leads us to the three dimensional plot shown in Figure 2.7.

A few key points to note when exciting SPR include the fact that, it only works for thin enough metal films (the thickness of the metal has to be determined and depends on the metal) and it only works for a specific polarisation of light. When we get to the Kretschmann configuration some of these ideas will be repeated but will be more specific.

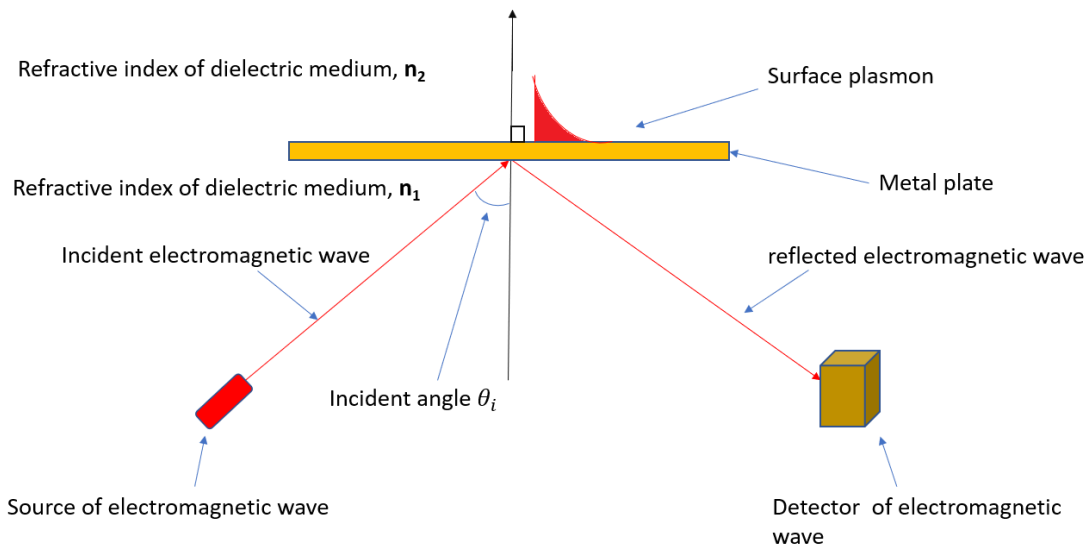


Figure 2.4: Exciting surface plasmons. The surface plasmon is on the surface of the metals plate.

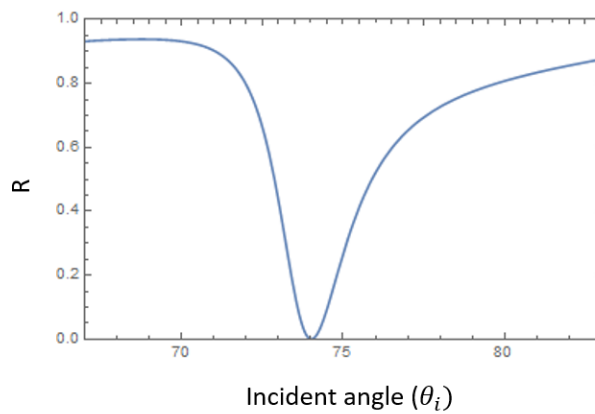


Figure 2.5: SPR dip with resonance angle. R is the reflected intensity at fixed refractive index of the dielectric materials $n_1 = 1.5$ and $n_2 = 1.39$.

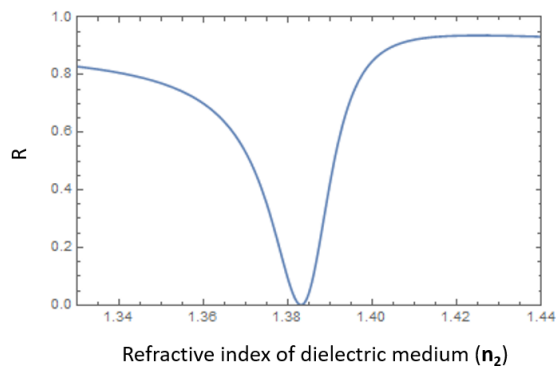


Figure 2.6: SPR dip with refractive index of the dielectric material. R is the reflected intensity at fixed incident angle $\theta = 73^\circ$ and $n_1 = 1.5$.

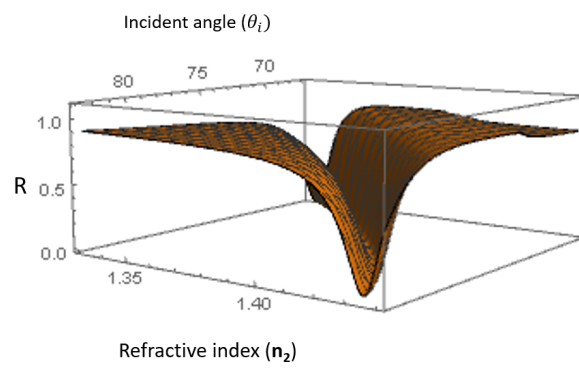


Figure 2.7: SPR dip with refractive index of both the dielectric material and incident angle. The refractive index $n_1 = 1.5$.

2.1.1 Evanescent waves

In this section we want to discuss evanescent waves. They are important in the discussion of SPR and this section gives intuition into what evanescent waves are and how they come about as well as why they are relevant for SPR. We begin by building the intuition around the phenomenon known as total internal reflection then lead on to building an intuition about evanescent waves.

We begin by assuming that we have a plane wave incident on some interface at an angle, θ_i , as shown in the ray diagram in Figure 2.8. We see that a portion of the wave will be transmitted at an angle, θ_t , and a portion will be reflected back at an angle, θ_r .

Considering Maxwell's equations and applying general boundary conditions for electromagnetic radiation we can derive a formula to describe the relationship between the angles of incidence, θ_i , and transmission, θ_t , and the indices of refraction of the regions we find them in, n_1 and n_2 , respectively. This mathematical relationship is commonly referred to as Snell's law. The relationship is used in reference to light or other waves passing through a boundary between two different isotropic media and is useful in giving us a picture of how changing the incidence angle can result in us getting total internal reflection.

Mathematically Snell's law is expressed as follows

$$n_1 \sin(\theta_i) = n_2 \sin(\theta_t). \quad (2.1)$$

At first glance it may seem that one can generate solutions for any possible combination of, n_1 , n_2 , $\sin(\theta_i)$, and $\sin(\theta_t)$. Intuitively this would suggest that for any angle of incidence we allow we expect that there is a measurable angle of transmission. However we start to run into problems when we try to solve for a general θ_t , i.e., we rewrite Eq. (2.1) above as

$$\theta_t = \arcsin((n_1/n_2)\sin(\theta_i)). \quad (2.2)$$

We see that if $(n_1/n_2)\sin(\theta_i) > 1$, then we have a problem because we cannot get a real solution for, θ_t . This is mathematically equivalent to $\sin(\theta_i) > \frac{n_2}{n_1}$.

The incident angle such that, $\theta = \arcsin(n_2/n_1)$, is known as the critical angle and is usually written as, θ_c . At and above the critical angle we no longer get a solution for the transmitted angle, or we have angle of refraction of 90-degrees. The interpretation of this phenomenon is usually that there is no longer a transmitted wave and we get what is known as total internal reflection, i.e., all the incident light is reflected back into the region with refractive index, n_1 . This however is not the complete story and this leads us to a phenomenon known as evanescent waves.

Consider the electric field of the incident electromagnetic wave propagating in Figure 2.8. If we consider the Figure to be an XY plane then we can represent the electric field of the transmitted beam as Eq. (2.3) (we are not interested in the incident and reflected beams). This is known as the planar travelling wave solution of the wave equation, with a harmonic time dependence,

$$\mathbf{E} = \mathbf{E}_0 e^{i(\mathbf{k} \cdot \mathbf{x} - \omega t)}. \quad (2.3)$$

The field propagates in the \mathbf{x} and \mathbf{y} direction and is constant in the \mathbf{z} component hence we have

$$\mathbf{E} = \mathbf{E}_0 e^{i(k_x x + k_y y - \omega t)}. \quad (2.4)$$

Here ω is the temporal angular frequency of the wave and \mathbf{E}_0 is an amplitude. The magnitude of the wave vector for the transmitted beam is given as

$$|\mathbf{k}| = \frac{n_2 \omega}{c}. \quad (2.5)$$

Due to boundary conditions the wave vector can be expressed as

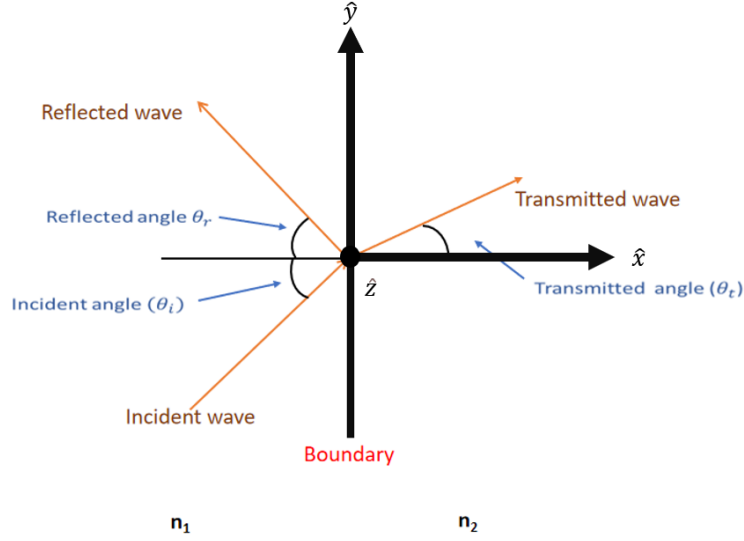


Figure 2.8: Ray diagram showing that a portion of the wave will be transmitted at an angle, θ_t , and a portion will be reflected back at an angle, θ_r .

$$\mathbf{k} = \frac{n_2\omega}{c}\cos(\theta_t)\hat{\mathbf{x}} + \frac{n_2\omega}{c}\sin(\theta_t)\hat{\mathbf{y}}. \quad (2.6)$$

Substituting the x and y components of \mathbf{k} in Eq. (2.4) we get

$$\mathbf{E} = \mathbf{E}_0(e^{i\frac{n_2\omega}{c}\cos(\theta_t)x} \times e^{i\frac{n_2\omega}{c}\sin(\theta_t)y} \times e^{-i\omega t}). \quad (2.7)$$

When we consider the condition for total internal reflection, i.e., $\frac{n_1}{n_2}\sin(\theta_t) > 1$ the term with $\sin(\theta_t)$, i.e., $\frac{n_2\omega}{c}\sin(\theta_t)y$ is always real because $\sin(\theta_t) = \frac{n_1}{n_2}\sin(\theta_i)$, which is real. We however do not have such a general expression for $\cos(\theta_t)$, but we know that $\cos^2(\theta_t) + \sin^2(\theta_t) = 1$ from which it follows that $\cos(\theta_t) = \sqrt{1 - \sin^2(\theta_t)}$. Hence, if we set the condition that $\sin^2(\theta_t) > 1$ ($\theta_i > \theta_c$) then we see that $\cos(\theta_t)$ becomes an imaginary number.

We can express, $\cos(\theta_t)$ as some arbitrary imaginary number for this total internal reflection condition, i.e., $\cos(\theta_t) = i\epsilon$. Hence we have that our electric field, \mathbf{E} , can be generalized as $\mathbf{E} = \mathbf{E}_0e^{-i\omega t}e^{in_2\frac{\omega}{c}\sin(\theta_t)y}e^{-n_2\frac{\omega}{c}\epsilon x}$. If we take the real part of the electric field to get the physical field here we get $\text{Re}(\mathbf{E}) = \mathbf{E}_0\cos(n_2\frac{\omega}{c}\sin(\theta_t)y - \omega t)e^{-n_2\frac{\omega}{c}\epsilon x}$. Peatross and Ware detail this in chapter 3.5 of their book [44]. Physically there is no reason why such an electrical field would not exist, it is a real electrical field in the x direction. Specifically it is plane wave in the y direction modulated by some exponential decay. We thus have a wave in the transmitted region that is oriented along the boundary and gets rapidly weaker as we get further and further from the boundary. Such a wave is called an evanescent wave and is difficult to detect because it falls off after a few wavelengths. Evanescent waves are accessible for use in practice. For instance we can detect them by inducing frustrated total internal reflection as shown in the Figure 2.9. Figure 2.9 is not an exact representation of the process, for instance the incident and reflection angles are somewhat off, but is aimed at pointing out the principle ideas behind frustrated total internal reflection.

So we have the incident region with refractive index n_1 on either side and n_2 in the middle. We then consider a plane wave from the left and assume most of it is reflected back (i.e., we are above the critical angle). This means that in our n_2 region we will have an evanescent wave which decays exponentially. If the other boundary, i.e., the other n_1 region is close enough the real wave will come out on the other side(i.e., coupled off in this region). This is what we call frustrated total internal reflection.

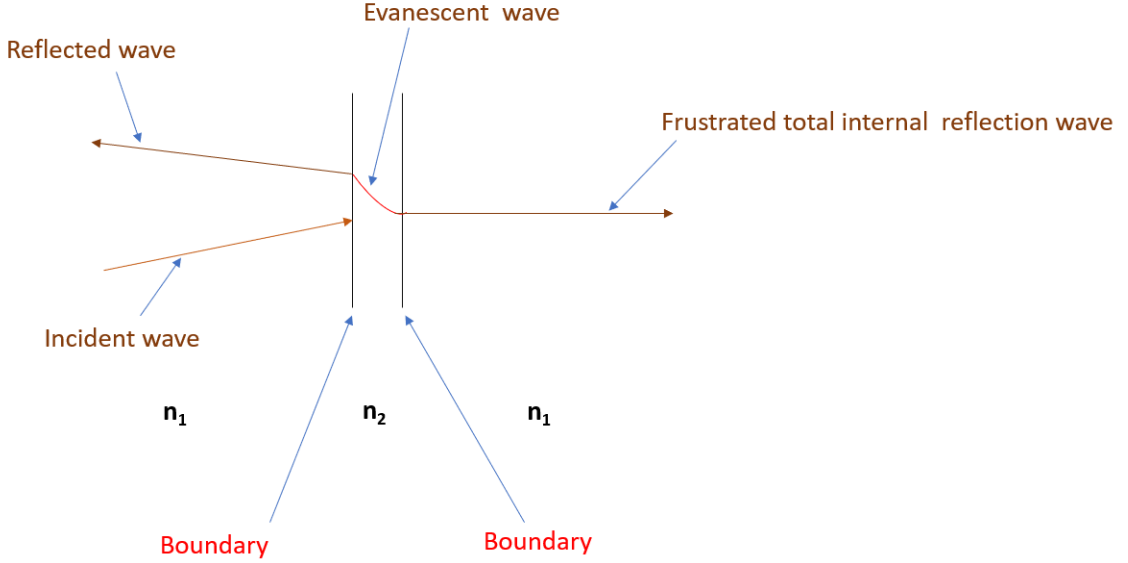


Figure 2.9: Frustrated total internal reflection.

2.1.2 Evanescent waves and surface plasmons

In this section we will look at a more formal description of excitation of the evanescent waves and exciting a surface plasmon by looking at a derivation from Ref. [22]. We can use Maxwells equations to derive the classical field expressions for surface plasmons supported by a single interface. Starting with the wave equation shown below

$$\nabla^2 \mathbf{E} - \frac{\epsilon}{c^2} \frac{\partial^2 \mathbf{E}}{\partial t^2} = 0. \quad (2.8)$$

Here, \mathbf{E} is the electric field, c is the speed of light and ϵ is the dielectric function of the material where we find the electric field. Assuming a harmonic time dependence of our electric field, we can write our electric vector field as $\mathbf{E}(\mathbf{r}, t) = \mathbf{E}(\mathbf{r})e^{-i\omega t}$. If we substitute the harmonic time electric field expression into the wave equation above we get

$$\nabla^2 \mathbf{E} - k_0^2 \epsilon \mathbf{E} = 0. \quad (2.9)$$

Here, k_0 is the free-space propagation constant, $k_0 = \frac{\omega}{c}$. The above equation is called the Helmholtz equation. When considering a two-dimensional two-layer geometry in which each layer is an infinite half-space, as shown in Figure 2.10, the surface waves propagate along the y -direction and are constant in the x -direction, hence we can write out our electric field expression as $\mathbf{E}(\mathbf{r}) = \mathbf{E}(z)e^{ik_y y}$. k_y is the wave vector component parallel to the interface. If we substitute this into the Helmholtz equation we get the following

$$\frac{\partial^2 \mathbf{E}(z)}{\partial z^2} + (k_0^2 \epsilon - k_y^2) \mathbf{E}(z) = 0. \quad (2.10)$$

For the magnetic field $\mathbf{H}(z)$, we have

$$\frac{\partial^2 \mathbf{H}(z)}{\partial z^2} + (k_0^2 \epsilon - k_y^2) \mathbf{H}(z) = 0. \quad (2.11)$$

Using Maxwells curl equations we can solve the above two Eqs. (2.10) and (2.11) to get the field amplitudes and the propagation constant k_y as shown below,

$$\nabla \times \mathbf{E}(\mathbf{r}, t) = -\mu_0 \frac{\partial \mathbf{H}(\mathbf{r}, t)}{\partial t}, \quad (2.12)$$

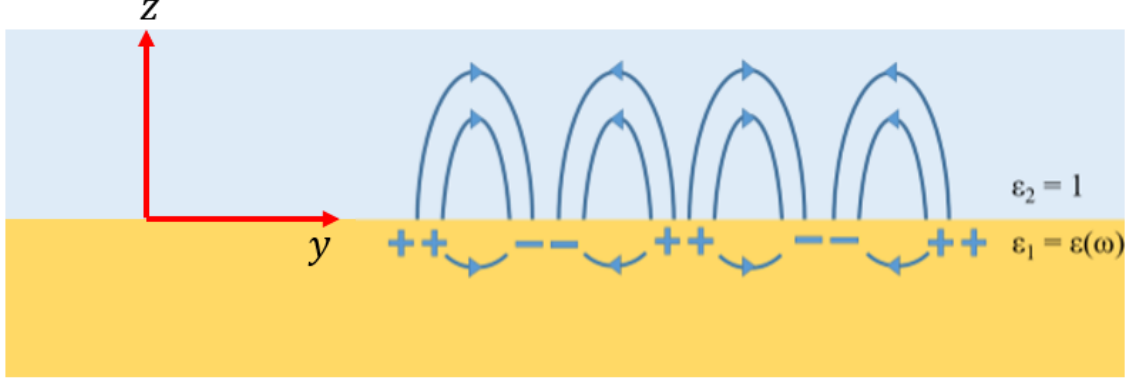


Figure 2.10: A two-layer geometry for a surface plasmon field. The region $z < 0$ is metallic with complex dielectric function $\epsilon(\omega)$. The dielectric region ($z > 0$) is air with $\epsilon = 1$. The interface between the regions is $z = 0$.

$$\nabla \times \mathbf{H}(\mathbf{r}, t) = \epsilon_0 \epsilon \frac{\partial \mathbf{E}(\mathbf{r}, t)}{\partial t}, \quad (2.13)$$

where ϵ_0 and μ_0 are the free-space permittivity and permeability respectively. ∇ is given as $\nabla = ik_y \hat{y} + \frac{\partial}{\partial z} \hat{z}$, $\frac{\partial}{\partial x} = 0$ and $\frac{\partial}{\partial t} = -i\omega$. This gives

$$\frac{\partial E_y}{\partial z} - ik_y E_z = -i\omega \mu_0 H_x, \quad (2.14)$$

$$\frac{\partial E_x}{\partial z} = -i\omega \mu_0 H_y, \quad (2.15)$$

$$ik_y E_x = i\omega \mu_0 H_z, \quad (2.16)$$

$$\frac{\partial H_y}{\partial z} - ik_y H_z = i\omega \epsilon \epsilon_0 E_x, \quad (2.17)$$

$$\frac{\partial H_x}{\partial z} = i\omega \epsilon \epsilon_0 E_y, \quad (2.18)$$

$$ik_y H_x = i\omega \epsilon \epsilon_0 E_z. \quad (2.19)$$

We need to satisfy the condition that the electric and magnetic vectors reside in orthogonal planes. This can be achieved in two distinct ways. We thus define two-modes, a transverse-magnetic (TM) and transverse-electric (TE) mode where, the TM mode satisfies the condition that $H_y = H_z = E_x = 0$. For TM modes we can use Eqs. (2.14)-(2.19) to calculate, E_y and E_z and we use Eq. (2.11) to calculate H_y .

$$E_y = -\frac{i}{\omega \epsilon_0 \epsilon} \frac{\partial H_x}{\partial z}, \quad (2.20)$$

$$E_z = -\frac{k_y}{\omega \epsilon_0 \epsilon} H_x, \quad (2.21)$$

$$\frac{\partial^2 H_x}{\partial z^2} + (k_0^2 \epsilon - k_y^2) H_x = 0. \quad (2.22)$$

These Eqs.(2.20)-(2.22) are solved separately because the value of ϵ varies in different materials, e.g., air or the prism. The ϵ for air is almost one at standard temperature and pressure and is one in a

vacuum. For metals this is more complicated because ϵ depends of the wavelength of the light which is being used to probe, i.e., $\epsilon = \epsilon(\omega)$. For metals $\epsilon(\omega)$ is a complex number with a negative real part describing the optical response of the material, and an imaginary part describing absorptive loss. It can be measured experimentally or estimated theoretically using the Drude Model [54],

$$\epsilon(\omega) = 1 + \frac{\omega_p^2}{\omega + i\gamma_p\omega}, \quad (2.23)$$

where ω_p is the plasma frequency and γ_p is the electron collision frequency.

To solve Eq. (2.22) we make the substitution below

$$k_j = k_y^2 - k_0^2\epsilon, \quad (2.24)$$

where k_j is the wave vector component perpendicular to the interface with $j = 1$ for the metal region and $j = 2$ for the air region. The solution of the differential equation is of the form $e^{ik_y y} e^{\pm k_j z}$. This is the form of evanescent surface waves where we have $+k_1$ for the metal region and $-k_2$ for the air region. For the magnetic field we have

$$H_x(y, z) = \alpha_j e^{ik_y y} e^{-k_z z}, \quad (2.25)$$

where α_j is an amplitude and $k_z = (-1)^j k_j$. Substituting values for the magnetic field into Eqs.(2.20) and (2.21) gives us the values for the electric fields given as

$$E_y(y, z) = i\alpha_j \frac{k_z}{\omega\epsilon_0\epsilon_j} e^{ik_y y} e^{-k_z z}, \quad (2.26)$$

$$E_z(y, z) = -\alpha_j \frac{k_y}{\omega\epsilon_0\epsilon_j} e^{ik_y y} e^{-k_z z}. \quad (2.27)$$

The electric field vector in each of the layers is given as

$$\mathbf{E}(\mathbf{r}, t) = i\alpha_j \frac{k_z}{i\omega\epsilon_0\epsilon_j} e^{ik_y y} e^{-k_z z} (\hat{\mathbf{y}} + \frac{ik_y}{k_z} \hat{\mathbf{z}}) e^{-i\omega t}. \quad (2.28)$$

By enforcing continuity of H_x and $\epsilon_i E_z$ at $z = 0$ it follows that

$$H_{x1} = H_{x2}, \quad (2.29)$$

which implies

$$\alpha_1 = \alpha_2. \quad (2.30)$$

We also have

$$E_{y1} = E_{y2}, \quad (2.31)$$

which implies

$$\frac{k_2}{k_1} = -\frac{\epsilon_2}{\epsilon_1}. \quad (2.32)$$

Using this last equation with Eq. (2.24), we arrive at the dispersion relation given below as

$$k_y = k_0 \sqrt{\frac{\epsilon_1 \epsilon_2}{\epsilon_1 + \epsilon_2}} = k_0 \sqrt{\frac{\epsilon(\omega)}{\epsilon(\omega) + 1}}. \quad (2.33)$$

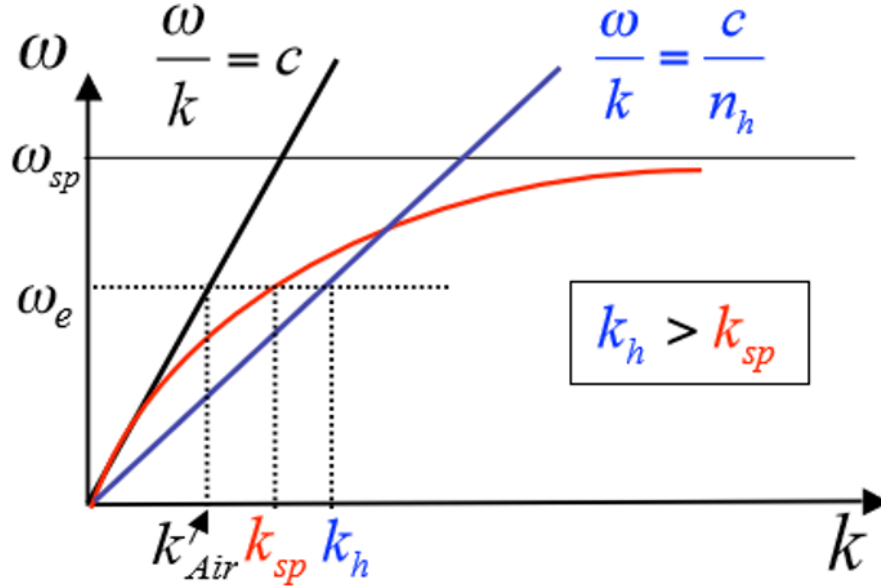


Figure 2.11: Figure showing propagation relations in different media. The h in the subscript of the wave number k stands for high index medium. This Figure was taken from Ref. [79].

2.1.3 Coupling strategies and sensing techniques

The surface plasmon is a charge density oscillation that occurs at the interface of two media with dielectric constants of opposite signs, such as a metal and a dielectric [74]. The existence of this surface plasmons is dictated by the electromagnetic properties of the metal. Typically gold or silver are used to excite surface plasmons for the reason that their electromagnetic properties are more suitable when giving a visible response.

The propagation dispersion relation is useful for describing plasmon excitation and propagation. It gives us a picture of whether not SPR can occur. We can look at different propagation relations in different media to have a better understanding of SPR in the Krestchamnn configuration. Figure 2.11 gives us a picture of propagation relations in different media.

The problem in Figure 2.11 is that the surface plasmon modes for an air-metal interface lie below the light line in air and hence there cannot be coupling since surface plasmon modes cannot couple to the far field and vice versa (reciprocity theorem). A trick to use to resolve this problem (excite modes below the light line) is to introduce a high-index medium (for example a prism). In Figure 2.11 we see how it is that surface plasmons at a metal/glass interface can not be excited by light in the glass. Surface plasmons at a metal-dielectric interface can only be excited when the excitation condition is satisfied, i.e., the mode matching condition $k_{\parallel \text{SiO}_2} = k_{\parallel \text{SP}}$ for a specific incidence angle called the resonance angle θ . Figure 2.12 shows this as a crossing point between the dispersion curves, where light in the glass leaks through to air on the other side of a thin metal layer and a surface plasmon at the metal/air interface can be excited by the evanescent field.

We require techniques such as the ones mentioned above to excite surface plasmons, this is because of the momentum mismatch which arises due to the fact that $k_{\text{SPP}} > k_0$. The key challenge today in SPR nano-sensor development lies in providing robust integrated SPR sensors that are increasingly more sensitive [43]. In general there are four basic methods to excite the surface plasmon: prism coupling, waveguide coupling, fibre optic coupling and grating coupling. Though prism coupling is the most convenient SPR configuration and generally has the best sensing LOD, the prism itself is

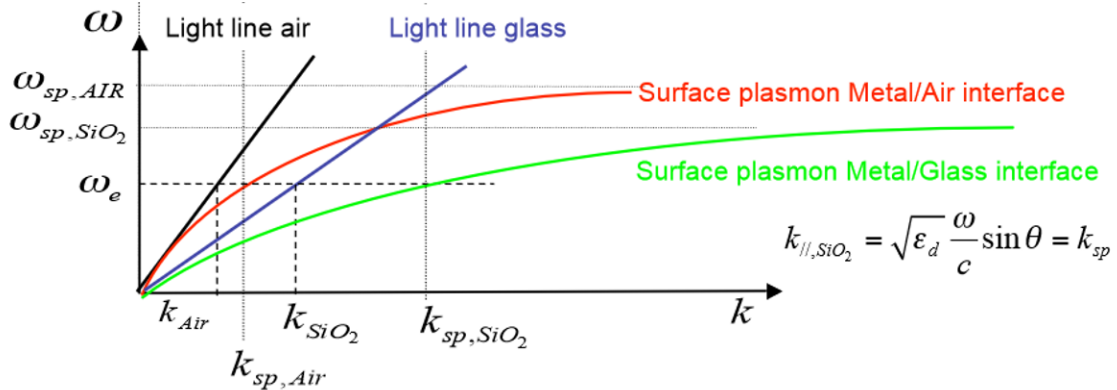


Figure 2.12: Figure showing propagation relations in a Kretschmann prism setup and why surface plasmons at the metal-glass interface cannot be excited. Surface plasmons are excited at the metal-air interface by making use of a SiO₂ prism. We can see this from the meeting of the blue dispersion line from the prism with the red dispersion curve of the surface plasmon in the air/metal interface. Surface plasmons at the metal/glass interface can not be excited, i.e., the green curve. This figure was taken from Ref. [79].

quite bulky and rather difficult to integrate with other optical and electrical components. Waveguide coupling offers a good alternative to the prism as the waveguide is robust and easy to integrate with other optical and electrical components. However small the sensing LOD offered by these different methods is, they also come with two fundamental restrictions that limit their applications. The first is that the evanescent field in SPR structures only penetrates into the surrounding medium for about 100 nm. This makes it very difficult to detect large target molecules like cells and bacteria [43]. The second problem is that there is only one surface plasmon to detect the refractive index (RI) change, hence it is impossible to differentiate the surface RI change and the bulk solution RI change. Models have been proposed to overcome this problem which enable the sensor to be able to differentiate the background RI change and surface bound RI change [57], and have a longer penetration length in the surrounding medium.

There are four main SPR sensing techniques which have been reported, i.e., intensity, wavelength, angle, and phase interrogations. In this thesis we will focus on two: intensity and phase sensing, as they are the two main techniques used in the quantum regime [69]. When we consider phase sensing we will stick to theoretical results in this thesis, however for intensity sensing we will look at both theory and experimental work with the Kretschmann configuration. In the intensity interrogation SPR at fixed incident angle, the shift of the SPR dip is translated into the change of reflectivity in the linear region of the SPR angular or spectral response curve [40]. There are various implementations of SPR sensing which can be used for intensity sensing where the shift of the SPR dip can be monitored by measuring the change of reflectivity in the linear region of the SPR angular or spectral response curve. Developments in nanostructure engineering, nanotechnology have also made plasmonic nanoparticle-based SPR sensing possible [40]. Setups have been developed which allow for quantum plasmonic phase sensing to be done [7]. In such setups, the changes in the refractive index are picked up in the phase of the optical signal rather than the transmission amplitude. Due to their ability to perform sensing below the diffraction limit, nanowires can be used as the sensing medium in the quantum phase sensing setup [38].

2.1.4 SPR experimental setup

The SPR experiment using the Kretschmann configuration can be implemented in the lab using optical elements that can be mounted on common optical tables. The equipment we use was purchased from Thorlabs. For the classical part, our setup includes a 785nm wavelength semiconductor diode

un-polarised monochromatic laser light source with 50 mW average power. When we implement the quantum version of the setup we replace the laser with a single-photon source which is described in detail in section 2.4. We use a microscope objective ($\times 20$) with a calibrated aperture to act as a beam expander which enlarges the laser beam and produces a collimated beam. Light from the microscope objective goes to a half wave plate used to maximize the intensity of the out-coming beam and then through polarizing beam-splitter (PBS) which transmits horizontally (p) polarised light and reflects out the vertical (s) polarised light, followed by a half-wave plate which we can use to rotate the polarisation to s or p polarization, as shown in Figure 2.13.

Mirrors guide the beam towards a high-index equilateral prism ($n = 1.601$). We put SPR glass slides (gold coated slides of thickness 50nm) on top of the prism. We put index matching liquid between the surface of the prism and the gold slide to keep the refractive index relatively constant so that there is no extra layer between the gold slide and the prism. Using gold slides over depositing a thin film of gold on the surface of the prism has the advantage that it allows us to use optimised gold thin films (thickness of the gold thin film is critical as it dictates the amount of coupling that occurs) and allows one to replace the gold surface when it is damaged. Automated rotation stages are used for adjusting the incident angle θ_{ext} .

The reflected beam is collected with a CCD detector for the classical case and single-photon detectors for the quantum case and the intensity data is stored on a computer system. The image below shows how the components in the setup were arranged. The physical setup which we pass our signal through is known as the Kretschmann configuration and the setup is shown in Figure 2.13.

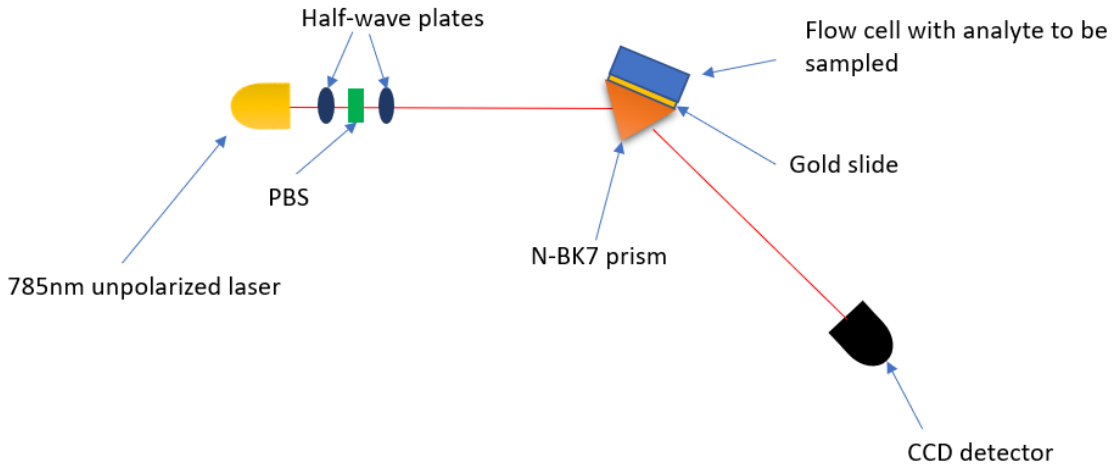


Figure 2.13: The experimental setup used for SPR. 785nm laser light is sent through two half wave plates and a PBS before hitting the prism with the gold slide exciting the surface plasmons in the metal-air interface. The light reflected from the prism is collected into a CCD detector.

2.1.5 SPR in biology

SPR-based biosensors have been used with considerable success in a wide range of fields, from fundamental biological studies to clinical diagnosis applications [34, 88]. In SPR biosensing, the adsorption by a targeted analyte is measured by tracking the change in the response unit (intensity, resonance angle, etc.) due to coupling of incident light to the propagating surface plasmon.

We have established in the previous section that when we fix the refractive index and change the resonance angle then we can see a resonance dip profile, as in Figure (2.4). When we change the

refractive index of the sample the dip position shifts either left or right depending on the change in refractive index of the dielectric medium above our metal plate. Figure 2.14 shows this shift.

In the SPR dip total internal reflection is attenuated when the light surface plasmon coupling conditions have been satisfied. This an effect called attenuated total internal reflection (ATR). We see the normalized reflectance drop down from near-unity to zero. We can certify that the incident light is converted into a surface plasmon mode. By solving Maxwells equations for the three-layer system we obtain the reflection coefficient written mathematically as

$$r_{\text{sp}} = \frac{e^{i2k_{2z}d}r_{23} + r_{12}}{e^{i2k_{2z}d}r_{23}r_{12} + 1}. \quad (2.34)$$

Where

$$r_{lm} = \frac{\frac{k_{lz}}{\epsilon_l} - \frac{k_{mz}}{\epsilon_m}}{\frac{k_{lz}}{\epsilon_l} + \frac{k_{mz}}{\epsilon_m}}. \quad (2.35)$$

Here $l, m \in \{1, 2, 3\}$, $k_{lz} = \sqrt{\epsilon_l k_0^2 + k_y^2}$ and $k_y^2 = \epsilon_l k_0^2 \sin^2 \theta_{\text{in}}$, $k_0 = \frac{\omega}{c}$. ϵ_l is the respective permittivity, and d is the thickness of the metal layer.

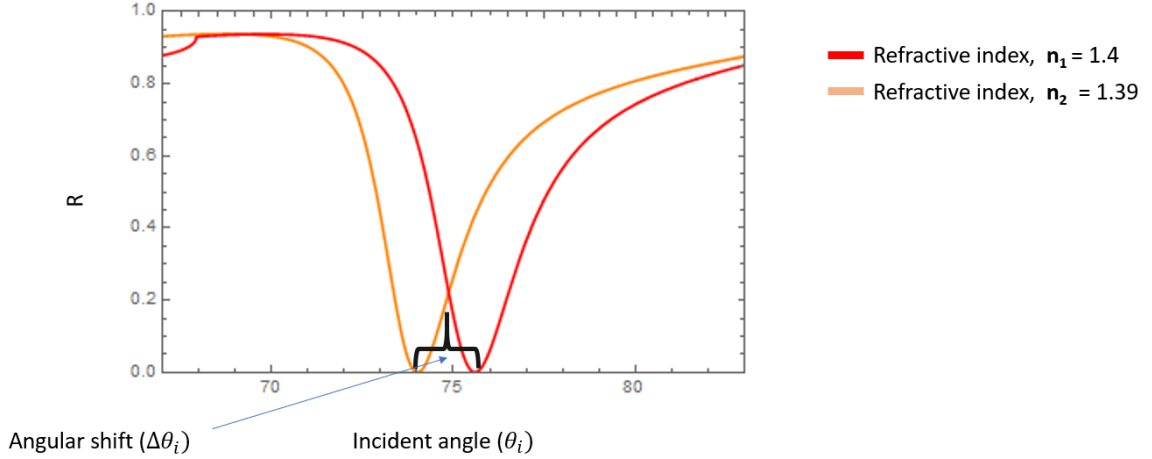


Figure 2.14: Shift in the angular position of the dip due to changing refractive index of the dielectric on top of the gold surface. At a refractive index of 1.39 we have the orange resonance curve but as the refractive index changes to 1.4 the dip shifts to the right and aligns with the red curve.

In kinetics studies researchers look at this angular shift as a function of time. This leads us to sensorgram plots of angular shifts vs time which are very important in sensing experiments because they allow us to determine parameters, known as binding constant in kinetics binding experiments. We will take a more detailed look at these in the next section.

2.1.6 SPR in drug kinetics

SPR is a technique that can be used for measuring bio-molecular interactions in real time in a label-free environment. A wide range of interactions can be investigated using SPR, i.e., protein-protein interactions, DNA-DNA interactions, lipid-protein interactions as well as interactions between biomolecules and non-biological materials. In the SPR setup one of the interactants is immobilized whilst the other, which is passed over the immobilized one, is allowed to free flow in solution.

Association and dissociation constants, k_a and k_d , respectively are measured and we can see the association and dissociation behaviour on a sensorgram display. SPR is used to analyze bio-molecular

interactions and this analysis is quite useful in the following ways: (1) Identifying the binding of interactants to each other, (2) Determining the affinity of the interactions of the interactants, (3) Measuring k_a and k_d , which are useful in helping us determine the association and dissociation rates, and (4) Calculation of the concentration of one of the interactants.

2.1.7 Interaction kinetics

Interaction kinetics refers to the binding and unbinding processes of ligands [64]. These interaction kinetics are divided into 3 phases, i.e., association, steady state, dissociation. Association refers to the binding of the ligand to its receptor, the steady state is the phase where equilibrium is reached as the amount of molecules binding equals the amount which is unbinding and dissociation is the breaking of bonds between the molecules.

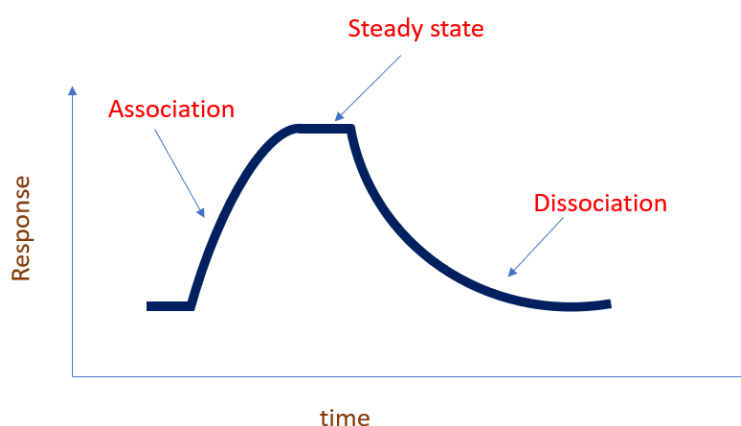


Figure 2.15: The three phases of interaction kinetics. The response unit is a generalization which can refer to a change in the resonance angle, the intensity or refractive index depending on what you are measuring.

When dissociation is very slow it takes a long time before the receptor-ligand complex can be broken apart, therefore a low pH or high salt is injected to break the interaction. This is known as regeneration.

The receptor-ligand complex concentration at any time in the system is, $k_a[L][R]$. Where k_a is the association constant measured in $[M^{-1}s^{-1}]$ (per molar per second), and is determined by collision rates between ligand and receptor molecules. At, $t = 0$, the ligand concentration can be taken as $[L_0]$ and the receptor concentration is taken as $[R_0]$. As the concentration of the receptor-ligand complex increases, the concentration of the ligands and receptor molecules decreases. At, $t \geq 0$, we have that the concentration of the ligands $[L] = [L_0] - [C]$ and the concentration of the receptors $[R] = [R_0] - [C]$.

Alternatively we can also look at backward reactions in the equilibrium state. A decrease in the concentration of the complex is directly proportional to the complex concentration, C , and the rate is given by Ck_d where k_d is the dissociation constant rate measured in $[s^{-1}]$ (per second). Dissociation is a first-order reaction.

The law of mass interaction or action states that the rate of a reaction is dependent on the concentration of reagents. This implies that the increasing rate and the decreasing rate of complex formation and destruction at equilibrium should be the same, i.e., $k_a[L][R] = k_d[C]$. It follows that we can obtain the dissociation equilibrium constant of the ligand-receptor interaction given by the

ratio $\frac{k_d}{k_a} = k_D = \frac{[L][R]}{[C]}$. The unit is the molar. The reciprocal of k_D , i.e., $\frac{1}{k_D} = k_A$ is called the affinity of the ligand-receptor interaction with a unit of per molar $[M^{-1}]$. A method/technique known as equilibrium dialysis can be used to measure affinities of L-R interactions. Equilibrium dialysis is a procedure where two solutions are separated by a semi-permeable membrane, allowing sufficient time to pass, the concentration of diffusible substances will be equal on both sides of the membrane. The initial concentrations of the two reactants are $[L_0]$ and $[R_0]$ respectively in a bio-sensor cham-

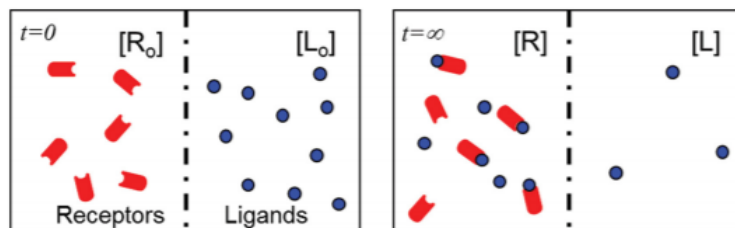


Figure 2.16: The figure shows the use of equilibrium dialysis technique to measure the affinity of a ligandreceptor interaction with a semi-permeable membrane shown by the dashed line in the middle of a water chamber. An important assumption is that the association and dissociation rates are of the same order of magnitude. Figure is taken from Ref. [64].

ber. The complex concentration changes with time before the reactions reach equilibrium and its evolution is given by

$$\frac{d[C]}{dt} = k_a[R][L] - k_d[C] \quad (2.36)$$

$$= k_a([R_0] - [C])([L_0] - [C]) - k_d[C]. \quad (2.37)$$

The reaction of the ligand-receptor is a second-order reaction. To solve the equation we use the pseudo-first-order approximation. We do this by supplying the ligand concentration to the bio-sensor chamber in great excess to the receptor concentration, which implies that $[L_0] \gg [R_0]$, hence the amount of ligand used in the binding interactions is negligible compared to the initial ligand concentration, i.e., $[L_0] - [C] \approx [L_0]$. It follows that

$$\frac{d[C]}{dt} = k_a([R_0] - [C])([L_0]) - k_d[C]. \quad (2.38)$$

The solution of the above pseudo-first-order equation is given as

$$[C] = \frac{[L_0][R_0]}{[L_0] + \frac{k_d}{k_a}} (1 - e^{-(k_a[L_0] + k_d)t}). \quad (2.39)$$

At time $t = \tau$, the complex concentration in the chamber would be increased to $[C_\tau]$. At this point in a SPR experiment this would be the time when the chamber is then washed by a buffer, e.g., water. The decreasing rate of the complex can be expressed as

$$\frac{d[C]}{dt} = -k_d[C]. \quad (2.40)$$

From the solution, we see the complex concentration decreases exponentially with time from the start of the elution process $t = \tau$. This is because the concentration of $[L]$ goes to zero with the introduction of the buffer. To get a full view of the rather complicated process which is happening here we refer to Figure 2.17.

From Figure 2.17 we can see clearly that when we push in the buffer we get a resonance dip. After we do that we allow the analyte to flow through and what we observe is that the resonance dip

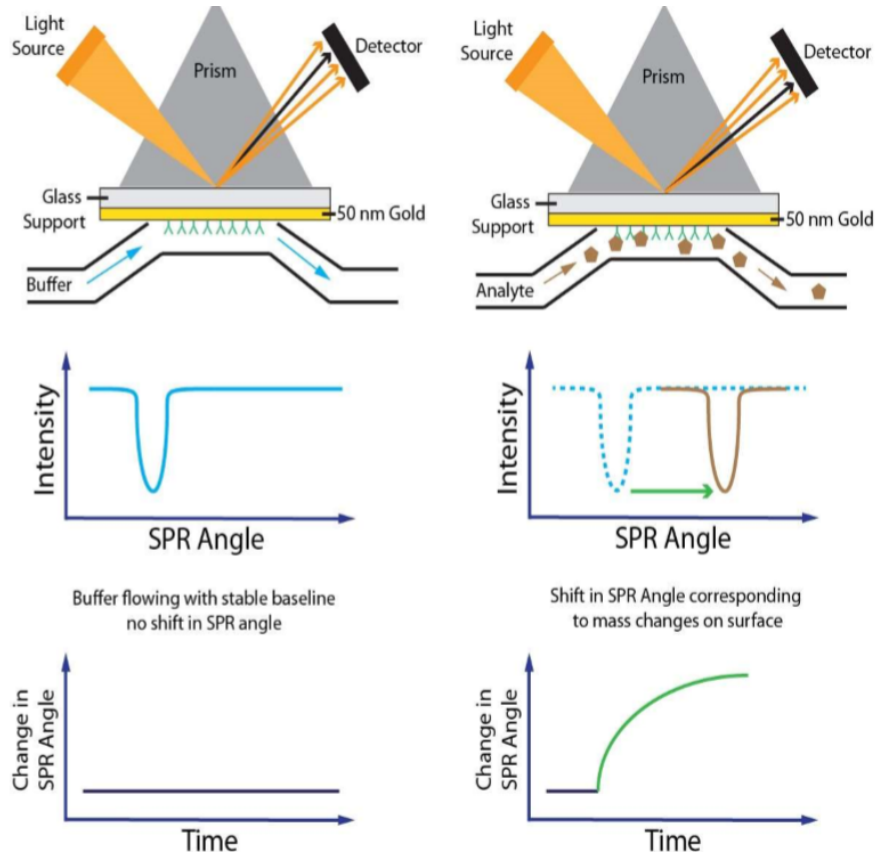


Figure 2.17: The three phases of interaction kinetics. The response unit is a generalization which can refer to a change in the resonance angle, the intensity or refractive index depending on what you are measuring. Figures were taken from [48].

shifts on the reflectance vs incident angle plot. Correspondingly we can keep track of this shift over time and plot a sensorgram which measures the angular shift vs time. From the mathematical model which follows next we will see that by fitting this sensorgram we will be able to extract the important binding parameters discussed in the section above. In the experiment we set/fix our angle in a region around the dip, the most sensitive region is to the left side of the dip and measure the reflectance change. Either the angle change $\Delta\theta$ or reflectance change ΔR can be used in the sensorgram. We will show how they are related in chapter 4.

If we follow the calculations in the paper by Xiao [64], we can formulate a mathematical model which gives the sensorgram for angular shift vs time. This mathematical model is very useful for theoretical simulations and helps us get an understanding of the binding kinetics which occur. The model is

$$\Delta\theta = \begin{cases} A_{\infty}(1 - e^{-k_s t}) & \text{if } 0 \leq t < \tau \\ A_{\tau}e^{-k_d(t-\tau)} & \text{if } t \geq \tau \end{cases}$$

where $\Delta\theta$ is a change in the resonance angle, t is time, A_{∞} and A_{τ} are functions of the concentrations of the sample, k_s , is an observable rate constant, and $k_s = k_a[L_0] + k_d$. We plot the change in the resonance angle $\Delta\theta$ as a function of time to get the sensorgram from which we extract the association and dissociation parameters.

2.2 Introduction to estimation theory

The chief aim in metrology is to study the fundamental limits to precision when estimating a parameter. The Cramér-Rao bound quantifies the optimal precision achievable with any measurement by giving a lower bound on the variance of an unbiased estimator of a deterministic parameter. The Cramér-Rao bound states that the Fisher information gives a limit on the precision (also called standard deviation or uncertainty, $\Delta\phi$) with which a general parameter, ϕ , may be determined. The Cramér-Rao bound is written mathematically as shown below,

$$\Delta\phi \geq \frac{1}{\sqrt{F}}. \quad (2.42)$$

Where F is the Fisher information and ϕ is the parameter being estimated.

In physics, i.e., both classical and quantum physics, many quantities which may be of interest are not directly accessible. This may either be in principle or due to experimental impediments. An example would be when we look at quantum mechanical systems where we are interested in measuring the entanglement and purity of the system, which are non-linear functions of the density matrix [27]. These quantities thus in principle do not correspond to a quantum observable. In such cases we can resort to indirect measurements inferring the value of the quantity of interest, i.e., through inspecting a set of data coming from the measurement of a different observable, or a set of observables [27]. Since we are not directly measuring, the indirect measurements we take are approximate or estimated values of the actual value. This leads us to the study of estimation theory.

Estimation theory is at the heart of quantum and classical metrology. Mathematical statisticians and physicists alike have long been interested in the problem of estimating values of parameters from observables which depend on these parameters. Estimation theory is described or defined as a branch of mathematical statistics which deals with measuring the precision with which we can estimate the values of parameters of a dataset which depends on these parameters. In general these parameters are assumed to be random variables.

2.2.1 Classical parameter estimation

In classical measurement systems, we use the probability distribution of measurement outcomes to define the the Fisher information whereas for quantum measurement processes, the quantum Fisher information is determined by the quantum state of the probe and the measurement.

2.2.2 Deriving the Cramér Rao bound

In this section we will derive the classical Cramer-Rao bound, that is an inequality which expresses a lower bound on the variance of unbiased estimators of a deterministic parameter. The derivation in this section follows Ref. [65]. The derivation may not be immediately obvious at first but the procedure follows rather trivial steps and should be easy to follow. Say we wish to approximate a parameter, θ , of some observable, $\bar{\mathbf{O}}$. Assuming that we know the probability distribution function $p(\bar{\mathbf{O}}, \theta)$ which relates these two quantities we can make the following mathematical statement

$$\int_{-\infty}^{\infty} p(\bar{\mathbf{O}}, \theta) d\bar{\mathbf{O}} = 1. \quad (2.43)$$

We can differentiate Eq. (2.43) above with respect to θ to get

$$\int_{-\infty}^{\infty} \frac{\partial}{\partial \theta} p(\bar{\mathbf{O}}, \theta) d\bar{\mathbf{O}} = \frac{\partial}{\partial \theta} 1 = 0. \quad (2.44)$$

It follows that,

$$\int_{-\infty}^{\infty} \frac{\partial}{\partial \theta} p(\bar{\mathbf{O}}, \theta) d\bar{\mathbf{O}} = 0. \quad (2.45)$$

We can rewrite the above expression as

$$\int_{-\infty}^{\infty} \frac{1}{p(\bar{\mathbf{O}}, \theta)} \left(\frac{\partial}{\partial \theta} p(\bar{\mathbf{O}}, \theta) \right) p(\bar{\mathbf{O}}, \theta) d\bar{\mathbf{O}} = 0. \quad (2.46)$$

The expression in the first part of the equation can be rewritten as

$$\frac{1}{p(\bar{\mathbf{O}}, \theta)} \left(\frac{\partial}{\partial \theta} p(\bar{\mathbf{O}}, \theta) \right) = \frac{\partial}{\partial \theta} \ln(p(\bar{\mathbf{O}}, \theta)), \quad (2.47)$$

where \ln is the natural logarithm. $\frac{\partial}{\partial \theta} \ln(p(\bar{\mathbf{O}}, \theta))$ is called the score and is labelled in some texts as I_{θ} . Hence we can rewrite Eq. (2.47) as

$$\int_{-\infty}^{\infty} \frac{\partial}{\partial \theta} \ln(p(\bar{\mathbf{O}}, \theta)) p(\bar{\mathbf{O}}, \theta) d\bar{\mathbf{O}} = 0. \quad (2.48)$$

We can go a step further and multiply both sides of the equation by θ , as shown below

$$\theta \times \int_{-\infty}^{\infty} \frac{\partial}{\partial \theta} \ln(p(\bar{\mathbf{O}}, \theta)) p(\bar{\mathbf{O}}, \theta) d\bar{\mathbf{O}} = \theta \times 0. \quad (2.49)$$

It follows easily that,

$$\int_{-\infty}^{\infty} \theta \frac{\partial}{\partial \theta} \ln(p(\bar{\mathbf{O}}, \theta)) p(\bar{\mathbf{O}}, \theta) d\bar{\mathbf{O}} = 0. \quad (2.50)$$

The expression for the expected value of an unbiased estimator, $\hat{\theta}$, for the parameter, θ , is given by

$$\mathbf{E}[\hat{\theta}] = \theta. \quad (2.51)$$

It follows that,

$$\int_{-\infty}^{\infty} \hat{\theta} p(\bar{\mathbf{O}}, \theta) d\bar{\mathbf{O}} = \theta. \quad (2.52)$$

Differentiating both sides with respect to θ we get

$$\frac{\partial}{\partial \theta} \int_{-\infty}^{\infty} \hat{\theta} p(\bar{\mathbf{O}}, \theta) d\bar{\mathbf{O}} = \frac{\partial}{\partial \theta} \theta. \quad (2.53)$$

It follows that

$$\int_{-\infty}^{\infty} \hat{\theta} \frac{\partial}{\partial \theta} p(\bar{\mathbf{O}}, \theta) d\bar{\mathbf{O}} = 1. \quad (2.54)$$

We then divide and multiply by $p(\bar{\mathbf{O}}, \theta)$ to get

$$\int_{-\infty}^{\infty} \hat{\theta} \frac{1}{p(\bar{\mathbf{O}}, \theta)} \frac{\partial}{\partial \theta} (p(\bar{\mathbf{O}}, \theta)) p(\bar{\mathbf{O}}, \theta) d\bar{\mathbf{O}} = 1, \quad (2.55)$$

where

$$\frac{1}{p(\bar{\mathbf{O}}, \theta)} \frac{\partial}{\partial \theta} p(\bar{\mathbf{O}}, \theta) = \frac{\partial}{\partial \theta} \ln(p(\bar{\mathbf{O}}, \theta)). \quad (2.56)$$

So it follows that

$$\int_{-\infty}^{\infty} \hat{\theta} \frac{\partial}{\partial \theta} \ln(p(\bar{\mathbf{O}}, \theta)) p(\bar{\mathbf{O}}, \theta) d\bar{\mathbf{O}} = 1. \quad (2.57)$$

Subtracting the left-hand side of Eq. (2.50) from Eq. (2.57) we get

$$\int_{-\infty}^{\infty} \hat{\theta} \frac{\partial}{\partial \theta} \ln(p(\bar{\mathbf{O}}, \theta)) p(\bar{\mathbf{O}}, \theta) d\bar{\mathbf{O}} - \int_{-\infty}^{\infty} \theta \frac{\partial}{\partial \theta} \ln(p(\bar{\mathbf{O}}, \theta)) p(\bar{\mathbf{O}}, \theta) d\bar{\mathbf{O}}. \quad (2.58)$$

This equals

$$\int_{-\infty}^{\infty} (\hat{\theta} - \theta) \frac{\partial}{\partial \theta} \ln(p(\bar{\mathbf{O}}, \theta)) p(\bar{\mathbf{O}}, \theta) d\bar{\mathbf{O}} = 1 - 0 = 1, \quad (2.59)$$

$(\hat{\theta} - \theta)$ can be considered as an estimation error. The above expression can be rewritten as

$$\mathbf{E}[(\hat{\theta} - \theta) \frac{\partial}{\partial \theta} \ln(p(\bar{\mathbf{O}}, \theta))] = 1. \quad (2.60)$$

Using the Cauchy-Schwartz inequality for random variables X and Y given by

$$\mathbf{E}[X^2] \mathbf{E}[Y^2] \geq \mathbf{E}^2[XY], \quad (2.61)$$

in Eq. (2.60) above, with $X = \hat{\theta} - \theta$ and $Y = \frac{\partial}{\partial \theta} \ln(p(\bar{\mathbf{O}}, \theta))$, we can write the expression as

$$\mathbf{E}[(\hat{\theta} - \theta)^2] \mathbf{E}[(\frac{\partial}{\partial \theta} \ln(p(\bar{\mathbf{O}}, \theta)))^2] \geq \mathbf{E}^2[(\hat{\theta} - \theta) \frac{\partial}{\partial \theta} \ln(p(\bar{\mathbf{O}}, \theta))], \quad (2.62)$$

but we know that

$$\mathbf{E}^2[(\hat{\theta} - \theta) \frac{\partial}{\partial \theta} \ln(p(\bar{\mathbf{O}}, \theta))] = 1^2 = 1, \quad (2.63)$$

so

$$\mathbf{E}[(\hat{\theta} - \theta)^2] \mathbf{E}[(\frac{\partial}{\partial \theta} \ln(p(\bar{\mathbf{O}}, \theta)))^2] \geq 1. \quad (2.64)$$

It follows that

$$\mathbf{E}[(\hat{\theta} - \theta)^2] \geq \frac{1}{\mathbf{E}[(\frac{\partial}{\partial \theta} \ln(p(\bar{\mathbf{O}}, \theta)))^2]}, \quad (2.65)$$

where $\mathbf{E}[(\hat{\theta} - \theta)^2]$ is the variance of the estimator assuming it is unbiased and $\mathbf{E}[(\frac{\partial}{\partial \theta} \ln(p(\bar{\mathbf{O}}, \theta)))^2]$ is called the Fisher information or the score of the parameter θ . The Fisher information of the parameter θ can be written as $F(\theta)$.

$$\mathbf{E}[(\hat{\theta} - \theta) \geq \frac{1}{F(\theta)^2}]. \quad (2.66)$$

This calculation was for the classical case, to convert it to the quantum regime we replace the probability $p(\bar{\mathbf{O}}, \theta)$ with the density operator ρ_θ and the integral $\int_{-\infty}^{\infty}$ can be replaced by the Trace operator, Tr , and the score or Fisher information with the quantum score, L_θ .

2.2.3 Quantum parameter estimation

We will now go from the classical Fisher information result to the quantum Fisher information result. We start by describing the analogy between the classical measurement systems and quantum measurement processes. In the classical setup we have the probability density function, $p(\bar{\mathbf{O}}, \theta)$, which is analogous to the density operator, ρ_θ , in the quantum setup. Similarly, the integral operation, $\int_{-\infty}^{\infty}$, is analogous to taking the Trace, Tr , in the quantum picture and the score, I_θ , defined above in the classical picture is replaced by a quantum analogue called the quantum score, L_θ . So moving from the classical Fisher information to the quantum picture involves just performing the mentioned substitutions or replacements and that is what we do in the section below.

2.2.4 Quantum Fisher information

In this section we will follow calculations in [28]. The classical Fisher information, $F(\theta)$, is given as

$$\mathbf{E}\left[\left(\frac{\partial}{\partial\theta}\ln(p(\bar{\mathbf{O}},\theta))\right)^2\right]=\int_{-\infty}^{\infty}\left(\frac{\partial}{\partial\theta}\ln(p(\bar{\mathbf{O}},\theta))\right)^2p(\bar{\mathbf{O}},\theta)d\bar{\mathbf{O}}. \quad (2.67)$$

This will now be changed to

$$F(\theta)=\text{Tr}(\mathbf{L}_\theta\mathbf{L}_\theta^\dagger\rho_\theta). \quad (2.68)$$

The classical Fisher information expression can be reduced as shown below

$$\int_{-\infty}^{\infty}\left(\frac{\partial}{\partial\theta}\ln(p(\bar{\mathbf{O}},\theta))\right)^2p(\bar{\mathbf{O}},\theta)d\bar{\mathbf{O}}=4\int_{-\infty}^{\infty}\left(\frac{\partial}{\partial\theta}(\sqrt{p(\bar{\mathbf{O}},\theta)})\right)^2p(\bar{\mathbf{O}},\theta)d\bar{\mathbf{O}}. \quad (2.69)$$

In the quantum picture this is written as

$$F(\theta)=4\text{Tr}\left(\left(\frac{\partial}{\partial\theta}(\rho_\theta^{\frac{1}{2}})\right)^2\right), \quad (2.70)$$

When the output state is a unitarily transformed pure state, i.e., a state defined as $|\phi'_\theta\rangle=U_\theta|\phi\rangle$ and whose derivative is given by $|\phi_\theta\rangle=\frac{\partial}{\partial\theta}U_\theta|\phi\rangle$ the Fisher information is given by

$$F(\theta)=4(|\langle\phi'_\theta|\phi'_\theta\rangle|-\langle\phi'_\theta|\phi_\theta\rangle)^2. \quad (2.71)$$

In phase sensing $U_\theta=e^{i\hat{n}\theta}$, hence the derivative

$$|\phi'_\theta\rangle=\frac{\partial}{\partial\theta}U_\theta|\phi\rangle=i\hat{n}U_\theta|\phi\rangle, \quad (2.72)$$

$$i\hat{n}U_\theta|\phi\rangle=i\hat{n}|\phi_\theta\rangle. \quad (2.73)$$

Using the definition of the Fisher information above we see that

$$|\langle\phi'_\theta|\phi'_\theta\rangle|=\langle\phi_\theta|\hat{n}^2|\phi_\theta\rangle=\langle\hat{n}^2\rangle, \quad (2.74)$$

$$|\langle\phi'_\theta|\phi_\theta\rangle|=-i\langle\phi_\theta|\hat{n}|\phi_\theta\rangle=-i\langle\hat{n}\rangle. \quad (2.75)$$

Hence, the Fisher information here becomes

$$F=4(\langle\hat{n}^2\rangle-\langle\hat{n}\rangle^2)=4V(\hat{n}). \quad (2.76)$$

The phase shift operator, U_θ , preserves photon number and hence we can evaluate the Fisher information for either the input state or the final state. This shows that fundamentally the sensitivity of a phase measurement on a pure quantum state depends solely on the photon number variance of the state in the signal arm of the interferometer. Of course this is only true in the case where we do not consider technical limitations such as the efficiency of our optical setup and photon number resolving detectors.

2.2.5 Quantum Fisher information example calculation

NOON state example

We will give an example in this section before we go into the details of the quantum description of light. A NOON state is written as follows

$$|\psi_{\text{NOON}}\rangle=\frac{1}{\sqrt{2}}(|N\rangle_1|0\rangle_2+|0\rangle_1|N\rangle_2). \quad (2.77)$$

The N00N state is defined as a quantum-mechanical many-body entangled state which represents a superposition of N particles in mode 1 with zero particles in mode 2 and vice versa . The first step in the calculation is

$$\langle \psi_{N00N} | \hat{n}_1 | \psi_{N00N} \rangle = \left(\frac{1}{\sqrt{2}} (\langle N|_1 \langle 0|_2 + \langle 0|_1 \langle N|_2) \right) \hat{n}_1 \left(\frac{1}{\sqrt{2}} (|N\rangle_1 |0\rangle_2 + |0\rangle_1 |N\rangle_2) \right). \quad (2.78)$$

Where $\hat{n}_1 = \hat{a}_1^\dagger \hat{a}_1$ and $\langle N|_1 \hat{a}_1^\dagger \hat{a}_1 |N\rangle_1 = N$, which gives

$$\left(\frac{1}{\sqrt{2}} (\langle N|_1 \langle 0|_2 + \langle 0|_1 \langle N|_2) \right) \hat{n}_1 \left(\frac{1}{\sqrt{2}} (|N\rangle_1 |0\rangle_2 + |0\rangle_1 |N\rangle_2) \right) = \frac{N}{2}. \quad (2.79)$$

Similarly,

$$\langle \psi_{N00N} | \hat{n}_1^2 | \psi_{N00N} \rangle = \left(\frac{1}{\sqrt{2}} (\langle N|_1 \langle 0|_2 + \langle 0|_1 \langle N|_2) \right) \hat{n}_1^2 \left(\frac{1}{\sqrt{2}} (|N\rangle_1 |0\rangle_2 + |0\rangle_1 |N\rangle_2) \right) = \frac{N^2}{2}. \quad (2.80)$$

We then have,

$$F = 4(\langle \psi_{N00N} | \hat{n}_1^2 | \psi_{N00N} \rangle - |\langle \psi_{N00N} | \hat{n}_1 | \psi_{N00N} \rangle|^2), \quad (2.81)$$

thus

$$F = N^2. \quad (2.82)$$

From Eq. (2.65)

$$\Delta\theta \geq \frac{1}{\sqrt{F}}. \quad (2.83)$$

For the N00N state this is

$$\Delta\theta = \mathbf{E}[(\hat{\theta} - \theta)^{\frac{1}{2}}]^2 \geq \frac{1}{N}. \quad (2.84)$$

The standard deviation bound (precision) is smaller than for the classical case [18],

$$\Delta\theta_{cl} = \mathbf{E}[(\hat{\theta} - \theta)^{\frac{1}{2}}]^2 \geq \frac{1}{\sqrt{N}}. \quad (2.85)$$

2.3 Quantum description of light

Quantum mechanics offers a number fascinating experimental results which are not very intuitive. There are mathematical models which have been developed over the years to explain the phenomena of quantum mechanics. We need to look at the different quantum mechanical models for light in order to be able to understand the various experimental results and techniques which have been established. We can review the types of predictions one can make about experimental outcomes of quantum mechanical systems from the mathematics of the quantum models [75].

Looking at classical mechanics, we find that an observable quantity is represented by a variable, x , for example where x may for instance represent the position of a particle. In the classical regime x is just a number which may vary as a function of time and/or other parameters. The outcome of an experiment which measures/obtains the position will just be a numerical value of x .

This is not particularly true for quantum mechanical systems as we generally do not get unique results but rather we get a range of results which occur with some probability. This means that we will measure certain values of x and these values lie within some probabilistic distribution curve. This means that there is a probability associated with the measurement of any one possible outcome. A consequence of this is that it becomes insufficient to present a single unique solution to describe all the possible outcomes of a particular quantum mechanical experiment. Ultimately we have to

represent variables as operators in quantum mechanics, for instance the position variable in the classical regime becomes a position operator.

States in quantum mechanics are written as $|\mathbf{x}\rangle$ and they contain the information about all the possible outcomes. Operators which represent an observable quantity in quantum mechanics have eigenstates associated with them whose eigenvalues represent the spectrum of possible results that a measurement of this observable can obtain. Generally we find that most systems are simply in statistical mixtures of various quantum states, which themselves are superposition of various eigenstates of some observable. In the rare case where the system is actually in an eigenstate of the observable we can measure a definite result.

In quantum theory we typically want to make predictions about the results of large ensembles of measurements and because we usually have large ensembles of quantum mechanical systems we often want to make predictions which are statistical in nature. For instance, we predict the average values of measurements performed on large ensembles of systems all prepared in the same state $|\sigma\rangle$ of the observable, represented by the operator $\hat{\mathbf{x}}$. We can do this by taking the expectation value of the observables operator

$$\langle \hat{\mathbf{x}} \rangle = \langle \sigma | \hat{\mathbf{x}} | \sigma \rangle. \quad (2.86)$$

Higher order moments can be investigated as well. We can look at $\hat{\mathbf{x}}^2$ which leads to the variance of the system, defined mathematically as

$$\langle \Delta \hat{\mathbf{x}}^2 \rangle = \langle \hat{\mathbf{x}}^2 \rangle - \langle \hat{\mathbf{x}} \rangle^2. \quad (2.87)$$

Classically non-zero variance (noise) is associated with imperfect preparation of the system. In the quantum regime ideally prepared systems will exhibit non-zero variance due to the probabilistic nature of the theory. This variance (non-zero fluctuations) is referred to as quantum noise. In quantum theory the characteristics of a system with respect to a particular observable are typically characterizable by the expectation values of all the moments of the observable's operator however, as most cases of interest exhibit Gaussian statistics, the system is completely (sufficiently) characterized by just the first and second order moments.

If we have a classical system characterized by the canonically conjugate variables x and p we can quantize the system using the canonical quantization procedure first pioneered by the mathematician and physicist Paul Dirac. In the procedure it sufficient to quantize the classical system by replacing x and p with the operators $\hat{\mathbf{x}}$ and $\hat{\mathbf{p}}$ in the Hamiltonian and replacing the classical Poisson bracket with the commutation relation

$$[\hat{\mathbf{x}}, \hat{\mathbf{p}}] = \hat{\mathbf{x}}\hat{\mathbf{p}} - \hat{\mathbf{p}}\hat{\mathbf{x}} = i\hbar. \quad (2.88)$$

2.3.1 Quantum states of light

Number or Fock states

This section follows calculations in Ref. [46]. The Hamiltonian for a single mode of the radiation field in terms of the number operator can be expressed as

$$\hat{H} = h\nu(\hat{n} + \frac{1}{2}). \quad (2.89)$$

The eigenvalues are $h\nu(n + \frac{1}{2})$ and the corresponding eigenstates can be represented as $|n\rangle$. These states are known as the number or Fock states and are eigenstates of the number operator \hat{n} , i.e.,

$$\hat{n} |n\rangle = \hat{a}^\dagger \hat{a} |n\rangle = n |n\rangle. \quad (2.90)$$

$\hat{a}^\dagger \hat{a}$ is the photon number operator meaning it counts the number of photons in the state $|n\rangle$. The operators \hat{a}^\dagger and \hat{a} are raising and lowering operators on the series of equally spaced eigenstates,

which generate new states as follows: $\hat{a}|n\rangle = \sqrt{n}|n-1\rangle$ so that \hat{a} lowers the energy eigenstate and \hat{a}^\dagger raises it according to $\hat{a}^\dagger|n\rangle = \sqrt{n+1}|n+1\rangle$.

We can generate all possible number states starting with the ground state $|0\rangle$ by a successive application of the creation operator \hat{a}^\dagger , $|n\rangle = \frac{(\hat{a}^\dagger)^n}{\sqrt{n!}}|0\rangle$ where $\sqrt{n!}$ is a normalization factor. The state $|n\rangle$ is called the n-photon state where n corresponds to the eigenvalue of the corresponding photon number operator. All states are orthogonal and complete. Since the photon number is exactly defined we measure/calculate the variance (V) to be zero

$$V_n = \langle \Delta \hat{n}^2 \rangle = \langle n | \Delta \hat{n}^2 | n \rangle = \langle n | \hat{n} \hat{n} | n \rangle - \langle n | \hat{n} | n \rangle^2 = 0. \quad (2.91)$$

The contrast between the classical and quantum descriptions of light can be highlighted by comparing the average value of the quadrature amplitudes for classical light and light in a number state. In the classical description of light an arbitrary quadrature amplitude, X^ϕ , can be described as a function of the phase angle, ϕ , according to

$$X^\phi = \cos\phi X_1 + \sin\phi X_2, \quad (2.92)$$

where X_1 and X_2 are the quadratures of X^ϕ . In the quantum regime we replace the quadrature variables with quadrature operators, we find the average value of the quadrature amplitude for light in a particular quantum state by taking the expectation value over the state of interest. The expectation value is taken as

$$\langle \hat{X}^\phi \rangle = \langle n | \hat{X}^\phi | n \rangle = 0, \quad (2.93)$$

where $\hat{X}_1 = \frac{1}{2}(\hat{a} + \hat{a}^\dagger)$ and $\hat{X}_2 = \frac{1}{2i}(\hat{a} - \hat{a}^\dagger)$. \hat{X}_1 and \hat{X}_2 are the real and imaginary parts of the annihilation operator. The result above is because of the orthogonality of the number states which ensures that all terms like $\langle n | \hat{a} | n \rangle$ and $\langle n | \hat{a}^\dagger | n \rangle$ are zero. We see that for the number state the average value is always zero irrespective/independent of the quadrature angle whereas in the classical regime we see that the quadrature amplitude oscillates as a function of the quadrature angle ϕ . These are clearly two very different descriptions of light. The vacuum state $|0\rangle$ ($n=0$) plays a very important role in quantum optical experiments and number states ($n > 0$) are a rather exotic resource as they are dissimilar to coherent states.

Coherent states

Incoherent light refers to light with many frequencies and waves out of phase, e.g., multi-mode thermal states whereas, coherent light refers to light with a small bandwidth of frequencies whose waves are all in phase. One chief disadvantage of the number states is that they are impractical

for the description of real laser beams [46], this is primarily because they do not represent a well defined phase. A coherent state $|\alpha\rangle$ is a state which has a well defined phase and such states are the closest quantum approximation to the field generated by a laser. Looking at an idealized way to produce light in the classical regime we start from an initial state with zero energy in the electric and magnetic fields and then the electric field is displaced by some means to some non-zero value given by a parameter α , where $\alpha > 0$. The now displaced electric field in turn displaces the magnetic field resulting in a propagating light field. If we stick to the same line of thought however in the

quantum regime this time we can think of ways to displace the vacuum state to some non-zero value in the hope of producing an oscillating field. However seeing that the vacuum state has zero energy we expect uniquely quantum features. A displacement operator, \hat{D} , is defined such that it has the effect of displacing the vacuum state by an amount α which is comparable to the complex classical amplitude.

$$|\alpha\rangle = \hat{D}(\alpha)|0\rangle. \quad (2.94)$$

The $|\alpha\rangle$ state is called the coherent state. The operator $\hat{D}(\alpha)$ is defined as $\hat{D}(\alpha) = e^{(\alpha\hat{a}^\dagger - \alpha^*\hat{a})}$. Some properties of the displacement operator are considered here as they prove to be useful in later calculations.

Property (1)

$$\hat{D}(\alpha)^\dagger = \hat{D}(\alpha)^{-1} = \hat{D}(-\alpha), \quad (2.95)$$

Property (2)

$$\hat{D}(\alpha)^\dagger \hat{a}^\dagger \hat{D}(\alpha) = \hat{a}^\dagger + \alpha, \quad (2.96)$$

Property (3)

$$\hat{D}(\alpha)^\dagger \hat{a} \hat{D}(\alpha) = \hat{a} + \alpha. \quad (2.97)$$

Coherent states are normalized to one

$$\langle \alpha | \alpha \rangle = 1. \quad (2.98)$$

This is due to the unitary nature of the displacement operator, another interesting feature of coherent states is that they are eigenstates of the annihilation operator \hat{a} ,

$$\hat{D}(\alpha)^\dagger \hat{a} | \alpha \rangle = \hat{D}(\alpha)^\dagger \hat{a} \hat{D}(\alpha) | 0 \rangle = (\hat{a} + \alpha) | 0 \rangle = \alpha | 0 \rangle. \quad (2.99)$$

Multiplying both sides with the operator \hat{D} results in the eigenvalue condition

$$\hat{a} | \alpha \rangle = \alpha | \alpha \rangle. \quad (2.100)$$

In a coherent state the expectation values for the quadrature amplitude operator are similar to classical variables. This is under the condition that we identify the displacement α with the classical complex amplitude with the average value of the field oscillating as a function of quadrature angle i.e,

$$\langle \hat{X}^\phi \rangle_\alpha = \cos\phi X_1 + \sin\phi X_2. \quad (2.101)$$

The expectation value of photon numbers in the coherent state is also similar to that of the classical regime,

$$\langle \hat{a}^\dagger \hat{a} \rangle_\alpha = |\alpha|^2. \quad (2.102)$$

The average values of the observables in the classical field are quite similar to those of coherent states. The chief difference between the number state which contains a finite amount of energy and coherent states is that coherent states do not contain a definite number of photons. This stems from the fact that a coherent state $|\alpha\rangle$ is made up of a superposition of number states. We see this in from the equation below

$$|\alpha\rangle = \sum_{n=0}^{\infty} |n\rangle \langle \alpha|n\rangle, \quad (2.103)$$

where

$$\langle \alpha|n\rangle = \frac{\alpha^n}{\sqrt{n!}} e^{-\frac{1}{2}|\alpha|^2}. \quad (2.104)$$

Two different coherent states are not orthogonal to each other

$$|\langle \alpha_1 | \alpha_2 \rangle|^2 = |\langle 0 | \hat{D}(\alpha_1)^\dagger \hat{D}(\alpha_2) | 0 \rangle|^2 = |e^{-\frac{1}{2}(|\alpha_1|^2 + |\alpha_2|^2) + \alpha_1^* \alpha_2}|^2, \quad (2.105)$$

then

$$|e^{-\frac{1}{2}(|\alpha_1|^2 + |\alpha_2|^2) + \alpha_1^* \alpha_2}|^2 = e^{-|\alpha_1 - \alpha_2|^2}. \quad (2.106)$$

Any two states with vastly different photon numbers will be approximately orthogonal as $|\alpha_1 - \alpha_2| \gg 1$. Thus coherent states form a basis which is over complete, however they can be used as a basis on which any state $|\psi\rangle$ can be expanded. The properties of coherent states are similar to those of classical coherent light and coherent states offer the closest quantum mechanical approximation of classical coherent light (laser light). Laser light can often be well approximated by a coherent state as is true of the statement that laser light can be approximated as idealized classical coherent

light in certain situations, for instance when a quantum mechanical description is needed. Coherent states are stable in regard to dissipation meaning a coherent state is transformed into another coherent state when attenuated. This means that the properties of the laser light remain similar after attenuation. Coherent states are extensively used in the modelling of laser-based experiments. In the lab (experimentally) we need two parameters to distinguish different states of light, that is the intensity and the phase, and since α is a complex number we find that its range of values and consequently the range of values of the coherent states require a two dimensional representation. The intensity has a simple quantum mechanical equivalent which is the number operator. The phase does not have a quantum mechanical equivalent and hence phase operators can only be approximated in a complex manner through a limit of a series of operators. Since the quadrature amplitude operators \hat{X}_1 and \hat{X}_2 are well behaved they lead to a pair of Hermitian operators that describe the field.

Squeezed state

For quantum states the Heisenberg uncertainty principle for the quadrature operator is $\Delta X_1^2 \Delta X_2^2 \geq \frac{1}{16}$, where ΔX_1^2 and ΔX_2^2 are quadratures variances, $\Delta X_i^2 = \langle \Delta X_i^2 \rangle$. Single-mode squeezed states are single mode states which saturate this inequality [33]. The noise in either one of the quadratures can be made smaller than in the other in squeezed states, therefore in general $\Delta X_1^2 \neq \Delta X_2^2$. A single-mode displaced squeezed vacuum state is represented mathematically as

$$|\alpha, r\rangle = \hat{D}(\alpha)\hat{S}(r)|0\rangle, \quad (2.107)$$

where $\hat{S}(r) = e^{\frac{1}{2}(r^* \hat{a}^2 - r \hat{a}^{\dagger 2})}$. The $\hat{S}(r)$ operator is called the squeezing operator and $r = |r|e^{i\theta}$ is a complex number where $|r|$ and θ are called the squeezing factor and the squeezing angle respectively.

Classical electrodynamics cannot fully describe features of squeezed states in general because squeezed states cannot be described as mixtures of coherent states, thus they are 'non-classical'. Nevertheless, squeezed states can be prepared relatively easily by using non-linear optical elements in the process of parametric down conversion [46]. Squeezed vacuum states possess vanishing mean values of their quadratures which makes them relevant for metrology. They are defined as

$$|r\rangle = \hat{S}(r)|0\rangle. \quad (2.108)$$

The squeezed vacuum state has an average number of photons $\langle \hat{n} \rangle = \sinh(2r)$, so despite their name, squeezed vacuum states contain photons, potentially a lot of them. We can express squeezed vacuum states in their Fock basis as shown below.

$$|r\rangle = \frac{1}{\sqrt{\cosh(|r|)}} \sum_{n=0}^{\infty} \frac{H_n(0)}{\sqrt{n!}} \left(\frac{\tanh(|r|)}{2}\right)^{\frac{n}{2}} e^{i\frac{n\theta}{2}} |n\rangle, \quad (2.109)$$

where $H_n(0)$ denotes values of the n -th Hermite polynomial at $x = 0$. For odd n , $H_n(x)$ is antisymmetric and thus $H_n(0) = 0$. This implies that squeezed vacuum states are superpositions of Fock states with only even photon numbers.

We can extend our study of squeezed states to the two-mode setup. We will begin by considering the two-mode squeezed vacuum (TMSV) state. Mathematically the state is generated from the vacuum by the two-mode squeezing operation shown below,

$$|\xi\rangle_2 = \hat{S}_2(\xi)|0, 0\rangle, \quad (2.110)$$

where $\hat{S}_2(\xi) = e^{(\xi^* \hat{a}\hat{b} - \xi \hat{a}^\dagger \hat{b}^\dagger)}$. The $\hat{S}_2(\xi)$ operator is called the two-mode squeezing operator and $\xi = |\xi|e^{i\theta}$ is a complex number where $|\xi|$ and θ are called the squeezing factor and the squeezing angle respectively.

It is worth noting the two-mode squeezed vacuum state is not a product of squeezed states in modes a and b, but rather it is correlated between the two modes. It is a superposition of terms with the same number of photons in both modes. We can see this more clearly by looking at the Fock basis,

$$|\xi\rangle_2 = \frac{1}{\cosh(|\xi|)} \sum_{n=0}^{\infty} (-1)^n e^{in\theta} \tanh^n |\xi| |n, n\rangle. \quad (2.111)$$

Various non-linear processes, such as three- and four-wave mixing can be used to generate TMSV states in a laboratory [46]. An alternative way to generate TMSV states is to mix two single-mode squeezed vacuum states with opposite squeezing angles on a 50/50 beam-splitter [46].

When we are interested in sensors operating in the high-intensity regime we can extend our study of squeezed states to the two-mode squeezed displaced (TMSD) state. This state is produced by performing the two-mode squeezing operation on a vacuum state in one mode and coherent state in the other mode. The intensity of the coherent state can be very high. The TMSD state is defined mathematically as

$$|\text{TMSD}\rangle = \hat{S}_2(\chi) |0\rangle_a |\alpha\rangle_b. \quad (2.112)$$

Appendix A shows a calculation of the sensing precision in a two-mode setup when using a TMSD state as input. TMSD states can be generated via a four-wave mixing process in a double-lambda configuration provided by a ^{85}Rb vapor cell [72].

Mixed states

The Fock states and coherent states are pure field states. In general we can have mixed states, which are defined to be field states that are in an incoherent mixture of different pure states. Typically we represent mixed states by a density operator, ρ which can be written as $\rho = a |\sigma_1\rangle \langle\sigma_1| + a_2 |\sigma_2\rangle \langle\sigma_2| + \dots$ which represents a mixture of the states $|\sigma_1\rangle, |\sigma_2\rangle, |\sigma_3\rangle, \dots$ and so forth, with probability weights given by a_1, a_2, a_3, \dots . An important thing to note is the fact that mixed states and superpositions of states are really different things. A mixed quantum state can be described as one which corresponds to a probabilistic mixture of pure states. Take for example the superposition state $|\phi\rangle = \frac{1}{\sqrt{2}}(|x\rangle + |y\rangle)$. The density operator of this state is written as $\rho = |\phi\rangle \langle\phi|$ and includes cross terms also.

The coherent, Fock, TMSV and TMSD states will all be used in this study in chapter 3. In chapter 5, the experimental part, we will consider single photons (n=1 Fock states).

2.4 Spontaneous parametric down conversion

This physical phenomenon of spontaneous parametric down conversion (SPDC) gives the most efficient way to produce single-photons and quantum correlations between optical fields. It was discovered at the end of the sixties [70]. The development of new kinds of laser systems and photon detectors allows SPDC to be used in advanced quantum technologies, such as quantum key distribution [52], quantum computing [52], tailoring of quantum states [108112], quantum imaging [15, 113] and quantum sensing [114].

Advances in quantum optics techniques for conducting experiments using single photons have stimulated much interest in the studies of the fundamentals of quantum mechanics which form the basis for applications such as quantum sensing, quantum computation and quantum cryptography [51]. At the heart of these experiments is the production of single photons. These single photons exhibit quantum mechanical properties which are used to encode information in a manner which does not have a classical equivalent.

One of the features provided by single photons is entanglement, a property that allows for the quantum states of any two or more single photons to be connected in such a manner that measuring

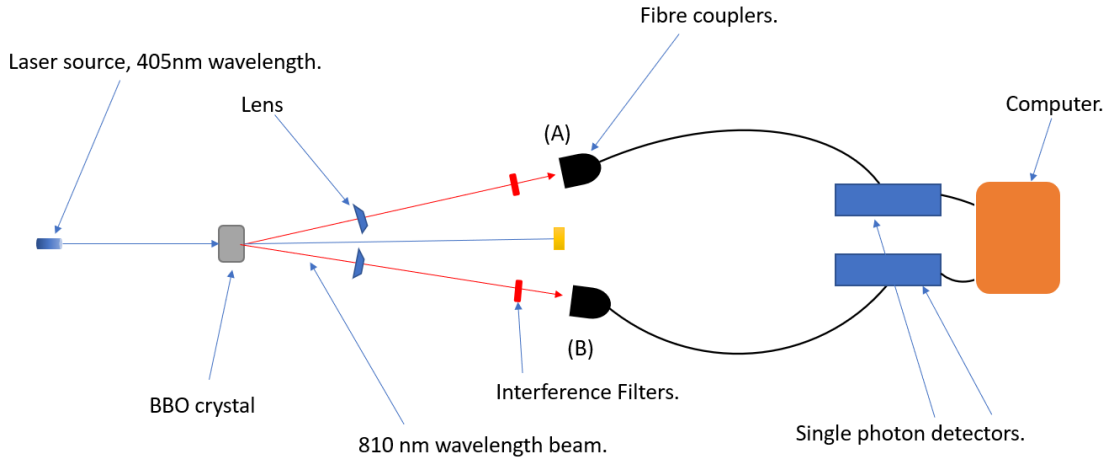


Figure 2.18: Setup of the single-photon source. A and B are the two modes.

the state of one of the single photons automatically defines the state of the other, even though neither particle is in its own well defined state before measurement [49]. Entanglement is a uniquely quantum mechanical resource (i.e., non-classical) that plays a key role in ensuring a speed up in computation and security in cryptography which is not achievable classically. Entanglement is a key resource for producing proof of principle experiments and it is important that we generate the single photons which can exhibit this feature.

SPDC is a reliable though probabilistic means of producing single photons [47]. The process begins with an intense pump laser beam which is sent towards a non-linear crystal or a non-linear optical medium such as KH_2PO_4 [52]. When the pump laser is incident on the crystal or medium there is a probability that two lower frequency photons (a correlated photon-pair) will be produced from the single pump photon.

2.4.1 Experimental setup for SPDC

The layout for a type 1 SPDC single-photon source used in chapter 5 shown in Figure 2.18. A 405 nm wavelength laser beam is sent towards a 3 mm thick $\beta\text{-BaB}_2\text{O}_4$ (BBO) crystal. The 405 nm wavelength beam is guided by some mirrors towards the crystal, and this is called the pump beam. When the pump beam hits the BBO crystal it undergoes SPDC, in which it breaks down into two beams of higher wavelength, i.e., 810 nm each. These are called the signal and idler. It must be noted that only a small percentage of pump photons undergo SPDC in the BBO crystal to produce the idler and signal photon pairs in the output beams.

The photon pairs come out at an angle of three degrees. The lenses after the crystal on both of the down-conversion arms are there to collimate the idler and signal beams, they also improve collection by the fibre-couplers, which consist of a 20x microscope objective and an XYZ-translation stage.

Interference filters (800 ± 20) nm are placed before the fibre couplers. These are used to clean up the beam and ensure we collect specific photon wavelengths. The fibre couplers are connected to single photon detectors which measure coincidence counts. The coincidence rate is the number of detections in arms A and B collectively that occur within eight nanoseconds (this is a chosen coincidence window, it can be changed in general). The count rate is monitored and displayed on a LABVIEW program.

2.4.2 Polarisation in non-linear optical materials

This section follows calculations from [59]. In order to understand how single photons are generated using SPDC we need to understand the non-linear response of materials to an applied electric field. If we let an electromagnetic field propagate through a dielectric material or medium, the electric field will behave in such a way that it redistributes the charges of the medium. The electric field acts on each individual particle within the medium that is, electrons, atoms or molecules. The displacement of charges is such that the positive charges lie in the direction of the electromagnetic field whereas the negative charges lie in the opposite direction of the field. This causes the material to become polarised in charge. If a weak electromagnetic field (small electric field amplitude) is introduced then the relationship between the polarisation, P , and the incident field E is approximately linear

$$P \approx \epsilon_0 \chi E. \quad (2.113)$$

Where χ is the linear susceptibility and ϵ_0 is the permittivity in free space. If we assume the electric fields and polarisation to be scalar quantities we can neglect the tensor nature of the polarisation. The linear susceptibility is a measure of how readily or easily the dielectric medium polarizes in response to the presence of an electromagnetic field. Lasers have a large electric field amplitude output and the experiments of interest in this paper are laser based and hence the above approximation though very useful in linear optics will not apply here. In this case higher order contributions of the electric field become significant and the following non-linear response of the material to the field becomes significant

$$P = \epsilon_0 [\chi^{(1)} E + \chi^{(2)} E^2 + \chi^{(3)} E^3 + \dots]. \quad (2.114)$$

Where $\chi^{(m)}$ for $m > 0$ are the susceptibilities for order m . If $m=1$ then $\chi^{(1)} = \chi$. The susceptibilities typically have small values. The dielectric material which is often used in quantum optics is a crystal, for example the BBO crystal. Only crystalline materials with the anisotropic (non-centrosymmetric property) give a non-zero square term in the polarisation expansion, that is $\chi^{(2)} \neq 0$. All crystalline materials give a non-zero cubic susceptibility tensor, that is $\chi^{(3)} \neq 0$. It is the case that $\chi^{(1)}$ determines the index of refraction and describes the linear reaction of crystals (refraction, dispersion). $\chi^{(1)}$ is also known as the linear polarisability. $\chi^{(2)}$ determines non-linear effects such as three-wave mixing and $\chi^{(3)}$ describes the tripling of the light frequency and hyper-parametric scattering.

2.4.3 Second-order non-linear processes

We now look at the second term in Eq. (2.114), which is called the second-order non-linear response of a dielectric material. The equation is given by

$$P^{(2)} = \epsilon_0 \chi^{(2)} E \cdot E. \quad (2.115)$$

There are three waves present, that is a response wave characterized by P and two pump E waves which is why the second-order non-linear processes are referred to as three-wave mixing processes. There are four possible three-wave mixing processes which can be obtained from this non-linearity [61].

An electric field made of two pump fields oscillating at angular frequencies, ω_1 , and, ω_2 , can be described by

$$E(r, t) = \frac{1}{2} (E_1 e^{i(k_1 r - \omega_1 t)} + E_2 e^{i(k_2 r - \omega_2 t)} + \text{c.c.}), \quad (2.116)$$

where E_1 and E_2 are the amplitudes of the first and second electric fields respectively and c.c. is the complex conjugate incident on the medium. If we substitute the above equation into the non-linear polarisation, Eq. (2.115), we get

$$P^{(2)} = \epsilon_0 \chi^{(2)} E^2,$$

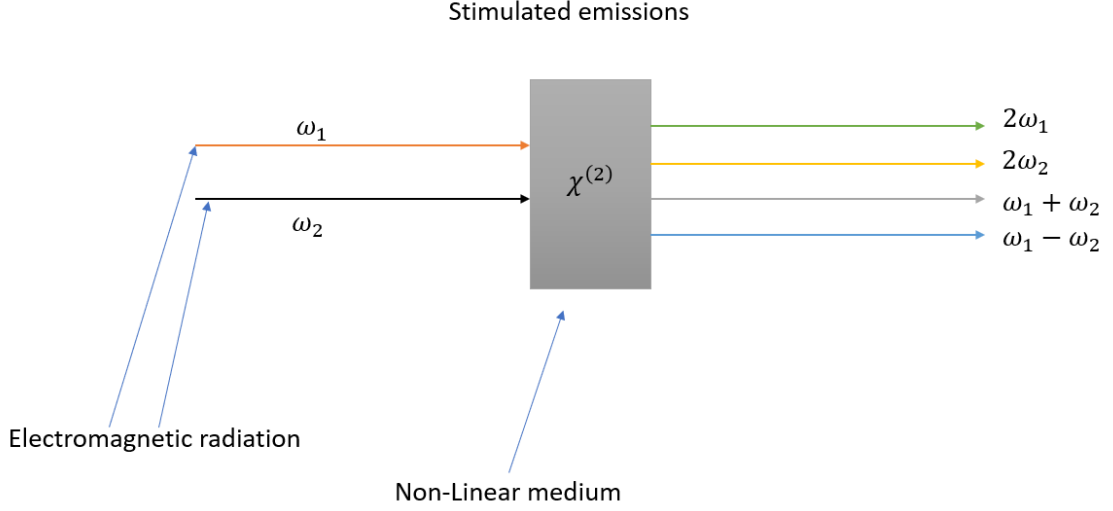


Figure 2.19: Second-order non-linear processes. When an electromagnetic field interacts with a non-linear medium having a non-linear susceptibility χ^2 , the resulting electromagnetic field contains second harmonics ($2\omega_1, 2\omega_2$), sum-frequency ($\omega_1 + \omega_2$) and difference-frequency ($\omega_1 - \omega_2$) components [66].

$$\begin{aligned}
&= \frac{1}{2}\epsilon_0\chi^2[|\mathbf{E}_1|^2 + |\mathbf{E}_2|^2] + \frac{1}{4}\epsilon_0\chi^2[(\mathbf{E}_1^2 e^{i(2k_1 r - 2\omega_1 t)} + \mathbf{E}_2^2 e^{i(2k_2 r - 2\omega_2 t)} \\
&+ 2\mathbf{E}_1\mathbf{E}_2 e^{i((k_1+k_2)r - (\omega_1+\omega_2)t)} + 2\mathbf{E}_1\mathbf{E}_2^* e^{i((k_1-k_2)r - (\omega_1-\omega_2)t)} + \text{c.c.}]. \quad (2.117)
\end{aligned}$$

In the above mathematical description the first two terms $[|\mathbf{E}_1|^2 + |\mathbf{E}_2|^2]$ correspond to optical rectification (a non-linear process where an optical field generates a quasi-DC non-linear polarisation). The second two terms in the equation represent second-harmonic generation. Each of the two incoming pump fields produce a second-harmonic field with half the wavelength of the pump field.

As is shown by the fifth term, the pump beam also generates a field oscillating at a frequency which is the sum of the original two frequencies. This process is known as sum-frequency generation. The last term is called difference-frequency generation because it is a generated field with a frequency which is a difference of the pump field frequencies. All terms are shown in Figure 2.19. Typically no more than one of the frequency components will be present with any appreciable intensity in the produced field [100]. This is because each term in Eq. (2.115) has its own phase-matching conditions and it is unlikely that more than one is satisfied for a given frequency component of the polarization.

The process of difference-frequency generation has many of its practical applications in the amplification of signals. For example, in optical parametric amplification a laser with frequency ω_p is used to pump a non-linear crystal. We find that the second harmonic term can generate its own second harmonic which consequently will be the fourth harmonic of the pump field, however only one of these can be possible when using a second-order medium, which one is determined by phase-matching conditions. Processes violating the conditions will be suppressed.

In this thesis the process which is of interest is SPDC. It can be described as a reverse process to sum-frequency generation and occurs when the pump field oscillating at angular frequency ω_p

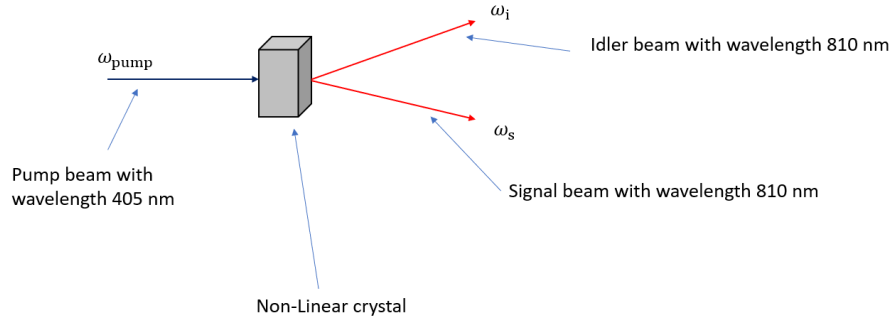


Figure 2.20: Spontaneous parametric down-conversion. A pump photon with frequency ω_p propagating towards a non-linear crystal is spontaneously down-converted into two photons with frequencies ω_s and ω_i [66].

generates two optical fields such that $\omega_1 + \omega_2 = \omega_p$. At the single-photon level this allows a photon of frequency ω_p from a pump beam incident on an anisotropic crystal to be converted into a correlated photon-pair at lower frequencies.

2.4.4 SPDC fundamentals

SPDC can be defined as a non-linear optical process by which a photon of frequency ω_p from a pump beam is converted into a correlated photon pair (correlated in time of emission, frequency and momentum) which are at lower frequencies [62]. The pump field is incident on a non-linear (as shown in Figure 2.20) crystal and though most of the photons from the pump field go through the crystal, occasionally (probabilistically) interactions between the pump field and molecules in the crystal result in the pump photon being broken into a correlated photon pair. The two photons are called the signal and idler and they have wave vectors k_s and k_i , and frequencies ω_s and ω_i , respectively.

The photon pairs produced are orthogonally polarised to the pump polarisation. The direction of the down-converted photons can be controlled by adjusting the angle between the pump photons and the optics axis of the crystal. The principles of the SPDC process can be understood by energy and momentum conservation.

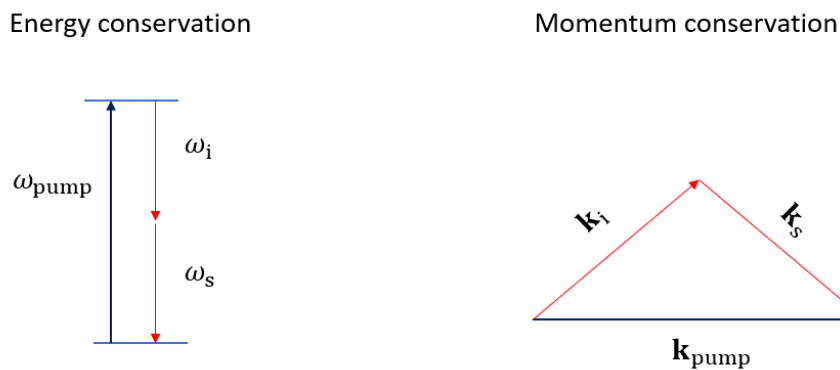


Figure 2.21: Energy and momentum diagrams of a single SPDC process. The process conserves energy and momentum, which implies that the frequencies of the photons satisfy $\omega_s + \omega_i = \omega_p$ and their wave vectors $\mathbf{k}_s + \mathbf{k}_i = \mathbf{k}_p$ [66].

The condition $\omega_s + \omega_i = \omega_p$ is known as the frequency-matching condition and $\mathbf{k}_s + \mathbf{k}_i = \mathbf{k}_p$ is

known as the phase-matching condition, as shown in Figure 2.21. SPDC is stimulated by vacuum fluctuations which results in the spontaneous conversion of an single photon into two. The incident energy is all transferred to the generated photons and none to the molecules of the crystal, meaning the crystal is left unchanged and hence the process is parametric. The process is called a down-conversion process because the generated photons have a lower energy than the incident photon.

2.4.5 Choosing an appropriate crystal for SPDC

The frequency-matching and phase-matching conditions are quite useful in that they help us in selecting the correct crystal to produce SPDC [78]. Following the argument below we can see why this is the case. The wave vector \mathbf{k}_i and \mathbf{k}_s can be expressed as

$$\mathbf{k}_j = \frac{n_j(\omega_j)\omega_j\mathbf{s}_j}{c}. \quad (2.118)$$

Where \mathbf{s}_j is a unit vector in the \mathbf{k}_j direction, c is the speed of light and $n_j(\omega_j)$ is the refractive index of the material which has a dependence on ω_j . We can thus rewrite the phase matching condition as

$$n_p(\omega_p)\omega_p\mathbf{s}_p = n_s(\omega_s)\omega_s\mathbf{s}_s + n_i(\omega_i)\omega_i\mathbf{s}_i. \quad (2.119)$$

If the down-conversion is degenerate then we have that $\omega_s = \omega_i = \omega_p/2$ (satisfies the frequency-matching condition). The minimal magnitude of $|\mathbf{k}_s| + |\mathbf{k}_i|$ can still satisfy the phase-matching conditions in the case when the pump beam and the down-converted fields are collinear, meaning that the unit vectors all point in the same direction. Thus the above equation reduces to

$$n_p(\omega_p)\omega_p = n_s\left(\frac{\omega_p}{2}\right)\frac{\omega_p}{2} + n_i\left(\frac{\omega_p}{2}\right)\frac{\omega_p}{2}. \quad (2.120)$$

In order for the equation to be satisfied the target modes and the refractive indices for the pump need to be the same. This means that $n_i = n_s = n_p$. In general this condition would be true for an isotropic crystal, where we can set $n_i = n_s = n_p = n$ and hence the above equation reduces to

$$n(\omega_p) = n\left(\frac{\omega_p}{2}\right). \quad (2.121)$$

Unfortunately, since the refractive index, n , for many dielectric materials decreases as the pump frequency increases we find that both frequency-matching and phase-matching conditions cannot be satisfied at the same time in an isotropic medium [78].

Fortunately, this can be resolved by using an anisotropic birefringent crystal. In the crystal, photons with different polarisations carry different refractive indices and such a crystal allows the pump beam and at least one of the down-converted light beams to have opposite polarisations. This is because it has two different refractive indices, n_o , and, n_e , one for the ordinarily, (o), and the other for extraordinarily, (e), polarised light respectively.

One example of a birefringent crystal is the uniaxial crystal (one with a single axis of symmetry known as the optical axis), which responds to light polarised parallel to the optic axis known as the e -ray or the extraordinary ray. A uniaxial crystal is called a negative uniaxial crystal if, $n_e < n_o$. Therefore the o -ray undergoes a constant larger refractive index and the e -ray experiences a refractive index which depends on the direction of propagation. We can thus mix waves in the anisotropic material in such a way as to satisfy the phase-matching conditions. This means that the extraordinary refractive index, n_e , for a pump beam with a wavelength of 405nm is equal to the ordinary refractive index, n_o , for the degenerate down-converted beams at a wavelength of 810nm. That is,

$$n_e(\omega_p) = n_o\left(\frac{\omega_p}{2}\right). \quad (2.122)$$

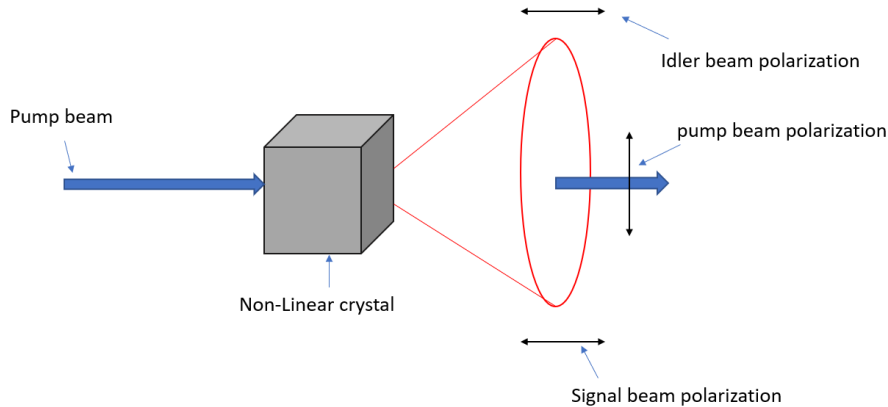


Figure 2.22: SPDC Type-I: Degenerate, idler and signal cone are identical and overlap.

Thus a pump beam which is parallel polarised to the optical axis cannot 'down convert' into a mode co-propagating with the pump beam, however one with an orthogonal polarisation can. Thus it follows that the ideal crystal to induce SPDC is a negative uni-axial, anisotropic birefringent crystal, for example a BBO crystal.

2.4.6 Phase matching

There are two types of phase matching used in a uni-axial crystal, that is Type-1 and Type-2 phase matching. In Type-1 phase matching, the down-converted beams have the same polarisation which is orthogonal to the pump beam. For example an ordinary, (*o*), polarised pump photon can create an extraordinary, (*e*), polarised photon. Type-1 phase matching is the one used in chapter 5 and can be summarized as

$$e \rightarrow oo, \quad (2.123)$$

or

$$o \rightarrow ee. \quad (2.124)$$

Because the down-converted photons emerge in different directions, the possible directions of the photon pair forms a set of concentric cones. The size of the cones depends on the opening angles which depend on the frequency of light, so the cones can be represented using different colors [81]. By changing the angle of the pump beam allows us to change the size emission cone. The phase matching condition implies that the conjugate photons must emerge on opposite sides of the concentric cone. There are infinitely many ways to chose the signal and idler photons, however by selecting a frequency for either of the photons we restrain the frequency of the conjugate photon to only two possibilities [99]. In the degenerate case ($\omega_i = \omega_s$) the cones overlap and collapse into a single cone in which the signal and idler photons can be found on opposite sides of the same beam, as shown in Figure 2.22.

2.5 Quantum plasmonic sensing

SPR sensors are used for studying binding kinetics between bio-molecular species. Plasmonic nanosensors have become a powerful tool for bio-sensing applications [73, 84]. This is because they are able to overcome the limitations of conventional optical sensors in terms of sensitivity, flexibility and photo-stability [48]. As the field has grown new detection schemes have been developed and are being incorporated into a wide variety of biological and medical applications. The key driving force

behind research in plasmonic nano-sensors is the improvement of precision measurements. Some of the strategies which are being considered in the improvement of precision include sensing based on target-induced local refractive index changes, colorimetric sensing based on localised SPR sensing, and coupling and amplification of sensitivity detection based on nanoparticle growth [48].

While SPR-based plasmonic nanosensors are available commercially, the SPR instrumentation in use today is limited by the precision they can achieve when measuring the reflectivity of light from the sensor. Such limitations lead to problems in applications, for example, in studying the drug kinematics for drugs used to treat various HIV-1 virus mutations it is important that the precision be higher than currently available in commercially available SPR-based nanosensors [48]. In order to overcome this, researchers need to look deeper into the physics of the sensor and consider more fundamental resources of optics, i.e., quantum mechanical resources [28].

The limitations of currently available SPR-based nano-sensors can be overcome by the study of the quantum nature of light. In particular, the preparation of light in squeezed states that make use of the uncertainty principle can enhance the precision [35, 36], as well as entangled multi-photon states [39, 38]. The potential enhancement in the sensing performance of plasmonic devices using quantum optical resources has been inspired by recent efforts to show that both quantum and plasmonic resonance features can be combined to give many beneficial properties [39, 38].

The central aim of this chapter is to investigate intensity based plasmonic sensing. We will look at quantum optical resources and find out how they can be used to enhance the precision of plasmonic SPR-based bio-sensors. In chapter 4, emphasis will be on investigating the applications of these bio-sensing devices in the characterization of reaction kinetics.

2.5.1 Classical intensity based sensing

Here we will calculate the intensity measurement, $\langle \hat{M} \rangle$, for a pair of coherent states. This serves as a classical benchmark. In the next section we will formulate a general expression for $\langle \hat{M} \rangle$ which is useful for calculating the intensity measurement of other quantum states, such as the Twin Fock and product squeezed states, amongst others. We start with the input states $|\alpha\rangle_1 |\alpha\rangle_2$, where $N=$

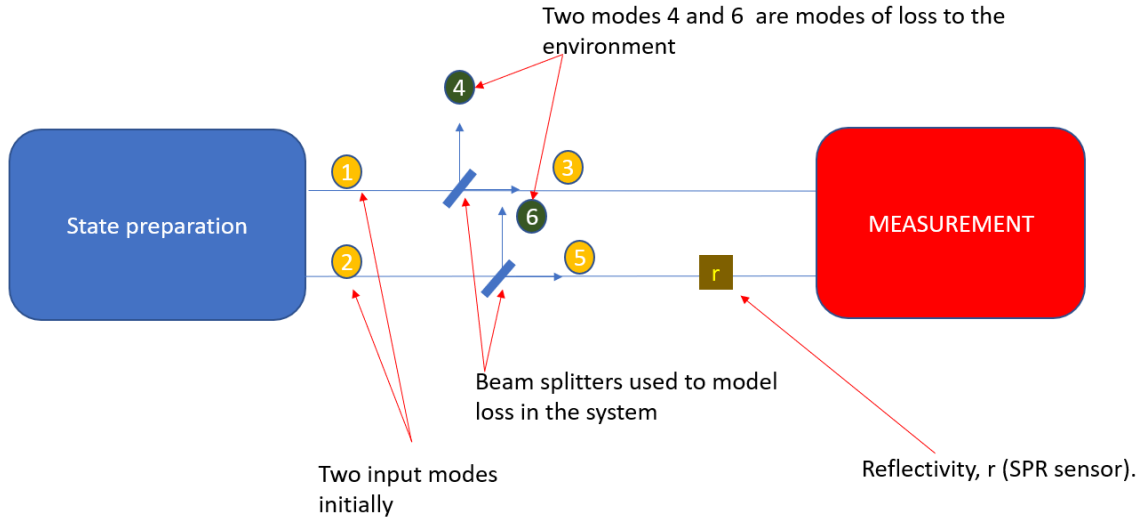


Figure 2.23: Theoretical model for two-mode plasmonic intensity sensing.

$|\alpha|^2$, and consider the setup shown in Figure 2.23. After the states go through the beam splitters which models the loss in each mode (η_1 in mode 1 and η_2 in mode 2) we get

$$|\alpha\rangle_1 |\alpha\rangle_2 \xrightarrow{\text{loss}} \left| \eta_1^{\frac{1}{2}} \alpha \right\rangle_3 \left| (1 - \eta_1)^{\frac{1}{2}} i\alpha \right\rangle_4 \left| \eta_2^{\frac{1}{2}} \alpha \right\rangle_5 \left| (1 - \eta_2)^{\frac{1}{2}} i\alpha \right\rangle_6. \quad (2.125)$$

As mode 5 passes through the prism of an SPR sensor the state amplitude is scaled by a factor of r , which is called the reflectivity of the sensor ($r = r_{\text{sp}}$) from Eq. (2.34). The state becomes

$$\left| \eta_1^{\frac{1}{2}} \alpha \right\rangle_3 \left| (1 - \eta_1)^{\frac{1}{2}} i\alpha \right\rangle_4 \left| r\eta_2^{\frac{1}{2}} \alpha \right\rangle_5 \left| (1 - \eta_2)^{\frac{1}{2}} i\alpha \right\rangle_6. \quad (2.126)$$

The measurement is the observable, $\hat{M} = \hat{a}_5^\dagger \hat{a}_5 - \hat{a}_3^\dagger \hat{a}_3$, which represents an intensity difference measurement between the output modes 3 and 5. The next step is therefore to calculate $\langle \hat{a}_3^\dagger \hat{a}_3 \rangle$ as

$$\langle \hat{a}_3^\dagger \hat{a}_3 \rangle = \text{Tr}_{3456} \{ \hat{a}_3^\dagger \hat{a}_3 \otimes \mathbf{1}_{456} \rho \}, \quad (2.127)$$

$$\begin{aligned} &= \left\langle \eta_1^{\frac{1}{2}} \alpha \right\rangle_3 \left\langle (1 - \eta_1)^{\frac{1}{2}} i\alpha \right\rangle_4 \left\langle r\eta_2^{\frac{1}{2}} \alpha \right\rangle_5 \left\langle (1 - \eta_2)^{\frac{1}{2}} i\alpha \right\rangle_6 \hat{a}_3^\dagger \hat{a}_3 \\ &\left| \eta_1^{\frac{1}{2}} \alpha \right\rangle_3 \left| (1 - \eta_1)^{\frac{1}{2}} i\alpha \right\rangle_4 \left| r\eta_2^{\frac{1}{2}} \alpha \right\rangle_5 \left| (1 - \eta_2)^{\frac{1}{2}} i\alpha \right\rangle_6. \end{aligned}$$

This reduces to

$$\langle \hat{a}_3^\dagger \hat{a}_3 \rangle = \eta_1 |\alpha|^2. \quad (2.128)$$

The next step is to calculate $\langle \hat{a}_5^\dagger \hat{a}_5 \rangle$. It follows a similar process to the calculation of $\langle \hat{a}_3^\dagger \hat{a}_3 \rangle$ and it gives

$$\langle \hat{a}_5^\dagger \hat{a}_5 \rangle = |r|^2 \eta_2 |\alpha|^2. \quad (2.129)$$

The next step is to calculate \hat{M} as

$$\langle \hat{M} \rangle = \langle \hat{a}_5^\dagger \hat{a}_5 \rangle - \langle \hat{a}_3^\dagger \hat{a}_3 \rangle = |r|^2 \eta_2 |\alpha|^2 - \eta_1 |\alpha|^2 = (|r|^2 \eta_2 - \eta_1) N. \quad (2.130)$$

In order to calculate the precision of the measurement of \hat{M} we need to calculate the standard deviation (uncertainty) $\langle \Delta \hat{M} \rangle$. The next step is therefore to calculate $\langle \hat{M}^2 \rangle$ as

$$\langle \hat{M}^2 \rangle = \langle (\hat{a}_5^\dagger \hat{a}_5 - \hat{a}_3^\dagger \hat{a}_3)^2 \rangle. \quad (2.131)$$

This expands to

$$\langle \hat{M}^2 \rangle = \langle \hat{a}_5^\dagger (\hat{a}_5^\dagger \hat{a}_5) \hat{a}_5 \rangle + \langle \hat{a}_3^\dagger \hat{a}_3 \rangle - 2 \langle \hat{a}_3^\dagger \hat{a}_3 \hat{a}_5^\dagger \hat{a}_5 \rangle + \langle \hat{a}_3^\dagger (\hat{a}_3^\dagger \hat{a}_3) \hat{a}_3 \rangle + \langle \hat{a}_3^\dagger \hat{a}_3 \rangle. \quad (2.132)$$

So it follows that

$$\begin{aligned} \langle \hat{M}^2 \rangle &= \left\langle \eta_1^{\frac{1}{2}} \alpha \right\rangle_3 \left\langle (1 - \eta_1)^{\frac{1}{2}} i\alpha \right\rangle_4 \left\langle r\eta_2^{\frac{1}{2}} \alpha \right\rangle_5 \left\langle (1 - \eta_2)^{\frac{1}{2}} i\alpha \right\rangle_6 \hat{M}^2 \\ &\left| \eta_1^{\frac{1}{2}} \alpha \right\rangle_3 \left| (1 - \eta_1)^{\frac{1}{2}} i\alpha \right\rangle_4 \left| r\eta_2^{\frac{1}{2}} \alpha \right\rangle_5 \left| (1 - \eta_2)^{\frac{1}{2}} i\alpha \right\rangle_6, \\ &= (\eta_2 |r|^2 |\alpha|^2)^2 + \eta_2 |r|^2 |\alpha|^2 - 2\eta_1 \eta_2 |\alpha|^4 |r|^2 + (\eta_1 |\alpha|^2)^2 + \eta_1 |\alpha|^2. \end{aligned} \quad (2.133)$$

The next step is to calculate $\langle \Delta \hat{M} \rangle = \sqrt{\langle \hat{M}^2 \rangle - \langle \hat{M} \rangle^2}$ as

$$\langle \Delta \hat{M} \rangle = [(\eta_2 |r|^2 |\alpha|^2)^2 + \eta_2 |r|^2 |\alpha|^2 - 2\eta_1 \eta_2 |\alpha|^4 |r|^2 + (\eta_1 |\alpha|^2)^2 + \eta_1 |\alpha|^2 - (|r|^2 \eta_2 - \eta_1)^2 |\alpha|^2]^{\frac{1}{2}}. \quad (2.134)$$

This reduces to

$$\langle \Delta \hat{M} \rangle = |\alpha| \sqrt{\eta_2 |r|^2 + \eta_1} = \sqrt{N} \sqrt{\eta_2 |r|^2 + \eta_1}. \quad (2.135)$$

2.5.2 Quantum intensity-based plasmonic sensing

Using the model in Figure 2.23 we can formulate a general expression for the uncertainty in the measurement for different states. To calculate this general expression we start with the expression,

$\langle \Delta \hat{M} \rangle = \sqrt{\langle \hat{M}^2 \rangle - \langle \hat{M} \rangle^2}$, which in the Schrödinger picture (where operators are fixed and states evolve) reduces to

$$\langle \Delta \hat{M} \rangle = [\langle \psi_{\text{out}} | (\hat{a}^\dagger (\hat{a}^\dagger \hat{a}) \hat{a} + \hat{a}^\dagger \hat{a} - 2\hat{b}^\dagger \hat{b} \hat{a}^\dagger \hat{a} + \hat{b}^\dagger (\hat{b}^\dagger \hat{b}) \hat{b} + \hat{b}^\dagger \hat{b}) | \psi_{\text{out}} \rangle - \langle \psi_{\text{out}} | (\hat{a}^\dagger \hat{a} - \hat{b}^\dagger \hat{b}) | \psi_{\text{out}} \rangle^2]^{\frac{1}{2}}. \quad (2.136)$$

Here \hat{a} and \hat{a}^\dagger correspond to the operators for the bottom mode in Figure 2.23 and \hat{b} and \hat{b}^\dagger are for the top mode. We calculate each individual component of the above expression and write them out one-by-one. The first one is

$$\langle \hat{a}^\dagger (\hat{a}^\dagger \hat{a}) \hat{a} \rangle = \langle \psi_{\text{out}} | \hat{a}^\dagger (\hat{a}^\dagger \hat{a}) \hat{a} | \psi_{\text{out}} \rangle. \quad (2.137)$$

We substitute $|\psi_{\text{out}}\rangle = \hat{U} |\psi_{\text{in}}\rangle$, where \hat{U} is a unitary operator and get the Heisenberg picture expectation value

$$\langle \hat{a}^\dagger (\hat{a}^\dagger \hat{a}) \hat{a} \rangle = \langle \psi_{\text{in}} | \hat{U}^\dagger \hat{a}^\dagger \hat{U} \hat{U}^\dagger \hat{a}^\dagger \hat{U} \hat{U}^\dagger \hat{a} \hat{U} \hat{U}^\dagger \hat{a} \hat{U} | \psi_{\text{in}} \rangle. \quad (2.138)$$

We have that $\hat{U}^\dagger \hat{a} \hat{U} = \hat{a}_{\text{out}}$, and similarly for \hat{a}^\dagger , leading to

$$\langle \hat{a}^\dagger (\hat{a}^\dagger \hat{a}) \hat{a} \rangle = \langle \psi_{\text{in}} | \hat{a}_{\text{out}}^\dagger (\hat{a}_{\text{out}}^\dagger \hat{a}_{\text{out}}) \hat{a}_{\text{out}} | \psi_{\text{in}} \rangle, \quad (2.139)$$

where $\hat{a}_{\text{out}} = r\eta_a \hat{a}_{\text{in}} + \hat{f}_a$. \hat{f}_a term is a noise term. It follows that

$$\langle \hat{a}^\dagger (\hat{a}^\dagger \hat{a}) \hat{a} \rangle = |r|^4 \eta_a^4 (\langle \psi_{\text{in}} | \hat{a}_{\text{in}}^\dagger (\hat{a}_{\text{in}}^\dagger \hat{a}_{\text{in}}) \hat{a}_{\text{in}} | \psi_{\text{in}} \rangle). \quad (2.140)$$

The expectation value of terms involving \hat{f} is zero as the noise bath starts in the vacuum, this can be shown in another calculation, see Appendix H. Next we will calculate $\langle \hat{a}^\dagger \hat{a} \rangle$ given by

$$\langle \hat{a}^\dagger \hat{a} \rangle = \langle \psi_{\text{out}} | \hat{a}^\dagger \hat{a} | \psi_{\text{out}} \rangle. \quad (2.141)$$

It follows that

$$\langle \hat{a}^\dagger \hat{a} \rangle = \langle \psi_{\text{in}} | \hat{U}^\dagger \hat{a}^\dagger \hat{U} \hat{U}^\dagger \hat{a} \hat{U} | \psi_{\text{in}} \rangle, \quad (2.142)$$

which gives

$$\langle \hat{a}^\dagger \hat{a} \rangle = \langle \psi_{\text{in}} | \hat{a}_{\text{out}}^\dagger \hat{a}_{\text{out}} | \psi_{\text{in}} \rangle, \quad (2.143)$$

$$= |r|^2 \eta_a^2 (\langle \psi_{\text{in}} | \hat{a}_{\text{in}}^\dagger \hat{a}_{\text{in}} | \psi_{\text{in}} \rangle). \quad (2.144)$$

As before the noise terms \hat{f}_a cancel out. The next step is to calculate $\langle \hat{b}^\dagger (\hat{b}^\dagger \hat{b}) \hat{b} \rangle$ and $\langle \hat{b}^\dagger \hat{b} \rangle$. This follows the exact same process as the calculations for $\langle \hat{a}^\dagger (\hat{a}^\dagger \hat{a}) \hat{a} \rangle$ and $\langle \hat{a}^\dagger \hat{a} \rangle$ above with the exception that $\hat{b}_{\text{out}} = \eta_b \hat{b}_{\text{in}} + \hat{f}_b$, which gives

$$\langle \hat{b}^\dagger (\hat{b}^\dagger \hat{b}) \hat{b} \rangle = \eta_b^4 (\langle \psi_{\text{in}} | \hat{b}_{\text{in}}^\dagger (\hat{b}_{\text{in}}^\dagger \hat{b}_{\text{in}}) \hat{b}_{\text{in}} | \psi_{\text{in}} \rangle). \quad (2.145)$$

Next we have

$$\langle \hat{b}^\dagger \hat{b} \rangle = \eta_b^2 (\langle \psi_{\text{in}} | \hat{b}_{\text{in}}^\dagger \hat{b}_{\text{in}} | \psi_{\text{in}} \rangle). \quad (2.146)$$

We then calculate the cross term $\langle \hat{a}^\dagger \hat{a} \rangle \langle \hat{b}^\dagger \hat{b} \rangle$,

$$\langle \hat{a}^\dagger \hat{a} \rangle \langle \hat{b}^\dagger \hat{b} \rangle = |r|^2 \eta_a^2 \eta_b^2 (\langle \psi_{\text{in}} | \hat{a}_{\text{in}}^\dagger \hat{a}_{\text{in}} | \psi_{\text{in}} \rangle) (\langle \psi_{\text{in}} | \hat{b}_{\text{in}}^\dagger \hat{b}_{\text{in}} | \psi_{\text{in}} \rangle). \quad (2.147)$$

Next, we calculate $\langle \hat{a}^\dagger \hat{a} - \hat{b}^\dagger \hat{b} \rangle^2$

$$\langle \hat{a}^\dagger \hat{a} - \hat{b}^\dagger \hat{b} \rangle^2 = (|r|^2 \eta_a^2 \langle \psi_{\text{in}} | \hat{a}_{\text{in}}^\dagger \hat{a}_{\text{in}} | \psi_{\text{in}} \rangle - \eta_b^2 \langle \psi_{\text{in}} | \hat{b}_{\text{in}}^\dagger \hat{b}_{\text{in}} | \psi_{\text{in}} \rangle)^2, \quad (2.148)$$

$$\begin{aligned}
&= |r|^4 \eta_a^4 \langle \psi_{\text{in}} | \hat{a}_{\text{in}}^\dagger \hat{a}_{\text{in}} | \psi_{\text{in}} \rangle^2 + \eta_b^4 \langle \psi_{\text{in}} | \hat{b}_{\text{in}}^\dagger \hat{b}_{\text{in}} | \psi_{\text{in}} \rangle^2 \\
&\quad - 2|r|^2 \eta_a^2 \eta_b^2 \langle \psi_{\text{in}} | \hat{a}_{\text{in}}^\dagger \hat{a}_{\text{in}} | \psi_{\text{in}} \rangle \langle \psi_{\text{in}} | \hat{b}_{\text{in}}^\dagger \hat{b}_{\text{in}} | \psi_{\text{in}} \rangle.
\end{aligned}$$

We then add everything together to get $\langle \Delta \hat{M} \rangle$

$$\begin{aligned}
\langle \Delta \hat{M} \rangle &= [|r|^4 \eta_a^4 \langle \psi_{\text{in}} | \hat{a}_{\text{in}}^\dagger (\hat{a}_{\text{in}}^\dagger \hat{a}_{\text{in}}) \hat{a}_{\text{in}} | \psi_{\text{in}} \rangle + |r|^2 \eta_a^2 \langle \psi_{\text{in}} | \hat{a}_{\text{in}}^\dagger \hat{a}_{\text{in}} | \psi_{\text{in}} \rangle + \eta_b^4 \langle \psi_{\text{in}} | \hat{b}_{\text{in}}^\dagger (\hat{b}_{\text{in}}^\dagger \hat{b}_{\text{in}}) \hat{b}_{\text{in}} | \psi_{\text{in}} \rangle + \\
&\quad \eta_b^2 \langle \psi_{\text{in}} | \hat{b}_{\text{in}}^\dagger \hat{b}_{\text{in}} | \psi_{\text{in}} \rangle + 2|r|^2 \eta_a^2 \eta_b^2 \langle \psi_{\text{in}} | \hat{a}_{\text{in}}^\dagger \hat{a}_{\text{in}} | \psi_{\text{in}} \rangle \langle \psi_{\text{in}} | \hat{b}_{\text{in}}^\dagger \hat{b}_{\text{in}} | \psi_{\text{in}} \rangle - (|r|^4 \eta_a^4 \langle \psi_{\text{in}} | \hat{a}_{\text{in}}^\dagger \hat{a}_{\text{in}} | \psi_{\text{in}} \rangle^2 \\
&\quad + \eta_b^4 \langle \psi_{\text{in}} | \hat{b}_{\text{in}}^\dagger \hat{b}_{\text{in}} | \psi_{\text{in}} \rangle^2 - 2|r|^2 \eta_a^2 \eta_b^2 \langle \psi_{\text{in}} | \hat{a}_{\text{in}}^\dagger \hat{a}_{\text{in}} | \psi_{\text{in}} \rangle \langle \psi_{\text{in}} | \hat{b}_{\text{in}}^\dagger \hat{b}_{\text{in}} | \psi_{\text{in}} \rangle)]^{\frac{1}{2}}.
\end{aligned}$$

The above is the general expression for $\langle \Delta \hat{M} \rangle$ in two-mode quantum intensity based plasmonic sensing [38]. We will now show examples of the application of the general formula in calculating $\langle \Delta \hat{M} \rangle$ for a two-mode coherent state and two-mode Fock state.

2.5.3 Quantum case with two-mode Fock state

When the input is a two-mode Fock state, i.e., $|N\rangle_a |N\rangle_b$, we have that

$$\begin{aligned}
\langle \Delta \hat{M} \rangle_{\text{Fock}} &= [|r|^4 \eta_a^4 \langle N|_a \langle N|_b \hat{a}_{\text{in}}^\dagger (\hat{a}_{\text{in}}^\dagger \hat{a}_{\text{in}}) \hat{a}_{\text{in}} |N\rangle_a |N\rangle_b + |r|^2 \eta_a^2 \langle N|_a \langle N|_b \hat{a}_{\text{in}}^\dagger \hat{a}_{\text{in}} |N\rangle_a |N\rangle_b \\
&\quad + \eta_b^4 \langle N|_a \langle N|_b \hat{b}_{\text{in}}^\dagger (\hat{b}_{\text{in}}^\dagger \hat{b}_{\text{in}}) \hat{b}_{\text{in}} |N\rangle_a |N\rangle_b + \eta_b^2 (\langle N|_a \langle N|_b \hat{b}_{\text{in}}^\dagger \hat{b}_{\text{in}} |N\rangle_a |N\rangle_b) + \\
&\quad 2|r|^2 \eta_a^2 \eta_b^2 \langle N|_a \langle N|_b \hat{a}_{\text{in}}^\dagger \hat{a}_{\text{in}} |N\rangle_a |N\rangle_b \langle N|_a \langle N|_b \hat{b}_{\text{in}}^\dagger \hat{b}_{\text{in}} |N\rangle_a |N\rangle_b - (|r|^4 \eta_a^4 \langle N|_a \langle N|_b \hat{a}_{\text{in}}^\dagger \hat{a}_{\text{in}} |N\rangle_a |N\rangle_b^2 \\
&\quad + \eta_b^4 \langle N|_a \langle N|_b \hat{b}_{\text{in}}^\dagger \hat{b}_{\text{in}} |N\rangle_a |N\rangle_b^2 - 2|r|^2 \eta_a^2 \eta_b^2 \langle N|_a \langle N|_b \hat{a}_{\text{in}}^\dagger \hat{a}_{\text{in}} |N\rangle_a |N\rangle_b \langle N|_a \langle N|_b \hat{b}_{\text{in}}^\dagger \hat{b}_{\text{in}} |N\rangle_a |N\rangle_b)]^{\frac{1}{2}}.
\end{aligned}$$

This simplifies to

$$\langle \Delta \hat{M} \rangle_{\text{Fock}} = [|r|^4 \eta_a^4 N(N-1) + |r|^2 \eta_a^2 N + \eta_b^4 N(N-1) + \eta_b^2 N - |r|^4 \eta_a^4 N^2 - \eta_b^4 N^2]^{\frac{1}{2}}. \quad (2.149)$$

It follows that

$$\langle \Delta \hat{M} \rangle_{\text{Fock}} = N^{\frac{1}{2}} [-|r|^4 \eta_a^4 + |r|^2 \eta_a^2 - \eta_b^4 + \eta_b^2]^{\frac{1}{2}}. \quad (2.150)$$

2.5.4 Classical case with two-mode coherent state

When the input is a two-mode coherent state, i.e., $|\alpha\rangle_a |\alpha\rangle_b$, we have that

$$\begin{aligned}
\langle \Delta \hat{M} \rangle_{\text{Coherent}} &= [|r|^4 \eta_a^4 (\langle \alpha|_a \langle \alpha|_b \hat{a}_{\text{in}}^\dagger (\hat{a}_{\text{in}}^\dagger \hat{a}_{\text{in}}) \hat{a}_{\text{in}} | \alpha\rangle_a | \alpha\rangle_b) + |r|^2 \eta_a^2 \langle \alpha|_a \langle \alpha|_b \hat{a}_{\text{in}}^\dagger \hat{a}_{\text{in}} | \alpha\rangle_a | \alpha\rangle_b \\
&\quad + \eta_b^4 \langle \alpha|_a \langle \alpha|_b \hat{b}_{\text{in}}^\dagger (\hat{b}_{\text{in}}^\dagger \hat{b}_{\text{in}}) \hat{b}_{\text{in}} | \alpha\rangle_a | \alpha\rangle_b + \eta_b^2 \langle \alpha|_a \langle \alpha|_b \hat{b}_{\text{in}}^\dagger \hat{b}_{\text{in}} | \alpha\rangle_a | \alpha\rangle_b + \\
&\quad 2|r|^2 \eta_a^2 \eta_b^2 \langle \alpha|_a \langle \alpha|_b \hat{a}_{\text{in}}^\dagger \hat{a}_{\text{in}} | \alpha\rangle_a | \alpha\rangle_b \langle \alpha|_a \langle \alpha|_b \hat{b}_{\text{in}}^\dagger \hat{b}_{\text{in}} | \alpha\rangle_a | \alpha\rangle_b - (|r|^4 \eta_a^4 \langle \alpha|_a \langle \alpha|_b \hat{a}_{\text{in}}^\dagger \hat{a}_{\text{in}} | \alpha\rangle_a | \alpha\rangle_b^2 \\
&\quad + \eta_b^4 \langle \alpha|_a \langle \alpha|_b \hat{b}_{\text{in}}^\dagger \hat{b}_{\text{in}} | \alpha\rangle_a | \alpha\rangle_b^2 - 2|r|^2 \eta_a^2 \eta_b^2 \langle \alpha|_a \langle \alpha|_b \hat{a}_{\text{in}}^\dagger \hat{a}_{\text{in}} | \alpha\rangle_a | \alpha\rangle_b \langle \alpha|_a \langle \alpha|_b \hat{b}_{\text{in}}^\dagger \hat{b}_{\text{in}} | \alpha\rangle_a | \alpha\rangle_b)]^{\frac{1}{2}}.
\end{aligned}$$

This simplifies to

$$\langle \Delta \hat{M} \rangle_{\text{Coherent}} = [|r|^4 \eta_a^4 |\alpha|^4 + |r|^2 \eta_a^2 |\alpha|^2 + \eta_b^4 |\alpha|^4 + \eta_b^2 |\alpha|^2 - |r|^4 \eta_a^4 |\alpha|^4 - \eta_b^4 |\alpha|^4]^{\frac{1}{2}}. \quad (2.151)$$

It follows that

$$\langle \Delta \hat{M} \rangle_{\text{Coherent}} = [|\alpha|^2 |r|^2 \eta_a^2 + |\alpha|^2 \eta_b^2]^{\frac{1}{2}}. \quad (2.152)$$

$\langle \Delta \hat{M} \rangle$ values for coherent and Fock states are shown in Figure 2.24. We can see that the measurement uncertainty $\langle \Delta \hat{M} \rangle$ of the Fock state goes below the standard quantum limit (coherent state bound).

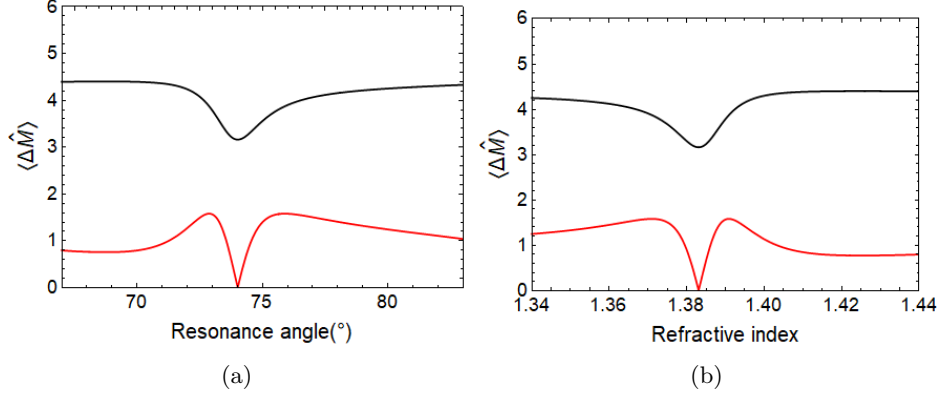


Figure 2.24: Comparing $\langle \Delta \hat{M}_{\text{coherent}} \rangle$ with $\langle \Delta \hat{M}_{\text{fock}} \rangle$. (a) The case where the refractive index of the analyte being sensed is fixed and we change the resonance angle. The refractive index of the analyte is 1.39. (b) The case where the resonance angle of the analyte being sensed is fixed and we change the refractive index. The resonance angle is 73° . The red line is the Fock state and the black line is the coherent state. These plots assume that there is no system loss in the setup, i.e., $\eta_a = \eta_b = 1$. The photon number $N = |\alpha|^2 = 10$.

This is the same as the result from the previous calculation of $\langle \Delta \hat{M} \rangle_{\text{Coherent}}$ with $\eta_1^{\frac{1}{2}} = \eta_a$ and $\eta_2^{\frac{1}{2}} = \eta_b$. We can calculate $\langle \Delta \hat{M} \rangle$ for other states, such as the NOON, Fock, product-squeezed, two-mode squeezed vacuum and two-mode squeezed displaced state.

We can take a step forward and take a ratio, R , which compares the noise of the classical to quantum case and can be thought of as the ratio of the enhancement in the precision. R is defined as $R = \frac{\langle \Delta \hat{M} \rangle_{\text{Coherent}}}{\langle \Delta \hat{M} \rangle_{\text{Fock}}}$. It follows that

$$R = \frac{\langle \Delta \hat{M} \rangle_{\text{Coherent}}}{\langle \Delta \hat{M} \rangle_{\text{Fock}}} = \frac{[|\alpha|^2 |r|^2 \eta_a^2 + |\alpha|^2 \eta_b^2]^{\frac{1}{2}}}{N^{\frac{1}{2}} [-|r|^4 \eta_a^4 + |r|^2 \eta_a^2 - \eta_b^4 + \eta_b^2]^{\frac{1}{2}}}. \quad (2.153)$$

We have that $|\alpha|^2 = N$, so the above equation reduces to

$$R = \frac{\langle \Delta \hat{M} \rangle_{\text{Coherent}}}{\langle \Delta \hat{M} \rangle_{\text{Fock}}} = \frac{[|r|^2 \eta_a^2 + \eta_b^2]^{\frac{1}{2}}}{[-|r|^4 \eta_a^4 + |r|^2 \eta_a^2 - \eta_b^4 + \eta_b^2]^{\frac{1}{2}}}. \quad (2.154)$$

By setting, $\eta_a = \eta_b = \eta$, we can reduce the expression even further and have

$$R = \frac{\langle \Delta \hat{M} \rangle_{\text{Coherent}}}{\langle \Delta \hat{M} \rangle_{\text{Fock}}} = \frac{[|r|^2 + 1]^{\frac{1}{2}}}{[-|r|^4 \eta^2 + |r|^2 - \eta^2 + |r|^2 + 1]^{\frac{1}{2}}}. \quad (2.155)$$

The enhancement ratio R is plotted in Figure 2.25 for varying resonance angle and refractive index. At specific points we can see that the enhancement ratio R is maximized. This is the region of the dip. In this region the measured uncertainty of the Fock state is minimized against that of the coherent state. Experimentally this is the region where we want to take measurements.

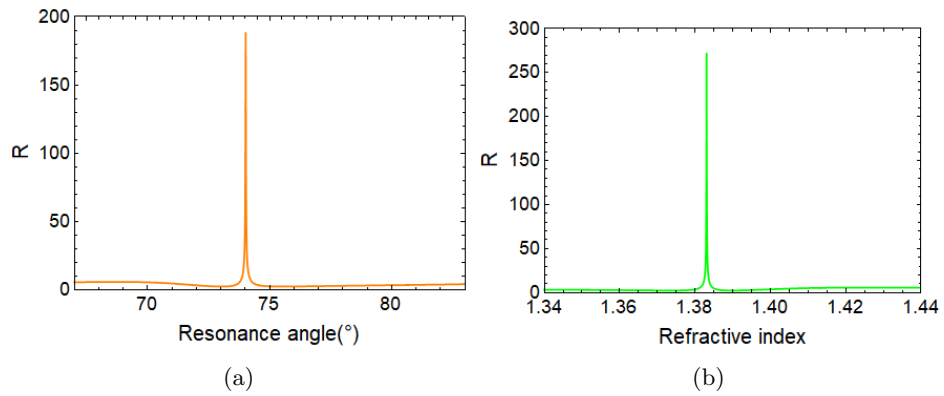


Figure 2.25: Enhancement ratio R . (a) The case where the refractive index of the analyte being sensed is fixed and we change the resonance angle. The refractive index is 1.39 (b) The case where the resonance angle of the analyte being sensed is fixed and we change the refractive index. The resonance angle is 73° . These plots assume that there is no system loss in the setup, i.e., $\eta_a = \eta_b = 1$. The photon number $N = |\alpha|^2 = 10$.

Chapter 3

Measurement of binding kinetics using quantum plasmonic sensing

The common approach in taking measurements in drug kinetics is to measure the resonant angle shift as a function of time, as given in Eq. (2.41). We call this the angle model. In this chapter we want to construct an equation which models the intensity change (reflectance) as a function of time and we call this the R model. The reason for using the R model is that the precision measurement $\langle \hat{M} \rangle$ is a function of the intensity and so in the R model we can actually see the impact of using quantum states.

We construct the R model by making use of the mathematical representation of the angle model. The refractive index is changing with time so we construct an equation of the refractive index of the analyte as a function of time using the angle model. Once we have our time dependent refractive index equation we can substitute it into Eq. (2.34) and this gives us a mathematical expression for our R model. The calculation which follows shows how we got the refractive index as a function of time.

We start with the expression, $\theta(t) = \theta(0) + \Delta\theta(t)$, where $\theta(t)$ is the resonance angle in radians at any time, t , and $\Delta\theta(t)$ is a shift in that angle due to a change in refractive index of the sample. From Chapter 2 we already know that

$$\Delta\theta(t) = \begin{cases} A_\infty(1 - e^{-k_s t}) & \text{if } 0 \leq t < \tau, \\ A_\tau e^{-k_d(t-\tau)} & \text{if } t \geq \tau. \end{cases}$$

Here A_∞ and A_τ are functions of the concentrations of the sample, k_s is an observable rate constant and k_d is the dissociation constant. τ is the time in seconds over which binding occurs. The values of these parameters are easily found from a study using the angle model. Our aim is to translate this to the R model. From Eq. (2.33) we have that when the exciting field is on resonance with the surface plasmon the following relation holds

$$\theta(t) = \sin^{-1}\left(\frac{\sqrt{n_2^2(t)n_g^2}}{n_1\sqrt{n_2^2(t) + n_g^2}}\right). \quad (3.2)$$

Where $n_g^2 = \epsilon_g$ is the refractive index of the gold layer on which the analyte is placed, $n_2^2(t) = \epsilon_2$ is the refractive index of the analyte and n_1^2 is the refractive index of the prism. At $t=0$, for theoretical purposes n_2^2 can be set to an arbitrary refractive index which we can write as $n_2^2(0)$. The arbitrary value corresponds to the refractive index of the analyte before the binding reactions occur (essentially the buffer solution). So we have that

$$\sin^{-1}\left(\frac{\sqrt{n_2^2(t)n_g^2}}{n_1\sqrt{n_2^2(t)+n_g^2}}\right) = \sin^{-1}\left(\frac{\sqrt{n_2^2(0)n_g^2}}{n_1\sqrt{n_2^2(0)+n_g^2}}\right) + \begin{cases} A_\infty(1 - e^{-k_s t}) & \text{if } 0 \leq t < \tau, \\ A_\tau e^{-k_d(t-\tau)} & \text{if } t \geq \tau. \end{cases}$$

We can set the left hand side as $A(t)$ to give

$$A(t) = \sin^{-1}\left(\frac{\sqrt{n_2^2(0)n_g^2}}{n_1\sqrt{n_2^2(0)+n_g^2}}\right) + \begin{cases} A_\infty(1 - e^{-k_s t}) & \text{if } 0 \leq t < \tau, \\ A_\tau e^{-k_d(t-\tau)} & \text{if } t \geq \tau. \end{cases}$$

Thus

$$\sin(A) = \frac{\sqrt{n_2^2(t)n_g^2}}{n_1\sqrt{n_2^2(t)+n_g^2}}, \quad (3.5)$$

hence

$$\sin^2(A) = \frac{n_2^2(t)n_g^2}{n_1^2(n_2^2(t)+n_g^2)}. \quad (3.6)$$

Simplifying further we arrive to an expression for the refractive index of the analyte as a function of time written as

$$n_2^2(t) = \frac{n_1^2 n_g^2 \sin^2(A)}{n_g^2 - n_1^2 \sin^2(A)}, \quad (3.7)$$

with $n_g^2 \rightarrow \text{Re}[n_g^2]$, where $\text{Re}[n_g^2]$ is used as an approximation. We then substitute this refractive index value into the reflectance function Eq. (2.34) and thus we have the reflectance as a function of time, or R model. We plot this as shown in Figure 3.1.

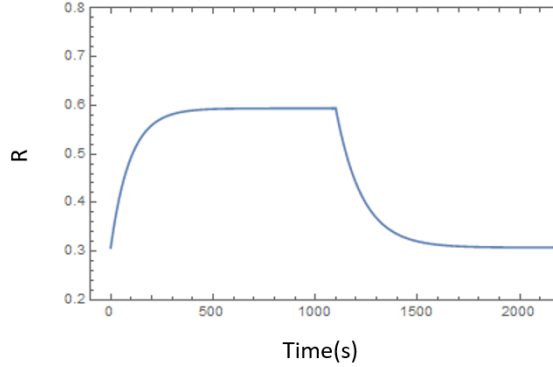


Figure 3.1: Reflectance as a function of time sensorgram for a binding reaction whose refractive index goes from 1.3352 to 1.3458. This is an ideal case where we have just extracted the kinetic parameters and used them to generate our model. In this model we used, $k_s = 10.5193 \times 10^{-3} \text{s}^{-1}$, $k_d = 7.85 \times 10^{-3} \text{s}^{-1}$, $\tau = 1100 \text{s}$, $A_\infty = 2.63928^\circ$, $A_\tau = 2.6393^\circ$, $\theta(0) = 71.0966^\circ$.

We would like our R model to be consistent with the $\Delta\theta$ model for a given study and so we need to check if the response of R to $n(t)$ is linear. This is because if the response of R with respect to $n(t)$ in the R model is different to the response of $\Delta\theta$ with respect to $n(t)$ (which is linear) that will lead to different binding rates being extracted. As a result the R model (from the extracted $n(t)$ model) will not fit an exponential model as well as the one we initially set for $\Delta\theta$ (for which the $\Delta\theta$ model from the extracted $n(t)$ model matches reasonably well).

By plotting the relationship between the reflectivity and $n(t)$ as shown in Figure 3.2, as $n(t)$ is linearly varied we found that the response in the R model was not linear, so we obtained a calibration factor which we used to linearise the response of R. This calibration factor would be measured in an experiment in a control study. Once we had linearised our R plots we used our modified R model to do our simulations with the confidence that the kinetic parameters will be identical to those of the kinetic model.

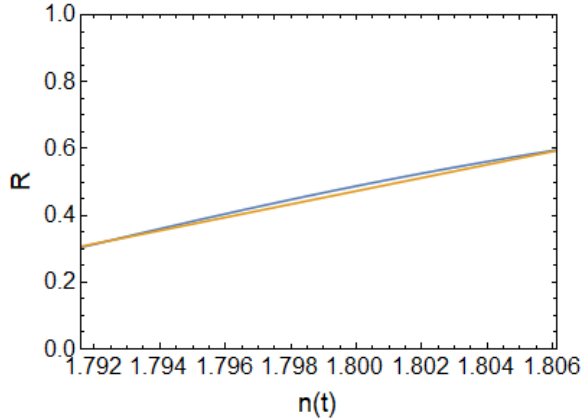


Figure 3.2: The blue line represents the non-linear response of an example R model, the orange line is the linear response. The corresponding sensorgrams (cf. Fig 3.1) are slightly distorted with respect to each other.

In order for our model to be representative of a real experiment we need to add measurement noise which arises as a result of the measurement process. The noise is also state dependent and we have calculated it previously as $\langle \Delta \hat{M} \rangle$ for the setup shown in Figure 2.23. For example, if the input signal is a two-mode Fock state then we add Gaussian noise with $\langle \Delta \hat{M}_{\text{Fock}} \rangle$ of the two-mode Fock state as the standard deviation of the noise. We also did this for the TMSV, TMSD and coherent states. After adding the noise we use a Newton-Gauss non-linear algorithm to fit the noisy sensorgrams so that we can extract kinetic parameters.

Even though the noise of a state like the Fock state is not Gaussian (it is binomial), the use of Gaussian noise is justified as we are using the sample mean as an estimator. Each point in the sensorgram corresponds to fluctuations of the sample mean (where a sample/point is made up of ν measured values) which follows a Gaussian distribution regardless of the underlying probability distribution for a state according to the central limit theorem. This assumes that the ν measurements can be made within a short enough time with respect to the time-scale of the sensorgram changes. Figure 3.3 shows a sensorgram with the noise added to an ideal sensorgram curve for a Fock state.

In order to get accurate statistics we ran Monte Carlo simulations of the noisy sensorgrams, this is done m times. All these sensorgrams can be obtained in an experiment in one full sweep of the sensorgram if the probing occurs fast enough for the sensorgram dynamics to be roughly constant, otherwise repeated runs would be required. For each of the m sensorgrams we fit the model and extracted out k_s and k_d from which we calculated k_a . From this we calculated the averages of the m sets of parameters which we extract. In this sense the parameter m plays the role of a set in the same way ν does for a set of measurements at a point in time of the sensorgram.

We were also interested in establishing a distribution profile of these parameter values so we repeated the described sequence p times. The value of p was established by looking at how the standard deviation in the k_s and k_d parameters fluctuates. We took a p -value where the standard deviation fluctuations are relatively stable. We set p as 1500, to stabilize the standard deviation fluctuations which can affect the repeatability of the results, as shown in Figure 3.4.

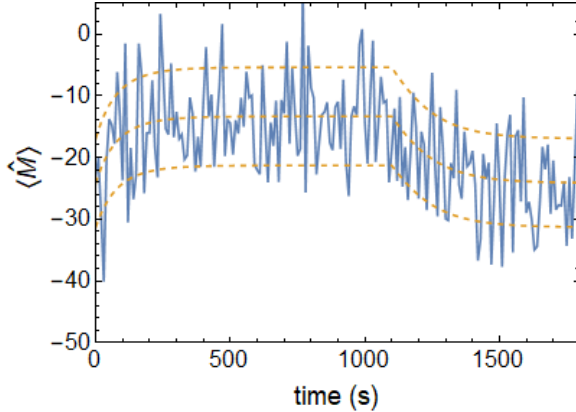


Figure 3.3: Plot of sensorgram with noise added to it. After we add noise to our ideal case it generally looks like this. The upper and lower dashed lines represent $\pm \frac{\langle \Delta \hat{M} \rangle}{\sqrt{\nu}}$. The middle dashed line is $\langle \Delta \hat{M} \rangle$ for $\nu \rightarrow \infty$. In the plot here we used photon number $N=5$, $\eta_a = 0.8$ and $\eta_b = 0.8$.

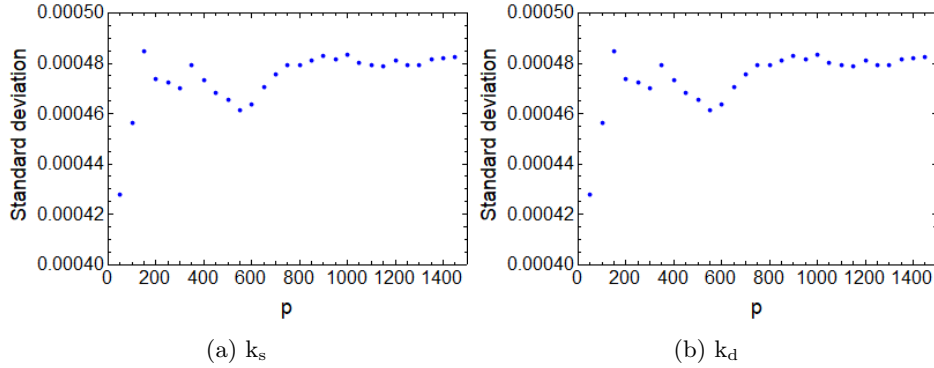


Figure 3.4: Standard deviation vs p values for k_s and k_d . The plots are for a coherent state, $m=10$ and $\nu = 100$.

In the next section we will show results for different estimations to the real value of the parameters and the errors in the measurement of these values. We also show the enhancement in the precision that the different quantum states have over the classical coherent state. At first we considered the case in which we have no loss in the probe mode ($a=2$) and reference mode ($b=1$) according to Figure 2.23, i.e. η_a and η_b are both equal to 1. We also considered a case which optimised the response of the TMSV and TMSD states, i.e., η_b was set to be equal to $\eta_a R$. Then we consider the case where there is loss, i.e., η_a and η_b are both 0.8. In this case we consider only the coherent state and two-mode Fock state which outperforms the TMSV and TMSD states. We look at cases where $m=10$ and $p=1500$ and $m=50$ and $p=1500$ and also the expected enhancement that occurs when m changes. Enhancement is a measure of the ratio of the standard deviation for the classical state versus the standard deviation of the respective quantum state in question, i.e., TMSV, TMSD and two-mode Fock state.

3.1 Large sensorgram deviation

In this section we model a sensorgram with parameters extracted from an experiment by Kausaitė et al. [20]. In the experiment they measured the real-time SPR curve showing immobilized BSA interaction with anti-BSA present in a sample, as shown in Figure 3.5. Using an ESPRIT commercial sensor they extracted the following parameters, $k_a = 9.36 \times 10^3 \text{M}^{-1}\text{s}^{-1}$, $k_d = 7.85 \times 10^{-3} \text{s}^{-1}$

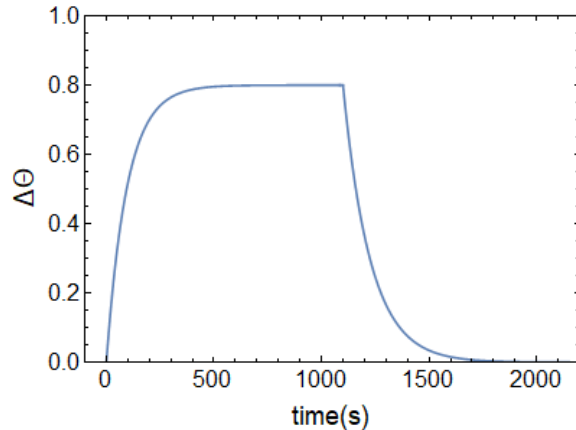


Figure 3.5: The angle model from Ref. [20].

and $L_0 = 274 \times 10^{-9} \text{M}$. Using these parameters we constructed an ideal case R model of the experiment and then added measurement noise. Having added the noise from the different states we use as input, we run Monte Carlo simulations as described previously. We then extracted parameters from each of the simulations run using a non-linear Newton-Gauss fit. We took statistics of the parameters to see the range of the fluctuations which arise in them due to the measurement noise. This section is titled, “Large sensorgram deviation” because in this experiment [20], the change in the refractive index and consequently the change in the reflectivity over time is relatively large. There are experiments where the change is extremely small [21] and we will consider this in the next section. From Ref. [97] we know that the TMSV and TMSD states do not give as good an enhancement as the two-mode Fock state when we consider loss and that is why we do not include them in the cases where we have loss i.e. $\eta_a = \eta_b = 0.8$. The R model used is shown in Figure 3.6.

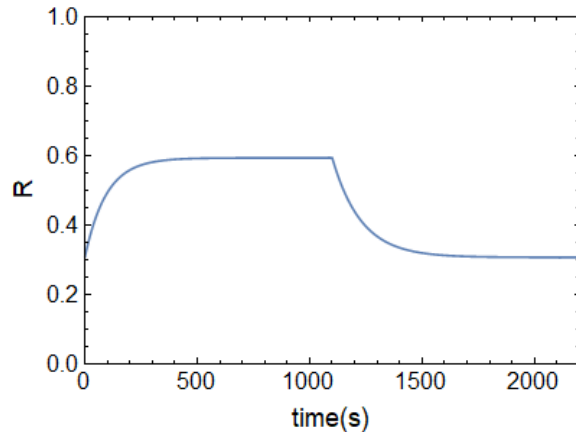


Figure 3.6: The R model for the angle model in Ref. [20].

In the figures in this section we look at estimations of the values of k_d , k_s , k_a for the different input states, i.e., Fock (Red), coherent (Black), TMSV (Green) and TMSD (Blue). We show results for different estimations to the real value of the parameters and the errors in the measurement of these values. We also show the enhancement that the different quantum states have over the classical coherent state. All the error plots that follow should be interpreted as showing the uncertainty for the kinetic value for a given set of m sensorgrams, each made of ν measurements of $\langle \hat{M} \rangle$ for each point in time. In other words, if m sensorgrams are taken then the value of the extracted kinetic value could lie anywhere within the error bar. The mean after many repetitions would then give the

point shown. Therefore a smaller error bar is advantageous when estimating a kinetic parameter when the number of measurements is limited for instance due to time constraints.

Standard two-mode case

In this standard case we consider both modes in Figure 2.23 and no loss, i.e., $\eta_a = \eta_b = 1$. In Figure 3.7 we show the dependence of ν for $m=10$ and in Figure 3.8 we show the dependence of ν for $m=50$ highlighting that increasing m improves the precision of the estimation of the kinetic parameters. The dotted lines in the top row (of the figures) are the actual kinetic values and in the bottom row they represent the expected enhancement obtained from the value of R at the midpoint of the sensorgram curve. Setting the noise to the standard two-mode case we see that the TMSV and TMSD states perform worse than the coherent state even as ν increases. The Fock state performs better than the coherent state.

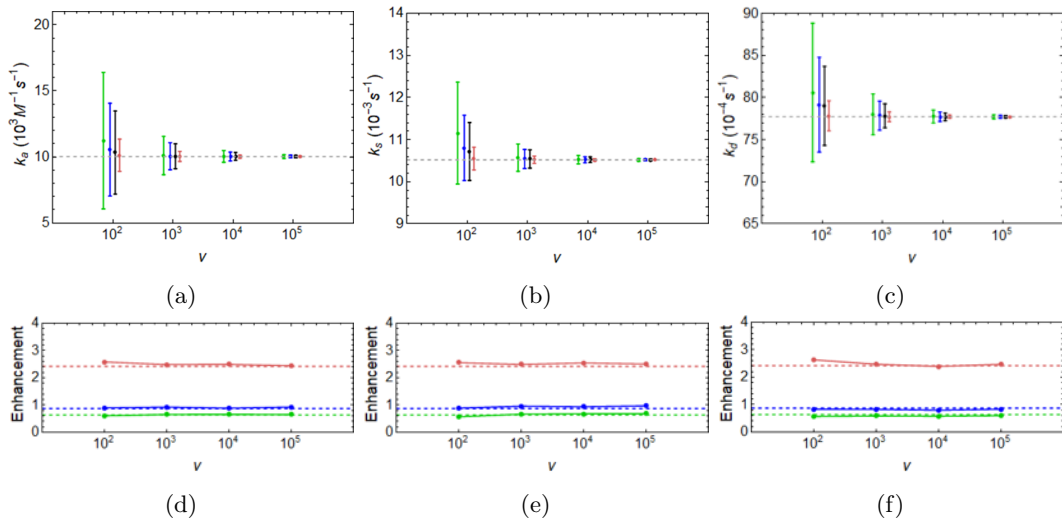


Figure 3.7: Two-mode standard results, ν dependence, with $p=1500$, photon number=10 and $m=10$ (no loss, i.e. $\eta_a = \eta_b = 1$).

In Figure 3.9 we show the dependence of the precision on the photon number N . There is a photon number dependence for the enhancement of the TMSV state which explains the decline in the enhancement we see in Figure 3.9. As the photon number increases the enhancement gets worse for the TMSV state.

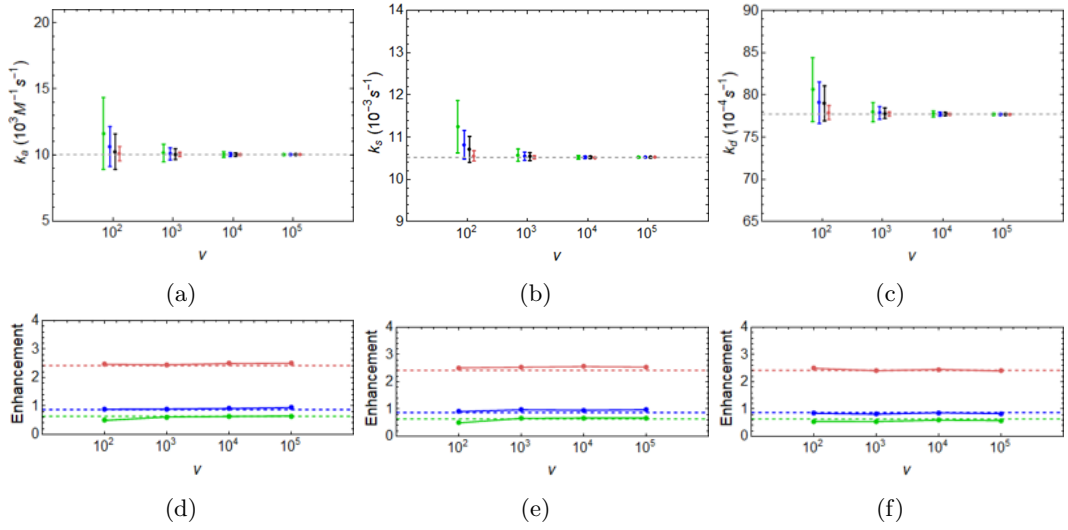


Figure 3.8: Two-mode standard results, ν dependence, with $p=1500$, photon number=10 and $m=50$ (no loss, i.e. $\eta_a = \eta_b = 1$).

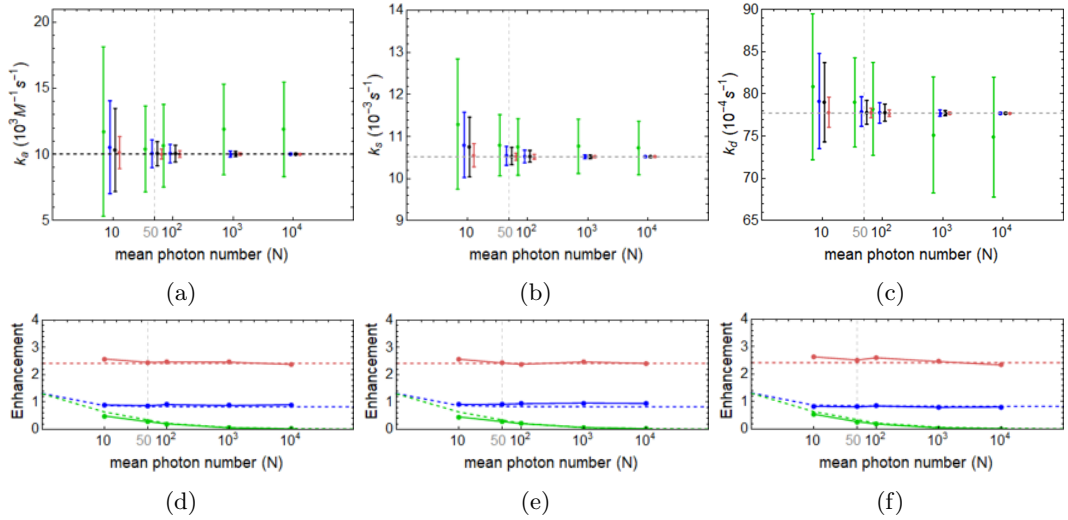


Figure 3.9: Two-mode standard results, photon number dependence, $m=10$, $p=1500$, $\nu = 100$ (no loss, i.e. $\eta_a = \eta_b = 1$).

Lossy standard two-mode case

In the lossy standard case we consider both modes in Figure 2.23 and loss, i.e., $\eta_a = \eta_b = 0.8$. In Figure 3.10 we show the dependence of ν for $m=10$ and in Figure 3.11 we show the dependence of ν for $m=50$ highlighting that increasing m improves the precision of the estimation of the kinetic parameters. The dotted lines in the top row (of the figures) are the actual kinetic values and in the bottom row they represent the expected enhancement obtained from the value of R at the midpoint of the sensorgram curve. Here we only look at the two-mode Fock state and the coherent state. Setting the noise to the lossy standard two-mode case we see that the Fock state performs better than the coherent state even as ν increases.

In Figure 3.12 we show the dependence of the precision on the photon number N in the case when we have loss in our setup. Even when we include loss we find that the two-mode Fock state out-performs the coherent state for both the photon number and ν dependence.

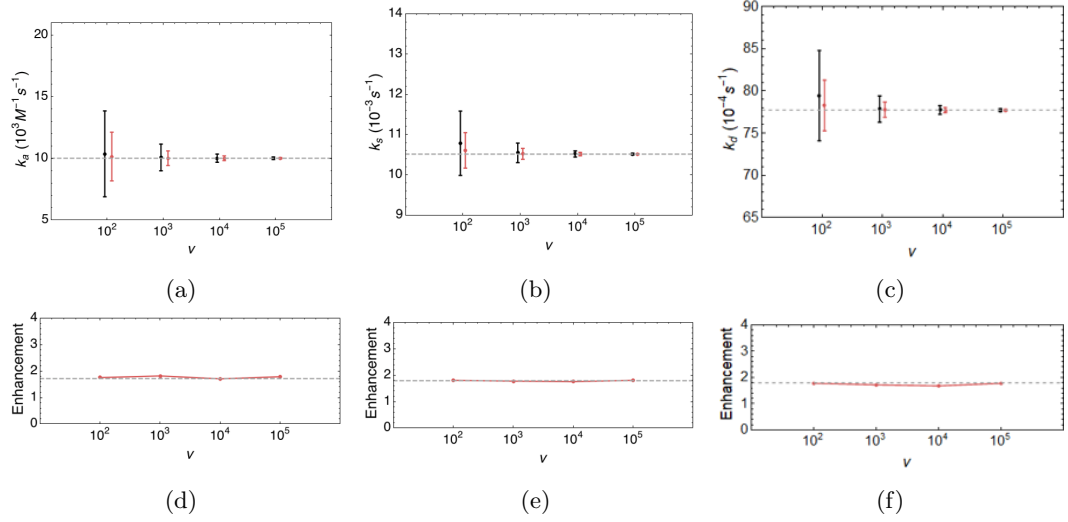


Figure 3.10: Two-mode standard results, ν dependence, with $p=1500$, photon number=10 and $m=10$ (loss, i.e. $\eta_a = \eta_b = 0.8$).

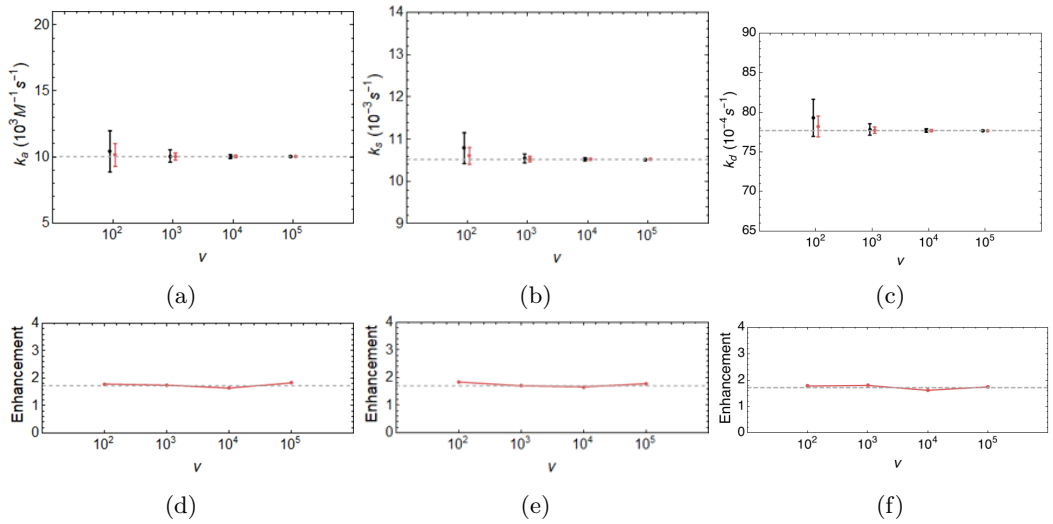


Figure 3.11: Two-mode standard results, ν dependence, with $p=1500$, photon number=10 and $m=50$ (loss, i.e. $\eta_a = \eta_b = 0.8$).

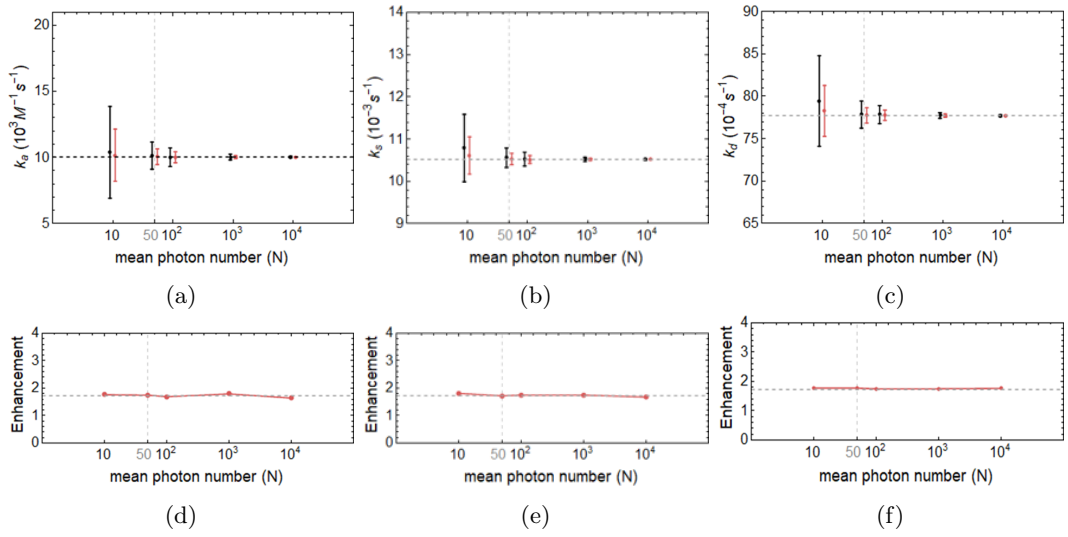


Figure 3.12: Two-mode standard results, photon number dependence, $m=10$, $p=1500$, $\nu = 100$ (loss, i.e. $\eta_a = \eta_b = 0.8$).

3.1.1 Optimized two-mode case

In the standard optimized case we consider both modes in Figure 2.23 where we set loss values which improve the enhancement of the TMSD and TSMV to give better parameter precision than the coherent state, i.e., $\eta_a=1$ and $\eta_b=\eta_a R$ where the midpoint of the R value is used. R is therefore fixed. In Figure 3.13 we show the dependence of ν for $m=10$. We no longer look at the case for $m=50$ because we have already established that it is consistent with the theory for the standard two-mode case. The dotted lines in the top row (of the figures) are the actual kinetic values and in the bottom row they represent the expected enhancement obtained from the value of R at the midpoint of the sensorgram curve. Setting the noise to the optimized case improves the enhancement of the TMSV and TMSD states to a point in which they perform better than the coherent state. The enhancement in all four states is very close but not exactly the same. The enhancement in the Fock state is reduced somewhat but the Fock state still gives the better enhancement overall.

In Figure 3.14 we show the dependence of the precision on the photon number N for the optimized two-mode case. A clear decrease in the enhancement of the TMSV state is visible and this is because the TMSV enhancement is dependent on the photon number. We study this in more detail in section 3.1.3, where we investigate enhancement changes with photon number.

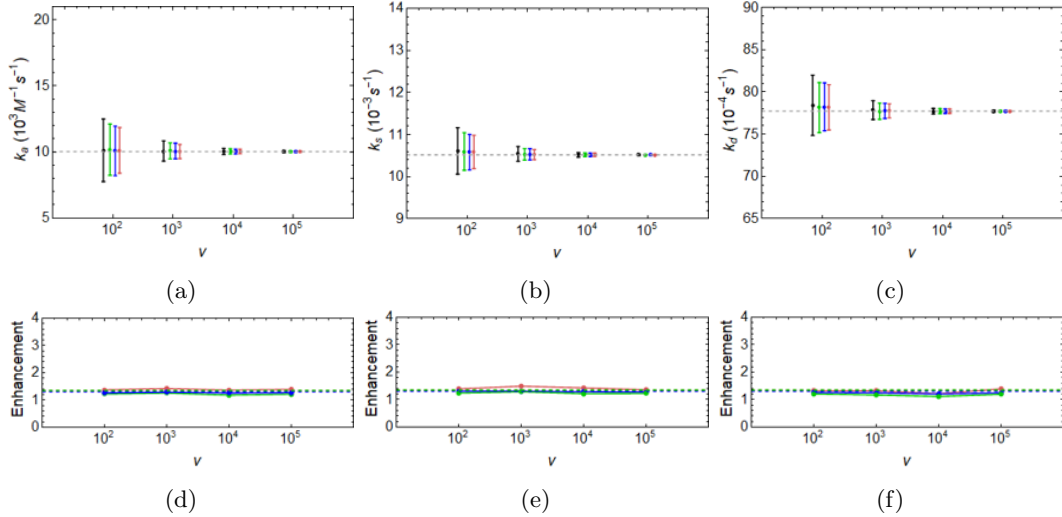


Figure 3.13: Two-mode standard results optimized, ν dependence, with $p=1500$, photon number=10 and $m=10$ (Optimized loss, i.e. $\eta_a = 1$ and $\eta_b = R\eta_a$).

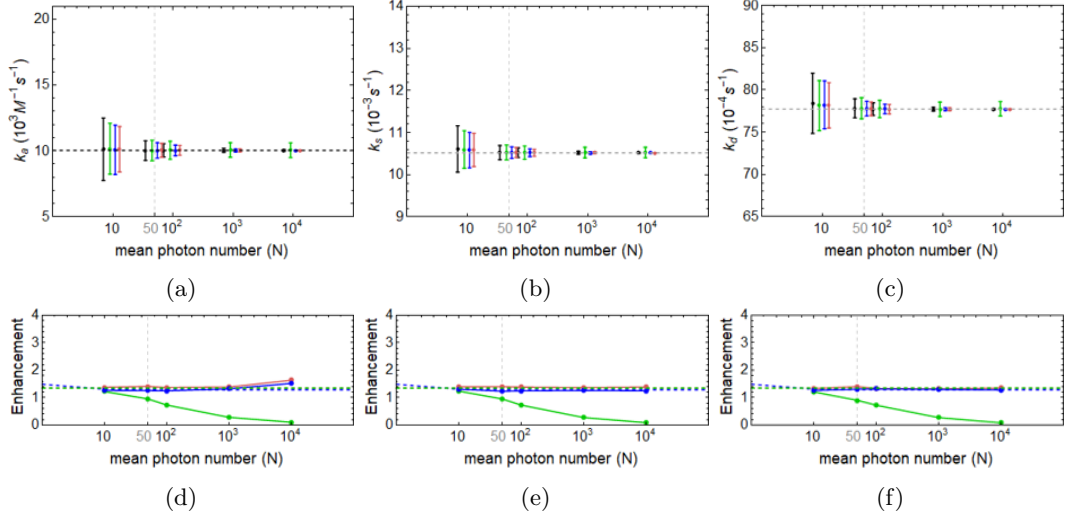


Figure 3.14: Two-mode standard results optimized, photon number dependence, with $p=1500$, $\nu = 100$ and $m=10$ (Optimized loss, i.e. $\eta_a = 1$ and $\eta_b = R\eta_a$).

Lossy optimized two-mode case

In the lossy two-mode optimised case we consider both modes in Figure 2.23 and loss, i.e., $\eta_a=0.8$ and $\eta_b=0.8R$. In Figure 3.15 we show the dependence on ν for $m=10$. When we set the noise to the lossy two-mode optimised case we find that the Fock state performs better than the coherent state. The precision improves with increasing ν . The enhancement remains constant throughout for all the kinetic parameters.

In Figure 3.16 we show the dependence on photon number for $m=10$. When we set the noise to the lossy two-mode optimised case we find that the Fock state performs better than the coherent state. The precision improves with increasing photon number. The enhancement remains constant throughout for all the kinetic parameters.

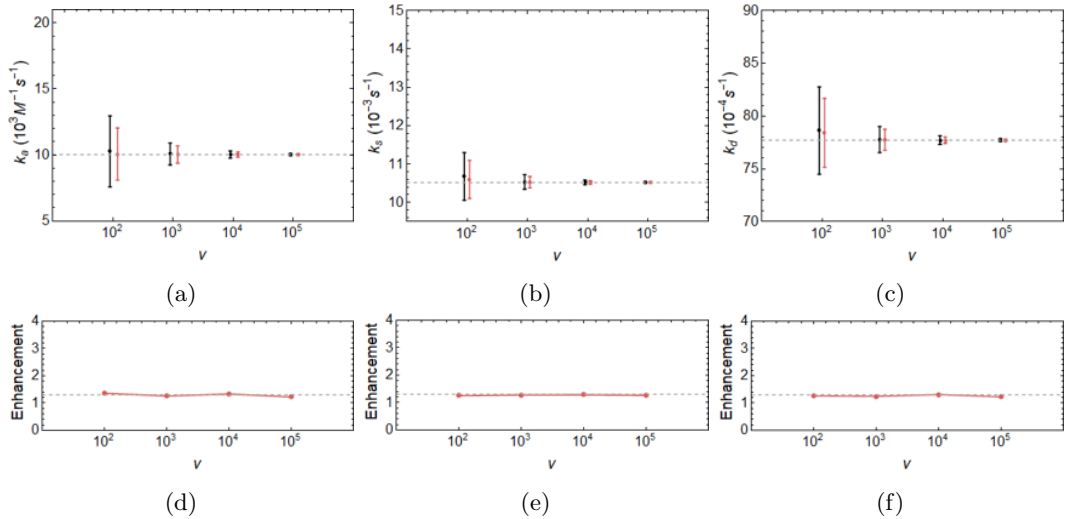


Figure 3.15: Two-mode standard results optimized, ν dependence, with $p=1500$, photon number=10 and $m=10$ (Optimized loss, i.e. $\eta_a = 0.8$ and $\eta_b = R\eta_a$).

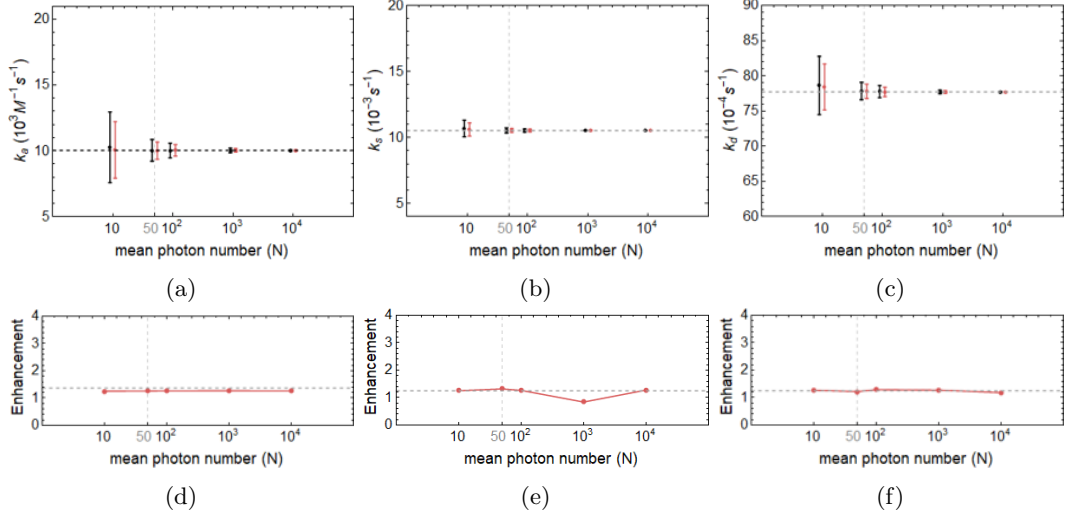


Figure 3.16: Optimized two-mode results, photon number dependence, with $p=1500$, $\nu = 100$ and $m=10$ (Optimized loss, i.e. $\eta_a = 0.8$ and $\eta_b = R\eta_a$).

3.1.2 Single-mode

In the single-mode case we consider both modes in Figure 2.23 and no loss, i.e., $\eta_a=1$ and $\eta_b=0$ (which makes the model effectively a single mode). In Figure 3.17 we show the dependence of ν . When we set the noise to the single-mode case we find that the Fock state performs better than the coherent state. The precision improves with increasing ν . The enhancement remains constant throughout for all the kinetic parameters.

In Figure 3.18 we show the parameter dependence on the photon number for $m=10$. When we set the noise to the single-mode optimised case we find that the Fock state performs better than the coherent state. The precision improves with increasing photon number. The enhancement remains constant throughout for all the kinetic parameters.

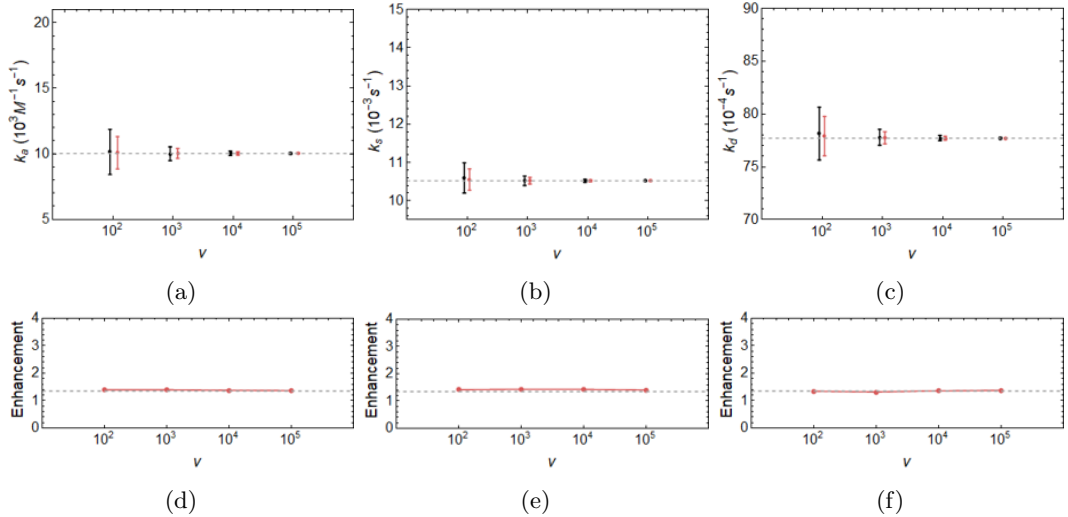


Figure 3.17: Single-mode results, ν dependence, with $p=1500$, photon number=10 and $m=10$ (No loss, i.e. $\eta_a = 1$ and $\eta_b = 0$).

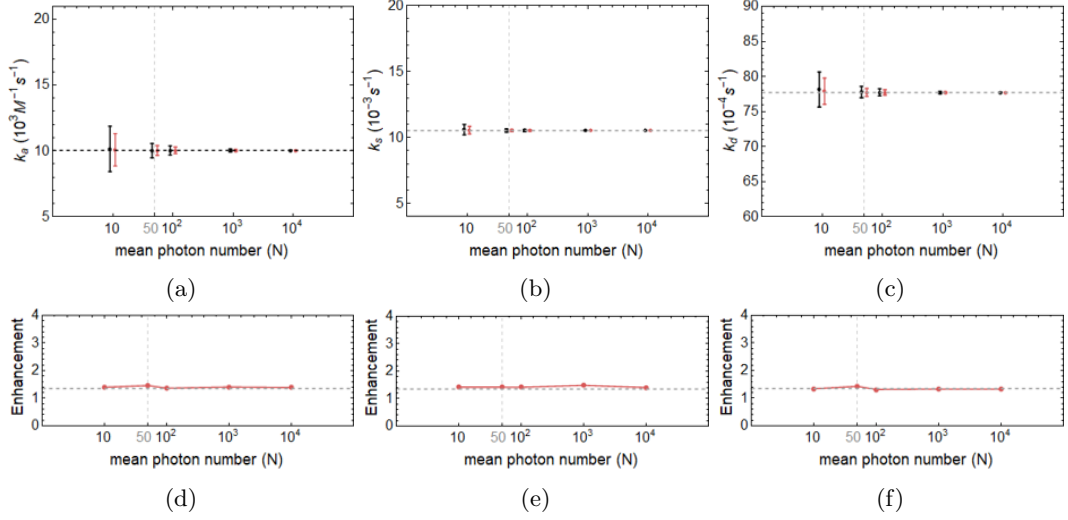


Figure 3.18: Single-mode results, photon number dependence, with $p=1500$, $\nu = 100$ and $m=10$ (No loss, i.e. $\eta_a = 1$ and $\eta_b = 0$).

Lossy single-mode

In the lossy single-mode case we consider both modes in Figure 2.23 and loss, i.e., $\eta_a=0.8$ and $\eta_b=0$. When we set the noise to the lossy single-mode case we find that the Fock state performs better than the coherent state. The precision improves with increasing ν . The enhancement remains constant throughout for all the kinetic parameters.

In Figure 3.19 we show the dependence on ν for $m=10$ and in Figure 3.20 we show the dependence on photon number for $m=10$. When we set the noise to the lossy single-mode case we find that the Fock state performs better than the coherent state. The precision improves with increasing photon number. The enhancement remains constant throughout for all the kinetic parameters.

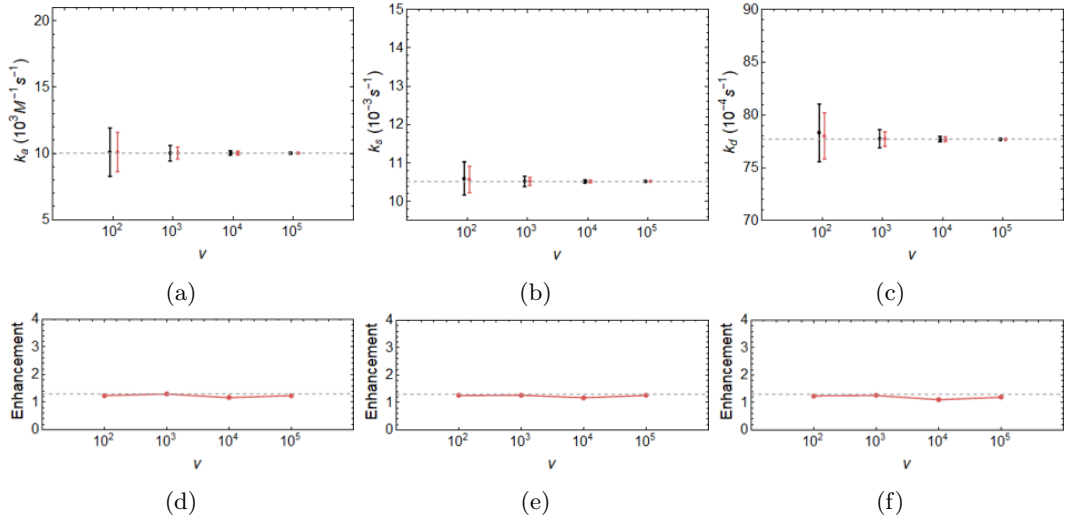


Figure 3.19: Single-mode results, ν dependence, with $p=1500$, photon number=10 and $m=10$ (loss, i.e. $\eta_a = 0.8$ and $\eta_b = 0$).

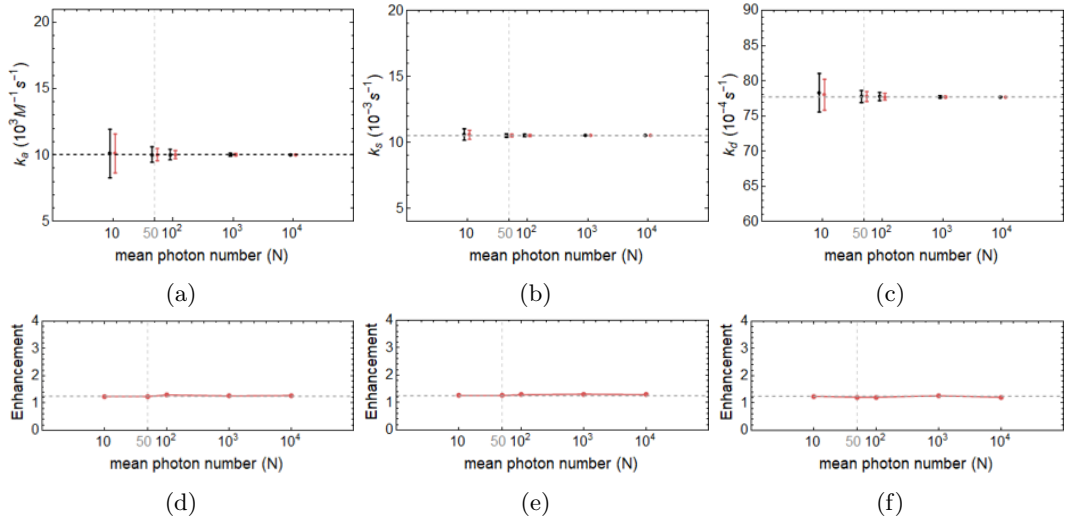


Figure 3.20: Single-mode results, photon number dependence, with $p=1500$, $\nu = 100$ and $m=10$ (loss, i.e. $\eta_a = 0.8$ and $\eta_b = 0$).

3.1.3 Enhancement with changing R value

We were interested to know how much of an impact changing the R value has on the enhancement we see when using quantum states of light. We did this for all states, i.e. the classical, Fock, TMSV and TMSD states for the case where we do not have loss and for the case where we do have loss. The plots are shown in the figures below. The non-shaded region is the region in which the sensorgram varies with R. The mid-point (dashed grey vertical line) is the value used in the enhancement plots earlier as the average enhancement for a given state. In this section we investigate the dependence of the enhancement in the different states to changes in the photon number and changes in ν . In the previous section we suspected that the enhancement in the TMSV state has a photon number dependence in which as the photon number increases the enhancement goes to zero rapidly away from the sensorgram midpoint of R on either side. We don't consider the single mode case here because the enhancement of the Fock state is the same as in the two-mode optimized case. In Figures 3.21 and 3.22 we see that the enhancement improves as the R value goes towards 1. The no loss case shows greater improvement in enhancement for higher R values than the loss case. In general the Fock state gives the best enhancement but it seems sensitive to the R value, the enhancement declines for the middle R values and then goes up as R approaches 1.

We also look at the enhancement with changing R as we change the photon number in Figure 3.23 for the standard two-mode case and in Figure 3.24 for the two-mode optimized case. For the two-mode optimized case the enhancement reaches its maximum at the middle R values. It seems the enhancement is also sensitive to changes in the R values. Whilst the enhancement is unaffected by a change in the photon number for all the other states the TMSV state is very sensitive to the change. The enhancement seems to drop as the photon number goes up.

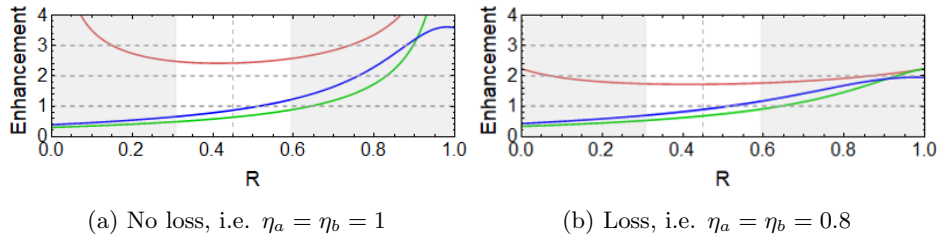


Figure 3.21: Enhancement with changing R value, $m=10$, $p=1500$, $\nu = 100$ and photon number=10.

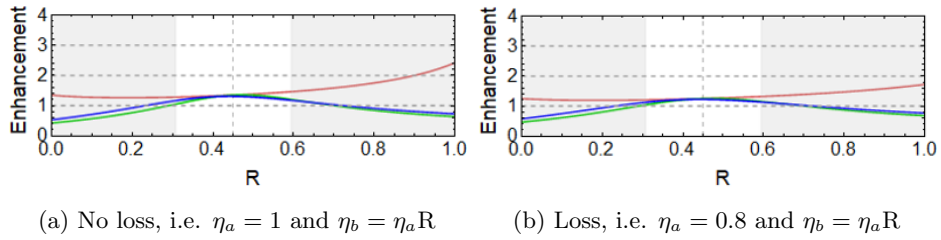


Figure 3.22: Enhancement with changing R value, $m=10$, $p=1500$, $\nu = 100$ and photon number=10.

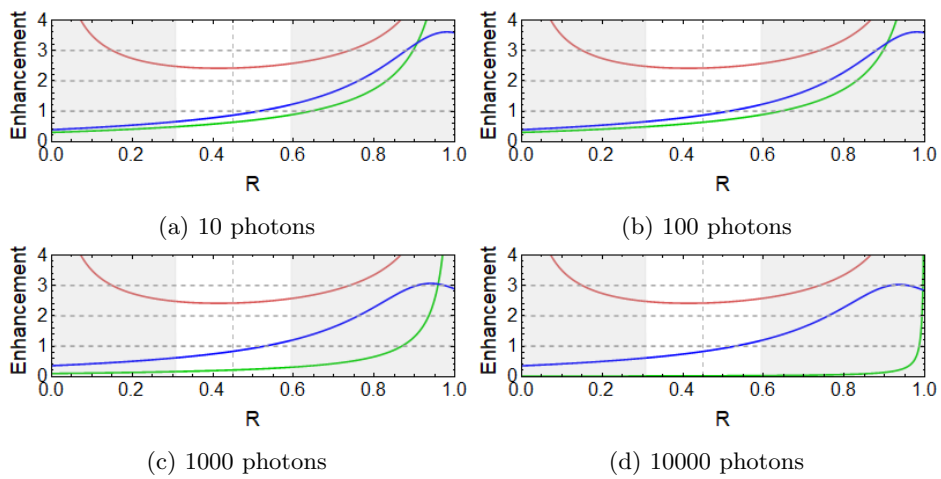


Figure 3.23: Enhancement with changing R value, $m=10$, $p=1500$, $\nu = 100$. This is for the standard two-mode.

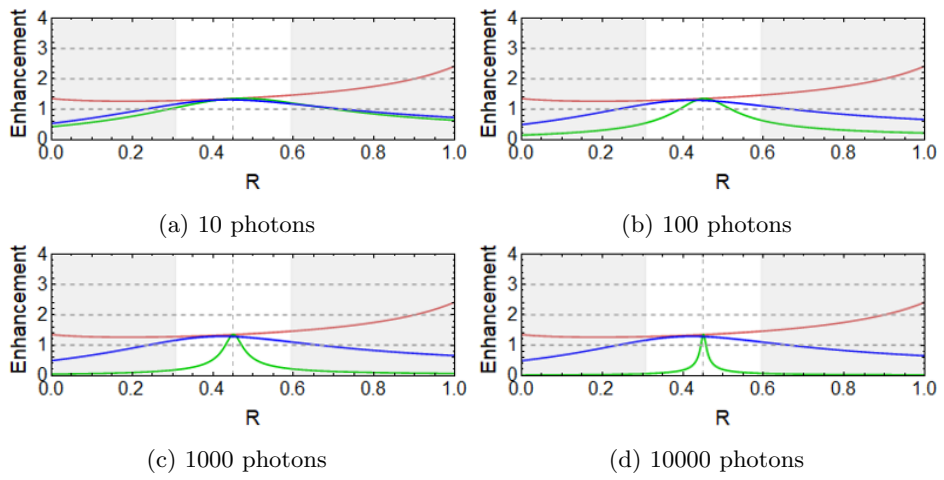


Figure 3.24: Enhancement with changing R value, $m=10$, $p=1500$, $\nu = 100$. This is for the optimized two-mode.

Conclusion

We can see that loss affects the enhancement in the precision, once we include loss the enhancement goes down. We can also see that for the standard two-mode case and the optimized case the enhancement in the TMSV state depends on photon number which explains why the precision of parameter estimation gets worse as we increase the photon number.

3.1.4 M-enhancement

We were also interested to know how much of an impact changing the m value has. We compared the precision of the $m=10$ and $m=50$ cases for ν and photon number varying as an example. The expected enhancement is the square root of $(50/10)$, which is approximately equal to 2.236. This is because for a set of m sensorgrams we expect the noise to be proportional to $\frac{1}{\sqrt{m}}$. We did this for all states, i.e. the classical, Fock, TMSV and TMSD states for the standard two-mode case where we do not have loss and all the parameters. We did not take measurements of $m=50$ for the states in the other cases, as we expect that the ratio will be consistent with the expected enhancement as it is for the no loss case we examined here and it would have been redundant to measure the M-enhancement. The coherent state is the benchmark classical state and normally the enhancement is not plotted as it is equal to 1, but here we are comparing m 's so we include the coherent state as enhancement changes with m . Now $m=10$ is the benchmark for enhancement. Figure 3.25 shows the enhancement of the k_d parameter for all the states when $m=50$ which is relatively constant. Figure 3.26 shows the enhancement of the k_s parameter for all the states when $m=50$ which is relatively constant and Figure 3.27 shows the enhancement of the k_a parameter for all the states when $m=50$ which is relatively constant.

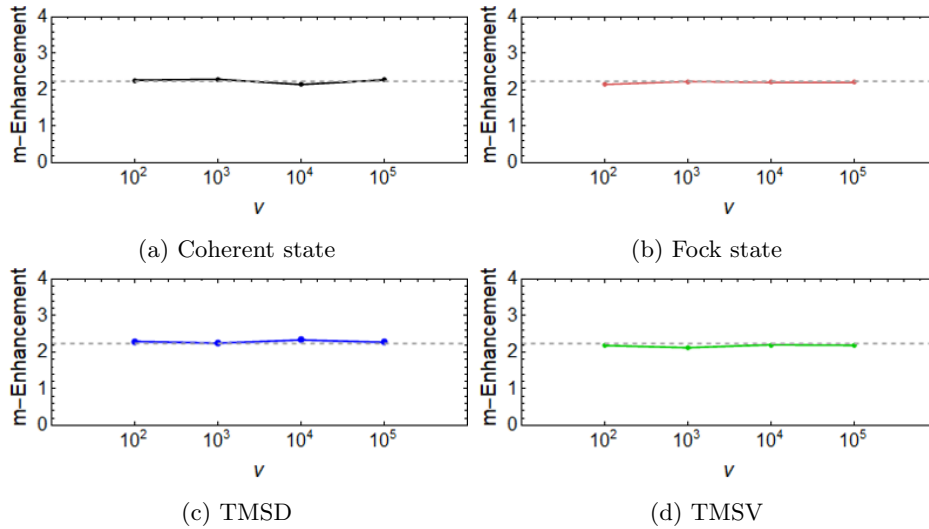


Figure 3.25: m-Enhancements for the k_d parameter, $\eta_a = \eta_b = 1$, $p=1500$ and photon number=10.

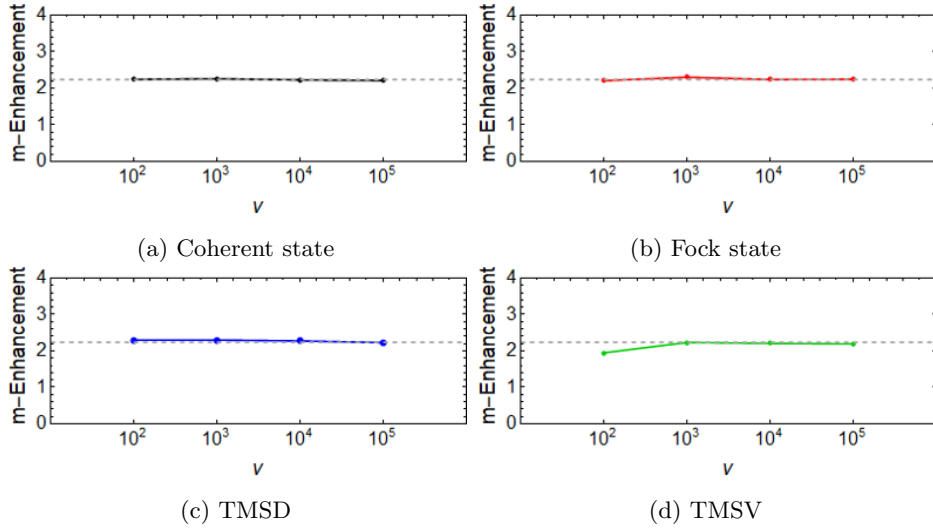


Figure 3.26: m-Enhancements for the k_s parameter, $\eta_a = \eta_b = 1$, $p=1500$ and photon number=10.

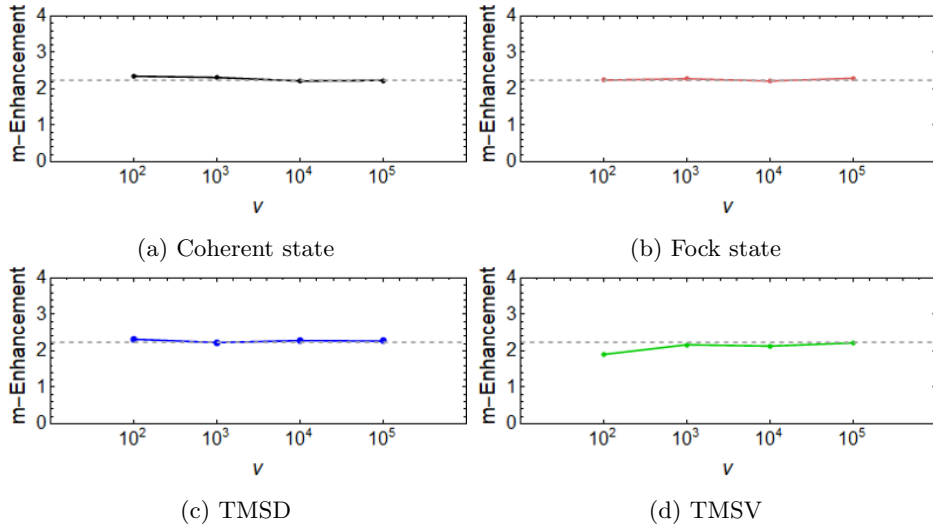


Figure 3.27: m-Enhancements for the k_a parameter, $\eta_a = \eta_b = 1$, $p=1500$ and photon number=10.

3.1.5 Conclusion

The two-mode standard case gives the best precision for the two-mode Fock state, the two mode optimized case improves the TMSV and TMSD, but it unfortunately reduces the two-mode Fock state. The single mode offers a similar enhancement to the optimized case but it is more practical for experiments as only one mode is required.

3.2 Small sensorgram deviation

We were interested to see how much of an effect using quantum states has in reducing the noise levels when we have very small changes in the refractive index. We are interested because in some experiments the changes in the refractive index are too small to be investigated using classical states and we are interested to see if such a case can be studied better with quantum states. When we looked at the real-time SPR curve showing immobilized BSA interaction with anti-BSA present in the sample in the previous section, we can see that the change in the refractive index was rather

significant.

Having established the performance of the different states for the sensorgram from the Kausite et al. paper [20] we were interested to see if the general results would hold true if we considered a system in which the refractive index change was very small. We were interested to know if there would be any change in performance. This led us to the paper by Lahiri et al. [21], where we consider the sensorgram for binding of immobilized bovine carbonic anhydrase II and its inhibitor benzene sulfonamide in PBS solution. We took the values of $k_a = 0.0038$, $k_d = 0.015$ and $L_0 = 2.1$ for our ideal model from the study. Looking at the change of refractive index curve we see that the change is very small, in a range from 1.3300 to 1.3303. Figure 3.28 shows the R model. The signal change here was very small. We had to increase ν from 100 to 100000 as the noise was otherwise too much due to the small signal change. As a result we focused only on changing the photon number in this section since we cannot really do a direct comparison when we are looking at the ν values. We only looked at the two-mode Fock state and the two-mode Coherent states as it is clear that the TMSD and TMSV states only work better than classical states when we use the optimised two-mode noise conditions and the enhancement in precision is similar to the Fock state in that case.

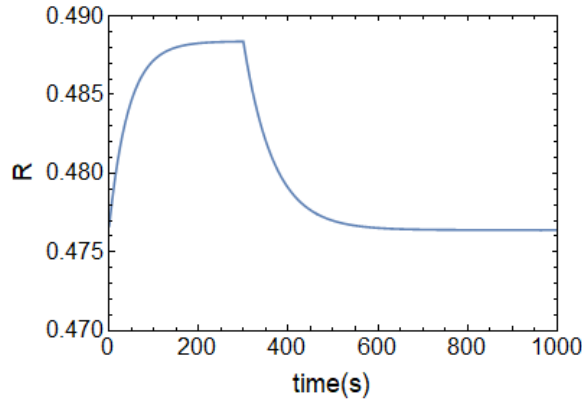


Figure 3.28: The R model for the angle model in Ref. [21].

Standard two-mode case

In this standard case we consider both modes in Figure 2.23 and no loss, i.e., $\eta_a = \eta_b = 1$. In Figure 3.29 we show the dependence of parameter precision on photon number. In Figure 3.30 we included loss hence we had $\eta_a = \eta_b = 0.8$. The dotted lines in the top row (of the figures) are the actual kinetic values and in the bottom row they represent the expected enhancement obtained from the value of R at the midpoint of the sensorgram curve. When we set the noise to the standard two-mode case we find that the Fock state performs better than the coherent state. The precision improves with increasing photon number. The enhancement remains constant throughout for all the kinetic parameters. This holds for with and without loss.

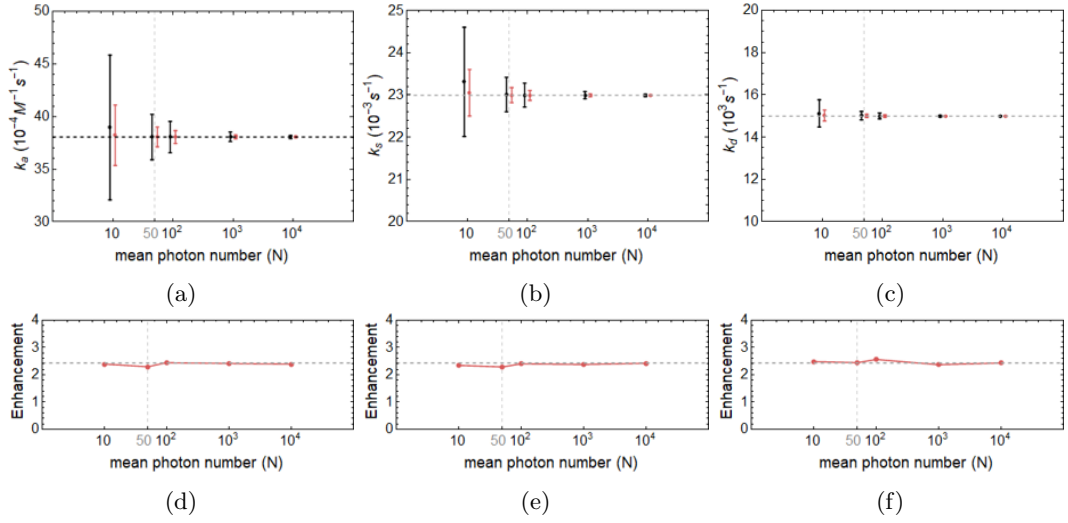


Figure 3.29: Two-mode standard results, photon number dependence, $m=10$, $p=1500$, $\nu = 100000$ (no loss, i.e. $\eta_a = \eta_b = 1$).

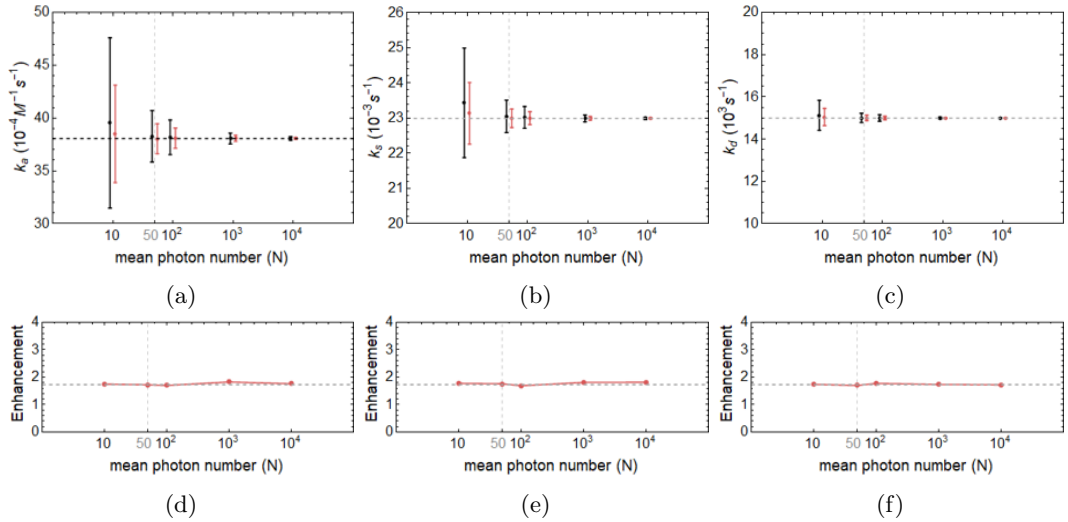


Figure 3.30: Two-mode standard results, photon number dependence, $m=10$, $p=1500$, $\nu = 100000$ (loss, i.e. $\eta_a = \eta_b = 0.8$).

Optimized two-mode case

In this standard case we consider both modes in Figure 2.23 and no loss, i.e., $\eta_a = 1$ and $\eta_b = R$. R is fixed. In Figure 3.31 we show the dependence of parameter precision on photon number. In Figure 3.32 we included loss hence, we had $\eta_a = 0.8$ and $\eta_b = 0.8R$. When we set the noise to the optimized two-mode case we find that the Fock state performs better than the coherent state. The precision improves with increasing photon number. The enhancement remains constant throughout for all the kinetic parameters. This holds for with and without loss.

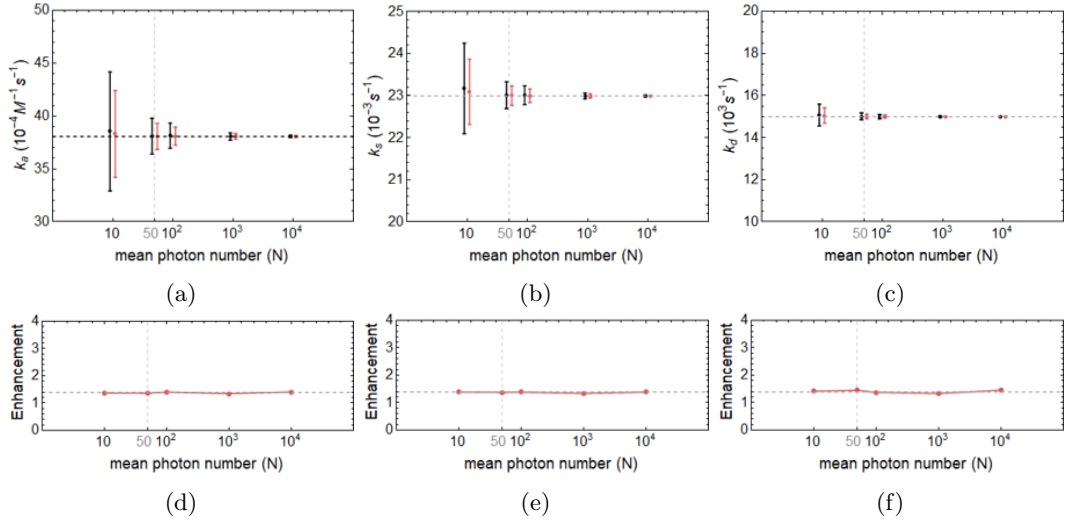


Figure 3.31: Two-mode standard results, photon number dependence, $m=10$, $p=1500$, $\nu = 100000$ (Optimized loss, i.e. $\eta_a = 1$ and $\eta_b = \eta_a R$).

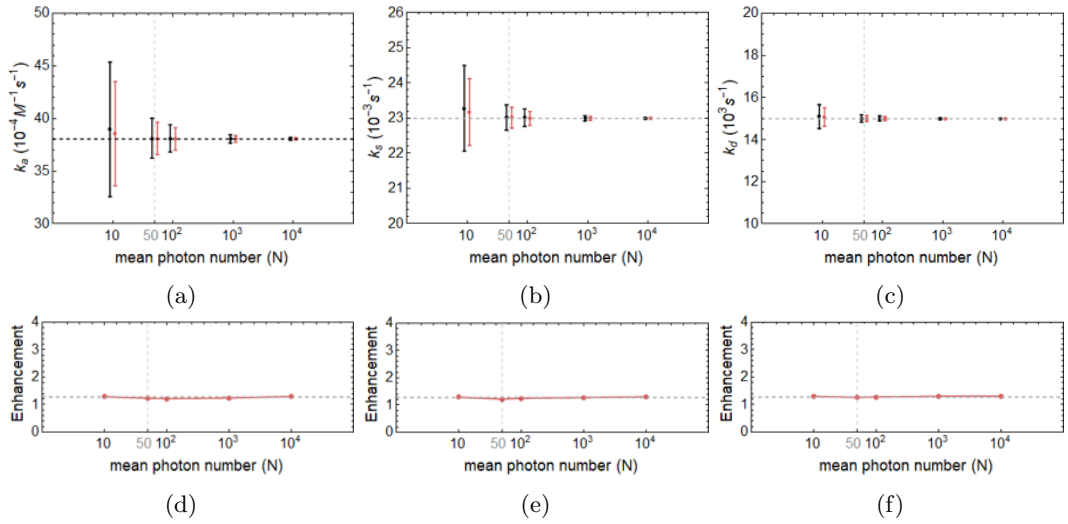


Figure 3.32: Two-mode standard results, photon number dependence, $m=10$, $p=1500$, $\nu = 100000$ (Optimized loss, i.e. $\eta_a = 0.8$ and $\eta_b = \eta_a R$).

Single-mode case

In this standard case we consider both modes in Figure 2.23 and no loss in mode a, i.e., $\eta_a = 1$ and $\eta_b = 0$. In Figure 3.33 we show the dependence of parameter precision on photon number. In Figure 3.34 we included loss hence we had $\eta_a = 0.8$ and $\eta_b = 0$. When we set the noise to the single-mode case we find that the Fock state performs better than the coherent state. The precision improves with increasing photon number. The enhancement remains constant throughout for all the kinetic parameters. This holds for with and without loss.

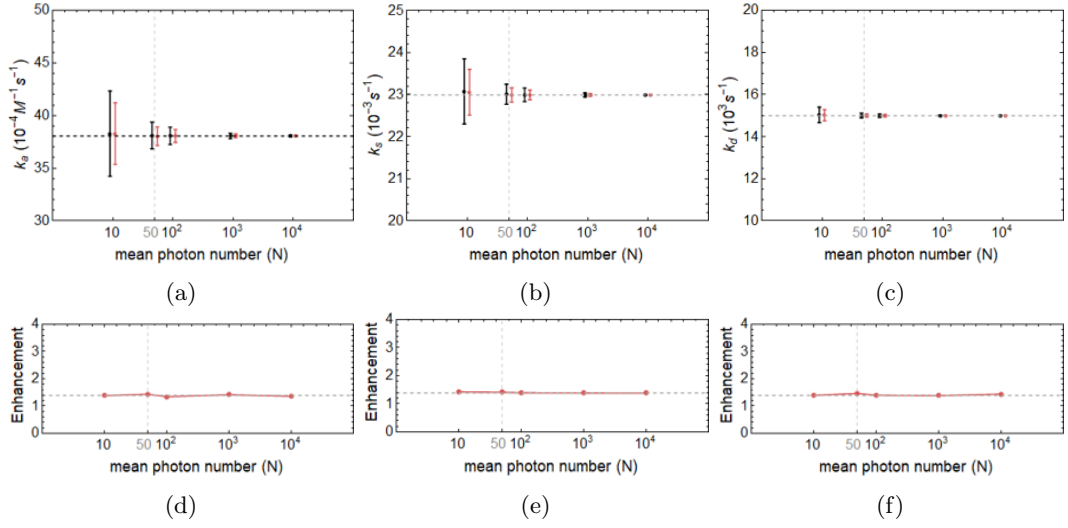


Figure 3.33: Single-mode standard results, photon number dependence, $m=10$, $p=1500$, $\nu = 100000$ (loss, i.e. $\eta_a = 1$ and $\eta_b = 0$).

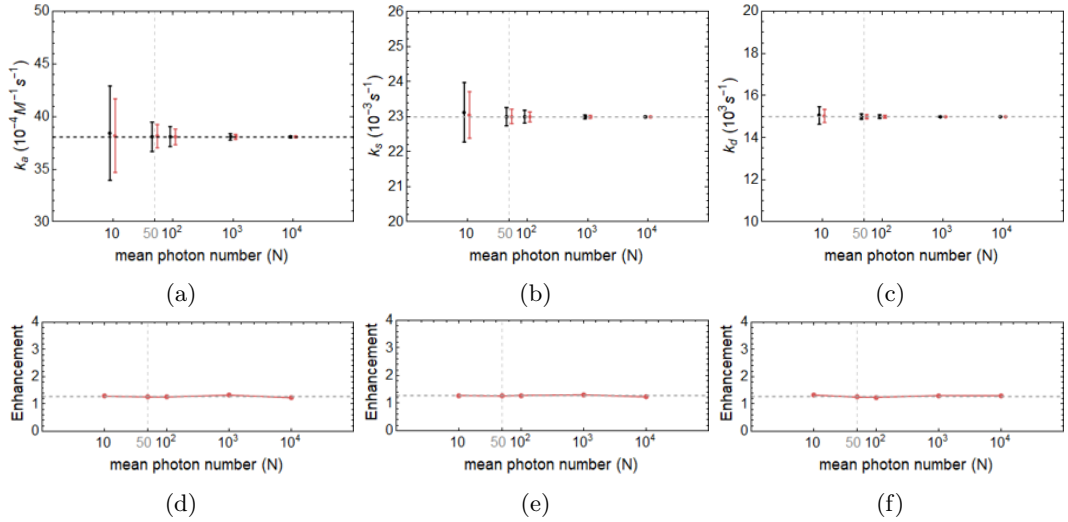


Figure 3.34: Single-mode standard results, photon number dependence, $m=10$, $p=1500$, $\nu = 100000$ (loss, i.e. $\eta_a = 0.8$ and $\eta_b = 0$).

Conclusion

The Fock state gives better precision and enhancement in all the cases, especially in the standard two-mode case. The single mode offers a similar enhancement to the optimized case but it is more practical for experiments as only one mode is required. Experimentally relevant m , p and ν values are described in chapter 5. However the values chosen here are roughly in the range of experimental feasibility. Values for η_a are also in the experimental range, i.e., $0 \rightarrow 0.8$.

Chapter 4

Application of quantum plasmonic sensing to HIV case study

The kinetics of the interaction between drug-resistant variants of HIV-1 protease and clinically used inhibitors are of particular interest in HIV studies [95]. An enzyme inhibitor is a molecule that binds to an enzyme and decreases its activity. HIV-1 protease is a retroviral aspartyl protease (retropepsin), an enzyme involved with peptide bond hydrolysis in retroviruses, that is essential for the life-cycle of HIV, the retrovirus that causes AIDS [37]. The HIV-1 protease variant is immobilized on a biosensor chip and the association and dissociation rate constants for interactions with inhibitors are determined. The kinetic parameters are important because they can be used in inhibitor design. Changes in the kinetic parameters reflect a change in the drug resistance capacity of the HIV-1 protease. Due to the importance of HIV drug studies we decided to use the kinetics as a test case for showing the benefits of a quantum approach.

In this section we made a model for R for a scenario involving HIV. We used values from the experiment by Shuman et al. [95], where we chose nelfinavir as the inhibitor and the wild-type enzyme for the reaction. We had to use a low concentration to be consistent with [95]. A low concentration meant that there was a smaller R change, even more so than that studied for the paper by Lahiri et al in chapter 3.

The following parameters were used: $k_a = 3.79 \times 10^5 \text{ M}^{-1}\text{s}^{-1}$, $k_d = 5.65 \times 10^{-4} \text{ s}^{-1}$ and $L_0 = 80 \times 10^{-9} \text{ M}$. We will show plots of the results for the parameter vs photon-number and for the case of the parameter vs ν . The R model is shown in Figure 4.1. Figure 4.2 is a picture of the HIV-1 protease structure in a complex with an inhibitor.

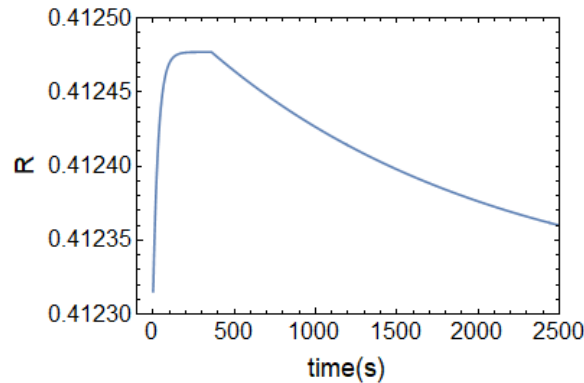


Figure 4.1: The R model for the angle model in Ref. [95].

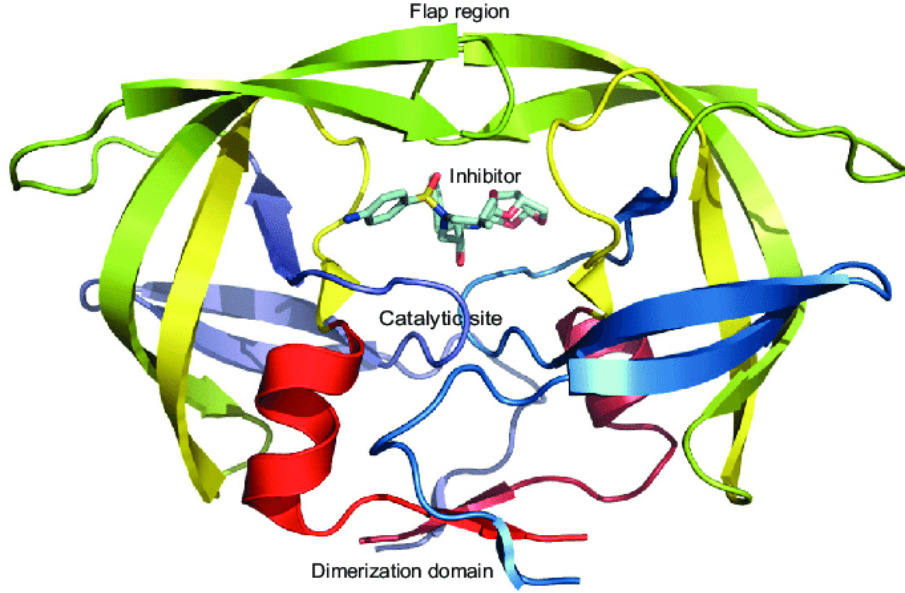


Figure 4.2: Structural model of the HIV-1 protease structure in a complex with an inhibitor taken from Ref. [16].

4.0.1 Standard two-mode case

In the standard case we consider both modes in Figure 2.23 and no loss, i.e., $\eta_a = \eta_b = 1$. In Figure 4.3 we show the dependence of ν for $m=10$ and in Figure 4.4 we show the dependence on photon number. The dotted lines in the top row (of the figures) are the actual kinetic values and in the bottom row they represent the expected enhancement obtained from the value of R at the midpoint of the sensorgram curve. When we set the noise to the standard two-mode case we find that the Fock state performs better than the coherent state. The precision improves with increasing ν and photon number. The enhancement remains constant throughout for all the kinetic parameters.

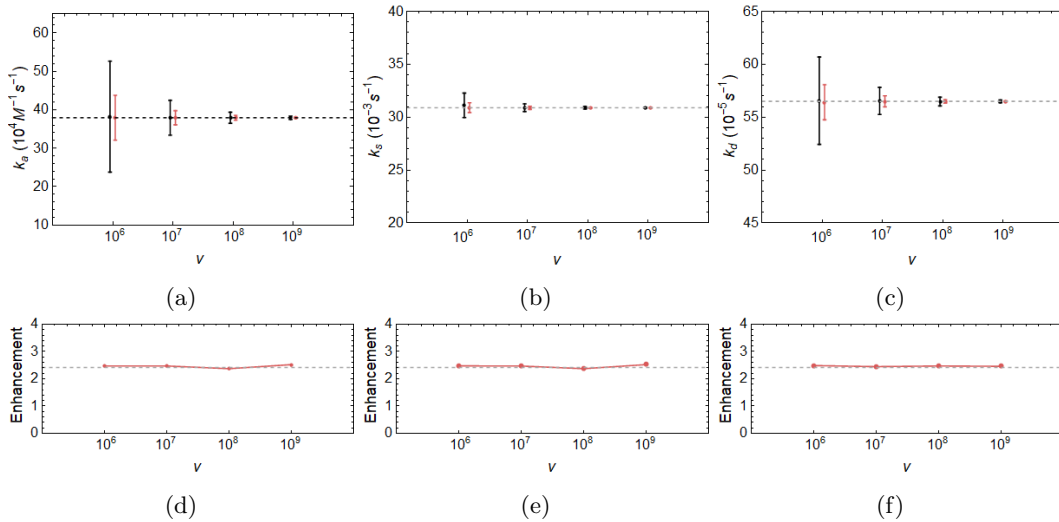


Figure 4.3: Two-mode standard results, ν dependence, $m=10$, $p=1500$, photon-number=5000 (no loss, i.e., $\eta_a = \eta_b = 1$).

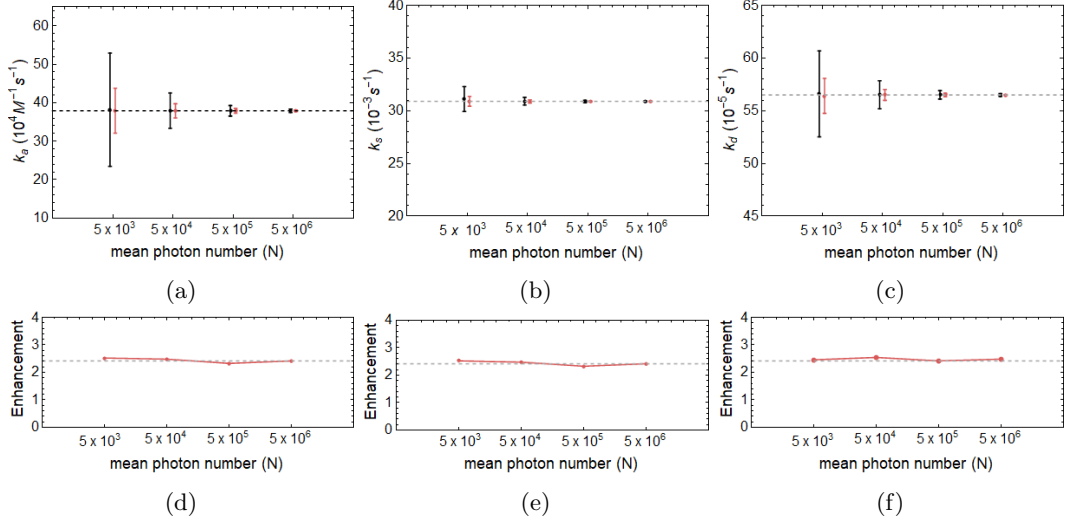


Figure 4.4: Two-mode standard results, photon number dependence, $m=10$, $p=1500$, $\nu = 10^6$ (no loss, i.e., $\eta_a = \eta_b = 1$).

Lossy standard two-mode case

In the lossy standard case we consider both modes in Figure 2.23 and loss, i.e., $\eta_a = \eta_b = 0.8$. In Figure 4.5 we show the dependence of ν for $m=10$ and in Figure 4.6 we show the dependence on photon number. The dotted lines in the top row (of the figures) are the actual kinetic values and in the bottom row they represent the expected enhancement obtained from the value of R at the midpoint of the sensorgram curve. When we set the noise to the lossy standard two-mode case we find that the Fockgram performs better than the coherent state. The precision improves with increasing ν and photon number. The enhancement remains constant throughout for all the kinetic parameters.

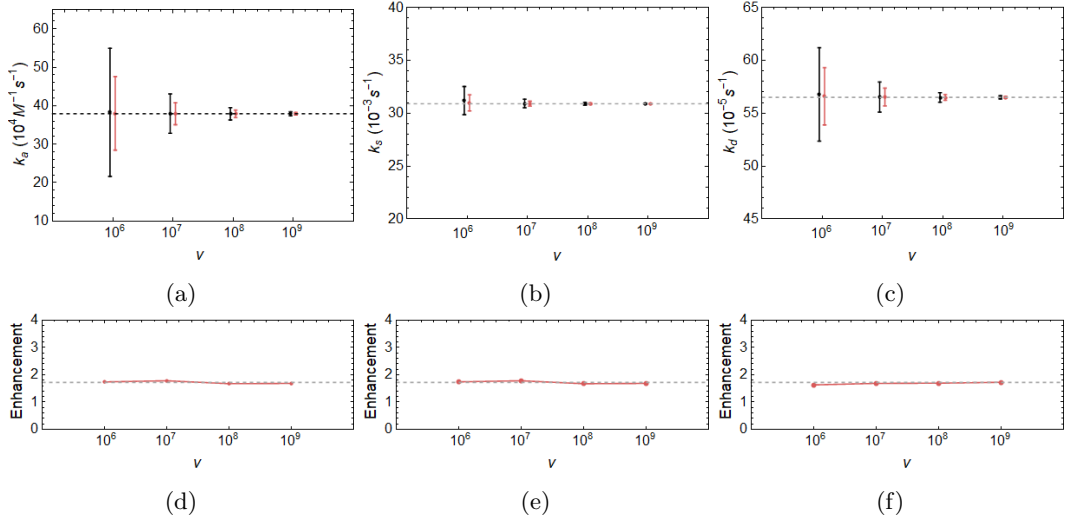


Figure 4.5: Balanced two-mode standard results, ν dependence, $m=10$, $p=1500$, photon-number=5000 (loss, i.e., $\eta_a = \eta_b = 0.8$).

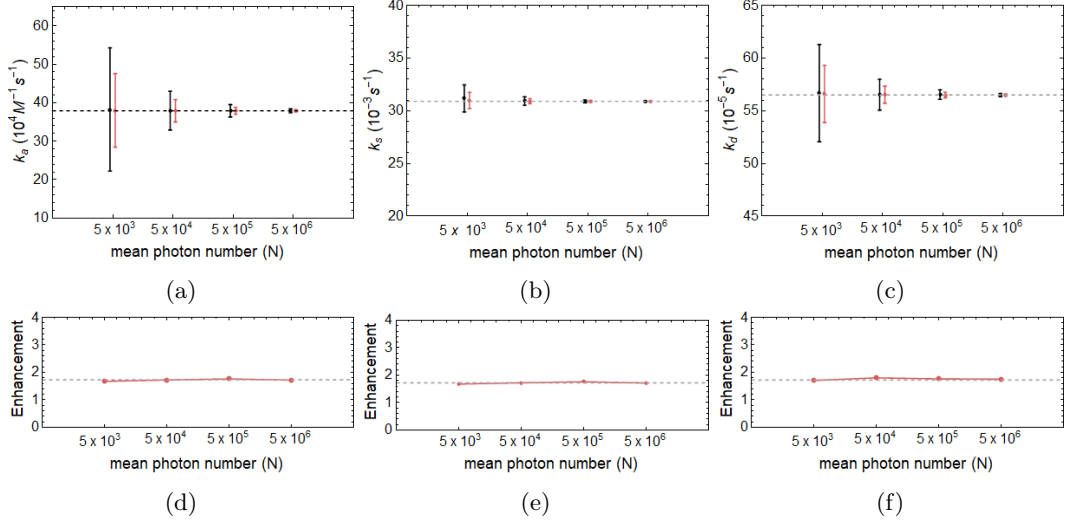


Figure 4.6: Two-mode standard results, photon number dependence, $m=10$, $p=1500$, $\nu = 10^6$ (loss, i.e., $\eta_a = \eta_b = 0.8$).

4.0.2 Optimized two-mode case

In this optimized case we consider both modes in Figure 2.23 and no loss, i.e., $\eta_a=1$ and $\eta_b=R$. In Figure(4.7) we show the dependence of ν for $m=10$ and in Figure 4.8 we show the dependence on photon number. The dotted lines in the top row (of the figures) are the actual kinetic values and in the bottom row they represent the expected enhancement obtained from the value of R at the midpoint of the sensorgram curve. When we set the noise to the optimized two-mode case we find that the Fock state performs better than the coherent state. The precision improves with increasing ν and photon number. The enhancement remains constant throughout for all the kinetic parameters.

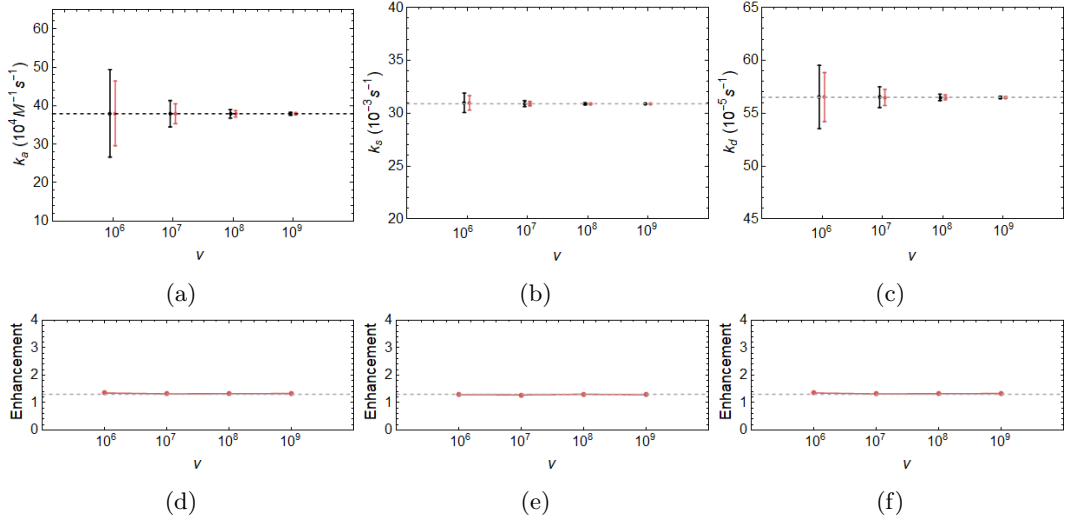


Figure 4.7: Optimized two-mode standard results, ν dependence, $m=10$, $p=1500$, photon-number=5000 (loss, i.e., $\eta_a = 1$ and $\eta_b = R$).

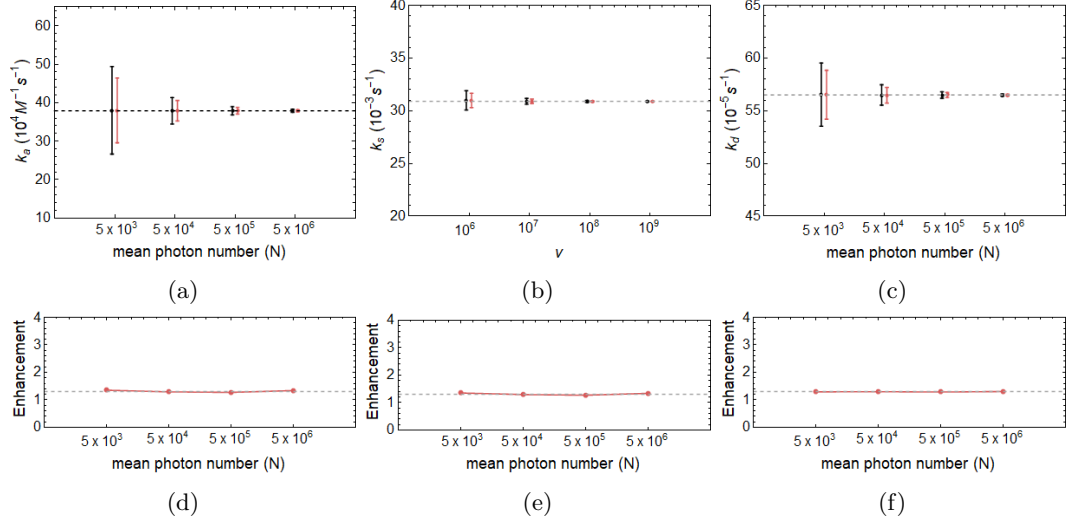


Figure 4.8: Optimized two-mode standard results, photon number dependence, $m=10$, $p=1500$, $\nu = 10^6$ (no loss, i.e., η_a and $\eta_b = R$).

Lossy optimized two-mode case

In the optimized case we consider both modes in Figure 2.23 and loss, i.e., $\eta_a=0.8$ and $\eta_b=0.8R$. In Figure 4.9 we show the dependence of ν for $m=10$ and in Figure 4.10 we show the dependence on photon number. The dotted lines in the top row (of the figures) are the actual kinetic values and in the bottom row they represent the expected enhancement obtained from the value of R at the midpoint of the sensorgram curve. When we set the noise to the lossy optimized two-mode case we find that the Fock state performs better than the coherent state. The precision improves with increasing ν and photon number. The enhancement remains constant throughout for all the kinetic parameters.

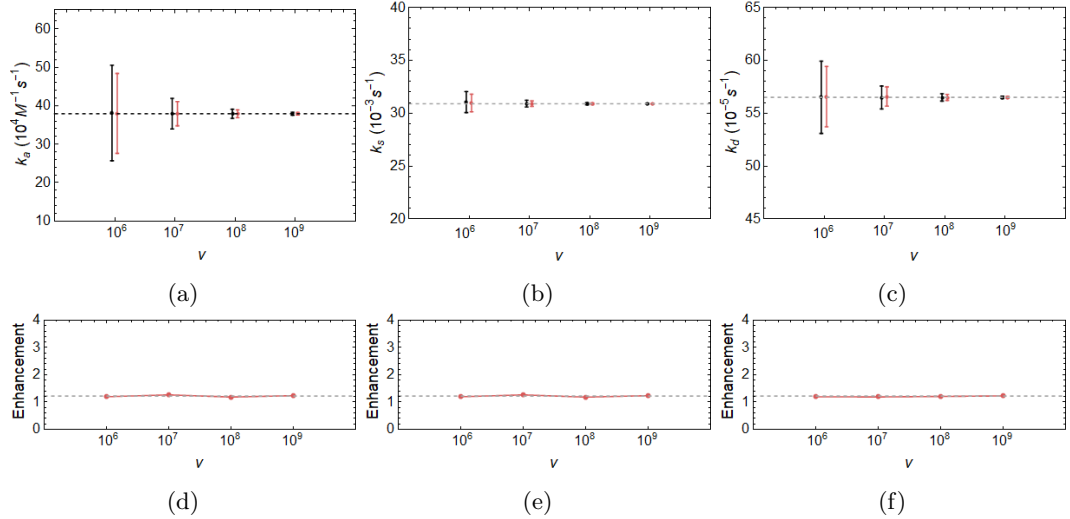


Figure 4.9: Optimized two-mode results, ν dependence, $m=10$, $p=1500$, photon-number=5000 (loss, i.e., $\eta_a = 0.8$ and $\eta_b = 0.8R$).

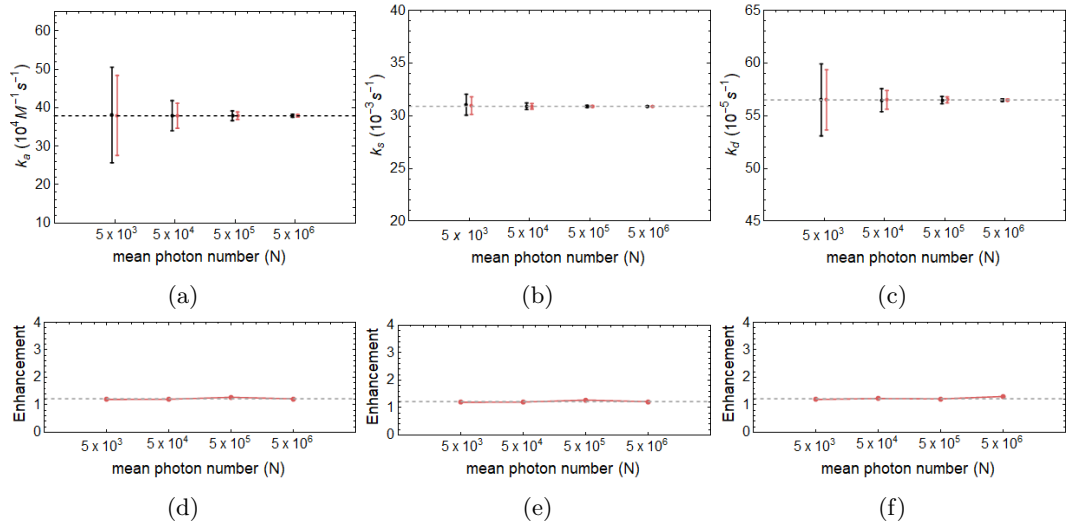


Figure 4.10: Optimized two-mode standard results, photon number dependence, $m=10$, $p=1500$, $\nu = 10^6$ (loss, i.e., $\eta_a =$ and $\eta_b = 0.8R$).

4.0.3 Single-mode case

In the single-mode case we consider both modes in Figure 2.23 and no loss, i.e., $\eta_a=1$ and $\eta_b=0$. In Figure 4.11 we show the dependence of ν for $m=10$ and in Figure 4.12 we show the dependence on photon number. The dotted lines in the top row (of the figures) are the actual kinetic values and in the bottom row they represent the expected enhancement obtained from the value of R at the midpoint of the sensorgram curve. When we set the noise to the single-mode case we find that the Fock state performs better than the coherent state. The precision improves with increasing ν and photon number. The enhancement remains constant throughout for all the kinetic parameters.

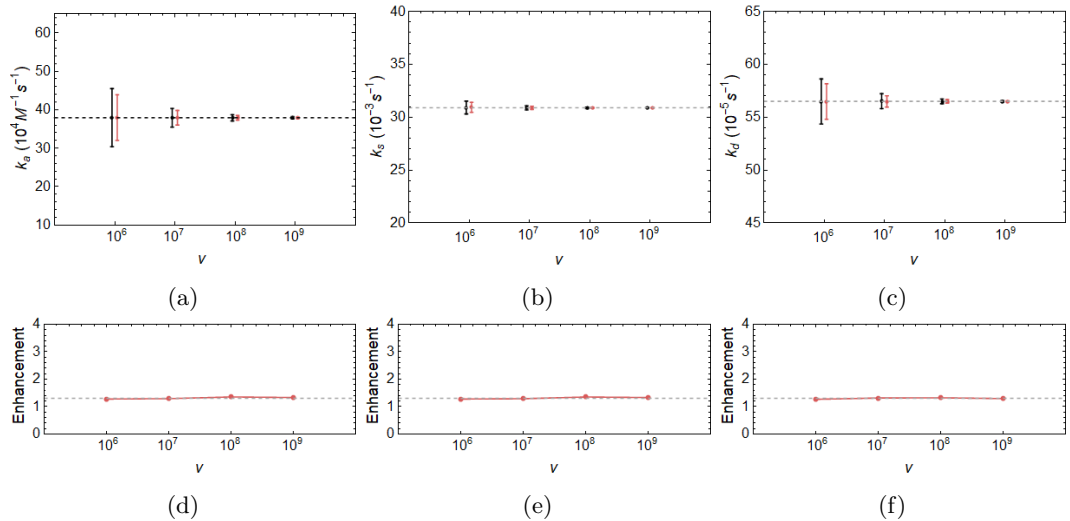


Figure 4.11: Single-mode standard results, ν dependence, $m=10$, $p=1500$, photon-number=5000 (no loss, i.e., $\eta_a = 1$ and $\eta_b = 0$).

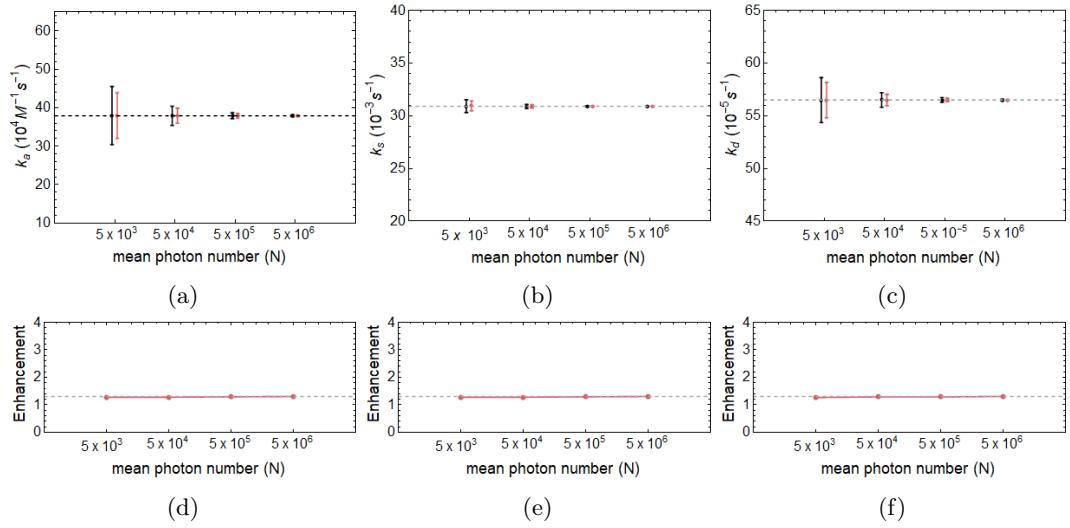


Figure 4.12: Single-mode standard results, photon number dependence, $m=10$, $p=1500$, $\nu = 10^6$ (no loss, i.e., $\eta_a = 1$ and $\eta_b = 0$).

Lossy single-mode case

In the single-mode case we consider both modes in Figure 2.23 and loss, i.e., $\eta_a=0.8$ and $\eta_b=0$. In Figure 4.13 we show the dependence of ν for $m=10$ and in Figure 4.14 we show the dependence on photon number. The dotted lines in the top row (of the figures) are the actual kinetic values and in the bottom row they represent the expected enhancement obtained from the value of R at the midpoint of the sensorgram curve. When we set the noise to the lossy single-mode case we find that the Fock state performs better than the coherent state. The precision improves with increasing ν and photon number. The enhancement remains constant throughout for all the kinetic parameters.

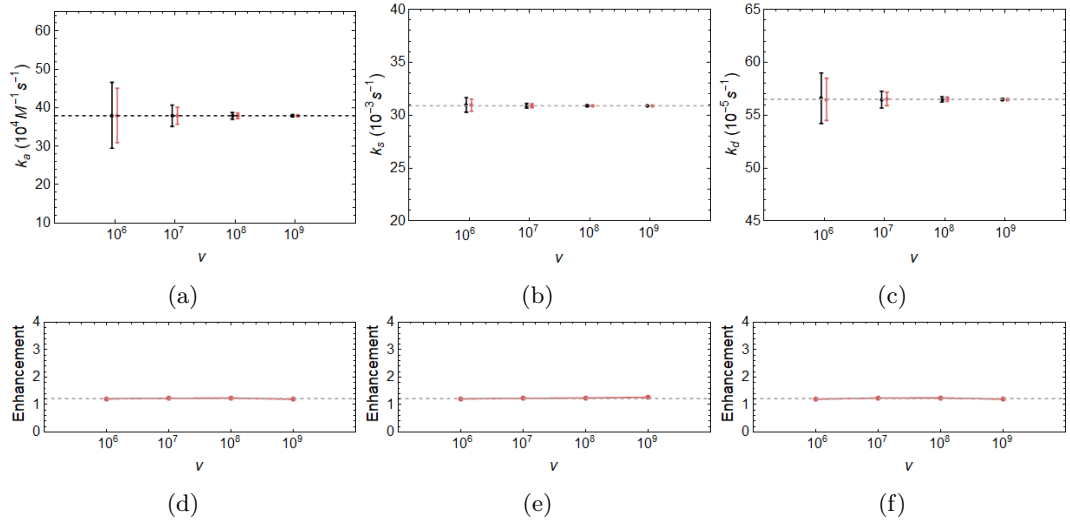


Figure 4.13: Single-mode results, ν dependence, $m=10$, $p=1500$, photon-number=5000 (loss, i.e., $\eta_a = 0.8$ and $\eta_b = 0$).

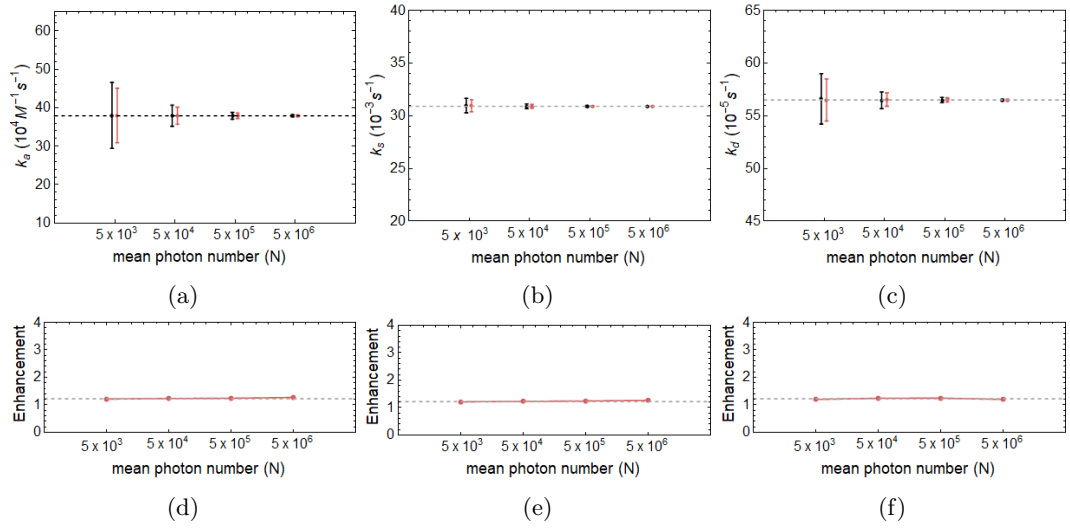


Figure 4.14: Single-mode results, photon number dependence, $m=10$, $p=1500$, $\nu = 10^6$ (loss, i.e., $\eta_a = 0.8$ and $\eta_b = 0$).

4.0.4 Conclusion

The Fock state gives better precision and enhancement in all the cases, especially in the standard two-mode case. The single mode offers a similar enhancement to the optimized case but it is more practical for experiments as only one mode is required.

Chapter 5

Experimental quantum plasmonic sensing

5.1 Plasmonic sensing with single photons from SPDC source

In this section we look at a way of implementing a quantum plasmonic sensing experiment, i.e., using quantum states of light in our SPR sensing setup. This is done by combining setups which we have discussed in previous chapters, i.e., the SPR and SPDC setups, as shown in Figure 5.1. Even though it might seem like we need a large number of photons when we want to compare the noise reduction to that with a coherent beam with many photons, the use of single photons is sufficient to demonstrate that a relative enhancement is obtainable [30].

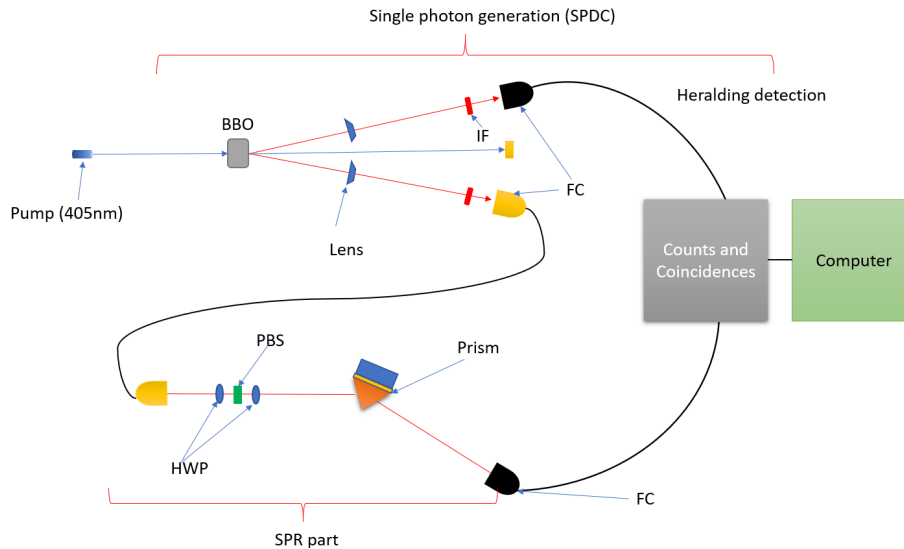


Figure 5.1: Experimental implementation of plasmonic sensing with single photons from a SPDC source.

In Figure 5.1 we measure coincidences and singles counts for the idler (top) and signal (bottom) arms. Out of ν single photons sent to the SPR setup (heralded by a detection in the top arm), we measure the number, N_t , of transmitted single photons. We used a 6 seconds averaging of our data with $\nu = 150$ in our analysis.

Due to the maximum transmission of the SPR setup of around 10% (as a result of losses from

mirrors, the prism, the fibre couplers and other components) the coincidence count was low and 6 seconds gave enough data to provide statistically relevant results. A larger average/integration time is not suitable due to the time scale on which the sensorgram changed and a need to get enough points on the sensorgram. This time scale can be seen in Figure 5.2 (a) for the singles. Increasing the pump power unfortunately increases the pump based noise in the singles and coincidences and is not desirable.

We repeat the independent and identical sampling of ν trials, μ times during the 6 seconds ($\mu = 2 \times 10^3$), which is checked to be large enough to calculate a steady standard deviation $\langle \Delta \hat{N} \rangle$, which is the noise in the average over μ repeated measurements. We use these statistical quantities to quantify the uncertainty in measurements. We count how many of the transmitted photons are found in the signal mode (given a photon was detected in the idler mode within 4ns), yielding the transmission of set i , $T(i) = N_t(i)/\nu$. The total expected mean is given by $\langle T_{\text{total}} \rangle = \sum_{i=1}^{\mu} \frac{1}{\mu} T(i)$.

We calculated the uncertainty, $\langle \Delta T_{\text{total}} \rangle$, using

$$\langle \Delta T_{\text{total}} \rangle = \sqrt{\frac{1}{\mu} \sum_{i=1}^{\mu} (T(i) - \langle T_{\text{total}} \rangle)^2}. \quad (5.1)$$

The theoretical model for the ideal case for quantum single-photon and classical (mean photon number at 1) states are given as [30]

$$\langle \Delta T_{\text{classical}} \rangle = \sqrt{\frac{\langle T_{\text{total}} \rangle}{\nu}}, \quad (5.2)$$

and

$$\langle \Delta T_{\text{quantum}} \rangle = \sqrt{\frac{\langle T_{\text{total}} \rangle (1 - \langle T_{\text{total}} \rangle)}{\nu}}. \quad (5.3)$$

The above quantum plasmonic sensor aims to estimate the observable rate constant k_s for the binding reaction between BSA and the gold surface in our plasmonic setup. We covered the surface of the gold with water first to establish a baseline for our reaction. We then added 2 percent BSA onto the surface of the gold and measured the change in the number of transmitted photons in the signal mode over time to get our sensorgram. As the refractive index on top of the gold surface changes, the number of transmitted photons in the signal mode changes whilst the idler mode remains constant as shown in Figure 5.2.

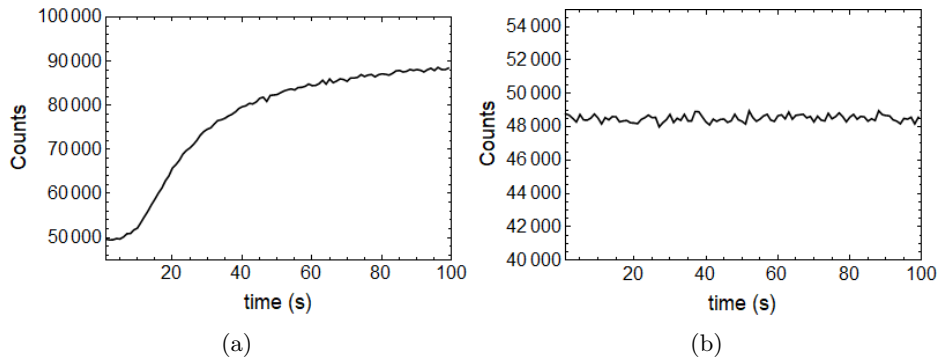


Figure 5.2: Plots (a) and (b) show how the counts change with time in the signal mode as the refractive index changes and how they are constant in the idler mode.

We collected the data for $N_t(i)$ as it changed with time using a Picoquant Timeharp 260 PICO. We used these values to calculate $\langle T_{\text{total}} \rangle$ and $\langle \Delta T_{\text{total}} \rangle$, as shown in Figure 5.3.

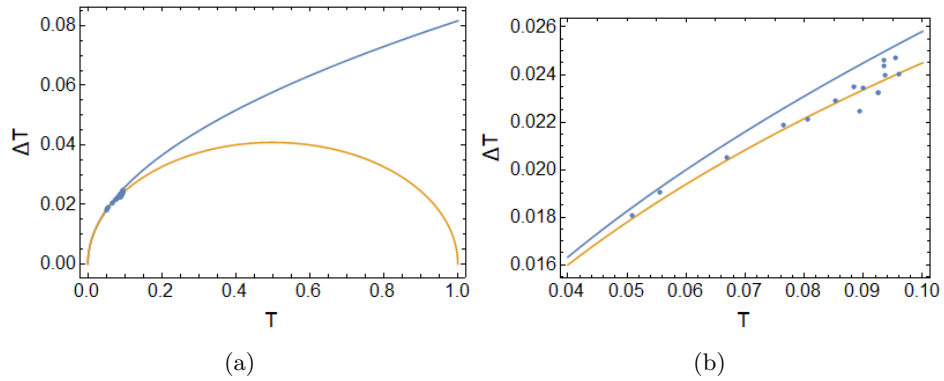


Figure 5.3: Plots (a) and (b) show the relationship between T and ΔT , the orange line represents the region for quantum states and the blue line shows the region for classical states. The blue points in (a) are the data points we measured in our experiment. (b) Zoom in shows them more clearly for us to see the points.

Using these values we plotted a sensorgram of $\langle T_{\text{total}} \rangle$ vs time with $\langle \Delta T_{\text{total}} \rangle$ being used as the uncertainty in each measurement, as shown in Figure 5.4. We also look at error plots for the quantum experimental data and for the classical simulation data in Figure 5.5.

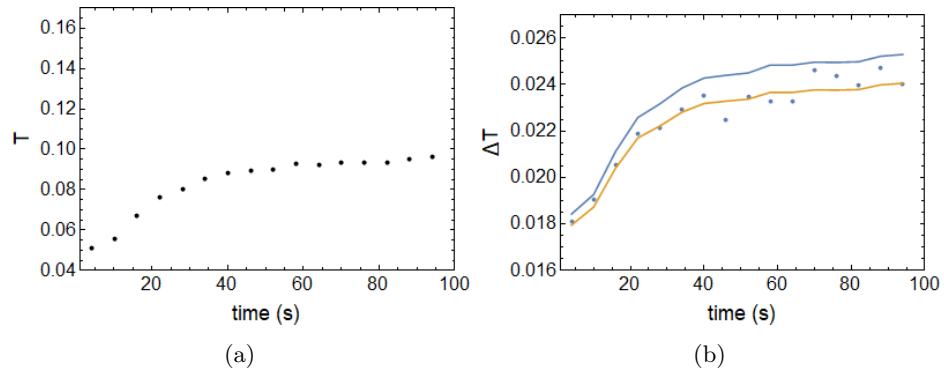


Figure 5.4: Plots (a) and (b) show the sensorgram as T changes with time. (b) shows how the uncertainty in T changes for the predicted classical case (blue line) and for the quantum case we measured (orange line).

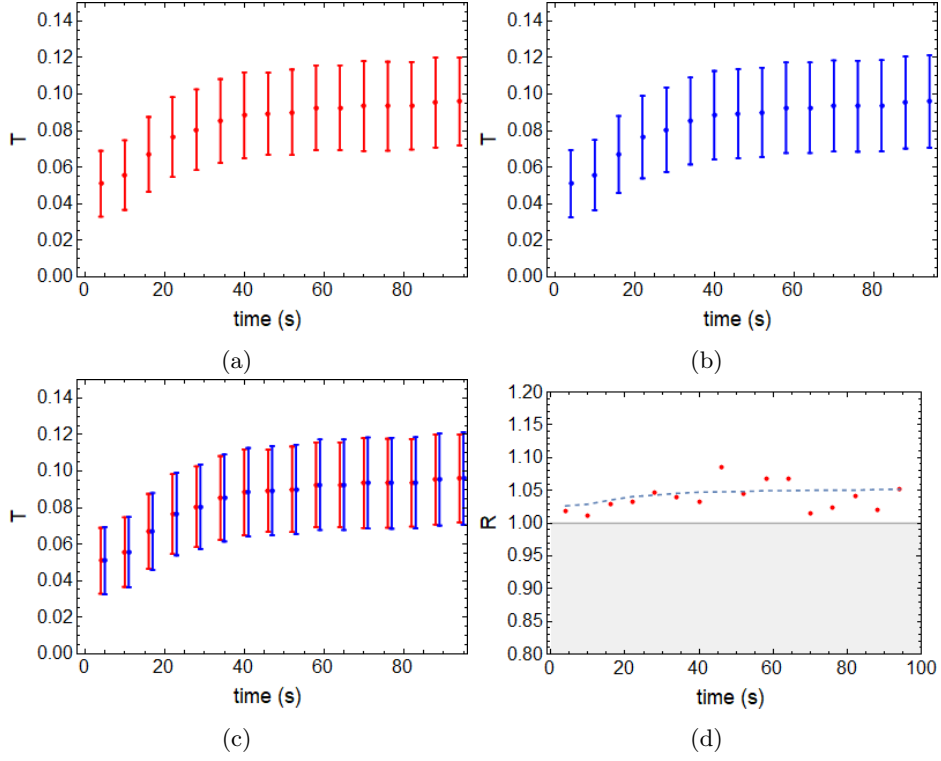


Figure 5.5: (a) Error-plot for quantum experimental data. (b) Error plot for classical simulated data. (c) shows these plots side by side, where a small reduction in the error can be seen for the quantum case over time. (d) shows how R changes at each point in time over the duration of the experiment, the grey shaded region represents the classical area and anything above represents the quantum area, the dotted blue line shows a general trend.

We use a Gauss-Newton non-linear fit as shown in Figure 5.6 to extract the k_s parameter using the model $T = a + b(1 - e^{-k_s(t-t_{on})})S(t - t_{on})$ where, $S(t - t_{on})$ is the unit step function and t_{on} is the start time for the dynamics. To do this we made a list of sets with m sensorgrams per set and p sets from our experimental data (as in the theory study) by a bootstrap sampling of the data. Each study individual sensorgram in a set of m is too noisy on its own so we averaged over m sensorgrams in a set before doing the fit, this gave an m dependence to the kinetic parameter k_s in addition to the ν dependence it already had. According to the ergodic principle, assuming each point in the sensorgram experiences stationary noise, we will get the same result if we average m sensorgrams then do the fit or do the fit on each of the m sensorgrams and then average the fit parameters (as in the theory study). We used an m value of 60 and a p value of 15 000 in this work, which gave a reasonable statistical stability. $R = \frac{\langle \Delta \dot{M}_{\text{quantum}} \rangle}{\langle \Delta \dot{M}_{\text{coherent}} \rangle}$.

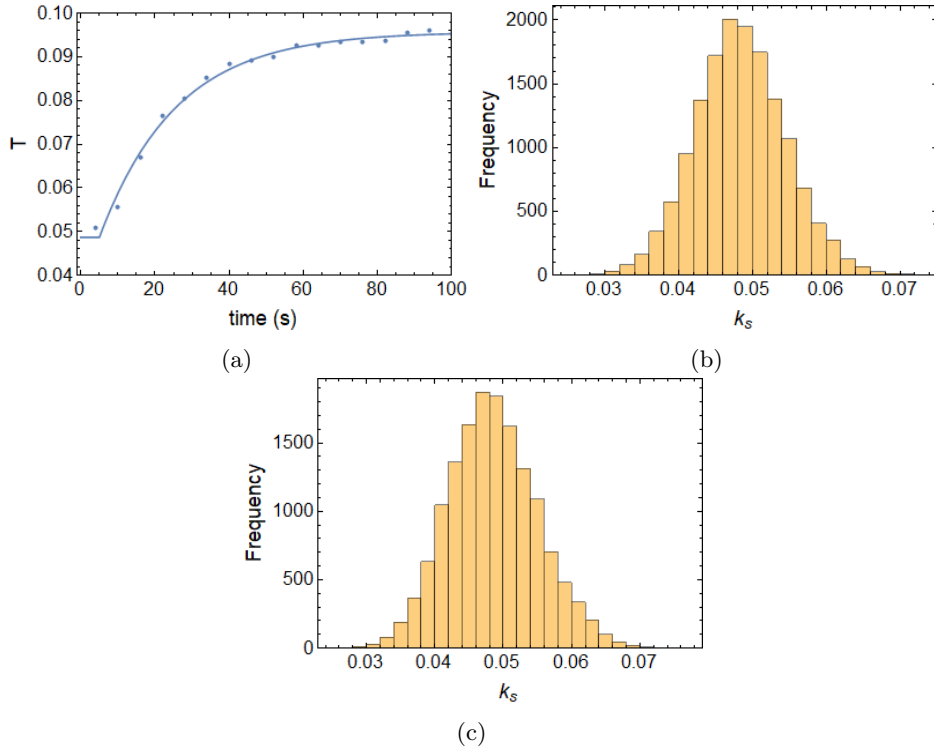


Figure 5.6: (a) Sensorgram fit using Gauss-Newton non-linear fit. (b) A histogram of the k_s value extracted from the fit using quantum data. (c) A histogram of the k_s value extracted from the fit using simulated classical data.

From the quantum case we extracted $k_s = 0.04841s^{-1}$ with $\Delta k_s = 0.00612s^{-1}$. Using Eq. (5.2) we also simulated a classical version of the sensorgram we extracted. We fit this noisy sensorgram in the same way as the quantum case and extracted the parameter k_s and found that the standard deviation of the parameter was larger as expected. From the classical case we extracted $k_s = 0.04855s^{-1}$ with $\Delta k_s = 0.00652s^{-1}$. Comparing the classical simulation and the quantum experiment parameters we look at a box-and-whisker plot shown in Figure 5.7.

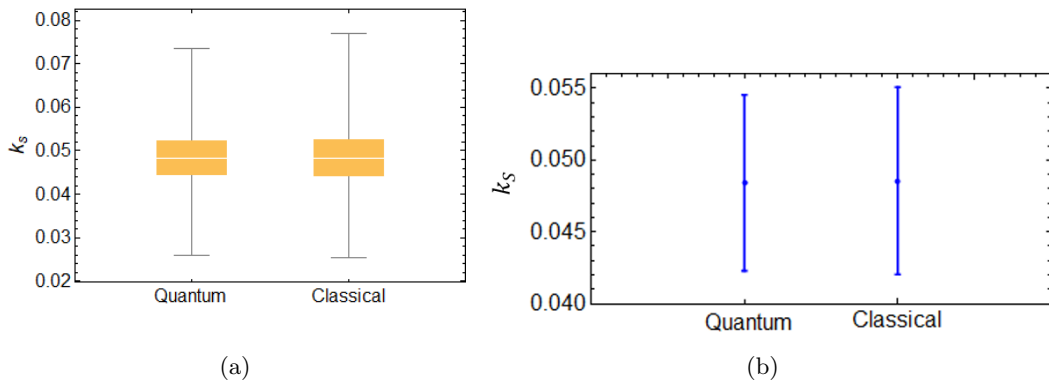


Figure 5.7: (a) Box-and-whisker plot for comparison of quantum experiment and classical simulation. The box plot shows us the shape of the distribution of the parameter k_s , its central value, and its variability. (b) A plot showing k_s values and Δk_s for the quantum and classical data.

Taking a ratio of the variance of the classical simulation data and the quantum experiment data

we find that there is a 13 percent enhancement in the variance and a 6 percent enhancement in the standard deviation ratio for the estimation of k_s . The quantum state gives slightly better precision. This is quite small because our T is small due to losses in the setup, i.e., it runs between 5-10 percent. Better enhancement could be achieved by reducing losses.

The results of this experiment have shown a small improvement in the precision of the estimation of the kinetic parameter k_s when using the quantum approach compared to the classical approach. In order to go forward and use the setup to improve the precision in measuring drug kinetics of HIV, two major advancements are required. The first is to reduce the overall losses in the setup so that the range of T is increased. As seen in Figure 5.3(a), the improvement in the precision ΔT gets better as T increases. The second advancement is the rate of single photons probing the SPR setup. As seen in Chapter 4, values of $\nu \sim 10^6$ and $N \sim 10^3$ are required due to the small reflectivity change of the SPR sensor. While it is the case that $N \sim 10^3$ can be achieved by considering single photons as opposed to $N = 1000$ number states due to all photons being non-interacting, the problem is that it means νN trials (heralding photons) are required for each of the μ sets within the averaging time of a point on the sensorgram, of say 6 seconds.

This evaluates to $\frac{\mu\nu N}{6} \sim 10^{11}$ photons per second. Regardless of what source may produce such a high rate of photons, current single photon detectors are limited to $\approx 10^7$ detections per second. Thus at present the use of single photons for HIV drug kinetics sensing is unfortunately out of technological reach. Alternative approaches may consider the use of squeezed states, such as TMSD states, which have a higher intensity (larger N) and do not require single-photon detection.

Figure 5.8 is a picture of our actual setup in the quantum optics lab at Stellenbosch University.

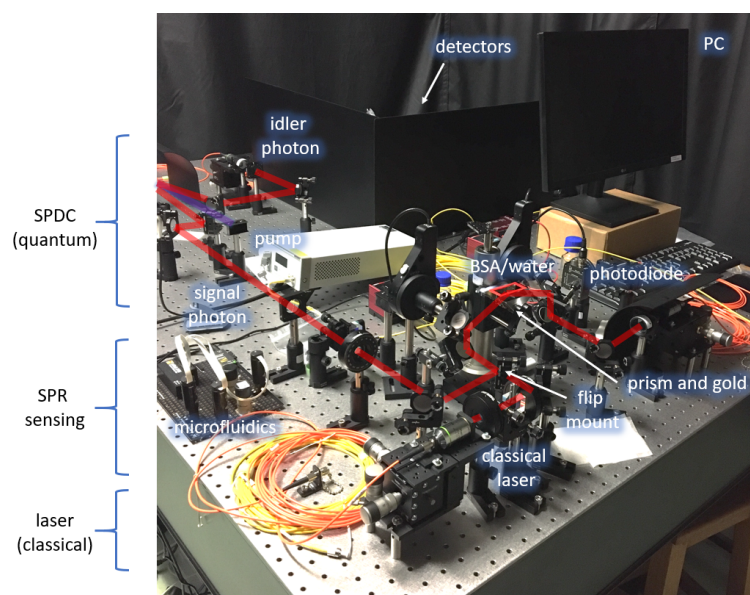


Figure 5.8: Picture of the plasmonic sensing setup and the SPDC single photon source.

Chapter 6

Conclusion

The aim of this thesis was to understand and explore further the use of quantum mechanical systems in metrology and sensing, specifically biochemical sensing. We considered a theoretical implementation of a general intensity-sensing setup and showed that Fock states, which are quantum states of light, allow us to perform measurements with less noise in the measurement. They have a higher detection limit than the classical coherent state. We then showed that when we use these states in an SPR experiment we can extract better estimations of the kinetic parameters from our sensorgrams. Whilst some work has previously been done on quantum plasmonic bio-sensing [30, 35, 36, 38, 39, 97] the novelty in the work proposed in this thesis is that it focuses on kinetics in the Kretschmann configuration using intensity as the sensor signal. In this thesis we looked at the coherent state as the limit of precision in the classical regime, therefore in chapters 3 and 4 when we mention classical states we are really talking about the coherent state. The coherent state allows us to reach the standard quantum limit and therefore it makes sense to make comparisons with it when looking at quantum states. We were interested in understanding how much of an enhancement in precision we would get if we used quantum states compared to the coherent state.

The thesis began by introducing some basic ideas which are important in order to understand the new work which was introduced in chapter 3 of this thesis. Chapter one gave a overview of research in plasmonics. We gave a historical perspective of how research has developed over the past 50 years in the area of plasmonics, specifically in SPR research. We also looked at how applications have been developed in plasmonics, for example with companies like Biacore which have commercialised SPR technologies. SPR is a mature technology and has been shown to be useful in many areas of research.

Chapter 2 was a literature review chapter which looked into plasmonics and metrology and how these two subjects can come together as one and how they become useful for applications in research and industrial technology. We looked at some theory work connected to exciting surface plasmons and how these excited surface plasmons lead themselves to applications in biology and drug kinetics. In chapter 2 we also looked at different states of light and how using quantum states of light allows us to break the shot noise limit set in classical metrology. We also looked at estimation theory, which is an important topic in metrology. We also looked at exciting single photons using SPDC. Lastly we looked at two mode plasmonic sensing, both classical and quantum.

Chapter 3 introduced new work in the field, conducted during the course of my PhD. It was shown that for a two-mode system the Fock state measured data gives the best estimations of parameters, even though it gets worse when we try to optimize for the other quantum states. When we optimize, the TMSV and TMSD give better results than the coherent states, and we observe some enhancement. For the single mode case only the Fock state gave an enhancement in both the Kausaite and Lahiri studies. However we found that in general for cases when our R value is high, the TMSV and TMSD states can also give a better enhancement than the coherent states. However, the sensitivity of the sensor is not as good here and so this range does not provide an overall enhancement

compared to the optimal classical case. So quantum states do in general provide an enhancement in comparison to the coherent state, but we have to be mindful of a situation where some quantum states will not be as useful, such as the particular scenario we considered.

Chapter 4 looked at an application of this work in studying HIV. We looked at showing what happens when a small refractive index change occurs during binding and unbinding of an inhibitor in HIV. In chapter 4 the main conclusion is that the Fock state gives better precision and enhancement in all the cases, especially in the standard two-mode case. The single mode offers a similar enhancement to the optimized case but it is more practical for experiments as only one mode is required. In chapter 4 we wanted to see if the Fock state would still perform better than the coherent state given that the refractive index change is smaller. We find that the Fock state outperforms the coherent state. This is a particular case of interest due to the prevalence of the HIV virus in Africa. The theoretical work here is important because it opens the way for future experimental work in HIV drug kinetics using quantum biosensors.

Chapter 5 looked at experimental work which we did, where we used single photons from an SPDC source to excite SPR. We generated a sensorgram from the binding reaction between BSA and our gold surface and measured the kinetic constant k_s . We found a small enhancement in the precision of the parameter. Although we only observed a small enhancement (due to the low efficiency of our setup), it is sufficient as a proof of concept. We managed to show that using quantum states do give a parameter precision enhancement over classical states. These results lay the foundation for future experimental work. We were only able to get the binding part of our sensorgram due to complications with our fluidics setup, which controls the inflow and outflow of our BSA sample. We struggled with blockages in our setup which we hope to resolve. We also experienced delays in our experimental work due to the closure of our labs during the lock-down period as a result of the Covid-19 pandemic.

The use of quantum states of light was intensively investigated in this thesis with the aim of improving the precision, performance, and limit of detection of SPR biosensors. We showed theoretically that indeed we can achieve an enhancement. Experimentally we showed proof of concept and with better efficiency in our single-photon source we can get a higher precision. There is much promise in this field of research and much to be done before we can fully benefit from the quantum technologies we are developing here. In our future work we will look at signal-to-noise ratios when we use the different quantum states and quantum imaging.

Appendix A

Calculations for phase measurements using NOON and coherent states

We begin our quantum treatment of phase sensing by considering interferometry with NOON states.

A.1 Phase measurements using NOON states

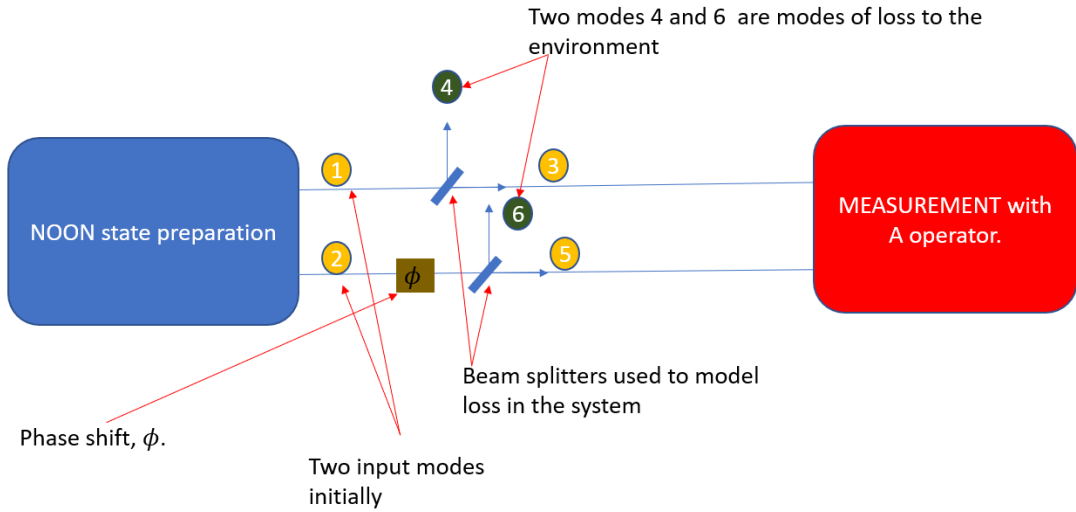


Figure A.1: Theoretical model for two-mode phase sensing using NOON states.

The setup shown above shows the steps in measuring the uncertainty (precision) in the phase added to a NOON state. The first step is to pass the state through a phase shifter to add the phase,

$$\frac{|N\rangle_1 |0\rangle_2 + |0\rangle_1 |N\rangle_2}{\sqrt{2}} \xrightarrow{\mathbf{PS}} \frac{|N\rangle_1 |0\rangle_2 + e^{i\phi N} |0\rangle_1 |N\rangle_2}{\sqrt{2}}. \quad (\text{A.1})$$

Where N is the number of photons in a particular mode, \mathbf{PS} , stands for phase shifter and ϕ is the phase. In the Heisenberg picture, the above NOON state can be expressed as shown below,

$$\frac{|N\rangle_1 |0\rangle_2 + e^{i\phi N} |0\rangle_1 |N\rangle_2}{\sqrt{2}} = \frac{(a_1^\dagger)^N |0\rangle_1 |0\rangle_2 + e^{i\phi N} (a_2^\dagger)^N |0\rangle_1 |0\rangle_2}{\sqrt{2N!}}, \quad (\text{A.2})$$

where

$$\hat{a}_1^\dagger = \eta_1^{\frac{1}{2}} \hat{a}_3^\dagger + i(1 - \eta_1)^{\frac{1}{2}} \hat{a}_4^\dagger \quad (\text{A.3})$$

and

$$\hat{a}_2^\dagger = \eta_2^{\frac{1}{2}} \hat{a}_5^\dagger + i(1 - \eta_2)^{\frac{1}{2}} \hat{a}_6^\dagger. \quad (\text{A.4})$$

Substituting the above equations into Eq. (A.2) we get

$$\frac{(\eta_1^{\frac{1}{2}} \hat{a}_3^\dagger + i(1 - \eta_1)^{\frac{1}{2}} \hat{a}_4^\dagger)^N |0\rangle_3 |0\rangle_4 |0\rangle_5 |0\rangle_6 + e^{i\phi N} (\eta_2^{\frac{1}{2}} \hat{a}_5^\dagger + i(1 - \eta_2)^{\frac{1}{2}} \hat{a}_6^\dagger)^N |0\rangle_3 |0\rangle_4 |0\rangle_5 |0\rangle_6}{\sqrt{2N!}}. \quad (\text{A.5})$$

We want to resolve each part of the sum individually so we label the two parts of the equation part 1 and part 2,

$$\text{Part1} = \frac{(\eta_1^{\frac{1}{2}} \hat{a}_3^\dagger + i(1 - \eta_1)^{\frac{1}{2}} \hat{a}_4^\dagger)^N |0\rangle_3 |0\rangle_4 |0\rangle_5 |0\rangle_6}{\sqrt{2N!}}. \quad (\text{A.6})$$

Using the binomial theorem we can rewrite the above expression, part 1 can be written as $(x + y)^N = \sum_{k=0}^N \binom{N}{k} x^{N-k} y^k$

$$\text{Part1} = \frac{1}{\sqrt{2N!}} \sum_{k=0}^N \binom{N}{k} (\eta_1^{\frac{1}{2}} \hat{a}_3^\dagger)^{N-k} (i(1 - \eta_1)^{\frac{1}{2}} \hat{a}_4^\dagger)^k |0\rangle_3 |0\rangle_4 |0\rangle_5 |0\rangle_6, \quad (\text{A.7})$$

$$= \frac{1}{\sqrt{2N!}} \sum_{k=0}^N \binom{N}{k} \eta_1^{\frac{N-k}{2}} (\hat{a}_3^\dagger)^{N-k} i^k (1 - \eta_1)^{\frac{k}{2}} (\hat{a}_4^\dagger)^k |0\rangle_3 |0\rangle_4 |0\rangle_5 |0\rangle_6, \quad (\text{A.8})$$

$$\text{Part2} = \frac{e^{iN\phi}}{\sqrt{2N!}} \sum_{k=0}^N \binom{N}{k} \eta_2^{\frac{N-k}{2}} (\hat{a}_5^\dagger)^{N-k} i^k (1 - \eta_2)^{\frac{k}{2}} (\hat{a}_6^\dagger)^k |0\rangle_3 |0\rangle_4 |0\rangle_5 |0\rangle_6. \quad (\text{A.9})$$

The measurement operator \hat{A} is defined as

$$\hat{A}_{\text{NOON}} = |N\rangle_3 |0\rangle_5 \langle 0|_3 \langle N|_5 + |0\rangle_3 |N\rangle_5 \langle N|_3 \langle 0|_5, \quad (\text{A.10})$$

$$\begin{aligned} \langle \hat{A}_{\text{NOON}} \rangle &= \langle 0|_3 \langle 0|_4 \langle 0|_5 \langle 0|_6 \left(\frac{1}{\sqrt{2N!}} \sum_{k=0}^N \binom{N}{k} \eta_1^{\frac{N-k}{2}} (\hat{a}_3^\dagger)^{N-k} (-1)^k i^k (1 - \eta_1)^{\frac{k}{2}} (\hat{a}_4^\dagger)^k + \right. \\ &\frac{e^{-iN\phi}}{\sqrt{2N!}} \sum_{k=0}^N \binom{N}{k} \eta_2^{\frac{N-k}{2}} (\hat{a}_5^\dagger)^{N-k} (-1)^k i^k (1 - \eta_2)^{\frac{k}{2}} (\hat{a}_6^\dagger)^k \rangle \langle N|_3 |0\rangle_5 \langle 0|_3 \langle N|_5 + |0\rangle_3 |N\rangle_5 \langle N|_3 \langle 0|_5 \\ &\left. \left(\frac{1}{\sqrt{2N!}} \sum_{k=0}^N \binom{N}{k} \eta_1^{\frac{N-k}{2}} (\hat{a}_3^\dagger)^{N-k} i^k (1 - \eta_1)^{\frac{k}{2}} (\hat{a}_4^\dagger)^k + \frac{e^{iN\phi}}{\sqrt{2N!}} \sum_{k=0}^N \binom{N}{k} \eta_2^{\frac{N-k}{2}} (\hat{a}_5^\dagger)^{N-k} i^k (1 - \eta_2)^{\frac{k}{2}} (\hat{a}_6^\dagger)^k \right) \right. \\ &\left. |0\rangle_3 |0\rangle_4 |0\rangle_5 |0\rangle_6 \right). \end{aligned}$$

The above expression can be simplified to the expression below, the reduction in the expression is due to the fact that there are specific states that remain, i.e., the ‘N’ photon and the ‘0’ photon state when we take the measurement whereas the rest vanish. We thus have

$$\begin{aligned} \langle \hat{A}_{\text{NOON}} \rangle &= \frac{1}{2} \left(\binom{N}{0} \eta_1^{\frac{N}{2}} \langle N|_3 \langle 0|_4 \langle 0|_5 \langle 0|_6 + e^{-iN\phi} \binom{N}{0} \eta_2^{\frac{N}{2}} \langle 0|_3 \langle 0|_4 \langle N|_5 \langle 0|_6 \right) \\ &(|N\rangle_3 |0\rangle_5 \langle 0|_3 \langle N|_5 + |0\rangle_3 |N\rangle_5 \langle 0|_3 \langle 0|_5) \left(\binom{N}{0} \eta_1^{\frac{N}{2}} |N\rangle_3 |0\rangle_4 |0\rangle_5 |0\rangle_6 + e^{iN\phi} \binom{N}{0} \eta_2^{\frac{N}{2}} |0\rangle_3 |0\rangle_4 |N\rangle_5 |0\rangle_6 \right). \end{aligned}$$

This simplifies to

$$\langle \hat{A}_{\text{NOON}} \rangle = \frac{\eta_1^{\frac{N}{2}} \eta_2^{\frac{N}{2}} e^{iN\phi} + \eta_1^{\frac{N}{2}} \eta_2^{\frac{N}{2}} e^{-iN\phi}}{2}, \quad (\text{A.11})$$

which simplifies to

$$\langle \hat{A}_{\text{NOON}} \rangle = (\eta_1 \eta_2)^{\frac{N}{2}} \cos(N\phi). \quad (\text{A.12})$$

The next step is to calculate $\langle \hat{A}_{\text{NOON}}^2 \rangle$

$$\langle \hat{A}_{\text{NOON}}^2 \rangle = |N\rangle_3 |0\rangle_5 \langle N|_3 \langle 0|_5 + |0\rangle_3 |N\rangle_5 \langle 0|_3 \langle N|_5 \quad (\text{A.13})$$

$$\begin{aligned} \langle \hat{A}_{\text{NOON}}^2 \rangle &= \langle 0|_3 \langle 0|_4 \langle 0|_5 \langle 0|_6 \left(\frac{1}{\sqrt{2N!}} \sum_{k=0}^N \binom{N}{k} \eta_1^{\frac{N-k}{2}} (\hat{a}_3)^{N-k} (-1)^k i^k (1-\eta_1)^{\frac{k}{2}} (\hat{a}_4)^k + \right. \\ &\frac{e^{-iN\phi}}{\sqrt{2N!}} \sum_{k=0}^N \binom{N}{k} \eta_2^{\frac{N-k}{2}} (\hat{a}_5)^{N-k} (-1)^k i^k (1-\eta_2)^{\frac{k}{2}} (|N\rangle_3 |0\rangle_5 \langle N|_3 \langle 0|_5 + |0\rangle_3 |N\rangle_5 \langle 0|_3 \langle N|_5) \\ &\left. \left(\frac{1}{\sqrt{2N!}} \sum_{k=0}^N \binom{N}{k} \eta_1^{\frac{N-k}{2}} (\hat{a}_3^\dagger)^{N-k} i^k (1-\eta_1)^{\frac{k}{2}} (\hat{a}_4^\dagger)^k + \frac{e^{iN\phi}}{\sqrt{2N!}} \sum_{k=0}^N \binom{N}{k} \eta_2^{\frac{N-k}{2}} (\hat{a}_5^\dagger)^{N-k} i^k (1-\eta_2)^{\frac{k}{2}} (\hat{a}_6^\dagger)^k \right) \right. \\ &\left. |0\rangle_3 |0\rangle_4 |0\rangle_5 |0\rangle_6 \right). \end{aligned}$$

The surviving terms are

$$\begin{aligned} \langle \hat{A}_{\text{NOON}}^2 \rangle &= \frac{1}{2} \left(\binom{N}{0} \eta_1^{\frac{N}{2}} \langle N|_3 \langle 0|_4 \langle 0|_5 \langle 0|_6 + e^{-iN\phi} \binom{N}{0} \eta_2^{\frac{N}{2}} \langle 0|_3 \langle 0|_4 \langle N|_5 \langle 0|_6 \right) \\ &(|N\rangle_3 |0\rangle_5 \langle N|_3 \langle 0|_5 + |0\rangle_3 |N\rangle_5 \langle 0|_3 \langle N|_5) \left(\binom{N}{0} \eta_1^{\frac{N}{2}} |N\rangle_3 |0\rangle_4 |0\rangle_5 |0\rangle_6 + e^{iN\phi} \binom{N}{0} \eta_2^{\frac{N}{2}} \right. \\ &\left. |0\rangle_3 |0\rangle_4 |N\rangle_5 |0\rangle_6 \right). \end{aligned}$$

From which it follows

$$\langle \hat{A}_{\text{NOON}}^2 \rangle = \frac{\eta_1^N + \eta_2^N}{2}. \quad (\text{A.14})$$

The next step is to calculate $\langle \Delta \hat{A}_{\text{NOON}} \rangle$, which is defined as

$$\langle \Delta \hat{A}_{\text{NOON}} \rangle = \sqrt{\langle \hat{A}_{\text{NOON}}^2 \rangle - \langle \hat{A}_{\text{NOON}} \rangle^2}, \quad (\text{A.15})$$

$$\langle \Delta \hat{A}_{\text{NOON}} \rangle = \sqrt{\frac{\eta_1^N + \eta_2^N}{2} - (\eta_1 \eta_2)^N \cos^2(N\phi)}. \quad (\text{A.16})$$

It follows that

$$\Delta\phi = \langle \Delta \hat{A}_{\text{NOON}} \rangle \left| \frac{\partial \langle \Delta \hat{A}_{\text{NOON}} \rangle}{\partial \phi} \right|^{-1} = \frac{\sqrt{\frac{\eta_1^N + \eta_2^N}{2} - (\eta_1 \eta_2)^N \cos^2(N\phi)}}{N(\eta_1 \eta_2)^{\frac{N}{2}} |\sin(N\phi)|}. \quad (\text{A.17})$$

The above is a general solution, however we can start to make assumptions to see the effect they have. If we assume one mode has more loss than the other we can set $\eta_1 = \eta$ and $\eta_2 = 1$, from which it follows that

$$\Delta\phi = \frac{\sqrt{\frac{(\eta)^N + 1}{2} - (\eta)^N \cos^2(N\phi)}}{N(\eta)^{\frac{N}{2}} |\sin(N\phi)|}. \quad (\text{A.18})$$

We can find the minimum possible value for $\Delta\phi$ by setting $N\phi = \frac{\pi}{2}$. This leads to [85]

$$\Delta\phi_{\min} = \frac{\sqrt{(1 + \eta^{-N})/2}}{N}. \quad (\text{A.19})$$

If instead we had set $\eta_1 = \eta_2 = \eta$ then

$$\Delta\phi_{\min} = \frac{1}{\eta^{\frac{N}{2}} N}. \quad (\text{A.20})$$

A.1.1 Optimizing the quantum case

In this case we start with a N00N state with unbalanced weights, i.e.,

$$\sqrt{a_N} |N\rangle_1 |0\rangle_2 + \sqrt{a_0} |0\rangle_1 |N\rangle_2. \quad (\text{A.21})$$

Where $a_0 = \frac{\eta_2^{\frac{N}{2}}}{\eta_1^{\frac{N}{2}} + \eta_2^{\frac{N}{2}}}$ and $a_N = 1 - a_0$. The calculation follows the procedure of the balanced N00N state so to avoid repetition we skip to the expectation value of \hat{A} , i.e., $\langle \hat{A} \rangle$,

$$\langle \hat{A} \rangle = 2\sqrt{a_0}\sqrt{a_N}\eta_1^{\frac{N}{2}}\eta_2^{\frac{N}{2}}\cos N\phi. \quad (\text{A.22})$$

Similarly the calculation for $\langle \hat{A}^2 \rangle$, follows as for the balanced weights case so we skip straight to the solution given below

$$\langle \hat{A}^2 \rangle = a_0\eta_1^N + a_N\eta_2^N. \quad (\text{A.23})$$

The next step is to calculate $\langle \Delta \hat{A}_{\text{NOON}} \rangle$ which is defined as

$$\langle \Delta \hat{A}_{\text{NOON}} \rangle = \sqrt{\langle \hat{A}^2_{\text{NOON}} \rangle - \langle \hat{A}_{\text{NOON}} \rangle^2}. \quad (\text{A.24})$$

$$\langle \Delta \hat{A}_{\text{NOON}} \rangle = \sqrt{a_0\eta_1^N + a_N\eta_2^N - (2\sqrt{a_0}\sqrt{a_N}\eta_1^{\frac{N}{2}}\eta_2^{\frac{N}{2}}\cos N\phi)^2}, \quad (\text{A.25})$$

which gives

$$\Delta\phi = \frac{\sqrt{a_0\eta_1^N + a_N\eta_2^N - (2\sqrt{a_0}\sqrt{a_N}\eta_1^{\frac{N}{2}}\eta_2^{\frac{N}{2}}\cos N\phi)^2}}{2N\sqrt{a_0}\sqrt{a_N}\eta_1^{\frac{N}{2}}\eta_2^{\frac{N}{2}}\sin N\phi}. \quad (\text{A.26})$$

We can simplify further by substituting a_0 and a_N above and setting $\phi = \frac{\pi}{2}$ from which we get

$$\Delta\phi = \frac{\sqrt{\frac{\eta_2^{\frac{N}{2}}}{\eta_1^{\frac{N}{2}} + \eta_2^{\frac{N}{2}}}\eta_1^N + \frac{\eta_1^{\frac{N}{2}}}{\eta_1^{\frac{N}{2}} + \eta_2^{\frac{N}{2}}}\eta_2^N}}{2N\sqrt{\frac{\eta_2^{\frac{N}{2}}}{\eta_1^{\frac{N}{2}} + \eta_2^{\frac{N}{2}}}\sqrt{\frac{\eta_1^{\frac{N}{2}}}{\eta_1^{\frac{N}{2}} + \eta_2^{\frac{N}{2}}}\eta_1^{\frac{N}{2}}\eta_2^{\frac{N}{2}}}}}. \quad (\text{A.27})$$

This can be reduced to

$$\Delta\phi = \frac{\eta_1^{\frac{N}{2}} + \eta_2^{\frac{N}{2}}}{2N(\eta_1\eta_2)^{\frac{N}{2}}}. \quad (\text{A.28})$$

If we consider loss in one arm thus set $\eta_1 = 1$ and $\eta_2 = \eta$. It follows that

$$\Delta\phi_{\min} = \frac{1 + \eta^{\frac{N}{2}}}{2N\eta^{\frac{N}{2}}}, \quad (\text{A.29})$$

which reduces to

$$\Delta\phi_{\min} = \frac{1 + \eta^{-\frac{N}{2}}}{2N}. \quad (\text{A.30})$$

This is the optimised result found in Demkowicz-Dobrzanski et al. [85].

A.2 Phase measurements using coherent states

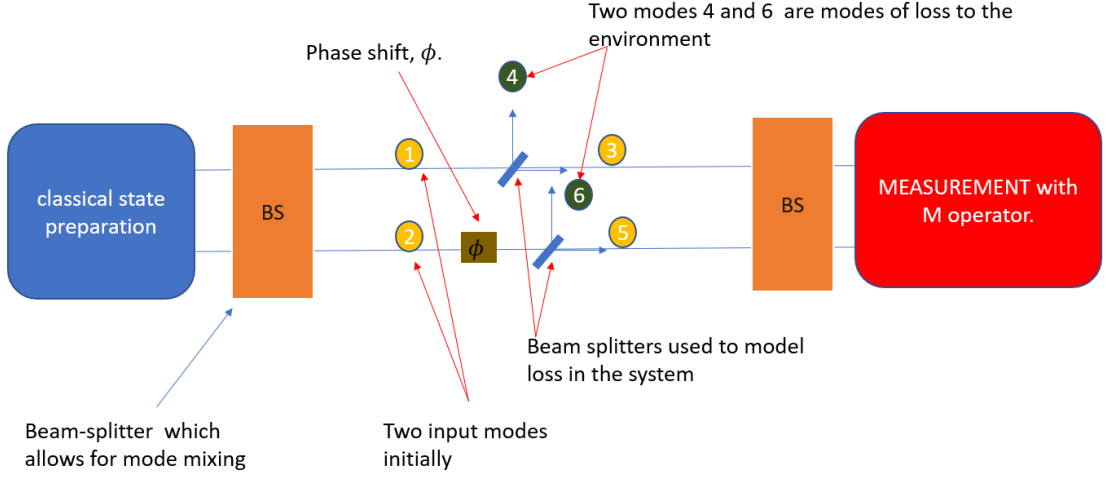


Figure A.2: Theoretical model for two-mode phase sensing using coherent states.

We start with the input states $\left|\frac{\alpha}{\sqrt{2}}\right\rangle_1$ and $\left|\frac{i\alpha}{\sqrt{2}}\right\rangle_2$. The first input mode goes through a phase shifter, PS_1 , to give

$$\left|\frac{\alpha}{\sqrt{2}}\right\rangle_1 \left|\frac{i\alpha}{\sqrt{2}}\right\rangle_2 \xrightarrow{PS_1} \left|\frac{e^{i\phi}\alpha}{\sqrt{2}}\right\rangle_1 \left|\frac{i\alpha}{\sqrt{2}}\right\rangle_2. \quad (\text{A.31})$$

For easier reading we relabel $|\alpha'\rangle = \left|\frac{e^{i\phi}\alpha}{\sqrt{2}}\right\rangle_1$ and $|\alpha''\rangle = \left|\frac{i\alpha}{\sqrt{2}}\right\rangle_2$. The beam splitters after the phase shifter model loss in system and hence we introduce loss modes as shown below

$$|\alpha'\rangle_1 = \left|\eta_1^{\frac{1}{2}}\alpha'\right\rangle_3 \left|(1-\eta_1)^{\frac{1}{2}}i\alpha'\right\rangle_4, \quad (\text{A.32})$$

and

$$|\alpha''\rangle_2 = \left|\eta_2^{\frac{1}{2}}\alpha''\right\rangle_5 \left|(1-\eta_2)^{\frac{1}{2}}i\alpha''\right\rangle_6. \quad (\text{A.33})$$

It follows that

$$|\alpha'\rangle_1 |\alpha''\rangle_2 \xrightarrow{\text{loss}} \left|\eta_1^{\frac{1}{2}}\alpha'\right\rangle_3 \left|(1-\eta_1)^{\frac{1}{2}}i\alpha'\right\rangle_4 \left|\eta_2^{\frac{1}{2}}\alpha''\right\rangle_5 \left|(1-\eta_2)^{\frac{1}{2}}i\alpha''\right\rangle_6 \quad (\text{A.34})$$

Substituting back $\alpha' = \frac{e^{i\phi}\alpha}{\sqrt{2}}$ and $\alpha'' = \frac{i\alpha}{\sqrt{2}}$ it follows that the output is

$$\left|\eta_1^{\frac{1}{2}}\frac{e^{i\phi}\alpha}{\sqrt{2}}\right\rangle_3 \left|(1-\eta_1)^{\frac{1}{2}}i\frac{e^{i\phi}\alpha}{\sqrt{2}}\right\rangle_4 \left|\eta_2^{\frac{1}{2}}\frac{i\alpha}{\sqrt{2}}\right\rangle_5 \left|(1-\eta_2)^{\frac{1}{2}}i\frac{i\alpha}{\sqrt{2}}\right\rangle_6. \quad (\text{A.35})$$

Applying a beam splitter to the above state we get

$$\xrightarrow{BS} \left|\frac{(\eta_1^{\frac{1}{2}}e^{i\phi}\frac{\alpha}{\sqrt{2}} - \eta_2^{\frac{1}{2}}\frac{\alpha}{\sqrt{2}})}{\sqrt{2}}\right\rangle_3 \left|(1-\eta_1)^{\frac{1}{2}}i\frac{e^{i\phi}\alpha}{\sqrt{2}}\right\rangle_4 \left|\frac{(\eta_1^{\frac{1}{2}}ie^{i\phi}\frac{\alpha}{\sqrt{2}} + \eta_2^{\frac{1}{2}}\frac{i\alpha}{\sqrt{2}})}{\sqrt{2}}\right\rangle_5 \left|(1-\eta_2)^{\frac{1}{2}}i\frac{i\alpha}{\sqrt{2}}\right\rangle_6. \quad (\text{A.36})$$

The next step is to calculate, $\langle \hat{n}_3 \rangle$, which we do as shown below

$$\langle \hat{n}_3 \rangle = \text{Tr}_{3456}(\hat{n}_3 \otimes \mathbb{1}_{456}\rho), \quad (\text{A.37})$$

which is equivalent to

$$\langle \hat{n}_3 \rangle = \langle \psi_{\text{out}} | \hat{n}_3 \otimes \mathbb{1}_{456} | \psi_{\text{out}} \rangle. \quad (\text{A.38})$$

We then have

$$\begin{aligned} \langle \hat{n}_3 \rangle &= \left\langle \left. \frac{(\eta_1^{\frac{1}{2}} e^{i\phi} \frac{\alpha}{\sqrt{2}} - \eta_2^{\frac{1}{2}} \frac{\alpha}{\sqrt{2}})}{\sqrt{2}} \right| \hat{a}_3^\dagger \hat{a}_3 \left. \frac{(\eta_1^{\frac{1}{2}} e^{i\phi} \frac{\alpha}{\sqrt{2}} - \eta_2^{\frac{1}{2}} \frac{\alpha}{\sqrt{2}})}{\sqrt{2}} \right\rangle_3 \left\langle \left. (1 - \eta_1)^{\frac{1}{2}} i \frac{e^{i\phi} \alpha}{\sqrt{2}} \right| \mathbb{1} \left. (1 - \eta_1)^{\frac{1}{2}} i \frac{e^{i\phi} \alpha}{\sqrt{2}} \right\rangle_4 \\ &\left\langle \left. \frac{(\eta_1^{\frac{1}{2}} i e^{i\phi} \frac{\alpha}{\sqrt{2}} + \eta_2^{\frac{1}{2}} \frac{\alpha i}{\sqrt{2}})}{\sqrt{2}} \right| \mathbb{1} \left. \frac{(\eta_1^{\frac{1}{2}} i e^{i\phi} \frac{\alpha}{\sqrt{2}} + \eta_2^{\frac{1}{2}} \frac{\alpha i}{\sqrt{2}})}{\sqrt{2}} \right\rangle_5 \left\langle \left. (1 - \eta_2)^{\frac{1}{2}} i \frac{i\alpha}{\sqrt{2}} \right| \mathbb{1} \left. (1 - \eta_2)^{\frac{1}{2}} i \frac{i\alpha}{\sqrt{2}} \right\rangle_6. \end{aligned}$$

This reduces to

$$\langle \hat{n}_3 \rangle = \frac{|\alpha|^2}{4} (\eta_1 + \eta_2 - 2\eta_1^{\frac{1}{2}} \eta_2^{\frac{1}{2}} \cos\phi). \quad (\text{A.39})$$

Calculating, $\langle \hat{n}_5 \rangle$, follows a similar procedure, so we will just skip to final result

$$\langle \hat{n}_5 \rangle = \frac{|\alpha|^2}{4} (\eta_1 + \eta_2 + 2\eta_1^{\frac{1}{2}} \eta_2^{\frac{1}{2}} \cos\phi). \quad (\text{A.40})$$

Calculating, $\langle \hat{M} \rangle = \langle \hat{n}_5 \rangle - \langle \hat{n}_3 \rangle$, we get

$$\langle \hat{n}_5 \rangle - \langle \hat{n}_3 \rangle = \frac{|\alpha|^2}{4} (\eta_1 + \eta_2 + 2\eta_1^{\frac{1}{2}} \eta_2^{\frac{1}{2}} \cos\phi) - \frac{|\alpha|^2}{4} (\eta_1 + \eta_2 - 2\eta_1^{\frac{1}{2}} \eta_2^{\frac{1}{2}} \cos\phi). \quad (\text{A.41})$$

$$= |\alpha|^2 \eta_1^{\frac{1}{2}} \eta_2^{\frac{1}{2}} \cos\phi. \quad (\text{A.42})$$

Next we calculate, $\langle \hat{M} \rangle^2$

$$\langle \hat{M} \rangle^2 = (|\alpha|^2 \eta_1^{\frac{1}{2}} \eta_2^{\frac{1}{2}} \cos\phi)^2. \quad (\text{A.43})$$

Next we calculate, $\langle \hat{M}^2 \rangle = \langle (\hat{a}_5^\dagger \hat{a}_5 - \hat{a}_3^\dagger \hat{a}_3)^2 \rangle$

$$\langle \hat{M}^2 \rangle = \left(\frac{|\alpha|}{2}\right)^4 16|\alpha|^2 \eta_1^{\frac{1}{2}} \eta_2^{\frac{1}{2}} \cos^2\phi + 2\left(\frac{|\alpha|}{2}\right)^2 (\eta_1 + \eta_2). \quad (\text{A.44})$$

Then we calculate, $\langle \Delta \hat{M} \rangle = \sqrt{\langle \hat{M}^2 \rangle - \langle \hat{M} \rangle^2}$. This reduces to

$$\langle \Delta \hat{M} \rangle = \sqrt{\left(\frac{|\alpha|}{2}\right)^4 16|\alpha|^2 \eta_1^{\frac{1}{2}} \eta_2^{\frac{1}{2}} \cos^2\phi - (|\alpha|^2 \eta_1^{\frac{1}{2}} \eta_2^{\frac{1}{2}} \cos\phi)^2 + 2\left(\frac{|\alpha|}{2}\right)^2 (\eta_1 + \eta_2)}. \quad (\text{A.45})$$

$$= \sqrt{\frac{1}{2} |\alpha|^2 (\eta_1 + \eta_2)}. \quad (\text{A.46})$$

Next we calculate, $\frac{\partial \langle \hat{M} \rangle}{\partial \phi}$,

$$\frac{\partial \langle \hat{M} \rangle}{\partial \phi} = |\alpha|^2 (\eta_1 \eta_2)^{\frac{1}{2}} \sin\phi. \quad (\text{A.47})$$

Then we calculate $\Delta\phi = \frac{\langle \Delta \hat{M} \rangle}{\left| \frac{\partial \langle \hat{M} \rangle}{\partial \phi} \right|}$ for $\phi = \frac{\pi}{2}$

$$\Delta\phi = \frac{\langle \Delta\hat{M} \rangle}{|\frac{\partial \langle \hat{M} \rangle}{\partial \phi}|} = \frac{\sqrt{\frac{1}{2}|\alpha|^2(\eta_1 + \eta_2)}}{|\alpha|^2(\eta_1\eta_2)^{\frac{1}{2}}}. \quad (\text{A.48})$$

When, $\eta_1 = \eta_2 = 1$, i.e., there is no loss then $\Delta\phi = \frac{1}{\sqrt{N}}$. We can find the minimum possible value for, $\Delta\phi$, by setting $\phi = \frac{\pi}{2}$ and this gives us

$$\Delta\phi_{\min} = \frac{\sqrt{\frac{1}{2}(\eta_1 + \eta_2)}}{|\alpha|\eta_1^{\frac{1}{2}}\eta_2^{\frac{1}{2}}}. \quad (\text{A.49})$$

We can optimize the classical case to get a better result of $\Delta\phi$ as shown in the next section.

A.2.1 Optimizing the classical case

Starting of with the general expression for $\Delta\phi$ in the classical case

$$\Delta\phi = \frac{(\sqrt{\frac{1}{2}|\alpha|^2}(\eta_1 + \eta_2))}{|\alpha|^2\eta_1^{\frac{1}{2}}\eta_2^{\frac{1}{2}}|\sin\phi|}. \quad (\text{A.50})$$

We can substitute, $\eta_1 = k_1T$ and $\eta_2 = k_2(1 - T)$, where, T , is a weighting on the beam splitter in mode 1 and k_1, k_2 are rational numbers. Substituting these into $\Delta\phi$, we get

$$\Delta\phi_{\min} = \frac{\sqrt{\frac{1}{2}(k_1T + k_2(1 - T))}}{|\alpha|k_1^{\frac{1}{2}}T^{\frac{1}{2}}k_2^{\frac{1}{2}}(1 - T)^{\frac{1}{2}}}. \quad (\text{A.51})$$

We go on to make another substitution $T = \frac{\sqrt{k_2}}{\sqrt{k_2} + \sqrt{k_1}}$

$$\Delta\phi_{\min} = \frac{\sqrt{\frac{1}{2}(k_1\frac{\sqrt{k_2}}{\sqrt{k_2} + \sqrt{k_1}} + k_2(1 - \frac{\sqrt{k_2}}{\sqrt{k_2} + \sqrt{k_1}}))}}{|\alpha|k_1^{\frac{1}{2}}\frac{\sqrt{k_2}}{\sqrt{k_2} + \sqrt{k_1}}^{\frac{1}{2}}k_2^{\frac{1}{2}}(1 - \frac{\sqrt{k_2}}{\sqrt{k_2} + \sqrt{k_1}})^{\frac{1}{2}}}. \quad (\text{A.52})$$

The above expression can be simplified to

$$\Delta\phi_{\min} = \frac{\sqrt{k_2} + \sqrt{k_1}}{2\sqrt{Nk_1k_2}}. \quad (\text{A.53})$$

This is the optimal state in Demkowicz-Dobrzanski et al. [85]. If we consider loss in one arm then we have, $k_1 = 1, k_2 = \eta$, it follows that

$$\Delta\phi_{\min} = \frac{\sqrt{1} + \sqrt{\eta}}{2\sqrt{N\eta}}. \quad (\text{A.54})$$

Appendix B

Calculation of the precision for a two-mode squeezed displaced vacuum state

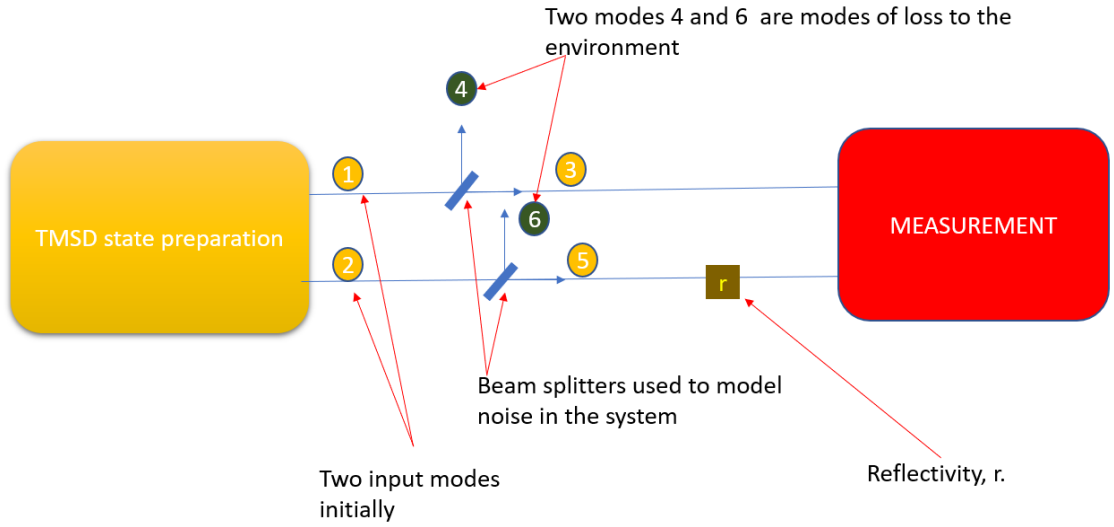


Figure B.1: Theoretical model for 2 mode intensity sensing.

The two-mode squeezed displaced state (TMSD) is defined as $|\text{TMSD}\rangle = \hat{S}_{12}(\chi) |0\rangle_1 |\alpha\rangle_2$, where $\hat{S}_{12}(\chi) = e^{(\chi^* \hat{a}_1 \hat{a}_2 - \chi \hat{a}_1^\dagger \hat{a}_2^\dagger)}$ with $\chi = |\chi| e^{i\theta}$. The goal of this section is to calculate the term $\langle \hat{\Delta M} \rangle$ which from the general form derived in section 2.5.2 equals

$$[\langle (\hat{a}_1^\dagger \hat{a}_1)^2 \rangle + \langle (\hat{a}_2^\dagger \hat{a}_2)^2 \rangle - 2\langle \hat{a}_1^\dagger \hat{a}_1 \hat{a}_2^\dagger \hat{a}_2 \rangle - (\langle \hat{a}_2^\dagger \hat{a}_2 \rangle - \langle \hat{a}_1^\dagger \hat{a}_1 \rangle)^2]^{\frac{1}{2}}, \quad (\text{B.1})$$

when $\eta_a = \eta_b = |r|^2 = 1$. We start off by calculating, $\langle \hat{a}_1^\dagger \hat{a}_1 \rangle$, which is given by

$$\langle \hat{a}_1^\dagger \hat{a}_1 \rangle = \langle 0|_2 \langle \alpha|_1 \hat{S}^\dagger \hat{a}_1^\dagger \hat{a}_1 \hat{S} |\alpha\rangle_1 |0\rangle_2 \quad (\text{B.2})$$

$$= \langle 0|_2 \langle \alpha|_1 \hat{S}^\dagger \hat{a}_1^\dagger \hat{S} \hat{S}^\dagger \hat{a}_1 \hat{S} |\alpha\rangle_1 |0\rangle_2. \quad (\text{B.3})$$

We have that $\hat{S}^\dagger \hat{a}_1^\dagger \hat{S} = \cosh(|\chi|) \hat{a}_1^\dagger + \hat{a}_2 \sinh(|\chi|) e^{-i\theta}$ and $\hat{S}^\dagger \hat{a}_1 \hat{S} = \cosh(|\chi|) \hat{a}_1 + \hat{a}_2^\dagger \sinh(|\chi|) e^{i\theta}$. So we substitute these in the equation above to get

$$= \langle 0|_2 \langle \alpha|_1 (\cosh(|\chi|) \hat{a}_1^\dagger + \hat{a}_2 \sinh(|\chi|) e^{-i\theta}) (\cosh(|\chi|) \hat{a}_1 + \hat{a}_2^\dagger \sinh(|\chi|) e^{i\theta}) |\alpha\rangle_1 |0\rangle_2. \quad (\text{B.4})$$

A lot of mixed terms come out but they all vanish. the terms which remain are

$$= \cosh^2(|\chi|) \langle 0|_2 \langle \alpha|_1 \hat{a}_1^\dagger \hat{a}_1 |\alpha\rangle_1 |0\rangle_2 + \sinh^2(|\chi|) \langle 0|_2 \langle \alpha|_1 \hat{a}_2 \hat{a}_2^\dagger |\alpha\rangle_1 |0\rangle_2. \quad (\text{B.5})$$

We can apply normal ordering to the second term to get

$$\sinh^2(|\chi|) \langle 0|_2 \langle \alpha|_1 \hat{a}_2 \hat{a}_2^\dagger |\alpha\rangle_1 |0\rangle_2 = \sinh^2(|\chi|) \langle 0|_2 \langle \alpha|_1 (\hat{a}_2^\dagger \hat{a}_2 + 1) |\alpha\rangle_1 |0\rangle_2. \quad (\text{B.6})$$

The final result is

$$\boxed{\langle \hat{a}_1^\dagger \hat{a}_1 \rangle = \cosh^2(|\chi|) |\alpha|^2 + \sinh^2(|\chi|)}. \quad (\text{B.7})$$

The next step is to calculate, $\langle \hat{a}_2^\dagger \hat{a}_2 \rangle$, which is given by

$$= \langle 0|_2 \langle \alpha|_1 \hat{S}^\dagger \hat{a}_2^\dagger \hat{S} \hat{S}^\dagger \hat{a}_2 \hat{S} |\alpha\rangle_1 |0\rangle_2. \quad (\text{B.8})$$

We have that $\hat{S}^\dagger \hat{a}_2^\dagger \hat{S} = \cosh(|\chi|) \hat{a}_2^\dagger + \hat{a}_1 \sinh(|\chi|) e^{-i\theta}$ and $\hat{S}^\dagger \hat{a}_2 \hat{S} = \cosh(|\chi|) \hat{a}_2 + \hat{a}_1^\dagger \sinh(|\chi|) e^{i\theta}$. So we substitute these in the equation above to get

$$= \langle 0|_2 \langle \alpha|_1 (\cosh(|\chi|) \hat{a}_2^\dagger + \hat{a}_1 \sinh(|\chi|) e^{-i\theta}) (\cosh(|\chi|) \hat{a}_2 + \hat{a}_1^\dagger \sinh(|\chi|) e^{i\theta}) |\alpha\rangle_1 |0\rangle_2. \quad (\text{B.9})$$

A lot of mixed terms come out but they all vanish. The terms which remain are

$$= \cosh^2(|\chi|) \langle 0|_2 \langle \alpha|_1 \hat{a}_2^\dagger \hat{a}_2 |\alpha\rangle_1 |0\rangle_2 + \sinh^2(|\chi|) \langle 0|_2 \langle \alpha|_1 \hat{a}_1 \hat{a}_1^\dagger |\alpha\rangle_1 |0\rangle_2. \quad (\text{B.10})$$

We can apply normal ordering to the second term and get

$$\sinh^2(|\chi|) \langle 0|_2 \langle \alpha|_1 \hat{a}_1 \hat{a}_1^\dagger |\alpha\rangle_1 |0\rangle_2 = \sinh^2(|\chi|) \langle 0|_2 \langle \alpha|_1 (\hat{a}_1^\dagger \hat{a}_1 + 1) |\alpha\rangle_1 |0\rangle_2. \quad (\text{B.11})$$

The final result is

$$\boxed{\langle \hat{a}_2^\dagger \hat{a}_2 \rangle = \sinh^2(|\chi|) |\alpha|^2 + \sinh^2(|\chi|)}. \quad (\text{B.12})$$

The resulting equation for $\langle \hat{M} \rangle = \langle \hat{a}_2^\dagger \hat{a}_2 \rangle - \langle \hat{a}_1^\dagger \hat{a}_1 \rangle$ when we include the loss terms η_1 and η_2 is $\langle \hat{M} \rangle = |r|^2 \eta_2^2 \langle \hat{a}_2^\dagger \hat{a}_2 \rangle - \eta_1^2 \langle \hat{a}_1^\dagger \hat{a}_1 \rangle$

$$\langle \hat{a}_2^\dagger \hat{a}_2 \rangle - \langle \hat{a}_1^\dagger \hat{a}_1 \rangle = |r|^2 \eta_2^2 (\sinh^2(|\chi|) |\alpha|^2 + \sinh^2(|\chi|)) - \eta_1^2 (\cosh^2(|\chi|) |\alpha|^2 + \sinh^2(|\chi|)). \quad (\text{B.13})$$

The next step is to calculate $\langle (\hat{a}_1^\dagger \hat{a}_1)^2 \rangle = \langle \hat{a}_1^\dagger \hat{a}_1 \hat{a}_1^\dagger \hat{a}_1 \rangle$. With normal ordering this becomes $\langle (\hat{a}_1^\dagger \hat{a}_1)^2 \rangle = \langle \hat{a}_1^\dagger \hat{a}_1^\dagger \hat{a}_1 \hat{a}_1 + \hat{a}_1^\dagger \hat{a}_1 \rangle$. We will start off by calculating, $\langle \hat{a}_1^\dagger \hat{a}_1^\dagger \hat{a}_1 \hat{a}_1 \rangle$, which is

$$\begin{aligned} \langle \hat{a}_1^\dagger \hat{a}_1^\dagger \hat{a}_1 \hat{a}_1 \rangle &= \langle [\cosh(|\chi|) \hat{a}_1^\dagger + \hat{a}_2 \sinh(|\chi|) e^{-i\theta}] \times [\cosh(|\chi|) \hat{a}_1^\dagger + \hat{a}_2 \sinh(|\chi|) e^{-i\theta}] \\ &\times [\cosh(|\chi|) \hat{a}_1 + \hat{a}_2^\dagger \sinh(|\chi|) e^{i\theta}] \times [\cosh(|\chi|) \hat{a}_1 + \hat{a}_2^\dagger \sinh(|\chi|) e^{i\theta}] \rangle. \end{aligned}$$

The calculation is rather long, with the final result for the calculation is given below

$$\boxed{\langle \hat{a}_1^\dagger \hat{a}_1^\dagger \hat{a}_1 \hat{a}_1 \rangle = \cosh^4(|\chi|) |\alpha|^4 + 4|\alpha|^2 \sinh^2(|\chi|) \cosh^2(|\chi|) + 2\sinh^4(|\chi|)} \quad (\text{B.14})$$

We do a similar thing to calculate $\langle (\hat{a}_2^\dagger \hat{a}_2)^2 \rangle = \langle \hat{a}_2^\dagger \hat{a}_2 \hat{a}_2^\dagger \hat{a}_2 \rangle$. With normal ordering this becomes $\langle (\hat{a}_2^\dagger \hat{a}_2)^2 \rangle = \langle \hat{a}_2^\dagger \hat{a}_2^\dagger \hat{a}_2 \hat{a}_2 + \hat{a}_2^\dagger \hat{a}_2 \rangle$. We will start off by calculating, $\langle \hat{a}_2^\dagger \hat{a}_2^\dagger \hat{a}_2 \hat{a}_2 \rangle$, which is

$$\begin{aligned} \langle \hat{a}_2^\dagger \hat{a}_2^\dagger \hat{a}_2 \hat{a}_2 \rangle &= \langle [\cosh(|\chi|) \hat{a}_2^\dagger + \hat{a}_1 \sinh(|\chi|) e^{-i\theta}] \times [\cosh(|\chi|) \hat{a}_2^\dagger + \hat{a}_1 \sinh(|\chi|) e^{-i\theta}] \\ &\times [\cosh(|\chi|) \hat{a}_2 + \hat{a}_1^\dagger \sinh(|\chi|) e^{i\theta}] \times [\cosh(|\chi|) \hat{a}_2 + \hat{a}_1^\dagger \sinh(|\chi|) e^{i\theta}] \rangle. \end{aligned}$$

The calculation is rather long, with the final result for the calculation given below

$$\boxed{\langle \hat{a}_2^\dagger \hat{a}_2^\dagger \hat{a}_2 \hat{a}_2 \rangle = \sinh^4(|\chi|) |\alpha|^4 + 4|\alpha|^2 \sinh^4(|\chi|) + 2\sinh^4(|\chi|)}. \quad (\text{B.15})$$

The next step is to calculate $\langle \hat{a}_1^\dagger \hat{a}_1 \hat{a}_2^\dagger \hat{a}_2 \rangle$. We can rewrite the expression as

$$\langle \hat{a}_1^\dagger \hat{a}_1 \hat{a}_2^\dagger \hat{a}_2 \rangle = \langle \hat{S}^\dagger \hat{a}_1^\dagger \hat{S} \hat{S}^\dagger \hat{a}_1 \hat{S} \hat{S}^\dagger \hat{a}_2 \hat{S} \rangle. \quad (\text{B.16})$$

It follows that

$$\begin{aligned} \langle \hat{a}_1^\dagger \hat{a}_1 \hat{a}_2^\dagger \hat{a}_2 \rangle &= \langle [\cosh(|\chi|) \hat{a}_1^\dagger + \hat{a}_2 \sinh(|\chi|) e^{-i\theta}] \times [\cosh(|\chi|) \hat{a}_1 + \hat{a}_2^\dagger \sinh(|\chi|) e^{i\theta}] \\ &\times [\cosh(|\chi|) \hat{a}_2^\dagger + \hat{a}_1 \sinh(|\chi|) e^{-i\theta}] \times [\cosh(|\chi|) \hat{a}_2 + \hat{a}_1^\dagger \sinh(|\chi|) e^{i\theta}] \rangle. \end{aligned}$$

The calculation is rather long, with the result given below

$$\boxed{\langle \hat{a}_1^\dagger \hat{a}_1 \hat{a}_2^\dagger \hat{a}_2 \rangle = \cosh^2(|\chi|) \sinh^2(|\chi|) (|\alpha|^4 + |\alpha|^2 + 2|\alpha| + 1) + \sinh^4(|\chi|) (|\alpha|^2 + 1)}. \quad (\text{B.17})$$

The next step is to calculate $\langle \Delta \hat{M} \rangle$ by combining the terms as shown here

$$\langle \Delta \hat{M} \rangle = [(\langle \hat{a}_1^\dagger \hat{a}_1 \rangle^2) + (\langle \hat{a}_2^\dagger \hat{a}_2 \rangle^2) - 2\langle \hat{a}_1^\dagger \hat{a}_1 \hat{a}_2^\dagger \hat{a}_2 \rangle - (\langle \hat{a}_2^\dagger \hat{a}_2 \rangle - \langle \hat{a}_1^\dagger \hat{a}_1 \rangle^2)]^{\frac{1}{2}}. \quad (\text{B.18})$$

When we include the loss terms see section 2.25

$$\begin{aligned} \langle \Delta \hat{M} \rangle &= [|\text{r}|^4 \eta_1^4 (\cosh^4(|\chi|) |\alpha|^4 + 4|\alpha|^2 \sinh^2(|\chi|) \cosh^2(|\chi|) + 2\sinh^4(|\chi|)) + \text{r}^2 \eta_1^2 (\cosh^2(|\chi|) |\alpha|^2 + \sinh^2(|\chi|)) \\ &+ \eta_2^4 (\sinh^4(|\chi|) |\alpha|^4 + 4|\alpha|^2 \sinh^4(|\chi|) + 2\sinh^4(|\chi|)) + \eta_2^2 (\sinh^2(|\chi|) |\alpha|^2 + \sinh^2(|\chi|)) \\ &- 2|\text{r}|^2 \eta_1^2 \eta_2^2 (\cosh^2(|\chi|) \sinh^2(|\chi|) (|\alpha|^4 + |\alpha|^2 + 2|\alpha| + 1) + \sinh^4(|\chi|) (|\alpha|^2 + 1)) \\ &- [\eta_2^2 (\sinh^2(|\chi|) |\alpha|^2 + \sinh^2(|\chi|)) - |\text{r}|^2 \eta_1^2 (\cosh^2(|\chi|) |\alpha|^2 + \sinh^2(|\chi|))]^{\frac{1}{2}}. \end{aligned}$$

This simplifies to

$$\begin{aligned} \langle \Delta \hat{M} \rangle &= [2|\text{r}|^4 \eta_1^4 \cosh^2(|\chi|) \sinh^2(|\chi|) |\alpha|^2 + |\text{r}|^4 \eta_1^4 \sinh^4(|\chi|) \\ &+ |\text{r}|^2 \eta_1^2 (\cosh^2(|\chi|) |\alpha|^2 + \sinh^2(|\chi|)) + 2\eta_2^4 \sinh^4(|\chi|) |\alpha|^2 + \eta_2^4 \sinh^4(|\chi|) \\ &+ \eta_2^2 (\sinh^2(|\chi|) |\alpha|^2 + \sinh^2(|\chi|)) - 4|\text{r}|^2 \eta_1^2 \eta_2^2 |\alpha|^2 \cosh^2(|\chi|) \sinh^2(|\chi|) - 2\text{r}^2 \eta_1^2 \eta_2^2 \cosh^2(|\chi|) \sinh^2(|\chi|)]^{\frac{1}{2}}. \end{aligned}$$

By substituting, $\sinh^2(|\chi|) = \text{G}$, $\cosh^2(|\chi|) = \text{G} - 1$, $|\text{r}|^2 = \text{T}$, $\eta_1 = \eta_a^{\frac{1}{2}}$ and $\eta_2 = \eta_b^{\frac{1}{2}}$ we get the result.

$$\begin{aligned} \langle \Delta \hat{M} \rangle_{\text{TMSD}} &= [2\text{T}^2 \text{G} (\text{G} - 1) \eta_a^2 |\alpha|^2 + \text{T}^2 \text{G} \eta_a^2 (\text{G} - 1)^2 + \text{T} \eta_a (\text{G} |\alpha|^2 + (\text{G} - 1)) + 2\eta_b^2 \\ &(\text{G} - 1)^2 |\alpha|^2 + \eta_b^2 (\text{G} - 1)^2 + \eta_b ((\text{G} - 1) |\alpha|^2 + (\text{G} - 1)) - 4\text{T} \eta_a \eta_b \text{G} (\text{G} - 1) |\alpha|^2 \\ &- 2\text{T} \eta_a \eta_b \text{G} (\text{G} - 1)]^{\frac{1}{2}}. \end{aligned}$$

Appendix C

Two-dimensional and three-dimensional plots in quantum surface plasmon sensing

In SPR sensing the measured reflectivity, R , is a function of the incident angle, θ , as well as a function of the changing refractive index, n , on the surface of the gold. We can thus construct a three-dimensional model to show how R would vary with changes in both θ and n , as shown in Figure C.1. The plots used here are from a sensing setup in which the laser light had a wavelength of 810nm and the gold on the slide was 50nm thick and we made it using Eq. (2.34).

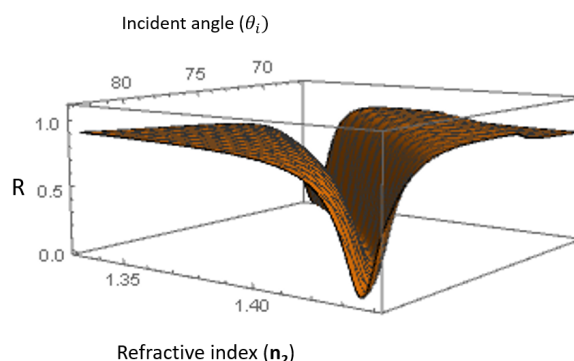


Figure C.1: SPR dip with refractive index of both the dielectric material and incident angle.

When we fix the incident angle θ and change the refractive index then we have the two dimensional representation shown in Figure C.2. We can also fix the refractive index and change the incident angle θ , then we will have the two-dimensional representation shown in Figure C.3. We have already seen this previously, but a clarification can be useful. We are also interested in the derivative of the reflectivity with respect to the incident angle and with respect to the refractive index. These are important in calculating the sensitivity of the setup. The sensitivity with respect to n is shown in Figure C.4.

We can make a three-dimensional plot for the derivative of the reflectivity R as well, since R depends on θ and n . The three-dimensional plot is shown in Figure C.5.

In order to compare the performance of the different types of SPR sensors, we define a general formula for the sensitivity of the sensor in response to changes in the refractive index of the sensitive layer, Δn , as

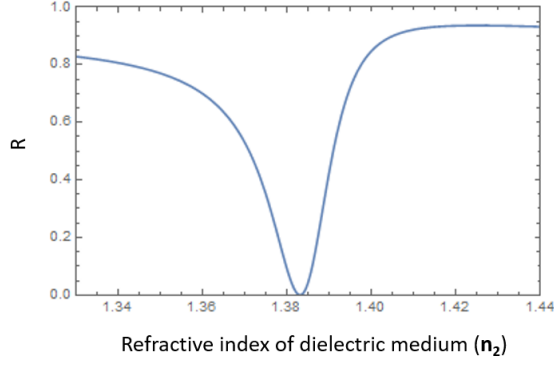


Figure C.2: SPR dip with changing refractive index of the dielectric material and incident angle fixed.

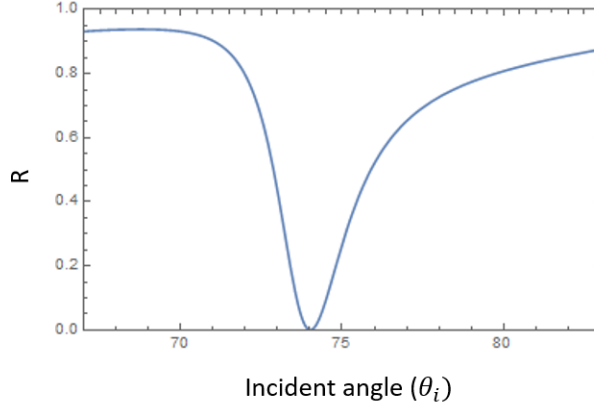


Figure C.3: SPR dip with fixed refractive index of the dielectric material and incident angle changing.

$$\Delta S = \frac{\Delta Q}{\Delta n}. \quad (\text{C.1})$$

Here Q can be any of the quantities $(\lambda_{\text{spr}}, \Theta_{\text{spr}}, R_{\text{spr}}, \phi_{\text{spr}})$.

In Figure C.6 and C.7 we look at the inflection point $n_{\text{analyte}}^{\text{inf}}$, which is a point at which the sensitivity is maximized. It is presented against an incidence angle in a range from 65.5° to 83.5° . Furthermore, the estimation precisions for the product coherent, twin Fock, and TMSV states are calculated at the inflection point given according to θ in Figure C.6. This follows from work done in Ref. [30].

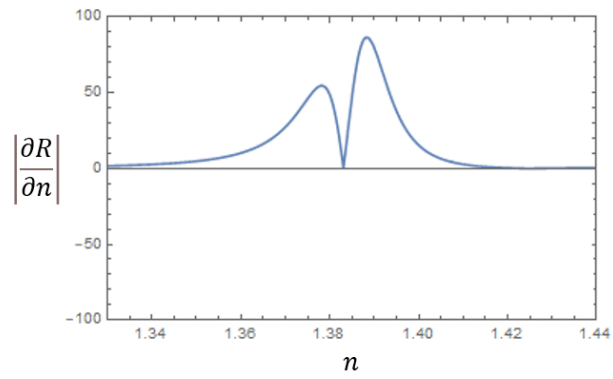


Figure C.4: Derivative of reflectivity, R , with respect to refractive index.

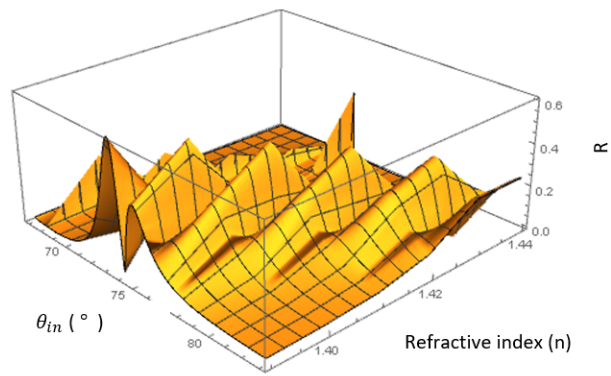


Figure C.5: Three-dimensional plot for the derivative of the reflectivity, R .

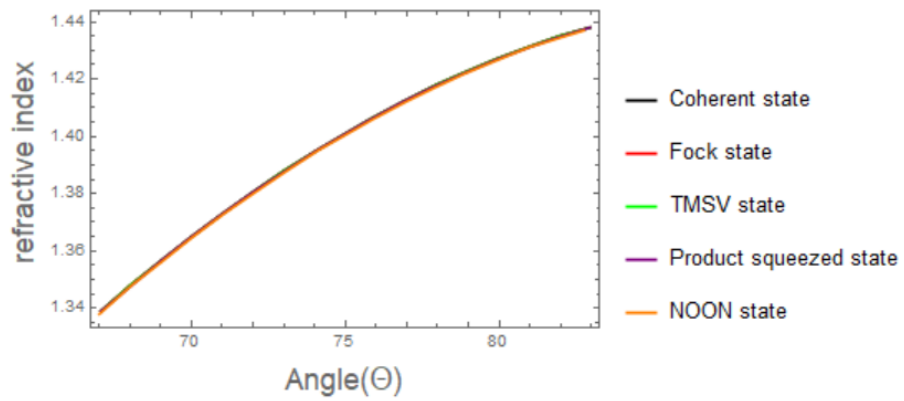


Figure C.6: Inflection point at which the sensitivity is maximized for different states.

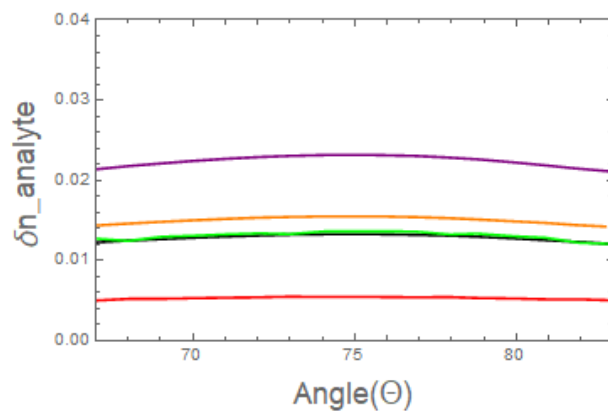


Figure C.7: Inflection point at which the estimate precision is minimized for different states.

Appendix D

General formula for the noise reduction in a two-mode system

We are often interested in measuring the classicality or non-classicality of a state and the answer to this often comes from looking at photon statistics. A factor called the Mandel Q parameter [71], can be used to measure the non-classicality of a state. Another factor called the Fano factor, F, can also be used to achieve the same purpose. The Fano factor can be written out mathematically as, $F = \frac{\langle \Delta \hat{n}^2 \rangle}{\langle \hat{n} \rangle}$ and the Mandel Q parameter is defined as

$$Q = \frac{\langle \Delta \hat{n}^2 \rangle - \langle \hat{n} \rangle}{\langle \hat{n} \rangle} = F - 1. \quad (\text{D.1})$$

The value of the Fano factor $F = 1$ or $Q = 0$ establishes a bound between classical and non-classical photon statistics. For classical states the value of F is lower bounded by unity, i.e., if $F \geq 1$, then we classify our state as being a classical state. Non-classical states can have F values in the range $0 \leq F < 1$, this corresponds to Q values in the range $-1 \leq Q < 0$. Losses in the detection process, i.e., including both losses in the optical path and the detector quantum efficiency, affect the statistics of a state and cause a deterioration in the F value as shown below

$$F_{\text{det}} = \eta F + 1 - \eta. \quad (\text{D.2})$$

Where η represents optical losses. It follows that in the presence of losses the lower bound for a non-classical state is $F_{\text{det}} = 1 - \eta$.

We can look at two-mode non-classical statistics. The degree of correlation between two-modes can be quantified and their non-classical features can therefore be quantified. We do this by defining the noise reduction factor (NRF), σ , is defined mathematically as

$$\sigma = \frac{\langle [\Delta(\hat{n}_1 - \hat{n}_2)]^2 \rangle}{\langle \hat{n}_1 + \hat{n}_2 \rangle} = \frac{\langle \Delta \hat{n}_1^2 \rangle + \langle \Delta \hat{n}_2^2 \rangle - 2\langle \Delta \hat{n}_1^2 \Delta \hat{n}_2^2 \rangle}{\langle \hat{n}_1 + \hat{n}_2 \rangle}. \quad (\text{D.3})$$

This is a ratio between the variance of the difference in the number of photons and the noise of two coherent states of equivalent energies [32]. The shot-noise level is given by the sum of the shot noise of the two-modes, $\langle \hat{n}_1 + \hat{n}_2 \rangle$. Non-classical bipartite states can have σ values in the range $0 \leq \sigma < 1$ and classical bipartite states have, $\sigma \geq 1$.

Here we will look at some general notation used in the calculations to follow and let $\hat{n}_a \rightarrow \hat{n}_{a_{\text{in}}}$ and $\hat{n}_b \rightarrow \hat{n}_{b_{\text{in}}}$, we then have

$$\langle \Delta \hat{n}_{a_{\text{in}}}^2 \rangle = \langle \hat{a}^\dagger \hat{a} \hat{a}^\dagger \hat{a} \rangle - \langle \hat{a}^\dagger \hat{a} \rangle^2, \quad (\text{D.4})$$

and

$$\langle \Delta \hat{n}_{b_{\text{in}}}^2 \rangle = \langle \hat{b}^\dagger \hat{b} \hat{b}^\dagger \hat{b} \rangle - \langle \hat{b}^\dagger \hat{b} \rangle^2, \quad (\text{D.5})$$

and

$$\langle \Delta \hat{n}_{\text{a}_{\text{in}}}^2 \Delta \hat{n}_{\text{b}_{\text{in}}}^2 \rangle = \langle \hat{a}^\dagger \hat{a} \hat{b}^\dagger \hat{b} \rangle - \langle \hat{a}^\dagger \hat{a} \rangle \langle \hat{b}^\dagger \hat{b} \rangle. \quad (\text{D.6})$$

It follows that for a two-mode state with N photons on average in each mode we have

$$\langle \hat{n}_{\text{a}_{\text{in}}} \rangle = \langle \hat{n}_{\text{b}_{\text{in}}} \rangle = N, \quad (\text{D.7})$$

and

$$\langle \Delta \hat{n}_{\text{a}_{\text{in}}}^2 \rangle = (Q + 1) \langle \hat{n}_{\text{a}_{\text{in}}} \rangle = (Q + 1)N, \quad (\text{D.8})$$

and

$$\langle [\Delta(\hat{n}_{\text{a}_{\text{in}}} - \hat{n}_{\text{b}_{\text{in}}})]^2 \rangle = (\langle \hat{n}_{\text{b}_{\text{in}}} \rangle + \langle \hat{n}_{\text{a}_{\text{in}}} \rangle) \sigma = 2N\sigma. \quad (\text{D.9})$$

Using Eqs.(D.6-D.8) above we can write the general equation for $\langle \Delta \hat{M} \rangle$, in terms of the Mandel factor Q and the noise reduction factor σ . The equation to write is

$$\begin{aligned} \langle \Delta \hat{M} \rangle = & [|r|^4 \eta_a^4 \langle \psi_{\text{in}} | \hat{a}_{\text{in}}^\dagger (\hat{a}_{\text{in}}^\dagger \hat{a}_{\text{in}}) \hat{a}_{\text{in}} | \psi_{\text{in}} \rangle + |r|^2 \eta_a^2 \langle \psi_{\text{in}} | \hat{a}_{\text{in}}^\dagger \hat{a}_{\text{in}} | \psi_{\text{in}} \rangle + \eta_b^4 \langle \psi_{\text{in}} | \hat{b}_{\text{in}}^\dagger (\hat{b}_{\text{in}}^\dagger \hat{b}_{\text{in}}) \hat{b}_{\text{in}} | \psi_{\text{in}} \rangle + \\ & \eta_b^2 \langle \psi_{\text{in}} | \hat{b}_{\text{in}}^\dagger \hat{b}_{\text{in}} | \psi_{\text{in}} \rangle + 2|r|^2 \eta_a^2 \eta_b^2 \langle \psi_{\text{in}} | \hat{a}_{\text{in}}^\dagger \hat{a}_{\text{in}} | \psi_{\text{in}} \rangle \langle \psi_{\text{in}} | \hat{b}_{\text{in}}^\dagger \hat{b}_{\text{in}} | \psi_{\text{in}} \rangle - (|r|^4 \eta_a^4 \langle \psi_{\text{in}} | \hat{a}_{\text{in}}^\dagger \hat{a}_{\text{in}} | \psi_{\text{in}} \rangle^2 \\ & + \eta_b^4 \langle \psi_{\text{in}} | \hat{b}_{\text{in}}^\dagger \hat{b}_{\text{in}} | \psi_{\text{in}} \rangle^2 - 2|r|^2 \eta_a^2 \eta_b^2 \langle \psi_{\text{in}} | \hat{a}_{\text{in}}^\dagger \hat{a}_{\text{in}} | \psi_{\text{in}} \rangle \langle \psi_{\text{in}} | \hat{b}_{\text{in}}^\dagger \hat{b}_{\text{in}} | \psi_{\text{in}} \rangle)]^{\frac{1}{2}}, \end{aligned}$$

which reduces to

$$\begin{aligned} \langle \Delta \hat{M} \rangle = & [\eta_b^4 (\langle \psi_{\text{in}} | \Delta \hat{n}_{\text{b}_{\text{in}}}^2 | \psi_{\text{in}} \rangle)^2 + \eta_b^2 (1 - \eta_b^2) (\langle \psi_{\text{in}} | \hat{n}_{\text{b}_{\text{in}}} | \psi_{\text{in}} \rangle) + |r|^4 \eta_a^4 (\langle \psi_{\text{in}} | \Delta \hat{n}_{\text{a}_{\text{in}}} | \psi_{\text{in}} \rangle)^2 \\ & + |r|^2 \eta_a^2 (1 - |r|^2 \eta_a^2) (\langle \psi_{\text{in}} | \hat{n}_{\text{a}_{\text{in}}} | \psi_{\text{in}} \rangle) + |r|^2 \eta_a^2 \eta_b^2 (\langle \psi_{\text{in}} | \Delta(\hat{n}_{\text{b}_{\text{in}}} - \hat{n}_{\text{a}_{\text{in}}}) | \psi_{\text{in}} \rangle)^2 \\ & - |r|^2 \eta_a^2 \eta_b^2 (\langle \psi_{\text{in}} | \Delta \hat{n}_{\text{a}_{\text{in}}} | \psi_{\text{in}} \rangle)^2 - |r|^2 \eta_a^2 \eta_b^2 (\langle \psi_{\text{in}} | \Delta \hat{n}_{\text{b}_{\text{in}}} | \psi_{\text{in}} \rangle)^2]]^{\frac{1}{2}}. \end{aligned}$$

Substituting the above expressions we get

$$\langle \Delta \hat{M} \rangle = [\eta_b^4 (Q + 1)N + (\eta_b^2 - \eta_b^4)N + |r|^4 \eta_a^4 (Q + 1)N + (|r|^2 \eta_a^2 - |r|^4 \eta_a^4)N + 2|r|^2 \eta_a^2 \eta_b^2 \sigma - 2|r|^2 \eta_a^2 \eta_b^2 (Q + 1)N]^{\frac{1}{2}}. \quad (\text{D.10})$$

This reduces to

$$\langle \Delta \hat{M} \rangle = N^{\frac{1}{2}} [(\eta_b^2 - |r|^2 \eta_a^2)^2 Q + 2|r|^2 \eta_a^2 \eta_b^2 \sigma + \eta_b^2 + |r|^2 \eta_a^2 (1 - 2\eta_b^2)]^{\frac{1}{2}}. \quad (\text{D.11})$$

Appendix E

Noise ratio (Noise reduction factor)

Here we show the ratio $\frac{\langle \hat{\Delta M}_{\text{quantum}} \rangle}{\langle \hat{\Delta M}_{\text{classical}} \rangle}$ varies with changing $|\alpha|^2$ values. We begin by replacing $|\alpha|^2$ with T for simplicity and write out the ratios,

$$\frac{\langle \hat{\Delta M}_{\text{Fock}} \rangle}{\langle \hat{\Delta M}_{\text{coherent}} \rangle} = \frac{-T^2\eta_a^2 + T\eta_a + \eta_b - \eta_b^2}{T\eta_a + \eta_b}. \quad (\text{E.1})$$

$$\frac{\langle \hat{\Delta M}_{\text{TMSV}} \rangle}{\langle \hat{\Delta M}_{\text{coherent}} \rangle} = \frac{(T^2\eta_a^2 + \eta_b^2 - 2T\eta_a\eta_b)(G|\alpha|^2 + G - 1) + \eta_b + T\eta_a(1 - 2\eta_b)}{T\eta_a + \eta_b}. \quad (\text{E.2})$$

$$\begin{aligned} \frac{\langle \hat{\Delta M}_{\text{TMSD}} \rangle}{\langle \hat{\Delta M}_{\text{coherent}} \rangle} &= (2T^2\eta_a^2G(G-1)|\alpha|^2 + T^2\eta_a^2(G-1)^2 + T\eta_a(G|\alpha|^2 + G - 1) + \\ &2\eta_b^2(G-1)^2|\alpha|^2 + \eta_b^2(G-1)^2 + \eta_b((G-1)|\alpha|^2 + G - 1) - 4T\eta_a\eta_bG(G-1)|\alpha|^2 - \\ &2T\eta_a\eta_bG(G-1))/(T\eta_a + \eta_b). \end{aligned}$$

$$\frac{\langle \hat{\Delta M}_{\text{Product-squeezed}} \rangle}{\langle \hat{\Delta M}_{\text{coherent}} \rangle} = \frac{(\eta_b - T\eta_a)(G|\alpha|^2 + G) + 2T\eta_a\eta_b(G|\alpha|^2 + G) + \eta_b + T\eta_a(1 - 2\eta_b)}{T\eta_b + \eta_b}. \quad (\text{E.3})$$

$$\frac{\langle \hat{\Delta M}_{\text{NOON}} \rangle}{\langle \hat{\Delta M}_{\text{coherent}} \rangle} = \frac{(\eta_b - T\eta_a)(G|\alpha|^2 + G - 1) + 4T\eta_a\eta_b(G|\alpha|^2 + G - 1) + \eta_b + T\eta_a(1 - 2\eta_b)}{T\eta_a + \eta_b}. \quad (\text{E.4})$$

Where G is the gain, and η_a and η_b are measures of loss in arms a and b of the two-mode setup. We set $G = 4.5$ and plot in Figures(E.1-E.3) these relationships for different values of loss, i.e., η_a and η_b values.

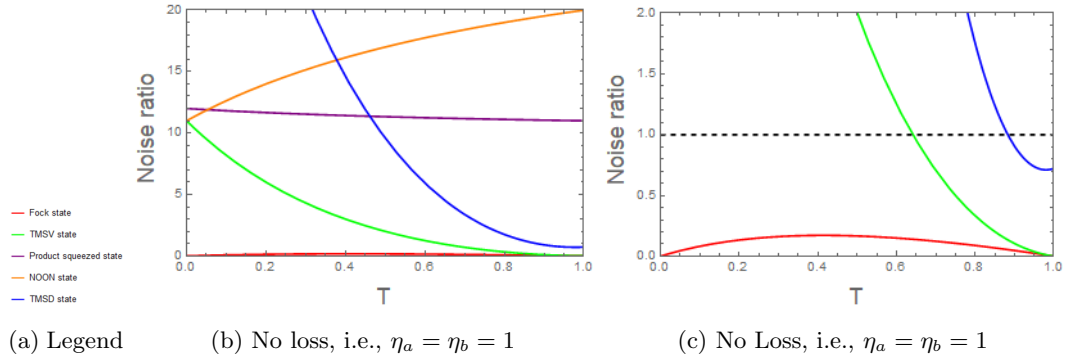


Figure E.1: Plot (a) shows the legend for the different states. Plots (b) and (c) show how the ratios for the different states vary with changing T values. Plot (b) shows the general behaviour whilst (c) shows the region where the quantum states beat the coherent state, i.e., the ratio values < 1 .

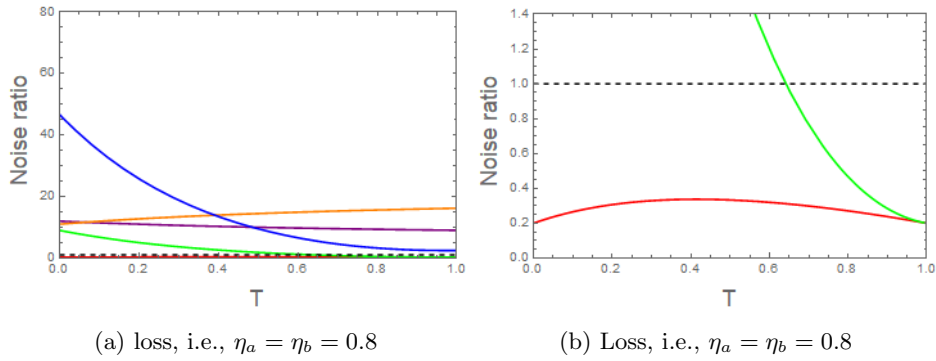


Figure E.2: Plots (a) and (b) show how the ratios for the different states vary with changing T values. Plot (a) shows the general behavior whilst (b) shows the region where the quantum states beat the coherent state, i.e., the ratio values < 1 .

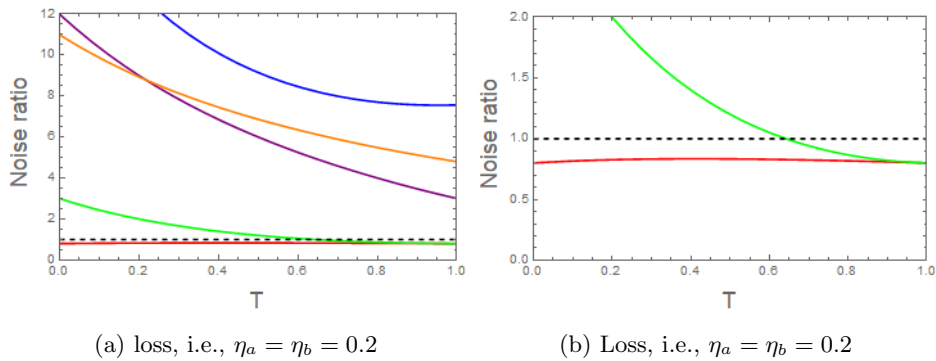


Figure E.3: Plots (a) and (b) show how the ratios for the different states vary with changing T values. Plot (a) shows the general behavior whilst (b) shows the region where the quantum states beat the coherent state, i.e., the ratio values < 1 .

Appendix F

Inferring a parameter from a quantum observable

If we wish to approximate a parameter, θ , of some observable, \mathbf{O} , we can construct an estimate of this parameter, say, $\tilde{\theta}$, which is built on a single outcome and thus corresponds to a function of the random variable, $\mathbf{O} : \tilde{\theta}(\mathbf{O})$. If we assume that \mathbf{O} fluctuates in a region around its mean, such that $\Delta\mathbf{O} \ll 1$, then we can locally Taylor expand $\tilde{\theta}$ to the first order around $\langle\mathbf{O}\rangle$ [53]

$$\tilde{\theta}(\mathbf{O}) = \tilde{\theta}(\langle\mathbf{O}\rangle) + \frac{\partial\tilde{\theta}}{\partial\mathbf{O}}(\mathbf{O} - \langle\mathbf{O}\rangle) + \dots \quad (\text{F.1})$$

If we truncate Eq. (F.1) to the first-order term, we can rearrange terms such that we have $\tilde{\theta}(\mathbf{O}) - \tilde{\theta}(\langle\mathbf{O}\rangle) = \Delta\tilde{\theta}$ and we already have $\mathbf{O} - \langle\mathbf{O}\rangle = \Delta\mathbf{O}$. By making these substitutions into Eq. (F.1) we obtain the error-propagation formula shown below

$$\boxed{\Delta\tilde{\theta} = \frac{\Delta\mathbf{O}}{\left|\frac{\partial\tilde{\theta}}{\partial\mathbf{O}}\right|}} \quad (\text{F.2})$$

The above equation is called the error-propagation formula and it quantifies the fluctuations of our parameter estimate, $\tilde{\theta}(\mathbf{O})$, around the true value of the parameter, θ . It quantifies the noise or uncertainty in the measured parameters which arises due to the stochasticity of the observable measurement.

Appendix G

From the Heisenberg picture to the Schrödinger picture

In the Schrödinger picture, the states change and the operators remain the same

$$|\psi(t)\rangle = \hat{U} |\psi(0)\rangle. \quad (\text{G.1})$$

where $|\psi(0)\rangle$ is the input state and $|\psi(t)\rangle$ is the output state. Hence the operator $\hat{O}(t) = \hat{O}(0) = \hat{O}$.

In the Heisenberg picture the opposite is true, the states remain the same and whilst the operators change

$$|\psi(t)\rangle = |\psi(0)\rangle = |\psi\rangle. \quad (\text{G.2})$$

where $|\psi(0)\rangle$ is the input state and $|\psi(t)\rangle$ is the output state. Hence the operator $\hat{O}(t) = \hat{U}^\dagger \hat{O}(0) \hat{U}$.

Appendix H

Calculating $\langle \hat{a}_{\text{out}}^\dagger \hat{a}_{\text{out}} \rangle$ used in the general formula for $\langle \Delta \hat{M} \rangle$

We start with

$$\hat{a}_{\text{out}}^\dagger = r\eta_a \hat{a}_{\text{in}}^\dagger + \hat{f}_a^\dagger. \quad (\text{H.1})$$

Then

$$\hat{a}_{\text{out}} = |r\eta_a \hat{a}_{\text{in}} + \hat{f}_a. \quad (\text{H.2})$$

It follows that

$$\hat{a}_{\text{out}}^\dagger \hat{a}_{\text{out}} = (r\eta_a \hat{a}_{\text{in}}^\dagger + \hat{f}_a^\dagger)(r\eta_a \hat{a}_{\text{in}} + \hat{f}_a). \quad (\text{H.3})$$

$$\hat{a}_{\text{out}}^\dagger \hat{a}_{\text{out}} = |r|^2 \eta_a^2 \hat{a}_{\text{in}}^\dagger \hat{a}_{\text{in}} + r\eta_a \hat{a}_{\text{in}}^\dagger \hat{f}_a + r\eta_a \hat{a}_{\text{in}} \hat{f}_a^\dagger + \hat{f}_a^\dagger \hat{f}_a. \quad (\text{H.4})$$

Next we will calculate

$$\hat{a}_{\text{out}}^\dagger \hat{a}_{\text{out}}^\dagger \hat{a}_{\text{out}} \hat{a}_{\text{out}} = (r\eta_a \hat{a}_{\text{in}}^\dagger + \hat{f}_a^\dagger)(|r|^2 \eta_a^2 \hat{a}_{\text{in}}^\dagger \hat{a}_{\text{in}} + |r\eta_a \hat{a}_{\text{in}}^\dagger \hat{f}_a + r\eta_a \hat{a}_{\text{in}} \hat{f}_a^\dagger + \hat{f}_a^\dagger \hat{f}_a)(r\eta_a \hat{a}_{\text{in}} + \hat{f}_a). \quad (\text{H.5})$$

This expands to

$$\begin{aligned} \hat{a}_{\text{out}}^\dagger \hat{a}_{\text{out}}^\dagger \hat{a}_{\text{out}} \hat{a}_{\text{out}} &= |r|^4 \eta_a^4 \hat{a}_{\text{in}}^\dagger \hat{a}_{\text{in}}^\dagger \hat{a}_{\text{in}} \hat{a}_{\text{in}} + |r|^3 \eta_a^3 \hat{a}_{\text{in}}^\dagger \hat{a}_{\text{in}}^\dagger \hat{f}_a \hat{a}_{\text{in}} + |r|^3 \eta_a^3 \hat{a}_{\text{in}}^\dagger \hat{f}_a^\dagger \hat{a}_{\text{in}} \\ &+ \hat{a}_{\text{in}} |r|^2 \eta_a^2 \hat{a}_{\text{in}}^\dagger \hat{f}_a^\dagger \hat{f}_a \hat{a}_{\text{in}} + |r|^3 \eta_a^3 \hat{f}_a^\dagger \hat{a}_{\text{in}}^\dagger \hat{a}_{\text{in}} \hat{a}_{\text{in}} + |r|^2 \eta_a^2 \hat{f}_a^\dagger \hat{a}_{\text{in}}^\dagger \hat{f}_a \hat{a}_{\text{in}} + |r|^2 \eta_a^2 \hat{f}_a^\dagger \hat{f}_a \hat{a}_{\text{in}} \hat{a}_{\text{in}} + r\eta_a \hat{f}_a^\dagger \hat{f}_a^\dagger \hat{f}_a \hat{a}_{\text{in}} + |r|^3 \eta_a^3 \hat{f}_a^\dagger \hat{f}_a^\dagger \hat{a}_{\text{in}} \hat{f}_a \\ &+ |r|^2 \eta_a^2 \hat{a}_{\text{in}}^\dagger \hat{a}_{\text{in}}^\dagger \hat{f}_a \hat{f}_a + |r|^2 \eta_a^2 \hat{a}_{\text{in}}^\dagger \hat{a}_{\text{in}}^\dagger \hat{f}_a \hat{f}_a + |r\eta_a \hat{f}_a^\dagger \hat{f}_a^\dagger \hat{a}_{\text{in}}^\dagger \hat{f}_a + |r|^2 \eta_a^2 \hat{f}_a^\dagger \hat{a}_{\text{in}}^\dagger \hat{a}_{\text{in}} \hat{f}_a + |r\eta_a \hat{f}_a^\dagger \hat{a}_{\text{in}} \hat{f}_a \hat{f}_a + |r\eta_a \hat{f}_a^\dagger \hat{f}_a^\dagger \hat{a}_{\text{in}} \hat{f}_a + \hat{f}_a^\dagger \hat{f}_a^\dagger \hat{f}_a \hat{f}_a. \end{aligned}$$

The calculation of, $\hat{b}_{\text{out}}^\dagger$, follows the exact same procedure.

Appendix I

Beamsplitter and phaseshifter

I.1 Action of the beam splitter

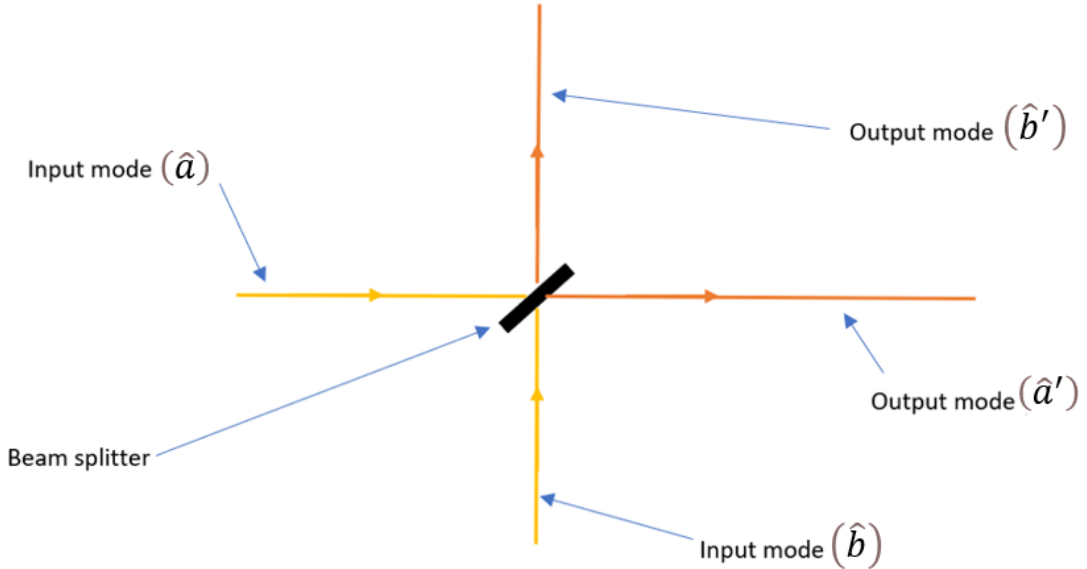


Figure I.1: Model of beamsplitter action.

It is important that we consider the action of a 50:50 beamsplitter as shown in figure I.1. If we consider a 50:50 beam splitter, with input beams given by operators \hat{a} and \hat{b} and output beams given by \hat{a}' and \hat{b}' , then the action of the beam splitter can be described by the transformation below

$$\hat{a} = \frac{1}{\sqrt{2}}(\hat{a}' + i\hat{b}') \quad \text{and} \quad \hat{b} = \frac{1}{\sqrt{2}}(\hat{b}' + i\hat{a}'). \quad (\text{I.1})$$

We can verify that the proper commutation relations are satisfied for these transformed operators, a necessary requirement for the preservation of unitarity across the beam splitter.

I.1.1 The action of a beam splitter on coherent states

$$|\alpha\rangle_a |\beta\rangle_b \xrightarrow{\text{BS}} \left| \frac{1}{\sqrt{2}}(\alpha + i\beta) \right\rangle_{a'} \left| \frac{1}{\sqrt{2}}(\beta + i\alpha) \right\rangle_{b'}. \quad (\text{I.2})$$

The photon number is preserved. Below is a proof for Eq. I.2,

$$|\alpha\rangle_a |\beta\rangle_b = \hat{D}_a(\alpha) \hat{D}_b(\beta) |0\rangle_a |0\rangle_b, \quad (\text{I.3})$$

where \hat{D} is the displacement operator, $\hat{D}_a(\alpha) = \exp[\alpha \hat{a}^\dagger - \alpha^* \hat{a}]$. Substituting this form of the equation into Eq. I.3 above and performing some algebraic calculations we get the equation below

$$\hat{D}_a(\alpha) \hat{D}_b(\beta) |0\rangle_a |0\rangle_b = \hat{D}_a\left(\frac{1}{\sqrt{2}}(\alpha + i\beta)\right) \hat{D}_b\left(\frac{1}{\sqrt{2}}(\beta + i\alpha)\right) |0\rangle_{a'} |0\rangle_{b'}. \quad (\text{I.4})$$

It follows from the above relation that

$$|\alpha\rangle_a |\beta\rangle_b \xrightarrow{\text{BS}} \hat{D}_a\left(\frac{1}{\sqrt{2}}(\alpha + i\beta)\right) \hat{D}_b\left(\frac{1}{\sqrt{2}}(\beta + i\alpha)\right) |0\rangle_{a'} |0\rangle_{b'}. \quad (\text{I.5})$$

We find that

$$\hat{D}_a\left(\frac{1}{\sqrt{2}}(\alpha + i\beta)\right) \hat{D}_b\left(\frac{1}{\sqrt{2}}(\beta + i\alpha)\right) |0\rangle_{a'} |0\rangle_{b'} = \left| \frac{1}{\sqrt{2}}(\alpha + i\beta) \right\rangle_{a'} \left| \frac{1}{\sqrt{2}}(\beta + i\alpha) \right\rangle_{b'}. \quad (\text{I.6})$$

hence we have derived Eq. I.2.

I.1.2 Phase shifter on coherent states

A phase shifter implements the following unitary operation onto the states

$$\hat{U}_{\text{PS}} = \exp[i\psi \hat{n}_b], \quad (\text{I.7})$$

where \hat{n}_b is a photon number operator

$$\hat{U}_{\text{PS}} \left| \frac{\alpha}{\sqrt{2}} \right\rangle_a \left| i \frac{\alpha}{\sqrt{2}} \right\rangle_b = \left| \frac{\alpha}{\sqrt{2}} \right\rangle_{a'} \left| i \frac{\alpha e^{i\psi}}{\sqrt{2}} \right\rangle_{b'}. \quad (\text{I.8})$$

Appendix J

Abbreviations

Bovine serum albumin (BSA)
Phosphate-buffered saline (PBS)
Limit of detection (LOD)
Standard quantum limit (SQL)
Surface plasmon resonance (SPR)
Spontaneous parametric down conversion (SPDC)
Two-mode squeezed vacuum (TMSV)
Two-mode squeezed displaced (TMSD)
 β -Barium Borate (BBO)
Interference filter (IF)
Fibre Coupler (FC)
Half wave plate (HWP)

Bibliography

- [1] P. Singh, Surface Plasmon Resonance: A Boon for Viral Diagnostics, *Life sciences Journal*, 8, 12245-12249 (2017).
- [2] T. Riedel, C. Rodriguez-Emmenegger, A. de los Santos Pereira, A. Bdajnkovb, P. Jinoch, P. Boltovets and E. Bryndaa, Diagnosis of EpsteinBarr virus infection in clinical serum samples by an SPR biosensor assay, *Biosensors and Bioelectronics*, 55, 278-284 (2014).
- [3] H. Hunt and A. Armani, Label-free biological and chemical sensors, *Nanoscale*, 2, 1544-1559 (2010).
- [4] P. Damborsk, J. vitel and J. Katrlk, Optical biosensors, *Essays in Biochemistry*, 60, 91-100 (2016).
- [5] P. Jahanshahi, Q. Wei, Z. Jie, M. Ghomeishi and S. Sekaran, Kinetic analysis of IgM monoclonal antibodies for determination of dengue sample concentration using SPR technique, *Bioengineered*, 17, 1-9 (2016).
- [6] B. Prabowo, R. Wang and M. Secario, Rapid detection and quantification of Enterovirus 71 by a portable surface plasmon resonance biosensor, *Biosensors and Bioelectronics*, 92, 186-191 (2017).
- [7] D. Kalashnikov, Z. Pan, A. Kuznetsov, and L. Krivitsky, Quantum spectroscopy of plasmonic nanostructures, *Physics Review X*, 4, 011049 (2014).
- [8] A. Otto, Excitation of nonradiative surface plasma waves in silver by the method of frustrated total reflection, *Zeitschrift fr Physik*, 216, 398-410 (1968).
- [9] E. Kretschmann and H. Raether, Radiative decay of non-radiative surface plasmon excited by light, *Zeitschrift fr Naturforschung*, 23, 2135-2136 (1968).
- [10] E. Kretschmann, Die Bestimmung optischer Konstanten von Metallen durch Anregung von Oberflächenplasmaschwingungen, *Zeitschrift fr Physik*, 241, 313-324 (1971).
- [11] D. Sage, K. Arai, D. Glenn, S. DeVience, L. Pham, L. Rahn-Lee, M. Lukin, A. Yacoby, A. Komeili and R. L. Walsworth, Optical magnetic imaging of living cells, *Nature*, 496, 486-489 (2013).
- [12] C. O' Connor, J. Adams, *Essentials of Cell Biology*, (NPG Education, Cambridge, MA, 2010).
- [13] H. Franquelim, A. Veiga, G. Weissmuller, N. Santos and M. Castanho, Unravelling the molecular basis of the selectivity of the HIV-1 fusion inhibitor sifuvirtide towards phosphatidylcholine-rich rigid membranes, *Biochimica Biophysica Acta*, 1798, 1234-1243 (2010).
- [14] M. Ebert, T. Grossman, E. Otten, R. Surkau, M. Thelen, M. Leduc, P. Bachert, M. Knopp and L. Schad, Nuclear magnetic resonance imaging with hyperpolarised helium-3, *The Lancet*, 347, 1297-1299 (1996).

- [15] M. Dietrich, K. Ogden and S. Katen, Structural insights into reovirus $\sigma 1$ interactions with two neutralizing antibodies, *Journal of Virology*, 91, 1-16 (2017).
- [16] Z. Lv, Y. Chu and Y. Wang, HIV protease inhibitors: a review of molecular selectivity and toxicity, *HIV/AIDS - Research and Palliative Care*, 7, 95104 (2015).
- [17] R. Ritchie, Plasma Losses by Fast Electrons in Thin Films, *Physical Review*, 106, 874881 (1957)
- [18] G. Matteo, Quantum Estimation for Quantum Technology, *International Journal of Quantum Information*, 7, 125137 (2011).
- [19] J. Dowling, Quantum Optical Metrology The Lowdown on High-N00N States, *Contemporary Physics*, 49, 125-143 (2008).
- [20] A. Kausaite, M. van Dijk, J. Castrop, A. Ramanaviciene, J. Baltrus, J. Acaite and A. Ramanavicius, Surface Plasmon Resonance Label-free Monitoring of Antibody Antigen Interactions in Real Time, *Biochemistry Molecular Biology Education*, 35, 57-63 (2007).
- [21] J. Lahiri, L. Isaacs, J. Tien and G. Whitesides, A Strategy for the Generation of Surfaces Presenting Ligands for Studies of Binding Based on an Active Esterase Common Reactive Intermediate: A Surface Plasmon Resonance Study, *Analytical Chemistry*, 71, 777-190 (1999).
- [22] S. Maier, *Plasmonics: Fundamentals and Applications*, (Springer, New York, 2007).
- [23] R. Wood, On a remarkable case of uneven distribution of light in a diffraction grating spectrum. *Philosophical magazine*, 4, 396-402 (1902).
- [24] H. Kimble, Y. Levin, A. Matsko, K. Thorne, and S. Vyatchanin, Conversion of conventional gravitational-wave interferometers into quantum non-demolition interferometers by modifying their input and or output optics, *Physics Review D*, 65, 022002 (2001).
- [25] O. Pluchery, Laboratory experiments for exploring the surface plasmon resonance, *European Journal of Physics*, 32, 585 (2011).
- [26] M. Malmqvist, BIACORE: An affinity biosensor system for characterization of bio-molecular interactions, *Biochemical Society Transactions*, 27, 335340 (1999).
- [27] M. Paris, Quantum estimation for quantum technology, *International journal of quantum information*, 7, 125-137 (2009).
- [28] M. Taylor and W. Bowen, Quantum metrology and its application in biology, *Physics Reports*, 615, 1-59 (2015).
- [29] M. Phelps, Positron emission tomography provides molecular imaging of biological processes, *Proceedings of the National Academy of Sciences of the United States of America*, 97, 92269233 (2000).
- [30] J. Lee, S. Yoon, H. Rah, M. Tame, C. Rockstuhl, S. Song, C. Lee and K. Lee, Quantum plasmonic sensing using single photons, *Optics Express*, 26, 29275 (2018).
- [31] J. Anker, Biosensing with plasmonic nanosensors, *Nature Materials*, 7, 442 (2008).
- [32] A. Meda, E. Losero, N. Samantaray, F. Scarimuto, S. Pradyumna, A. Avella, I. Ruo-Berchera and M. Genovese, Photon-number correlation for quantum enhanced imaging and sensing, *Journal of Optics*, 19, 094002 (2017).
- [33] D. Walls and G. Milburn, *Quantum Optics*, (SpringerVerlag, Berlin, 1995).
- [34] X. Hoa, A. Kirk and M. Tabrizian Towards Integrated and sensitive surface plasmon resonance biosensors: A review of recent progress, *Biosensors and Bioelectronics*, 23, 151-160 (2007).

- [35] W. Fan, B. Lawrie and R. Pooser, Quantum plasmonic sensing, *Physics Review A*, 92, 053812 (2015).
- [36] R. Pooser and B. Lawrie, Plasmonic Trace Sensing below the Photon Shot Noise Limit, *ACS Photonics*, 3, 8-13 (2016).
- [37] D. Davies, The structure and function of the aspartic proteinases, *Annual Review of Biophysics and Biophysical Chemistry*, 19, 189215 (1990).
- [38] C. Lee, F. Dieleman, C. Rockstuhl, S. Maier and M. Tame, Quantum Plasmonic Sensing: Beyond the Shot-Noise and Diffraction Limit, *ACS Photonics*, 3, 992-999 (2016).
- [39] J. Lee, T. Huynh, S. Lee, K. Lee, J. Lee, M. Tame, C. Rockstuhl and C. Lee, Quantum noise reduction in intensity-sensitive surface plasmon resonance sensors, *Physics Review A*, 96, 03383 (2017).
- [40] Y. Zeng, R. Hu, L. Wang, D. Gu, D. Gu, J. He, S. Wu, H. Ho, X. Li, J. Qu, B. Gao and Y. Shao, Recent advances in surface plasmon resonance imaging: detection speed, sensitivity and portability, *Nanophotonics*, 6, 5 (2017).
- [41] C. Caves, Quantum-mechanical noise in an interferometer, *Physics Review D*, 23, 16931708 (1981).
- [42] V. Giovannetti, S. Lloyd and L. Maccone, Quantum-enhanced measurements: beating the standard quantum limit, *Science*, 306, 13301336 (2004).
- [43] A. Touhami, *Biosensors and Nanobiosensors: Design and Applications. Nanomedicine*, (John Wiley and Sons, United states, 2008).
- [44] J. Peatross and M. Ware, *Physics of Light and waves*, (Brigham Young University, 2015).
- [45] D. James, P. Kwiat, W. Munro and A. White, Measurement of Qubits, *Physical Review A*, 64, 052312 (2001).
- [46] H. Bachor and T. Ralph, *A guide to experiments in quantum optics*, (Wiley, Germany, 2004).
- [47] C. Gerry and P. Knight, *Introductory Quantum Optics*, (Cambridge University Press, 2005).
- [48] I. Choi, Plasmonic Nanosensors: Review and Prospects, *IEEE Journal of Selected Topics in Quantum Electronics*, 18, 3 (2012)
- [49] A. Mair, A. Vaziri, G. Weihs and A. Zeilinger, Entanglement of the orbital angular momentum states of photons, *Nature*, 412, 313-316 (2001).
- [50] J. Homola, Surface Plasmon Resonance Sensors for Detection of Chemical and Biological Species, *Chem. Rev*, 108, 462-493 (2008).
- [51] E. Galvez, C. Holbrow, M. Pysher, J. Martin, N. Courtemanche, L. Heilig and J. Spencer, Interference of correlated photons: five quantum mechanics experiments for undergraduates, *American Journal of Physics*, 73, 127 (2005).
- [52] M. Nielson and I. Chuang, *Quantum Computation and quantum information*, 10th Anniversary edition, (Cambridge university press, 2001).
- [53] M. Barlow, *Statistics: A Guide to the Use of Statistical Methods in the Physical Sciences*, (Wiley, Manchester, 2013).
- [54] P. Drude, Zur elektronentheorie der metalle, *Physikalische Zeitschrift*, 1, 161 (1900).
- [55] L. Mandel, Sub-Poissonian photon statistics in resonance fluorescence, *Optics Letters*, 4, 205207 (1979).

- [56] J. Rarity and P. Tapster, Experimental violation of bells inequality based on phase and momentum, *Physics Review Letters*, 64, 2495-2498 (1990).
- [57] J. Guo, P. Keathley, and J. Hastings, Dual-mode surface-plasmon-resonance sensors using angular interrogation, *Optics Letters*, 33, 512-514 (2008).
- [58] J. Brendel, N. Gisin, W. Tittel and H. Zbinden, Pulsed energy time entangled twin-photon source for quantum communication, *Physical Review Letters*, 82, 2594-2597 (1999).
- [59] D. Klyshko, *Photons and non-linear optics*, (Gordon and Breach Science Publishers, Great Britain, 1988).
- [60] D. Strekalov, T. Pitman, W. Tittel, A. Sergienko, Y. Shih and P.G. Kwiat, Post selection free energy-time entanglement, *Physics Review A*, 54, 1-4 (1996).
- [61] Y. Ding, Efficient generation of far-infrared radiation from a periodically poled LiNbO₃ waveguide based on surface-emitting geometry, *Journal of the Optical Society of America B*, 5, 977-981 (2011).
- [62] L. Novotny and B. Hecht, *Principles of Nano-Optics*, (Cambridge University Press, New York, 2006).
- [63] J. Yerushalmy, Statistical problems in assessing methods of medical diagnosis with special reference to X-ray techniques, *Public Health Reports*, 62, 1432-49 (1947).
- [64] C. Xiao, A sensitivity benchmark for optical biosensors, *IOP Publishing Ltd*, 1-23 (2019).
- [65] B. Lambert, *A Students Guide to Bayesian Statistics*, (SAGE Publications Ltd, 2018).
- [66] D. Mago, PhD thesis, Implementation of a two-photon Michelson interferometer for Quantum-Optical Coherence Tomography (2012).
- [67] G. Stokes, The Stokes phenomenon and certain nth-order differential equations II. The Stokes phenomenon, *Transactions of the Cambridge Philosophical Society*, 9, 399 (1852).
- [68] E. Hecht and A. Zajac, *Optics*, (Addison-Wesley, Reading MA, 1974).
- [69] S. Pirandola, B. Bardhan, T. Gehring, C. Weedbrook and S. Lloyd, Advances in photonic quantum sensing, *Nature Photonics*, 12, 724733 (2018).
- [70] B. ZelDovich and N. Klyshko, Parametric generation of two-photon light in anisotropic layered media, *JETP Letters*, 9, 40 (1969).
- [71] L. Mandel, Sub-Poissonian photon statistics in resonance fluorescence, *Optics Letters*, 4, 205207 (1979).
- [72] C. McCormick, A. Marino, V. Boyer and P. Lett, Strong low-frequency quantum correlations from a fourwave-mixing amplifier, *Physics Review A* 78, 043816 (2008).
- [73] J. Anker, W. Hall, O. Lyandres, N. Shah, J. Zhao and R. Van Duyne, Biosensing with plasmonic nanosensors, *Nature Materials*, 7, 442 (2008).
- [74] B. Liedberg, Surface plasmon resonance for gas detection and biosensing, *Sensors and Actuators*, 4, 299 (1983).
- [75] Z. Ou, *Quantum Optics for Experimentalists* (Indiana University - Purdue University Indianapolis, 2017)
- [76] H. Bassa, S. Goyal, S. Choudhary, H. Uys, L. Disi, T. Konrad, Process tomography via sequential measurements on a single quantum system, *Physics Review Letters*, 92, 032102 (2015).

- [77] C. Osorio, S. Barreiro, M. Mitchell, and J. Torres, Spatial entanglement of paired photons generated in cold atomic ensembles, *Physics Review A*, 78, 052301 (2008).
- [78] P. Shun, PhD thesis, Towards a high quality polarization-entangled multi-photon source, National University of Singapore (2009).
- [79] S. Kawata, *Near-Field Optics and Surface Plasmon Polaritons*, (Topics in Applied Physics book series TAP, volume 81, 2001).
- [80] P. Kwiat, Ph.D, thesis, Non-classical effects from spontaneous parametric down conversion, *Adventures in quantum wonderland*, National University of California at Berkeley (1993).
- [81] P. Trojek, C. Schmid, M. Bourennane, H. Weinfurter and C. Kurtsiefer, Compact source of polarization-entangled photon pairs, *Optics Express*, 12, 276-281 (2004).
- [82] S. Walborn, C. Monken, S. Padua and P. Riberio, Spatial correlation, *Physics Review A*, 495, 87-139 (2010).
- [83] C. Gerry and P. Knight, *Introductory Quantum Optics*, (Cambridge University Press, 2005).
- [84] L. Guo , J. Jackman, H. Yang, P. Chen, N. Cho and D. Kim, Strategies for enhancing the sensitivity of plasmonic nanosensors, *Nanotoday*, 10, 213-239 (2015).
- [85] R. Demkowicz-Dobrzanski, M. Jarzyna and J. Koodyski, Quantum limits in optical interferometry, *Progress in Optics*, 60, 345 (2015).
- [86] C. Won, M. Olivo, *Surface Plasmon Resonance Imaging Sensors: A Review*, Springer Science Business Media New York (2014).
- [87] B. Rothenhuslar and W. Knoll, Surface-plasmon microscopy, *Nature*, 332, 615617 (1988).
- [88] J. Homola, Surface plasmon resonance sensors for detection of chemical and biological species, *Chemical Reviews*, 108, 462493 (2008).
- [89] D. Roberta, G. Spoto, Surface plasmon resonance imaging for nucleic acid detection, *Analytical and Bioanalytical Chemistry*, 405, 573584 (2013).
- [90] Y. Fang, Ligand-receptor interaction platforms and their applications for drug discovery, *Expert Opinion on Drug Discovery*, 7, 969988 (2012).
- [91] A. Shabani and T. Maryam, Design of a universal biointerface for sensitive, selective and multiplex detection of biomarkers using surface plasmon resonance imaging, *Analyst*, 138, 60526062 (2013).
- [92] M. Piliarik, P. Lucie and J. Homola, High-throughput SPR sensor for food safety, *Biosensors and Bioelectronics*, 24, 13991404 (2009).
- [93] C. Situ, M. Mooney, C. Elliott and J. Buijs, Advances in surface plasmon resonance biosensor technology towards high-throughput, food-safety analysis, *Trends in Analytical Chemistry*, 29, 13051315 (2010).
- [94] E. Mauriz, A. Calle, J. Mancls, A. Montoya and L. Lechuga, Multi-analyte SPR immunoassays for environmental biosensing of pesticides, *Analytical and Bioanalytical Chemistry*, 387, 14491458 (2007).
- [95] C. Shuman, P. Markgren, M. Hmlinen and U. Danielson, Elucidation of HIV-1 protease resistance by characterization of interaction kinetics between inhibitors and enzyme variants, *Antiviral Research*, 58, 235-242 (2003).

- [96] C. Jordan, A. Frutos, A. Thiel and R. Corn, Surface plasmon resonance imaging measurements of DNA hybridization adsorption and streptavidin/DNA multilayer formation at chemically modified gold surfaces, *Analytical Chemistry*, 69, 49395207 (1997).
- [97] M. Tame and C. Lee, Plasmonics and sensing beyond classical limit, *Proceedings of SPIE*, 11091, 110910J (2019).
- [98] C. Jordan and R. Corn, Surface plasmon resonance imaging measurements of electrostatic biopolymer adsorption onto chemically modified gold surfaces, *Analytical Chemistry*, 69, 14491456 (1997).
- [99] C. Tamayo, Ph.D, thesis, Spatial characterization of two photon states, Universitat Politècnica de Catalunya (2009).
- [100] R. Boyd, *Nonlinear Optics*, (Academic Press, New York, 2008).
- [101] B. Nelson, A. Frutos, J. Brockman and R. Corn, Near infrared surface plasmon resonance measurements of ultrathin films. 1. Angle shift and SPR imaging experiments, *Analytical Chemistry*, 71, 39283934 (1999).
- [102] B. Nelson, T. Grimsrud, M. Liles, R. Goodman and R. Corn, Surface plasmon resonance imaging measurements of DNA and RNA hybridization adsorption onto DNA microarrays, *Analytical Chemistry*, 73, 17 (2001).
- [103] K. Kim, S. Cheon, J. Park, H. Kim, J. Lee, I. Kim and H. Yi, Surface plasmon resonance (SPR) reflectance imaging: Far-field recognition of near-field phenomena, *Optics and Lasers in Engineering*, 50, 6473 (2012).